



**HAL**  
open science

# Etude d'états exotiques corrélés de la matière en basse dimension

Medha Soni

► **To cite this version:**

Medha Soni. Etude d'états exotiques corrélés de la matière en basse dimension. Condensed Matter [cond-mat]. Université Paul Sabatier - Toulouse III, 2016. English. NNT : 2016TOU30381 . tel-01760790

**HAL Id: tel-01760790**

**<https://theses.hal.science/tel-01760790>**

Submitted on 6 Apr 2018

**HAL** is a multi-disciplinary open access archive for the deposit and dissemination of scientific research documents, whether they are published or not. The documents may come from teaching and research institutions in France or abroad, or from public or private research centers.

L'archive ouverte pluridisciplinaire **HAL**, est destinée au dépôt et à la diffusion de documents scientifiques de niveau recherche, publiés ou non, émanant des établissements d'enseignement et de recherche français ou étrangers, des laboratoires publics ou privés.



# THÈSE

En vue de l'obtention du

## DOCTORAT DE L'UNIVERSITÉ DE TOULOUSE

Délivré par : *l'Université Toulouse 3 Paul Sabatier (UT3 Paul Sabatier)*

---

---

Présentée et soutenue le *16/09/2016* par :

Medha Soni

**Investigation of exotic correlated states of matter in low  
dimension**

---

---

### JURY

MADAME NATHALIE GUIHÉRY  
MONSIEUR GUILLAUME ROUX  
MONSIEUR ULRICH SCHOLLWÖCK  
MONSIEUR EDDY ARDONNE  
MONSIEUR MATTHIAS TROYER

President  
Rapporteur  
Rapporteur  
Examinateur  
Examinateur

---

**École doctorale et spécialité :**

*SDM : Physique de la matière - CO090*

**Unité de Recherche :**

*Laboratoire de Physique Théorique de Toulouse*

**Directeur de Thèse :**

*Didier POILBLANC*

**Rapporteurs :**

*Guillaume ROUX et Ulrich SCHOLLWÖCK*



# Acknowledgements

First and foremost, I would like to express my heartfelt gratitude to my supervisors Didier Poilblanc and Matthias Troyer for granting me this opportunity to pursue my doctoral studies under their guidance. I am extremely thankful to them for their availability, patience and invaluable guidance. I really value the time they devoted to me during my years of doctoral research. Throughout the course of the PhD, they provided encouragement, sound advice, good teaching and a lot of interesting ideas, making the journey extremely exciting.

I am grateful to Guillaume Roux and Ulrich Schollwöck for kindly accepting to be the referees for my thesis. I extend my gratitude to Nathalie Guihéry and Eddy Ardonne for being a part of the jury.

I would also like to thank my former professor at IIT, Suresh Sir, for being a great inspiration. Thank you for your teaching, guidance and the constant dose of motivation!

Many thanks to the best secretary possible, Malika, for taking care of all the (endless) administrative formalities and for helping me learn French.

I am very grateful to all the wonderful members of the FFC group at LPT for creating a stimulating ambience in the lab and the exchange of knowledge: Pierre, Mathieu, Sylvain, Nicolas, Fabien, Revaz, Aleksandra and Zoran. All the students and postdocs at LPT that made my stay enriching: Stefano, Gao, Nader, Marc, Xavier, Juan Pablo, Imam, David, Maxime, Guisepppe, Annaël, Bertrand, François, Vivek. Former members, Yasir and Anil, for helping me settle down comfortably in Toulouse. Thanks to all the PhD students of IRSAMC for the lunch and coffee breaks. Special thanks to Lionel, Guillaume, Isabelle, Mina, Muammar, Claudia, Thibaut, Diane, Fred, Sylvie, Sumiran for being wonderful friends. I am also thankful to those whose names I missed, for forgiving me!

I was fortunate to be surrounded by very friendly and talented people at the group at ETH Zurich and thank them all for making my stay extremely pleasant. Thank you Michele for helping me out with the project and otherwise. A special thanks to Jana for inspiring me in several ways and for being a wonderful friend. Many thanks to all other group members for providing a great environment: Juan, Andreas, Natalie, Ilia, Ethan, Vojtech, Dominik, Mario, Bettina, Guglielmo, Giuseppe, Jakub, Donjan, Slava, Alexey, Georg, Quansheng, Damian, Thomas, Alex, Kiryl.



On a personal note, I would like to thank my family for their love and confidence in me, for always encouraging me to aim high and making me what I am today. My parents, Papa, Mama and Daddy have supported me throughout my journey and helped me cross the hurdles that I encountered. Divya and Max have always been there when I needed emotional support. Didi and Jiju, I can't thank you enough for giving me a second home, for always welcoming me and pampering me. The precious moments spent with my little angels Alex and Myra were the best stress busters. Bhaiya and Marielena, thank you for the rejuvenating vacation and for the wonderful times we spent together. Abbu Didi, thank you for always being there and for leading the right path, for giving me a shoulder to cry and a companion to laugh endlessly.

My dearest friend, Manali, has stood by me through thick and thin. Thanks for all the amazing trips, never ending conversations and the crazy stuff we do! Thank you my friends in Zurich, Anvita and Sarvesh, for adding colour to the grey city!

A special thanks goes to my friend Camille for making my stay in Toulouse so very memorable. For making me believe in myself, for listening to all my complaints so patiently, for making me fall in love with the French culture, for all the little things that added immensely to my journey in France. Thank you Daniel for being a great friend and introducing me to Camille.

The most important mention is reserved for the end. Thank you, Lakshay, for all the support. There is absolutely no way I would have made it through without you!

# Contents

<b>I</b>	<b>Introduction</b>	<b>1</b>
<b>II</b>	<b>Numerical methods</b>	<b>11</b>
1	Exact Diagonalisation . . . . .	12
1.1	Implementation details . . . . .	13
1.1.1	Hilbert space . . . . .	13
1.1.2	Generating the Hamiltonian . . . . .	17
1.2	Lanczos Algorithm . . . . .	17
2	Matrix Product states . . . . .	20
2.1	General introduction to tensor networks . . . . .	20
2.2	Canonical form and Schmidt decomposition . . . . .	22
2.3	Ground state calculation . . . . .	27
2.4	Multigrid DMRG . . . . .	30
2.5	Time evolution . . . . .	31
2.6	Efficiency and errors in the DMRG algorithm . . . . .	32
<b>III</b>	<b>Ladders of non-Abelian anyons</b>	<b>35</b>
1	Introduction . . . . .	35
2	Warmup: One dimensional models . . . . .	38
2.1	Golden chain model . . . . .	38
2.2	Itinerant Fibonacci anyons in 1D . . . . .	39
3	Ladders of Fibonacci anyons . . . . .	40
3.1	Undoped ladders . . . . .	40
3.2	Doped ladders . . . . .	42
4	Phase diagrams . . . . .	44
4.1	Isolated rung limit . . . . .	44
4.2	Phase diagrams of weakly coupled rungs . . . . .	46
5	Discussion of phases and effective models . . . . .	48
5.1	Pairing and effective hard-core boson models . . . . .	48
5.2	Effective golden chains . . . . .	49
5.3	Effective $t$ - $J$ models: Two-leg ladder . . . . .	50
5.3.1	Effective model for charge degrees of freedom . . . . .	50
5.3.2	Numerical comparison between microscopic model and 1D $t$ - $J$ model . . . . .	52
5.4	Effective $t$ - $J$ models: Three-leg ladder . . . . .	56
5.4.1	Density $\rho < 1/3$ . . . . .	56

5.4.2	Density $1/3 < \rho < 2/3$ and $J_{\text{rung}} > 0$ . . . . .	56
5.4.3	Density $\rho > 2/3$ and $J_{\text{rung}} > 0$ . . . . .	58
5.4.4	Density $\rho > 2/3$ and $J_{\text{rung}} < 0$ . . . . .	58
5.5	Phase separation at large $J_{\text{rung}} > 0$ . . . . .	58
6	Effective model of heavy and light Fibonacci anyons . . . . .	59
6.1	The model . . . . .	59
6.2	Single particle dispersion . . . . .	61
6.3	Critical phase at generic fillings . . . . .	61
6.4	Possible topological gapped phase at $\tilde{\rho} = 1/2$ . . . . .	64
<b>IV Fermions in optical lattices</b>		<b>67</b>
1	Introduction . . . . .	68
2	Model . . . . .	70
3	Method . . . . .	71
4	Lattice loading protocols and observables . . . . .	72
5	Investigation of various target states . . . . .	74
5.1	Metallic target state . . . . .	74
5.2	Central band insulator . . . . .	76
5.3	Mott insulator target state . . . . .	78
5.4	Mott insulator with a metallic core . . . . .	83
<b>V Conclusion and perspectives</b>		<b>91</b>
<b>Appendix</b>		
<b>A Effective models</b>		<b>97</b>
1	Magnetic and Potential Interactions . . . . .	97
1.1	Two-leg ladder . . . . .	97
1.2	Three-leg ladder . . . . .	101
2	Kinetic terms . . . . .	104
2.1	Two-leg ladder . . . . .	104
2.2	Three-leg ladder . . . . .	108
3	Higher order terms . . . . .	112
<b>Bibliography</b>		<b>115</b>
<b>List of Publications</b>		<b>127</b>
<b>Résumé</b>		

# Chapter I

## Introduction

In condensed matter physics we have a wide variety of interesting models some of which are well understood and some that remain ambiguous to this date. Strongly correlated systems form an interesting area of research and provide plenty of systems that exhibit fascinating properties. Such systems have strong interactions between the constituent entities that are comparable to the dominant energy scale in the problem. As a result these interactions cannot be ignored or treated perturbatively, and we must treat the many-body interacting physics of the system in order to draw valid conclusions. The inability to reduce the problem to an effective one-body problem, leads us to go beyond mean field approaches.

Examples of such strongly correlated effects can be found in a wide variety of physical systems, such as superconductors, magnetic systems, quantum Hall systems, one-dimensional electronic systems etc. For instance, a key example is the case of Mott insulators where band theory fails to predict the correct conducting nature of the material. Band theory is based on an independent particle approach and predicts any material with a partially filled band (in particular with an odd number of electrons) to be a metal. This argument is violated for a couple of materials which are known to be tough insulators against the prediction of band theory. Such an effect can be understood when one takes into account the strongly correlated nature of the electrons in the material, giving rise to Mott insulators.

Fractional quantum Hall systems form another major subject of strongly correlated systems. They are characterised by the Hall conductivity being quantised at fractional multiples of  $e^2/h$  [1–3]. Such systems are known to exhibit quasiparticle excitations with fractional charge and fractional statistics. In particular, one cannot ignore the inter-particle interactions to obtain the correct physics in such a scenario. The quasiparticles in fractional quantum Hall systems are neither bosons nor fermions, rather somewhere in between. They are new entities called anyons. The simpler ones of this type being Abelian anyons where the statistics are any arbitrary phase, but more involved type of anyons are non-Abelian anyons where the exchange of two quasiparticles is associated with a unitary matrix.

Another example of strongly correlated systems is cold atoms in optical lattices.

Atomic gases form an interesting subject of study for various reasons [4–14]. Firstly, at low enough temperatures compared to the Fermi temperature they are able to attack the quantum mechanically degenerate regime with almost no imperfections. Secondly, the high degree of control and accuracy along with the variety of degrees of freedom inherently built in is a key feature of such systems. The interaction strength, confinement and lattice depth can be tuned independent of each other, making the setup extremely resourceful. Additionally, they allow us to mimic quantum systems of different quantum statistics and also mixtures of fermions and bosons. We can also study the effect of disorder and external perturbations by means of atomic gases. Different dimensions, lattice geometries can be created by playing with the laser beam intensities, orientation and polarisability. Optical lattices are able to realise condensed matter systems with the right dispersions and correlations. They are, hence, conceived as the quantum simulators of many-body physics and allow us to explore hard problems not studied theoretically or new physics of problems that have been widely studied.

This thesis includes the study of two projects. The first one dealing with non-Abelian anyons and the second one associated with the study of fermions in one dimensional optical lattices. Several works have explored combining anyons and optical lattices [15–17] following the generalisation to Pauli principle [18–20].

## Non-Abelian anyons

Symmetries are an indispensable part of physics. A symmetry is defined as a transformation acting on the system leaving it unchanged. Some symmetries are evident while some are rather subtle. Mathematically, the symmetry of a system is described by means of the action of a group on the system. There can be discrete symmetries such as reflection or continuous ones such as rotations, that are represented by discrete or continuous groups respectively. One important example is the exchange symmetry, namely what happens when we exchange two indistinguishable particles in the system. The exchange symmetry is intimately related to the statistics obeyed by the particle types in the system.

Quantum statistics is an important aspect of quantum mechanics and it lays down the rules for identifying different classes of particles. In three dimensions, exchanging two identical particles twice, is equivalent to doing no operation on them. In other words, the exchange operator must square to the identity. However, in two dimensions (2D) the scenario is very different where swapping the positions of two identical particles does not imply we did nothing to them. The wavefunction after exchanging identical particles twice might differ from the original one.

In three dimensions, the exchange of two particles in a quantum system can result in a phase change of either 0 or  $\pi$  for the wave function, leading to bosons and fermions respectively. Swapping particles twice keeps the wavefunction unchanged, while a single exchange at most picks up a sign. This in turn dictates the occupation of the single particle energy levels for bosons and fermions. While all

the bosons in a system could potentially condense into one single particle state, the fermions are not allowed to do so. The fermionic wavefunction must be antisymmetric under the exchange of two identical fermions, thus must vanish when identical fermions occupy the same state. The fermion and boson wavefunctions form the one-dimensional representations of the permutation group ( $S_N$ ) for  $N$  indistinguishable particles.

In two dimensions, the wavefunction enjoys much more freedom under an exchange. It could pick up an arbitrary phase or even a unitary matrix when two identical particles are swapped with each other. The term ‘anyon’ was coined by F. Wilczek since the wavefunction can acquire *any* phase when two particles are exchanged. Mathematically speaking, the anyonic wavefunctions form the representations of the Braid group, fermions and bosons being only special cases of anyons in two-dimensions. These anyons are observed as excitations, localised disturbances of the ground state in systems with topological order. Rich behaviour emerges especially for non-Abelian anyons, for which the exchange of two anyons is described by a unitary matrix [21, 22].

In the mathematical framework, quantum statistics is closely related to the notion of the fundamental group or the first homotopy group which is a topological invariant. This group forms the equivalence class of all closed paths in space, it determines whether two paths having the same end points could be continuously deformed into each other. The fundamental group for  $SO(d, 1)$  with  $d > 2$  is the discrete group  $\mathbf{Z}_2$ , thus allowing for only two possibilities - fermions and bosons. Whereas, in 2D the fundamental group  $\Pi_1(SO(2, 1)) = \mathbf{Z}$ , thus allowing an arbitrary phase change for the wavefunction. It is well known that such quantum systems give rise to anyonic quasiparticle excitations [23–25].

Non-Abelian anyons can be described as so-called quantum deformations of the usual  $SU(2)$  spins. Formally, they are described by  $SU(2)_k$  Chern-Simons theories. These  $SU(2)_k$  theories are obtained by ‘deforming’ the  $SU(2)$  algebra so as to retain only the first  $k + 1$  representations. The most widely studied models are the  $k = 2$  and  $k = 3$  theories that describe ‘Ising’ and ‘Fibonacci’ anyons respectively. The two-particle fusion rules for non-Abelian anyonic theories allow for multiple fusion channels. Thus, systems of many non-Abelian anyons are naturally associated with a degenerate ground state manifold. This is a salient feature of non-Abelian anyonic systems that can be employed for quantum computing [26–31].

As computational methods form an important part of the modern-age scientific research and analysis, one is encouraged to think of efficient ways to speed up computations. In 1982, it was suggested by Feynman that many-body quantum Hamiltonians could be solved exponentially faster on a quantum computer as compared to a classical one [32]. It was shown that a computer that uses quantum states for computation is more powerful than its classical counterpart [33, 34]. This hints towards the development of quantum computers and the whole field of quantum computing, to run present-day algorithms and possibly more advanced ones with significant speed up compared to the classical computing schemes.

We can look at quantum computation as a three stage process - creation of quantum bits (also called qubits, the quantum analog of classical bits), manipulating the bits to perform calculations and eventually measuring the final outcome. We would, ofcourse, need a reasonably large number of quantum gates to be able to implement all possible quantum algorithms. Any computer, classical or quantum, will be prone to errors which must be minimised in order for the computation to be reliable. In classical computers, the error correction is done by keeping multiple copies of information to tally them with one another. For a quantum computer, this method is not going to work, as a measurement leads to wavefunction collapse. If we intend to check for errors during an intermediate step of the calculation, the measurement would destroy the actual quantum state and hence the calculation. Thus, one needs to come up with other ways of building a practical quantum computer that would be fault-tolerant. It was shown that anyons could be used to implement fault-tolerant quantum computation [30, 35–37]. This would be a huge step forward as it would eliminate errors very effectively. The plausible application of non-Abelian anyons for fault-tolerant quantum computation has led to a significant amount of research in this field [38].

Quantum computing is a promising field of research that has the potential to outperform its classical counterpart. The degenerate ground state manifold of non-Abelian anyon models is separated from the excitation by an energy gap, a feature of all topological models, which can be considered as the relevant Hilbert space to implement quantum gates. The quantum gates are constructed such that exchange of anyons (braiding) are the only operations acting on the qubits. The action of a gate on any qubit would only be to ‘rotate’ it in the degenerate subspace. On this ground state manifold braiding of non-Abelian anyons acts in a non-commutative way, by bringing about a non-trivial transformation in the degenerate manifold of the many-quasiparticle Hilbert space. Thus, all operations are performed in a non-local way, rendering zero overlap with local perturbations, making the system naturally immune to errors. Thus, anyons can be effectively used for fault-tolerant quantum computation. Not all anyonic theories are known to be universal. Though Ising anyons (also an example of non-Abelian anyons) have been detected in the lab, it is however known that they are not suitable for universal quantum computation. Fibonacci anyons, on the other hand, have not yet been detected in the lab but do promise to be fit for universal quantum computation.

Owing to the potentially useful applications of Fibonacci anyons, they continue to attract the interest of several theoretical and experimental physicists. Models of interacting non-Abelian anyons draw motivation from quantum spin models, and in particular the Heisenberg model, which has been studied for a wide range of lattices including one-dimension (1D) chains and ladders of  $SU(2)$  spins. Non-Abelian anyons are expected to be present in topologically ordered systems including certain fractional quantum Hall states [39–42],  $p$ -wave superconductors [43], spin models [44–47], solid state heterostructures [48–53] and rotating Bose-Einstein condensates [54]. In particular, Fibonacci anyons occur as quasi holes in the  $\mathbb{Z}_3$  Read-Rezayi state which might be able to describe the  $\nu = 12/5$  frac-

tional quantum Hall state [55]. While several experiments have shown evidence for emergent Majorana modes [56–60], experimental evidence of Fibonacci anyons is yet to come. Interactions between non-Abelian anyons can be modelled by generalisations of the spin-1/2 Heisenberg model. These models have been studied for chains of Fibonacci anyons [61] including nearest neighbour couplings [62] and also longer range couplings [63] have been studied. Chains of higher spin quasiparticles have also been explored [64–68], critical phases have been identified and the corresponding conformal field theory (CFT) has been obtained from numerical simulations [69]. The effect of disorder for chains of Fibonacci anyons has been investigated [70, 71].

As a step towards understanding the collective behaviour of itinerant non-Abelian anyons, these chains can be doped with mobile holes, inspired by the electronic  $t$ - $J$  model [72–75]. Electrons confined in 1D can exhibit the phenomenon of “spin-charge separation”, where the spectrum can be interpreted in terms of two independent pieces, one arising from electric charge without spin, and the other from a spinon without any charge [76]. Analogously low-energy effective  $t$ - $J$  models have been analysed for the case of doped chains of Fibonacci (and Ising) anyons. These models exhibit a fractionalisation of the spectrum into charge and anyonic degrees of freedom [77, 78], an extension of a phenomenon that exists in Luttinger liquids [79–81]. As a step towards two dimensions, anyon models have been investigated on chains coupled to form so-called quantum *ladders* of non-Abelian anyons, which provide anyonic generalisations of the 2D quantum magnets [82, 83].

In the first project of this thesis, we have analysed the physics of mobile non-Abelian anyons beyond one-dimension, which is a general fundamental and timely issue. Our aim has been to construct the simplest possible model of 2D itinerant interacting anyons in close analogy to fermionic systems and inspired by the previous anyonic studies. As discussed later, this model takes the form of an anyonic 2D  $t$ - $J$  model very similar to its electronic 2D analog and to its 1D anyonic version mentioned above. Also a natural geometry to consider, interpolating between 1D and 2D, is the ladder geometry – e.g. a system of a finite number of coupled chains – used both for electronic spins and localised anyons. More precisely, we combine the anyonic models mentioned above, by studying *doped* quantum ladders of Fibonacci anyons consisting of two or three chains. In particular, we ask the question if spin-charge separation survives in the ladder model for non-Abelian anyons. Furthermore, in the study of this model, we have found a novel physical effective model that possibly hosts a topological gapped state.

## Fermions in optical lattices

Ultracold atoms in optical lattices engage the attention of several physicists, both from the experimental and theoretical points of view. These systems form an ideal setup to study strongly correlated systems under the influence of a periodic potential. This particular regime of strongly correlated systems is attained when



the interactions between the components of the system are much more important energetically than the kinetic energy. In the cold atoms setup a large interaction can be achieved by Feshbach resonances and the kinetic energy can be lowered by going to the deep lattice regime. Some aspects of these systems are explained by mean field theories whereas some remain unexplained. There are experiments that go beyond the presently available theoretical tools to investigate rather complex issues.

During the early years the focus of the cold atom experiments was on bosonic systems. Until the first realisation of the Bose-Einstein condensate (BEC) that came only in 1995 [84–86], the study of bosons was extremely intriguing, which continues to be the case even now. But soon after the success of the bosonic experiments, experimentalists and also theorists became interested in looking at the complementary system of fermions. The two have quite different statistics but similar range of temperatures to be in the quantum degenerate regime, where the wavepackets of individual atoms overlap.

The first success with cold Fermi gases came in 1999 [87] followed by a few others soon thereafter [88]. In the first realisation, the temperature attained was a fraction of the Fermi temperature by using a two spin component mixture of  $^{40}\text{K}$  atoms with a negative scattering length. For this gas, Bardeen-Cooper-Schrieffer (BCS) theory predicts the occurrence of a superfluid phase at low enough temperatures. Since the gas was extremely dilute the critical temperature for this transition was too small, much smaller than the temperatures obtained in the experiment. Thus, this superfluid phase could not be observed. The subsequent works [89, 90] did attain the quantum degeneracy regime by sympathetic cooling using fermion-boson mixtures. This cooling approach has also been fruitful in other experiments [91, 92].

The major breakthrough in the study of ultracold Fermi gases came with the understanding that Feshbach resonances could prove to be a huge aid in tuning the interaction strength and nature just by changing the magnetic field. The BEC-BCS crossover regime has been studied extensively for strongly interacting atomic Fermi gases [93–99]. The possibility to confirm the theoretical prediction of the superfluid-Mott insulator transition [100] by loading a BEC into an optical lattice and varying the depth of the lattice potential was given in 1998 [101] and observed in a seminal experiment in 2002 [102]. This was followed by experiments involving fermions [103] and Bose-Fermi mixtures [104, 105]. Several other experiments inspecting strongly correlated fermi gases in optical lattices have been successfully performed [106–112].

At the outset, the atomic gases seem to be quite far from electronic gases. Though dissimilar in certain respects, they are able to mimic the electronic gas quite efficiently. An electron gas has a Fermi temperature  $T_F \sim 10^4\text{K}$ , making them quantum mechanically degenerate even at room temperature. Typical densities of electron gas are of the order  $n \sim 10^{23}\text{cm}^{-3}$  and the dominant interaction being the Coulomb interaction between charged particles. The scenario is somewhat different for atomic gases. The dominant interactions in this case of neutral atoms are

the van der Waals and the Fermi temperature being of the order of nanoKelvin to microKelvin. Therefore, to be in the quantum mechanically degenerate regime, the temperature must be lower than a microKelvin, thus making *ultracold atomic gases* the interesting system to look at. Dilute gases do lead to some degree of cooling but not enough to reach the ultracold regime required to be quantum mechanically degenerate. Other cooling methods such as evaporative cooling or laser cooling must be employed to attain that low temperatures. These methods were first implemented for  $^{87}\text{Rb}$  and  $^{23}\text{Na}$  atoms in 1995 [84, 86]. The low densities used in cold atomic gas experiments  $n \sim 10^{13}\text{cm}^{-3}$ , however, are important for certain other reasons. Such densities render the atomic gases dilute in the sense that the inter-particle distance is much greater than the range of the interaction potential. These dilute gases suppress significantly the 3-body recombination rate compared to the 2-body collision rate which is important for re-thermalisation in the process of sample preparation. The atomic gas which is actually in a metastable state attains an optimal lifetime (seconds to minutes) ideal for experimental procedures, which would not be the case for densities lower than  $10^{12}\text{cm}^{-3}$ . It also turns out that this range of densities localises one atom per site on average in the optical lattices that can be created by the available lasers [113].

Modern cold atom experiments are able to perform single-site in situ imaging, thus behaving as a quantum gas microscope [114]. Noise correlations can be used to understand the nature of quantum correlations and fluctuations. However, some quantities of interest are yet to be reached in experiments, namely long range AFM order, d-wave superfluidity, exotic superfluidity for imbalanced spin populations etc. The major limitation to such measurements is the relatively high temperatures present in the fermionic gas experiments [115]. Efficient cooling methods and protocols must be designed in order to probe these exciting low-temperature phases [116].

In cold atom experiments, the choice of elements used depends on several factors, being able to cool them down to the desired limit being the most important constraint. Alkali elements are preferred for experiments due to their rather simple electronic structure. They have only one valence electron, and the completely filled orbitals along with the nucleus can be effectively treated as one core, making the system an an interesting candidate to investigate experimentally. Only two stable naturally occurring fermionic isotopes are known  $^{40}\text{K}$  and  $^6\text{Li}$ . The experimentalists choose  $^{40}\text{K}$  because they can be used with  $^{87}\text{Rb}$  as a bosonic coolant that has transition frequency similar to that of  $^{40}\text{K}$ . Also, deep lattices are easier to simulate due to the large mass of  $^{40}\text{K}$ .

The evaporative cooling of a trapped atomic cloud, i.e. without the optical lattice potential, has been proven to be a very effective process. Current protocols are able to achieve temperatures as low as  $T/T_F \approx 0.08$  [108, 109]. Such a low temperature is lost in the presence of the optical lattice. In principle the process of lattice loading should be performed adiabatically, but in practice one will always do so in a finite time, thus deviating from the completely adiabatic regime. The observation of temperatures higher than preferred are quantified by the amount of excess heat

generated in the system.

The breakdown of the adiabatic lattice loading for optical lattices has been investigated in multiple works [116, 117]. Optimising ramp shapes [118], fast-forward loading schemes [119] where an auxiliary potential assists in lattice loading, modulating trap frequency and shape during loading [120–123], starting from a low entropy interacting state [124], introducing compensating laser beams [125], using disordered potentials [126], Peltier cooling [127] are some ways to overcome effects of non-adiabaticities and achieve lower temperatures in optical lattices. Non-interacting fermions have been studied within superlattice geometries in the continuum [128] for both homogenous and trapped set ups. Density redistribution causes population of higher Bloch bands but can be handled by optimising the initial part of the loading schedule until the gap to higher Bloch bands opens up. Another way to cool down Fermi gases in a deep optical lattice is to use a Bose-Einstein condensate gas as a reservoir to transfer the excess entropy per particle [129].

Numerical studies based on the single-band approach inherently assume a deep optical lattice. The loading scheme starts from the shallow (or no) lattice regime, and is thus not captured by the former scheme. Previous studies have analysed optical lattices using theoretical mean field models in one dimension, but are unable to assess the effects of low-lying excitations. Our approach is based on the continuum model which is valid when the lattice is turned off, thus is able to record the entire loading schedule.

The study of non-adiabaticities in lattice loading and novel cooling schemes are important to achieve the desired low temperatures in experiments. In ref. [123] some of the authors studied a system of bosons in a 1D optical lattice in the continuum description. For homogenous systems without a confining trap only minimal heating effects, less than 1% of the effective hopping, were encountered even for reasonably short ramp times. Moreover the heating was seen to decrease significantly as longer ramp times were considered. This was in stark contrast to the finding when the Hamiltonian included a harmonic confinement, where the heating was maintained at a rather high value, remaining more or less constant with ramp time. The key point made by the authors was that the harmonic trap hindered the efficient density redistribution resulting in a final state which is qualitatively quite different from the desired target state. Thus, density redistribution effects were attributed as the major cause of excess heat generated in the system. This issue was overcome by introducing a protocol to dynamically reshape the trapping potential during the process of lattice loading in order to facilitate appropriate redistribution of particles in the lattice. In particular, the harmonic trap was linearly modulated during the optical lattice ramp up, which was observed to restore the scaling behaviour of the excess heat with ramp time as in the case of a homogenous system.

The second project in this thesis involves the investigation of the density redistribution effects for a 1D system of fermions. We aim to understand if defects caused by poor distribution of particles during lattice loading are important for

the fermionic case, forbidding the atoms to cool down to the desired level. Here we survey four different states, which would be referred to as *target states* in the following sections: (i) a metallic target state with a continuous local particle density, (ii) a Mott insulating state at the edges with a central band insulating bulk, (iii) a pure Mott insulator at unit filling and (iv) a Mott insulator at the edges with a central metallic core. The target states are characterised by different density profiles and depend on the chosen parameters of the model. The model admits a spatially dependent chemical potential that allows characteristically different phases, such as metallic and insulating ones to co-exist in the target states. We initially show that for the metallic state and the central band insulator, the simple adiabatic ramp already shows negligible defects, whereas the other states the pure Mott insulator and one with a metallic core suffer from heating effects during lattice loading. A scan of the time-evolution of the local density profile leads us to conclude that indeed density defects are the key problem, thus we focus our attention to devise protocols that allow better redistribution of particles during the ramping. Similar to the bosonic case we devise improved ramp up schemes where we dynamically change one or more parameters of the system in order to reduce density defects. All these schemes are geared towards broadening the initial peak of the number density at the trap centre. We show that this can be achieved in a number of ways, that will be suitable in the experiments. The first approach is to test the protocol put forward for bosons i.e. to dynamically reshape the trapping potential. Additionally in this work, we show that tuning the interaction strength, that comes about as one of the easier parameters to control in experiments, is another way to achieve lower temperatures. We also mention yet another approach where the interaction strength and trapping potential can be tuned simultaneously during the lattice loading that indeed brings down the excess heat in the system significantly. The optical lattices provide a high degree of control, making all the protocols straight-forward to test experimentally.

### Structure of the thesis

This thesis is organised as follows. In Chapter II we describe the numerical methods used to study the two different problems, namely exact diagonalisation for non-Abelian anyons and Matrix Product States for fermions in optical lattices. Chapter III presents our complete study on the subject of Fibonacci anyons commencing with a brief introduction to the subject, describing the model investigated, discussing the phase diagrams and the effective one-dimensional models obtained numerically and analytically and finally presenting a novel model obtained in our study - the heavy and light  $\tau$  model. In Chapter IV we describe our analysis of fermions in optical lattices. We discuss the model, explain the lattice loading protocols and present results of our investigation of various target states. Chapter V lays out the conclusions and perspectives of the projects explored in this thesis. In the technical appendix A, we outline the analytical calculations of effective models for the Fibonacci models.



# Chapter II

## Numerical methods

Condensed matter physics has a lot of interesting problems to offer, described by varied geometries, continuous or discrete models with different particle compositions, interactions between them, those obeying certain conservation laws etc. However, as the complexity of the problems grow, a huge majority of them become hard to solve exactly (or even with approximations) analytically. When we consider systems that include strong interactions between the particles (spins, fermions, bosons or anyons), there are strong correlations between the different components of the system. It thus becomes impossible to map the problem to a single particle problem, making it imperative to consider the many body picture thus making the analytical treatment increasingly harder. We are thus required to resort to other reliable methods that allow us to study the systems of interest, numerically approaching the problem being of particular interest. Our goal remains to study the system and its properties such as ground state energy, low lying excitations, entropy, correlation etc as accurately as possible.

Numerical methods have made tremendous progress in the last decades and provide us a good way to do so. To our aid we now have a wealth of numerical methods to treat problems of strongly correlated systems such as tensor network techniques, exact diagonalisation, monte carlo methods etc, each coming with their own advantages and drawbacks. Exact diagonalisation provides the spectrum of the system with high precision but is limited to very small system sizes. The quantum Monte Carlo methods are able to handle large system sizes, but are plagued with the sign problem thus rendering them inefficient for the study of fermionic systems in more than one dimension and spin models with frustrated interactions. Mean field approaches fail to capture the quantum correlations while stochastic series expansions are based on perturbation theory methods.

Tensor network algorithms have attracted the interest of many scientists in the recent past and made significant progress. Not that these methods are perfect for every scenario, but their efficiency is dependent on the amount and structure of entanglement in the system. There is now a whole sea of such methods, some examples being Density Matrix Renormalisation Group (DMRG), Projected Entangled Pair States (PEPS), Tensor Renormalisation Group (TRG), Tensor-Entanglement

Renormalisation Group (TERG), Monte Carlo Matrix Product States, Tree Tensor Networks, Continuous Matrix Product States etc. The DMRG method is found to be very useful for fermionic systems and frustrated spin systems in one-dimension but less advantageous in higher dimensions due to the growing entanglement. The method of PEPS is well suited for two dimensions but the computation cost growing rapidly with the dimensionality of the tensors, hampers the efficiency eventually. In this chapter we describe the numerical methods that we have used to examine the problems in this thesis. The ladder models of Fibonacci anyons were studied using Lanczos exact diagonalisation techniques. For the analysis of fermions in optical lattices, we used the Matrix Product States (MPS) that comes under the tensor network umbrella of numerical methods. We now discuss these two methods briefly.

## 1 Exact Diagonalisation

Ideally we would like to diagonalise the Hamiltonian completely in the relevant many-particle basis to obtain all the information about its energy eigenvalues and the corresponding eigenstates. In practice, this task is a huge challenge since the size of the Hilbert space (in which the Hamiltonian lives) is growing exponentially with the number of particles  $N$  in the system making the diagonalisation problem extremely hard with growing system size. Exact diagonalisation methods encompass several approaches that provide numerically exact results by directly diagonalising the Hamiltonian matrix for the system. These techniques restrict us to rather small system sizes such that the Hilbert space is tractable, thus making extrapolations to the thermodynamic limit (where  $N \rightarrow \infty$ ) hard and sometimes even unreliable.

The most straight-forward approach is to use the complete diagonalisation method, where the diagonalisation procedure yields all eigenvalues and eigenvectors of the Hamiltonian matrix. This approach, although the simplest to implement, is rather demanding in computation time and memory. In condensed matter physics we are very often interested only in the ground state along with the low-lying excitations. Thus we can exploit iterative diagonalisation methods that allow us to reach significantly larger system sizes than those that could be handled with the complete diagonalisation approach. These methods are also able to compute dynamical properties as well as treat finite temperature calculations. The largest system sizes studied using Exact Diagonalisation, for example, are known to be spin -1/2 models with  $N \approx 40$  spins in the lattice [130].

Even though exact diagonalisation methods are only able to treat small finite clusters, it is still advantageous to use these exact methods. Firstly, they provide benchmarks to test the validity of results obtained from other schemes such as Monte Carlo methods. Furthermore, this method serves as a good medium to learn more about the symmetry properties of the system. We can make use of the symmetries of the system to block-diagonalise the Hamiltonian into smaller

pieces. Each of these blocks can be considered as a separate matrix that can be diagonalised individually, thereby reducing the computational cost severely. Each block corresponds to a specific symmetry sector labelled by a good quantum number corresponding to the inherent symmetry of the system. Ofcourse, some symmetries would be rather simple to implement numerically while some typically hard. An important example of a widely implemented symmetry is the translation symmetry that leads to momentum conservation. The Hamiltonian is split into blocks (the number of blocks being equal to the length of system  $L$ ) labelled by the different momenta, which are then diagonalised individually. This symmetry gives an overall reduction in the size of the Hilbert space by a factor  $L$ , thus allowing us to push the calculations to larger system sizes. The use of these quantum numbers may eventually turn out to be useful for classifying the different excitations.

## 1.1 Implementation details

Our numerical simulations of non-Abelian anyons on two- and three-leg ladders have been performed by exact diagonalisation using the Lanczos algorithm as will be explained in section 1.2. We exploit periodic boundary conditions along the leg direction to implement translation symmetry. This allows us to block-diagonalise the Hamiltonian into  $L$  blocks labeled by the total momentum  $K = 2\pi\frac{m}{L}$  ( $m$  being an integer), which reduces the size of the Hilbert space, which is the major limiting factor in the simulations, by a factor  $L$ . We first explain how we generate the many-body basis and the Hamiltonian of the system which will eventually be diagonalised using a Lanczos routine.

### 1.1.1 Hilbert space

The model of doped Fibonacci ladders is described in terms of two quantum numbers : the  $U(1)$  charge and the anyonic spin. The most homogenous way to represent this system would be to keep information about both these quantum numbers on the bond labels of the fusion tree. However, since the  $U(1)$  charge is Abelian and counts the number of anyons in the system, it is advantageous to label it separately. Thus, the system is described by a fusion tree with two labels, one for each of the quantum numbers as shown in Fig. II.1. The  $U(1)$  charge is labeled by the position of the anyons on the sites (orange circles) and the non-Abelian anyonic spin is labeled by the bond labels (red circles) of the fusion tree.

We first need to store the basis states of the Hilbert space. We can compactly store the configuration by means of two separate integers, one each for the  $U(1)$  charge (site labels) and non-Abelian charge (bond labels). Each bit of these integers represents a single site (or bond) label which is set to 1 if an anyon is present on that particular site (or bond), otherwise is set to 0. The bond labels of the fusion tree are constrained by the fusion rules that must be satisfied on each trivalent vertex. For the Fibonacci theory, the fusion rules mean the following. If the site  $Y_i$  is labelled by 0, then the adjoining bond labels  $x_i$  and  $x_{i+1}$  must be identical.



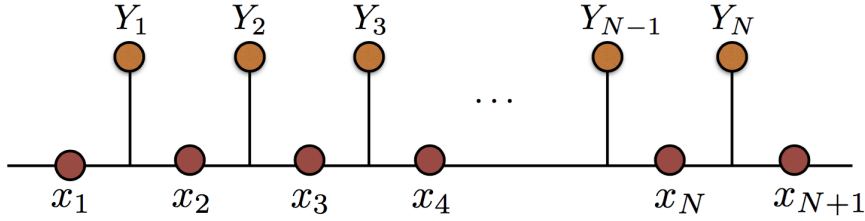


Figure II.1: Schematic representation of a fusion tree. The orange circles are the site labels and the red ones are the bond labels.

If the site  $Y_i$  is labelled by a 1, then the adjoining bond labels  $x_i$  and  $x_{i+1}$  can both not be 0 simultaneously but all other combinations of 0 and 1 are allowed, *i.e.*  $(x_i, x_{i+1}) \in \{(1, 0), (0, 1), (1, 1)\}$ .

Since the model conserves the number of particles in the system, the total number of 0's and 1's in the integers for the  $U(1)$  charge must be fixed in the system for a given particle density. Say, for example, we have a system of  $L$  sites with  $N$  particles. The integers for the site labels, hence, carry  $L$  bits. The set of site labels contains all those integers that have exactly  $N$  out of  $L$  bits set to 1. Let us call  $\mathcal{S}$  the set that contains all the possible states for the site labels consistent with the number of anyons in the system. Further for each element in  $\mathcal{S}$ , we enumerate all allowed configurations for the bond labels by imposing the fusion rules at every trivalent vertex of the fusion tree. The states for the bond labels belong to the set  $\mathcal{B}(|\psi_{\text{site}}\rangle)$  that is defined by the site labels.

We illustrate this method of writing the states in the Hilbert space for a section of the fusion path with two vacant sites and two anyons ( $L = 4, N = 2$ ). In figure II.2, we show two possible configurations for this case. The site labels are represented by blue (anyons) and white (holes) circles. The bond labels,  $x_i$ , are shown by red circles. The holes may be present on any two of the four sites, however we must record the information about their position since different site labels correspond to a different set of bond labels.

For example in figure II.2(a) the state for the site charges would read  $|\psi_{\text{site}}^a\rangle = |0011\rangle$  but for figure II.2(b) the corresponding state would be  $|\psi_{\text{site}}^b\rangle = |0101\rangle$ . Owing to the non-Abelian nature of the theory, for each of these site configurations we obtain several configurations for the bond labels that are consistent with the fusion rules.

For example, for the case II.2(a) the bond labels  $|\psi_{\text{bond}}^a\rangle$  belong to the set

$$|\psi_{\text{bond}}^a\rangle \in \mathcal{B}(|\psi_{\text{site}}^a\rangle) = \{|00010\rangle, |00011\rangle, |11101\rangle, |11110\rangle, |11111\rangle\} \quad (\text{II.1})$$

whereas for the case II.2(b) the bond labels  $|\psi_{\text{bond}}^b\rangle$  belong to the set

$$|\psi_{\text{bond}}^b\rangle \in \mathcal{B}(|\psi_{\text{site}}^b\rangle) = \{|00110\rangle, |00111\rangle, |11001\rangle, |11110\rangle, |11111\rangle\}. \quad (\text{II.2})$$

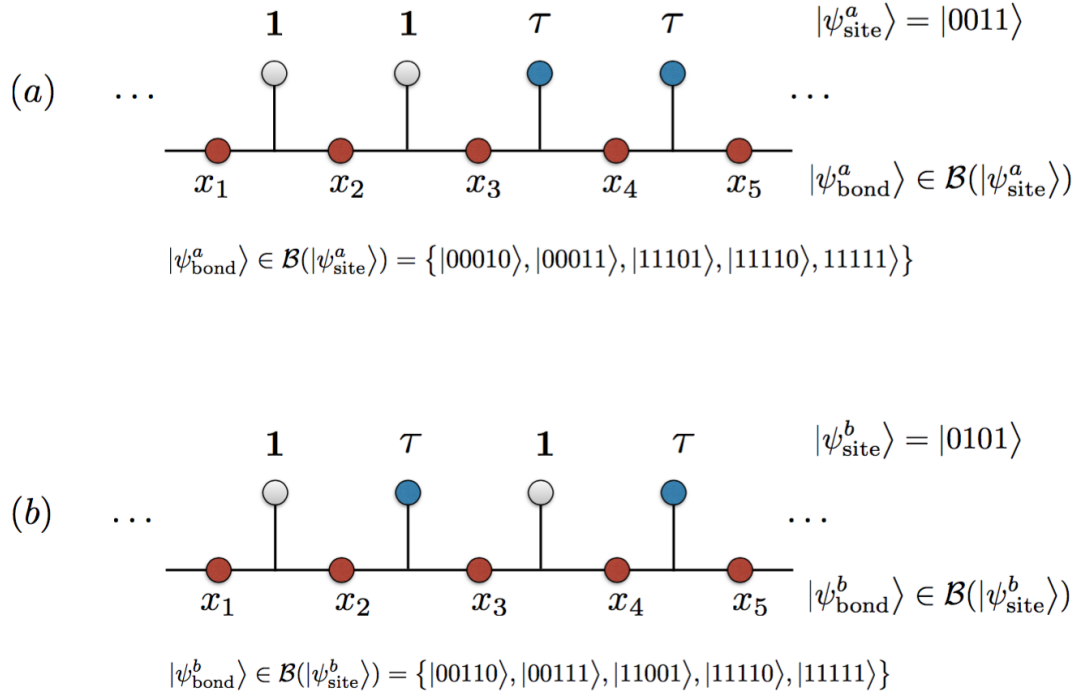


Figure II.2: Illustration of the Hilbert space for two possible site configurations for a section of the fusion path with two particles and two vacant sites. The state for the site labels is (a)  $|\psi_{\text{site}}^a\rangle = |0011\rangle$  and (b)  $|\psi_{\text{site}}^b\rangle = |0101\rangle$ . The state for the bond labels is  $|\psi_{\text{bond}}\rangle = |x_1x_2x_3x_4x_5\rangle \in \mathcal{B}(|\psi_{\text{site}}\rangle)$ .

The full quantum state is described by taking into account both  $|\psi_{\text{site}}\rangle$  and  $|\psi_{\text{bond}}\rangle$ . Thus, the Hilbert space  $\mathcal{H}$  is defined by the set  $\{|\psi_{\text{site}}\rangle \otimes |\psi_{\text{bond}}\rangle\} : |\psi_{\text{site}}\rangle \in \mathcal{S}, |\psi_{\text{bond}}\rangle \in \mathcal{B}(|\psi_{\text{site}}\rangle)$ . Note that for a golden chain/ladder ( $\rho = 1$ ) the state describing the site labels becomes redundant since all the site labels are identically equal to 1.

We would like to emphasise that the Hilbert space of the Fibonacci model is growing exponentially fast due to the multiple possibilities for the bond labels when the site is labelled by an anyon (bit representation 1). Moreover, the presence of holes adds permutations factors since all possible positions of the holes on the sites must be taken into account. The fusion rules impose constraints on the bond labels, which must be satisfied at every trivalent vertex, leading to a finally smaller subset of the set of all possible binary configurations. Computationally generating the Hilbert space is rather challenging for the following reasons. One has to first consider all possible  $2^L$  binary configurations for the site labels. Next, we must retain only those configurations for the site labels that have exactly  $N$  out of  $L$  bits set to 1. As explained above, every  $|\psi_{\text{site}}\rangle$  can generate multiple  $|\psi_{\text{bond}}\rangle$  states that are allowed by fusion rules. However, the number of these allowed  $|\psi_{\text{bond}}\rangle$  states is a tiny fraction of the total number of all possible binary configurations. For

Table II.1: Hilbert space sizes for doped ladders of Fibonacci anyons without charging energy.

$W$	$L$	Filling	Size of Hilbert space
2	8	$\rho = 3/4$	73322
3	6	$\rho = 5/18$	15708

every state belonging to the set of allowed site labels, we first consider all possible binary configurations of the bond labels and then implement the fusion constraint at every vertex for each of the bond states. After this round of elimination we obtain a set of valid states that are allowed by the fusion rules. This sequence of steps leads us to the Hilbert Space which is a heavily constrained subset of the full set of binary configurations. As the number of sites is growing, the number of states where the fusion constraint must be checked is growing exponentially fast, thus the generation of the full Hilbert space becomes more expensive in computation time.

Further, our system has a translation symmetry, i.e. it remains invariant if the site and bond labels are shifted by a certain amount. This enables us to write the wavefunctions as Bloch waves labeled by the momentum. The Hamiltonian becomes a block-diagonal operator and each of these blocks can be diagonalised individually. The Hilbert space is reduced by a factor of  $L$ , making the numerics much more tractable.

In Table II.1, we list the sizes of the Hilbert space (in the  $K = 0$  sector) for doped ladders. The Hilbert space sizes for their corresponding effective models are listed in Table II.2. Additionally in Table II.3, we mention the Hilbert space sizes of the largest chains we simulated for the heavy-light model.

Table II.2: Hilbert space sizes for effective models of doped Fibonacci ladders.

$L$	Filling	Model	Size of Hilbert space
8	$\tilde{\rho} = 1/2$	$t - J$	64
6	$\tilde{\rho} = 5/6$	$t - J$	11

Table II.3: Hilbert space sizes for effective 1D chains of the heavy-light model.

$L$	Filling	Model	Size of Hilbert space
8	$\tilde{\rho} = 1/2$	heavy-light	418
20	$\tilde{\rho} = 1/2$	heavy-light	139741760
20	$\tilde{\rho} = 1/4$	heavy-light	11726456

### 1.1.2 Generating the Hamiltonian

Local interactions are treated simply by multiplying the wavefunction with the Hamiltonian for the interaction. For a ladder geometry, we can choose a zig-zag fusion path so that we are able to minimise the range of interactions. The rung interactions are nearest neighbour interactions and the leg interactions defined in Eqs. (III.14) - (III.18) are longer range interactions, thus involving Braid matrices in addition to the interaction term. Note that since the F-matrix (Eq. III.4) and the Braid matrix (Eq. III.6) have a  $2 \times 2$  sub-block, they can generate up to two states per bond. A magnetic interaction written as Eq. III.8 also has a similar structure, thus giving up to two states per bond. The kinetic hop operator, on the other hand, yields only one state per bond. Thus, we can obtain up to  $2^{2W-1}$  states for magnetic interactions and  $2^{2W-2}$  states for kinetic terms acting along the leg direction. The non-zero entries for each row of the Hamiltonian matrix are thus growing exponentially with the width of the ladder giving rise to a dense matrix for the Hamiltonian. The action of this dense Hamiltonian on the wavefunction would turn out to be numerically expensive. So, instead of multiplying a single matrix with an exponentially large number of non-zero elements with the wavefunction, we implement the same process by iteratively multiplying the wavefunction by  $2W - 1$  sparse matrices as follows. We multiply the wavefunction successively with the Braid matrices, the number of braids depending on  $W$ . Thereafter, we treat the local interaction term. Subsequently we act one by one with all the inverse braid matrices to obtain the final wavefunction. The Hamiltonian is thus generated by successive multiplication of  $W - 1$  Braid matrices followed by multiplication with the interaction term and finally by  $W - 1$  inverse Braid matrices. Since the matrix is becoming denser with the width of the ladder, the exact diagonalisation becomes more and more computationally expensive and we can treat only medium sized systems numerically.

## 1.2 Lanczos Algorithm

Our interest lies in diagonalising the Hamiltonian matrix  $H$  to obtain its low-lying energy states. This is done by projecting the Hamiltonian to a smaller subspace of size  $M \ll \mathcal{H}$  (where  $\mathcal{H}$  is the dimension of the actual Hilbert space) that is chosen correctly so that the low lying states in this subspace converge efficiently to yield the low-lying states of the system. This can be achieved by a variety of iterative methods but we here describe the one we have used in our simulations, the Lanczos method [130–132]. This is a method of iterative diagonalisation that is based on the simple idea of the power method, *i.e.* by acting with powers of the matrix  $H$  we eventually converge to the maximal (in magnitude) eigenvalue of the system. To ensure that we obtain the ground state and not the highest state, we can always shift the Hamiltonian by a large positive constant  $c$ , which makes no difference to the physics.

The Hamiltonian  $H$  is projected on to a subspace of the Hilbert space of the system

called the *Krylov space*. This subspace is formed by the various powers of  $H$  acting on a randomly chosen normalised initial state, which we call  $|f_0\rangle$ . Thus the Krylov space of dimension  $M + 1$  is given by the set  $\{|f_0\rangle, H|f_0\rangle, \dots, H^M|f_0\rangle\}$ . We use this set of orthogonal states to construct the Lanczos basis that is orthonormal. The final goal is to reduce the matrix  $H$  to a tridiagonal form that can then be diagonalised easily using the available library routines. We now outline the algorithm. The starting state must necessarily have a non-zero overlap with the ground state, which will be the case for our randomly chosen initial state. In principle, one could also use physical arguments to choose a good initial state. At the next step, the state is given by

$$|f_1\rangle = H|f_0\rangle - a_0|f_0\rangle, \quad (\text{II.3})$$

where the orthogonality between the states  $|f_0\rangle$  and  $|f_1\rangle$  determines the value of the constant  $a_0$  given by

$$\langle f_0|f_1\rangle = \langle f_0|H|f_0\rangle - a_0\langle f_0|f_0\rangle = 0 \quad (\text{II.4})$$

$$\Rightarrow a_0 = \frac{\langle f_0|H|f_0\rangle}{\langle f_0|f_0\rangle} \quad (\text{II.5})$$

The next state is given by the previous two as

$$|f_2\rangle = H|f_1\rangle - a_1|f_1\rangle - b_0|f_0\rangle, \quad (\text{II.6})$$

where the coefficients  $a_1$  and  $b_0$  are determined by demanding that  $|f_2\rangle$  be orthogonal to both  $|f_0\rangle$  and  $|f_1\rangle$ . They take the values

$$a_1 = \frac{\langle f_1|H|f_1\rangle}{\langle f_1|f_1\rangle} \quad (\text{II.7})$$

$$b_0 = \frac{\langle f_0|H|f_1\rangle}{\langle f_0|f_0\rangle} = \frac{\langle f_1|f_1\rangle}{\langle f_0|f_0\rangle}, \quad (\text{II.8})$$

where we have once again used the orthonormality between  $|f_0\rangle$  and  $|f_1\rangle$ . Further, we can continue the same steps to obtain the  $m^{\text{th}}$  state as

$$|f_{m+1}\rangle = H|f_m\rangle - a_m|f_m\rangle - b_{m-1}|f_{m-1}\rangle, \quad (\text{II.9})$$

with the coefficients given as

$$a_m = \frac{\langle f_m|H|f_m\rangle}{\langle f_m|f_m\rangle} \quad (\text{II.10})$$

$$b_{m-1} = \frac{\langle f_m|f_m\rangle}{\langle f_{m-1}|f_{m-1}\rangle}. \quad (\text{II.11})$$

This process can be iterated for some reasonable value of  $m$  that can be set according to a convergence criterion for the energy or other such physical quantities. Once the (normalised) Lanczos basis vectors have been generated, the Hamiltonian can be expressed as a tridiagonal matrix in this basis that can be diagonalised using standard available routines.

The Lanczos method converges very efficiently for the ground state of small system sizes, requiring typically a few tens to hundreds of Lanczos vectors. One usually requires some more effort to obtain the excited states. It is also noted that eigenvalues converge faster than expectation values. Convergence can further be improved by choosing a better initial state, motivated by analytic calculations. Convergence to ground states can be escalated by taking linear combinations of previously obtained ground states as a starting point.

Sometimes it is noticed that the convergence of excited states could be slightly irregular. More specifically one could notice what looks like a converged state but with more iterations find a sudden change to another (lower) energy value. Thus, one must be careful to run several iterative steps to ensure proper convergence of the algorithm. One also notices that the number of iterations needed becomes quite large if the higher energy states are targeted. Another technical problem encountered in this routine is the appearance of ‘ghosts’ that are false eigenvalues that do not belong to the spectrum of the system. The ghosts are usually multiple copies of the same eigenvalue, thereby leading to a misinterpretation of the multiplicity of the eigenstate.

The reason why we encounter such spurious eigenvalues is due to the loss of orthogonality of the Lanczos basis. In theory, the Lanczos vectors are orthogonal to each other however when implemented numerically, this orthogonality might be lost due to finite machine precision. The way to remedy this issue is to re-orthogonalise the Lanczos vectors according to a Gram Schmidt Orthogonalisation procedure. This requires us to store all the Lanczos vectors, thus might lead to memory issues, in the case where the computation is being pushed to the limit of the computing resources.

In addition to the low-lying spectrum, the Lanczos method also allows us to calculate dynamical observables and to study non-equilibrium physics of strongly correlated systems. One can also perform calculations at finite temperatures. Such calculations are generally computationally demanding but can nevertheless be performed on small clusters, and used for benchmarking purposes. Exact diagonalisation results can be extrapolated to understand the thermodynamic limit, by using a finite size scaling analysis. However, any predictions of the infinite size limit drawn out of small cluster simulations must be treated with caution.

## 2 Matrix Product states

Tensor network methods have become excessively popular in the last few years due to the versatility they offer - they are able to handle large system sizes and also systems directly in the thermodynamic limit, systems with different symmetries, boundary conditions, particle types (fermions and bosons), frustrated spins etc. Though usually efficient in 1D, quantum entanglement poses the main limitation to these methods in higher dimensions. This approach is substantially different from other numerical techniques and as we shall see, is written in the language of tensor network diagrams which is preferable over complicated equations. It has allowed for the study of various properties such as real time evolution, finite temperature calculations[133–138].

We used the Matrix Product States (MPS) code of the ALPS libraries [139–141] to study the problem of one dimensional optical lattices. Additionally, since we are dealing with a dilute system we exploit the multigrid DMRG method [142] to obtain the ground state for initial Hamiltonian without the lattice and for the target Hamiltonian in the deep lattice limit. We use time evolution of the ALPS MPS code to study the lattice loading by starting from an initial state and changing the potential at every time step. This section gives a general description of the MPS and the multigrid DMRG methods for ground state optimisation and time evolution. We follow very closely the review articles [143, 144] for the notation and description provided in this section.

### 2.1 General introduction to tensor networks

A quantum Hamiltonian is written in a Hilbert space for the system which is usually growing exponentially with the system size. For example, a  $d$ -level system on a  $L$  site chain is described by a  $d^L$ -dimensional Hilbert space. Any quantum state on this lattice would be written as:

$$|\psi\rangle = \sum_{\sigma_1, \dots, \sigma_L} c_{\sigma_1, \dots, \sigma_L} |\sigma_1, \dots, \sigma_L\rangle, \quad (\text{II.12})$$

where  $\sigma_1, \dots, \sigma_L$  are the local Hilbert spaces on the  $L$  sites and the  $c$ 's are exponentially many coefficients that can be seen as a tensor of rank  $L$  with  $\mathcal{O}(d^L)$  coefficients. Fortunately, not all quantum states in this exponentially large Hilbert space are equally important. In nature, the Hamiltonians are usually local which infact is a huge help for us to simulate these Hamiltonians numerically. It is known that low-energy eigenstates of local, gapped Hamiltonians obey the area law of entanglement entropy, that means the entanglement entropy between two subsystems of the full system is proportional to the area between these two subsystems rather than their volume. The low-energy eigenstates, that we are actually interested in, are special and rather limited. These low-energy states infact follow the area law.

The method of MPS is a tensor network technique where all states/operators

are expressed as (a product of) tensors of varied ranks, in principle. A tensor network typically contains contractions of several tensors that serve as building blocks. As more and more tensors are involved in building the network it tends to get increasingly cumbersome to write down equations for the contractions that appear as summations over the relevant indices. These tensor networks are, for the sake of convenience, effectively represented by means of diagrams that make some of the properties evident. Before proceeding further we introduce, in Fig. II.3, the diagrammatic representations for some simple tensors. Any diagram with no open legs is a rank 0-tensor or a scalar (Fig. II.3(a)), one open leg is a rank-1 tensor or a vector (Fig. II.3(b)), two open legs is a rank-2 tensor or a matrix (Fig. II.3(c)), three open legs is a rank-3 tensor (Fig. II.3(d)) and so on. The c-tensor of rank  $L$  with dimension  $d^L$  is shown in Fig. II.3(e) and assuming we know how to break it down to a network that can be represented by one tensor per site, we get the diagram shown in Fig. II.3(f). This is precisely what is called a *Matrix Product State*.

Each of the tensors is a matrix of some maximal dimension  $D \times D$ , where  $D$  is called the bond dimension. The total number of parameters for a 1D MPS with  $L$  sites would be  $\sim \mathcal{O}(LdD^2)$ , where the  $d$  is the physical dimension of the system, the number of degrees of freedom. The bond dimension is directly related to the entanglement in the quantum state  $|\psi\rangle$ . The value of the bond dimension has to do with the quantum correlations of the wavefunction. As the entanglement in the system is growing, one has to also increase the bond dimension accordingly. Note that for bond dimension  $D \rightarrow \infty$ , the MPS wavefunction would be exact, however very good accuracy (depending on the system) could be obtained for  $D$  as large as a few hundreds. Clearly, for  $D = 1$ , the matrices are trivial and the MPS is just a product state, thus there is no entanglement in the system. For any  $D > 1$ , there is a finite amount of entanglement in the system.

The entanglement captured by a tensor network depends on  $D$  and the way the indices are connected. Same value of  $D$  for different geometries can have different properties. In general, one should try several values of successively increasing  $D$  to check for errors and convergence of physical observables such as energy.

For a translationally invariant system, all the tensors are alike. Infact to implement periodic boundary conditions is fairly simple in the MPS framework. One only needs to identify the first and the last site of the tensor network, thus take a trace of the MPS and the network looks like what is shown in Fig. II.3(g). This figure also makes properties like the cyclic property of the trace and translational invariance evident. The MPS shown in Fig. II.3(f) corresponds to open boundary conditions. From the diagram it is easy to observe that the dimensions of the first and last tensors on the chain differ from the rest of the tensors. The left most tensor is a row-vector while the right-most is a column vector.

If we were to represent each state by a tensor of an exponentially large dimension, it seems that we haven't gained anything in terms of computation advancement. We would like to somehow break down this tensor to smaller local pieces that capture effectively the non-local physics of the system. Then the action of operators,



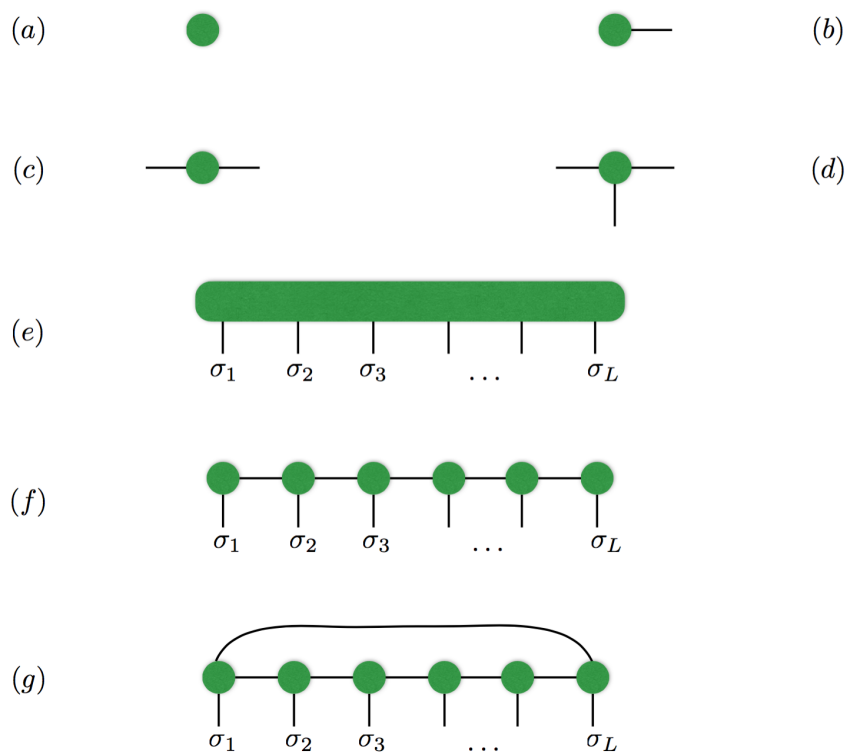


Figure II.3: Some simple tensor network diagrams. (a) Scalar, (b) vector, (c) Matrix, (d) Rank-3 tensor, (e) tensor of rank  $L$ , (f) decomposition of tensor in (e) to an MPS with open boundary conditions and one (local) tensor per site (g) MPS with periodic boundary conditions.

measurement of correlations, norms etc would be done by *contracting* the tensor network in the relevant way. These contractions are similar to matrix multiplications and as we shall see the order of contractions is important for the efficiency of the algorithm.

## 2.2 Canonical form and Schmidt decomposition

The method of singular value decomposition (SVD) helps us decompose the tensor of a large rank into smaller chunks. Since this is vital to the construction of MPS, we briefly recall what it tells us. SVD allows us to write any matrix (not necessarily square)  $M$  of dimensions  $(N_A, N_B)$  as the product

$$M = USV^\dagger, \quad (\text{II.13})$$

where  $U$  is a matrix of dimension  $(N_A, \min(N_A, N_B))$  whose columns form the left singular vectors with  $U^\dagger U = I$ ,  $S$  is a diagonal matrix of dimension  $(\min(N_A, N_B), \min(N_A, N_B))$  with non-negative entries. Its entries are called the singular values and the number of non-zero diagonal entries form the Schmidt rank of the matrix  $M$ , denoted as  $r$ . In the MPS method, it is particularly useful to sort the singular values in descending order, which is what we assume in the following.  $V^\dagger$  has

dimension  $(\min(N_A, N_B), N_B)$  whose rows form the right singular vectors. In the special case where  $M$  is a square matrix, both  $U$  and  $V$  are unitary.

A very important application of the SVD, which will be often used in the MPS scheme, is to approximate the matrix  $M$  of a rank  $r$  with a  $M'$  carrying rank  $r' < r$ , i.e. one picks the  $r'$  largest singular values of  $M$  setting the rest to zero. This also reduces the dimensions of  $U$  and  $V^\dagger$  appropriately. This is referred to as *truncation* in the MPS scheme and we will come back to it in the following.

SVD also helps us write the Schmidt decomposition of a quantum state. Consider a pure state  $|\psi\rangle$  living on a system with two partitions  $A$  and  $B$ . Then, we can write the state as :

$$|\psi\rangle = \sum_{ij} \Psi_{ij} |i\rangle_A |j\rangle_B, \quad (\text{II.14})$$

where  $\{|i\rangle_A\}$   $\{|j\rangle_B\}$  are orthonormal bases for the subsystems  $A$  and  $B$  with dimensions  $N_A$  and  $N_B$  respectively. Now, we can implement a SVD on the coefficient matrix  $\Psi_{ij}$  as follows

$$|\psi\rangle = \sum_{ij} \Psi_{ij} |i\rangle_A |j\rangle_B \quad (\text{II.15})$$

$$= \sum_{ij} \sum_k^{\min(N_A, N_B)} U_{ik} S_{kk} V_{kj}^\dagger |i\rangle_A |j\rangle_B \quad (\text{II.16})$$

$$= \sum_k^{\min(N_A, N_B)} S_{kk} \left( \sum_i U_{ik} |i\rangle_A \right) \left( \sum_j V_{jk}^* |j\rangle_B \right) \quad (\text{II.17})$$

$$= \sum_k^{\min(N_A, N_B)} s_k |k\rangle_A |k\rangle_B \quad (\text{II.18})$$

The sum over  $k$  when restricted to the positive non-zero singular values, gives the Schmidt decomposition. The benefit of the Schmidt decomposition is that the reduced density matrices take a very simple form and their eigenvalues are given by the square of the singular values, the eigenvectors being the left or right singular vectors, as the case maybe. It also makes the approximation of the MPS state  $|\psi\rangle$  to one of a reduced bond dimension rather simple, by simply considering truncating the sum to the desired value.

Having described the SVD, let us see how we can use it to decompose the  $d^L$  dimension tensor of Eq II.12 as a product of  $L$  individual tensors, one for each site. As we will see, there are three ways to do so giving rise to what we call (*i*) left canonical MPS (*i*) right canonical MPS and (*i*) mixed canonical MPS. We explain first how to generate a left canonical MPS and the sequence of steps is shown in Fig. II.4. We begin with the  $d^L$  dimensional vector  $c_{\sigma_1, \dots, \sigma_L}$  (Fig. II.4(a)) and reshape it to write it as a matrix of dimension  $(d, d^{L-1})$  as

$$c_{\sigma_1, \dots, \sigma_L} = \Psi_{\sigma_1, (\sigma_2, \dots, \sigma_L)} \quad (\text{II.19})$$

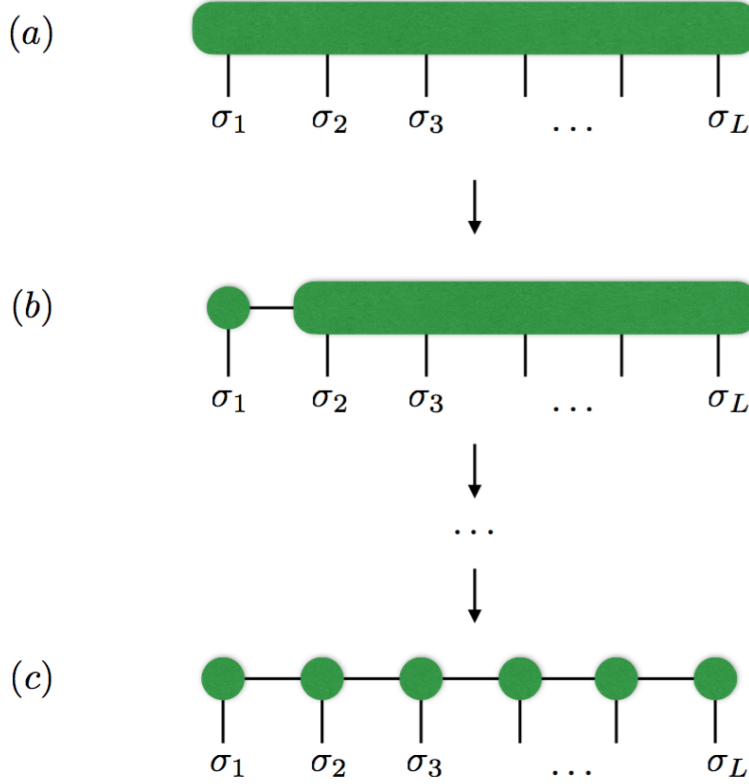


Figure II.4: (a) The initial tensor of dimension  $d^L$ , (b) After the first SVD the tensor for the first site is separated, (c) the final decomposition of the tensor into local tensors for each site.

Now we perform an SVD on this new matrix to obtain

$$\Psi_{\sigma_1, (\sigma_2, \dots, \sigma_L)} = \sum_{a_1}^{r_1} U_{\sigma_1, a_1} S_{a_1, a_1} V_{a_1, (\sigma_2, \dots, \sigma_L)}^\dagger \quad (\text{II.20})$$

$$= \sum_{a_1}^{r_1} U_{\sigma_1, a_1} c_{a_1 \sigma_2, \dots, \sigma_L}, \quad (\text{II.21})$$

where  $r_1$  is the rank of the singular value matrix such that  $r_1 \leq d$ . (Recall that the singular value matrix has dimension equal to the smaller of the two dimensions of the matrix undergoing the SVD.) In the last step we have multiplied the  $S$  and  $V^\dagger$  matrices to write them as a  $c$  tensor. The matrix  $U$  can be split into  $d$  row vectors  $A^{\sigma_1}$  with values given by  $A_{a_1}^{\sigma_1} = U_{\sigma_1, a_1}$ . By implementing this step, we have separated the tensor for the first site on the 1D chain to obtain a tensor network that looks like Fig. II.4(b). As we are considering open boundary conditions, this tensor is actually a row matrix. We repeat the same step by reshaping the tensor  $c_{a_1 \sigma_2, \dots, \sigma_L}$  as

$$c_{a_1 \sigma_2, \dots, \sigma_L} = \Psi_{(a_1, \sigma_2), (\sigma_3, \dots, \sigma_L)}, \quad (\text{II.22})$$

which is now a  $r_1 d \times d^{L-2}$  matrix. After another SVD, we get

$$c_{\sigma_1, \dots, \sigma_L} = \sum_{a_1=1}^{r_1} \sum_{a_2=1}^{r_2} A_{a_1}^{\sigma_1} U_{(a_1, \sigma_2), a_2} S_{a_2, a_2} V_{a_2, (\sigma_3, \dots, \sigma_L)}^\dagger \quad (\text{II.23})$$

$$= \sum_{a_1=1}^{r_1} \sum_{a_2=1}^{r_2} A_{a_1}^{\sigma_1} U_{(a_1, \sigma_2), a_2} C_{a_2 \sigma_3, \dots, \sigma_L} \quad (\text{II.24})$$

$$= \sum_{a_1=1}^{r_1} \sum_{a_2=1}^{r_2} A_{a_1}^{\sigma_1} A_{a_1, a_2}^{\sigma_2} \Psi_{a_2 \sigma_3, (\sigma_4, \dots, \sigma_L)}, \quad (\text{II.25})$$

where in the second step we have again clubbed the  $S$  matrix (of rank  $r_2 \leq r_1 d \leq d^2$ ) and the  $V^\dagger$  matrix and in the last step we have decomposed the  $U$  matrix as  $d$  matrices given by  $A_{a_1, a_2}^{\sigma_2} = U_{(a_1, \sigma_2), a_2}$ . Each of these  $A$  matrices are now of dimension  $(r_1 \times r_2)$  while the new tensor to be broken down is of dimension  $(r_2 d \times d^{L-3})$ . We can proceed in a similar way breaking down the tensor into smaller pieces site by site to finally obtain something that looks like

$$c_{\sigma_1, \dots, \sigma_L} = \sum_{a_1=1}^{r_1} \sum_{a_2=1}^{r_2} \dots \sum_{a_{L-1}=1}^{r_{L-1}} A_{a_1}^{\sigma_1} A_{a_1, a_2}^{\sigma_2} \dots A_{a_{L-2}, a_{L-1}}^{\sigma_{L-1}} A_{a_{L-1}}^{\sigma_L} \quad (\text{II.26})$$

$$= A^{\sigma_1} A^{\sigma_2} \dots A^{\sigma_{L-1}} A^{\sigma_L} \quad (\text{II.27})$$

Thus, we have rewritten the tensor  $c_{\sigma_1, \dots, \sigma_L}$  as a product of individual local tensors, formally known as a Matrix Product State. The final MPS is shown in Fig. II.4(c).

After each SVD, we have  $U^\dagger U = I$ . Since the  $A$  matrices are made out of the  $U$  matrices, this unitarity condition imposes a normalisation on the tensors of the MPS. More explicitly we have

$$U^\dagger U = I \quad (\text{II.28})$$

$$\text{or } \sum_{a_{l-1} \sigma_l} U_{a_l, (a_{l-1} \sigma_l)}^\dagger U_{(a_{l-1} \sigma_l), a_l'} = \delta_{a_l a_l'} \quad (\text{II.29})$$

$$\Rightarrow \sum_{a_{l-1} \sigma_l} A_{a_l, a_{l-1}}^{\sigma_l \dagger} A_{a_{l-1}, a_l'}^{\sigma_l} = \sum_{\sigma_l} (A^{\sigma_l \dagger} A^{\sigma_l})_{a_l, a_l'} = \delta_{a_l a_l'} \quad (\text{II.30})$$

$$\text{or } \sum_{\sigma_l} A^{\sigma_l \dagger} A^{\sigma_l} = I. \quad (\text{II.31})$$

Thus, we call the  $A$  matrices *left normalised*. An MPS made out of only left normalised matrices is called a left-canonical MPS. For DMRG simulations, it is also good to look at bipartitions of the system at some site  $l$  so that we have

$$|a_l\rangle_A = \sum_{\sigma_1, \dots, \sigma_l} (A^{\sigma_1} A^{\sigma_2} \dots A^{\sigma_l})_{1 \times a_l} |\sigma_1 \dots \sigma_l\rangle \quad (\text{II.32})$$

$$|a_l\rangle_B = \sum_{\sigma_{l+1}, \dots, \sigma_L} (A^{\sigma_{l+1}} A^{\sigma_{l+2}} \dots A^{\sigma_L})_{a_l \times 1} |\sigma_{l+1} \dots \sigma_L\rangle \quad (\text{II.33})$$

$$|\psi\rangle = \sum_{a_l} |a_l\rangle_A |a_l\rangle_B, \quad (\text{II.34})$$

where the subset  $|a_l\rangle_A$  is an orthonormal one due to the left normalisation condition but  $|a_l\rangle_B$  is not. This bipartition should therefore not be confused with a Schmidt decomposition even though it looks deceptively similar.

As an aside, we would like to mention we could have very well starting breaking down the tensor  $c_{\sigma_1, \dots, \sigma_L}$  starting at the right end, *i.e.* at the site  $\sigma_L$ . This would have given us, in a very similar way, a decomposition of the form

$$c_{\sigma_1, \dots, \sigma_L} = B^{\sigma_1} B^{\sigma_2} \dots B^{\sigma_{L-1}} B^{\sigma_L}, \quad (\text{II.35})$$

where the  $B$  matrices now obey  $BB^\dagger = I$ , meaning to say that they are right normalised. An MPS consisting of only  $B$  matrices should be called a right-canonical MPS. This notation of  $A$  and  $B$  matrices to denote left and right normalised matrices respectively will be used frequently in this chapter. As a third approach, we could even merge the first two schemes, namely start a site 1 and proceed rightwards up to some site  $l$  to obtain the matrices  $A^{\sigma_1} \dots A^{\sigma_l}$ . Further, sweep from right to left up to site  $l+1$  to get the  $B$  matrices  $A^{\sigma_{l+1}} \dots B^{\sigma_L}$ , leaving a matrix  $S$  that contains the singular values at the bond  $(l, l+1)$ . This is called the *mixed canonical MPS*. An intuitive bi-partition of the state at site  $l$  now gives a Schmidt decomposition since the matrices to the left are left normalised and those to the right are right normalised.

There are also some gauge degrees of freedom in the MPS framework. Note that we could consider the following transformation on the MPS tensors (no normalisation condition assumed here, thus denoted as  $M$ ) that leaves the tensor network unchanged

$$M^{\sigma_i} \rightarrow M^{\sigma_i} X \quad (\text{II.36})$$

$$M^{\sigma_{i+1}} \rightarrow X^{-1} M^{\sigma_{i+1}}. \quad (\text{II.37})$$

Let us study the maximal dimensions of these  $A$  matrices. Moving from left to right we find the dimensions to be  $1 \times d, d \times d^2, d^2 \times d^3, \dots, d^{L/2-1} \times d^{L/2}, d^{L/2} \times d^{L/2-1}, \dots, d \times 1$ . Notice that the dimensions of these matrices are growing exponentially with the physical dimension. Exact numerical calculations of these matrices would become increasingly difficult. Thus we will have to approximate these matrices by some smaller ones of maximal dimension given by the chosen bond dimension. The smaller matrices should capture all the physics of the original tensors, minimising the approximation errors. This procedure is called truncation which is imperative in tensor network studies. Here, we just retain the first  $D$  largest singular values to keep the largest matrix of dimension  $D \times D$ , dropping out additional rows and columns of the  $U$  and  $V^\dagger$  accordingly. If  $D$  is sufficiently large then, due to the exponentially decay of singular values, we should be able to minimise the error at this step. The error encountered due to truncation is the so called truncation error and can be tracked via the sum of the rejected singular values. This quantity should tend to zero as closely as possible.

We will also encounter situations when we start with a given MPS with bond dimension  $D$  but after some tensor manipulations end up with an MPS of a much larger bond dimension. This is the case, for instance, when two MPS are added

or a Matrix Product Operator (MPO) is applied to the MPS. In such situations we would need to compress the MPS back to its original (or some maximal) bond dimension. One of the ways to do so is to use this truncation procedure. Let us denote the enlarged state by  $|\psi'\rangle$  with bond dimension  $D'$ . The idea is to find a state  $|\tilde{\psi}\rangle$  that approximates  $|\psi'\rangle$  efficiently but has bond dimension  $D$ . In order to do so, we must shrink all the matrices of the MPS to dimension  $D \times D$ . We do so iteratively by truncating one tensor at a time. More explicitly we start from one end of the chain (say the right end), apply an SVD on the right-most matrix, truncate the  $U, S, V^\dagger$  matrices retaining only the  $D$  largest singular values, rescale the singular values in order to normalise the matrices. This gives us the truncated normalised matrix for the site  $L$ . At the end of this step we have decomposed the tensor at site  $L$  as a product of three truncated tensors  $\tilde{U}, \tilde{S}$  and the normalised MPS tensor  $B^{\sigma_L}$ . We proceed to the site  $L-1$  where now the tensor to be truncated is  $M^{\sigma_{L-1}} = A^{\sigma_{L-1}} \tilde{U} \tilde{S}$ , that has contributions from the truncated matrices at the last step. We sweep along the chain truncating one tensor at a time to finally obtain a compressed MPS  $|\tilde{\psi}\rangle$  that has all right-normalised tensors.

There is another way that is known by the name *variational compression* of the MPS. This relies on starting with a compressed state of the desired bond dimension and reducing its distance to the actual enlarged MPS. This variational procedure optimises the matrices one by one, sweeping back and forth in order to minimise the distance between the two MPS. Usually a SVD compressed state forms a good starting guess for this method and convergence should be achieved in a few iterations. This scheme relies heavily on the state with the reduced dimension, thus a good starting point is imperative to the fast convergence.

### 2.3 Ground state calculation

One of the most important questions we need to deal with is what are actually the coefficients of these tensors. We would like to somehow get the tensors to compute the ground state of a given Hamiltonian and then, if need be, perform further calculations on it. One way to look for the ground state is the so-called *variational optimisation*. The variational principle gives us a lower bound on the expectation value of the Hamiltonian. Namely it states that for a given Hamiltonian  $H$  and a quantum state  $|\Psi\rangle$ , we always have that

$$\frac{\langle \Psi | H | \Psi \rangle}{\langle \Psi | \Psi \rangle} \geq E_0 \quad (\text{II.38})$$

We would thus like to minimise the expression  $(\langle \Psi | H | \Psi \rangle - \lambda \langle \Psi | \Psi \rangle)$  as shown in Fig. II.5, where we have introduced a Lagrange multiplier  $\lambda$ . The value of  $\lambda$  that minimises this expression is the ground state energy of the Hamiltonian. Thus the ground state search is reduced to a minimisation problem.

The variables of this minimisation are the MPS tensors whose optimal expressions would eventually give us the ground state energy and wavefunction. Optimising all these tensors at the same time is a highly non-linear problem, unsolvable in

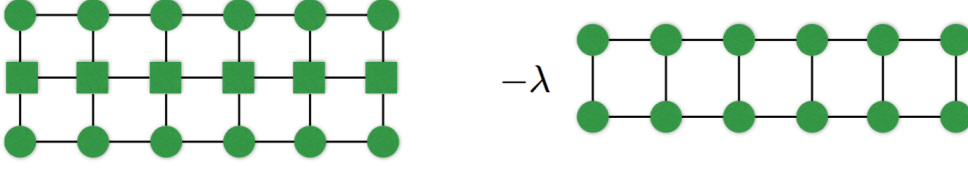


Figure II.5: The MPS network that provides the functional to be minimised to obtain the ground state. The diagram on the left represents the contracted expression for  $\langle \Psi | H | \Psi \rangle$  and on the right is the one for the norm  $\langle \Psi | \Psi \rangle$ .  $\lambda$  is a Lagrange multiplier.

practice, but it turns out that we have a way around it. We could proceed tensor by tensor, *i.e.* optimise one tensor at a time, keeping all others fixed. Hence, we must consider the following equation for all tensors  $M^*$ :

$$\frac{\partial}{\partial M^*} (\langle \Psi | H | \Psi \rangle - \lambda \langle \Psi | \Psi \rangle) = 0 \quad (\text{II.39})$$

In the diagrammatic language this can be written as

$$\sum_{\sigma'_i} \sum_{a'_{i-1}, a'_i} \sum_{b_{i-1}, b_i} L_{b_{i-1}}^{a_{i-1}, a'_{i-1}} W_{b_{i-1}, b_i}^{\sigma_i \sigma'_i} R_{b_i}^{a_i, a'_i} M_{a'_{i-1}, a'_i}^{\sigma'_i} - \lambda M_{a_{i-1}, a_i}^{\sigma_i} = 0, \quad (\text{II.40})$$

where the expressions for  $L$ ,  $W$  and  $R$  are shown in Fig. II.6. Note that the

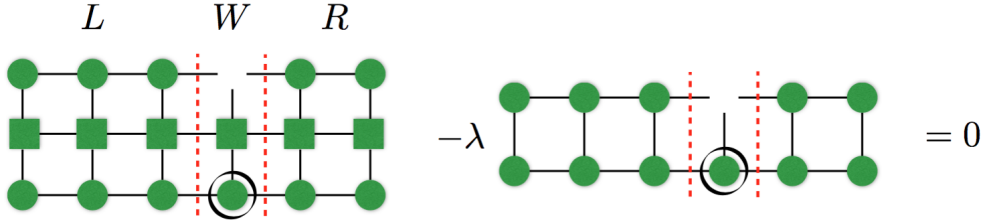


Figure II.6: The MPS contractions for the generalised eigenvalue problem to be solved. The matrix to be optimised is encircled.

expression for the norm in the second term would in general be the one shown in Fig. II.6 but since we assume that the matrices to the left of site  $l$  are left-orthogonalised and those to the right are right-orthogonalised, it reduces to the simple expression of Fig. II.7. This normalisation scheme reduces the generalised eigenvalue problem to a standard one. In order to solve this eigenvalue problem, we reshape the matrix  $M_{a'_{i-1}, a'_i}^{\sigma'_i}$  as a vector  $v_{\sigma_i a_{i-1} a_i}$ , as well as reshaping the product  $LWR$  as a matrix  $H$  so that

$$H_{(\sigma_i a_{i-1}, a_i), (\sigma'_i a'_{i-1}, a'_i)} = \sum_{b_{i-1}, b_i} L_{b_{i-1}}^{a_{i-1}, a'_{i-1}} W_{b_{i-1}, b_i}^{\sigma_i \sigma'_i} R_{b_i}^{a_i, a'_i}. \quad (\text{II.41})$$

Then we have the eigenvalue problem to solve as:

$$Hv = \lambda v, \quad (\text{II.42})$$

where  $H$  is a matrix of dimension  $dD^2 \times dD^2$ . Generally this is a large number to handle numerically but we require only the ground state eigenenergy and eigenstate. We can thus use an iterative eigensolver such as Lanczos or Jacobi-Davidson for this purpose. Solving Eq. II.42, we get the ground state energy  $\lambda_0$  and the corresponding eigenstate  $v_0$ . We reshape the optimised tensor  $v_{0\sigma_l a_{l-1} a_l}$  as a matrix and proceed to the next tensor. We now outline the algorithm used in the DMRG based variational optimisation of the MPS tensor network (see [143] for a detailed explanation).

- Start with a random state  $|\psi\rangle$  with right orthonormalised matrices.
- Calculate  $R$  values for site positions  $L - 1$  to 1 iteratively.
- Right sweep: Start at site  $l = 1$ , proceed up to  $L - 1$  by *sweeping to the right* as we explain now. Solve the eigenvalue problem by an iterative eigensolver for  $M^{\sigma_l}$  (the reshaped ground state eigenvector) using its current value as initial value. [This will be important in due course of the algorithm as the current value will become closer and closer to the actual one, giving huge computational benefit and accuracy to the eigensolver]. Once the new value for the tensor  $M^{\sigma_l}$  is obtained, left-normalise it by an SVD to get  $A^{\sigma_l}$ , the remaining matrices are absorbed in  $M^{\sigma_{l+1}}$  to the right. This tensor  $M^{\sigma_{l+1}}$  will be the starting guess to solve the eigenvalue problem at the next site. Calculate iteratively the expression for  $L$  by adding one site at a time. Move on by one site  $l \rightarrow l + 1$ .
- Left sweep: This time start at site  $l = L$  and proceed up to  $l = 2$  by *sweeping to the left* as follows. Solve the eigenvalue problem for  $M^{\sigma_l}$  with its present value as the starting guess for the eigensolver. Get its updated value, right normalise it by SVD to get  $B^{\sigma_l}$ . Absorb any remaining matrices to the left in  $M^{\sigma_{l-1}}$ , which form the initial guess for the eigenvalue solver at the next site. Get iteratively the expression for  $R$  by adding one site at a time. Proceed to the next site to the left  $l \rightarrow l - 1$ .
- The right and left sweep together constitute one sweep. Continue sweeping until convergence, defined by a criterion, is achieved.
- Convergence can be monitored by means of a convergence criterion. For

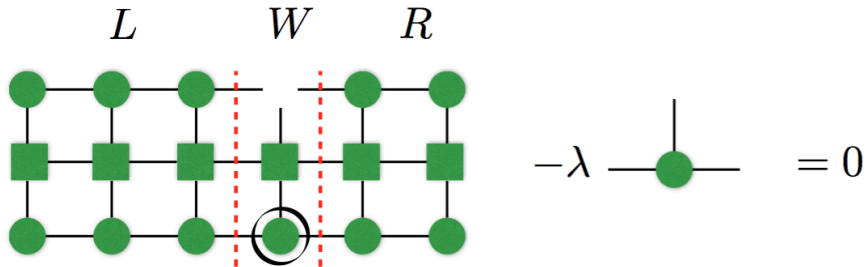


Figure II.7: The standard eigenvalue problem to solve in order to optimise the matrix  $M_{a_{l-1}, a_l}^{\sigma_l}$ .



example, we could look at the energy variance:  $\langle \Psi | H^2 | \Psi \rangle - (\langle \Psi | H | \Psi \rangle)^2$ . This quantity must tend to zero as closely as possible.

## 2.4 Multigrid DMRG

For systems with multiple length scales, the DMRG algorithm often does not converge to the correct ground state. The reason behind the poor convergence is that the variational optimisation does not manage to capture the large scale effects in the problem. For instance, dilute systems such as the lattice discretised model that we consider in this thesis suffer from this issue. The continuum models consist of a unit cell divided into several grid points, and carry only very few particles compared to the total number of sites in the system. Similar convergence problems are known to be solved by multigrid schemes in other fields as well [145, 146].

Such convergence issues can be overcome by using multigrid approaches, where the actual fine grained model is mapped onto successively coarser grids by merging  $n$  sites. The problem is first solved on the coarsest grid, to obtain its ground state. This state is already a fair approximation to the actual ground state of the target problem, and is used as the starting point to solve the model at the next finer grid. Repeating this *prolongation* procedure of starting from a coarse grid to successively optimise the ground state on finer grids is repeated until the actual target model is obtained. The computational ease and speed up is due to the quick convergence of large scale features in the coarse grained model. Thereafter, one only requires to optimise the local features.

A standard DMRG procedure will perform a variational optimisation on the bonds or site tensors of the continuum space, keeping all others fixed and sweeping back and forth until a convergence criterion is satisfied. This optimisation, carried out at a rather local level, is quite prone to being trapped in local minima. However, a multigrid DMRG (MG DMRG) method is useful to deal with dilute systems to converge to the correct ground state more efficiently [142].

In the MG DMRG optimisation, we start from the coarsest level that has one grid point per unit cell of length  $a$ . The first step is to optimise the wave function for the ground state at this level of coarse graining. Once we have obtained the ground state wavefunction, we use it as the initial state for the next finer grid, where we split every site into two. Each unit cell now carries two grid points. In Fig. II.8 we show the prolongation operation that doubles the number of sites. We run a variational ground state optimisation at this discretisation to obtain the ground state. The next finer grid again doubles the number of grid points per unit cell and uses the optimised wave function of the previous coarse grained model as the starting point. This process is repeated until we achieve the desired level of fine graining, which in our simulations corresponds to a spacing  $\Delta x = a/N_{\text{discr}}$  with  $N_{\text{discr}} = 16$  grid points per unit cell.

The first optimisation on the coarse grid is very fast and is able to capture the long range features of the problem. Using the prolonged solutions of the coarser grid

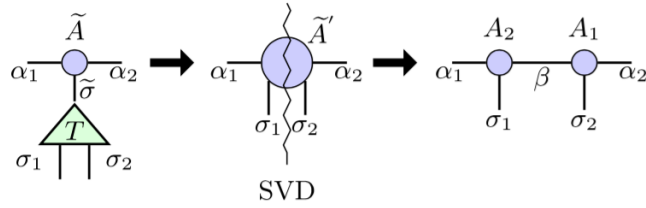


FIG. 4 (color online). Prolongation operation doubling the number of sites: First, we transform the basis  $\tilde{\sigma}$  of the initial matrix  $\tilde{A}$  into two new local bases  $\sigma_1$  and  $\sigma_2$ . With a singular value decomposition, we then split the rank-4 tensor  $\tilde{A}'$  into two matrices  $A_1$  and  $A_2$ .

Figure II.8: Figure showing prolongation operation taken from Ref. [142].

as initialisations for ground state wavefunctions on the finer lattices allows fast and reliable convergence to the right ground state, by fine tuning the local features. For modest values of the discretisation standard DMRG approaches fare well, but serious convergence issues arise for smaller values of the spacing  $\Delta x$  where the problem acquires vastly differing length scales.

## 2.5 Time evolution

Time evolutions can be simulated in the MPS framework by applying operators of the form  $e^{-iHt}$  or  $e^{-\beta H}$  that are used for real and imaginary time evolution respectively. The former quantity is useful in quantum mechanics for instance, and the latter in statistical mechanics where the inverse temperature can be seen as an imaginary time.

A local Hamiltonian, that contains only nearest neighbour interactions can be written as a sum of the form  $H = \sum_i h_i$ , where  $h_i$  is the interaction term between site  $i$  and  $i + 1$ . The total time can be split into small time steps of the form  $T = N\Delta t$ , where the number of intervals  $N \rightarrow \infty$  and the infinitesimal time step  $\Delta t \rightarrow 0$ . The unitary operator for each time step  $\Delta t$  is then given by

$$\begin{aligned} e^{-iH\Delta t} &= e^{-i(h_1+h_2+\dots+h_{L-1})\Delta t} \\ &= e^{-ih_1\Delta t} e^{-ih_2\Delta t} \dots e^{-ih_{L-1}\Delta t} + \mathcal{O}((\Delta t)^2) \end{aligned} \quad (\text{II.43})$$

The last step corresponds to a simple first-order Trotter decomposition on the Hamiltonian. The leading contribution to the error is from the commutator of the bond terms,  $[h_i, h_{i+1}]$ , that is in general non-zero. As long as  $\Delta t$  is small enough, this is a fair approximation. However, choosing a very small time step leads to a large number of time steps that could escalate computational cost. Higher order Trotter decompositions can be used to reduce the error.

It is worthy to note that for a nearest neighbour Hamiltonian all odd and all even bonds respectively act independent of each other. In other words time evolution

on all odd (and similarly all even) bonds commute with each other, thus can be applied at the same time. It is thus useful to split the Hamiltonian as the sum of odd and even parts as:

$$H = \sum_{i \text{ odd}} f_i + \sum_{j \text{ even}} g_j, \quad (\text{II.44})$$

where  $f_k(g_k)$  are bond operators on odd (even) bonds between sites  $k$  and  $k + 1$ . The unitary operator can then be written as

$$e^{-iH\Delta t} = \prod_{k \text{ odd}} e^{-if_k\Delta t} \prod_{j \text{ even}} e^{-ig_j\Delta t} + \mathcal{O}((\Delta t)^2). \quad (\text{II.45})$$

This product of two site operators can be implemented using the following procedure:

- Apply the unitary operator  $e^{-iH_{\text{odd}}\Delta t}$  to all odd bonds of the state  $|\psi(t)\rangle$ .
- To the MPS obtained after the previous step, apply the operator  $e^{-iH_{\text{even}}\Delta t}$  to all even bonds.
- The MPS now has a bond dimension  $d^2D$  which must be truncated to  $D$ . This can be done by SVD retaining only the  $D$  largest singular values.
- This completes one Trotter time step and we now have  $|\psi(t + \Delta t)\rangle$  which has been compressed back to dimension  $D$ .
- Time dependent observables can be evaluated and then repeat the procedure to obtain the wavefunction at the next time step.

A second order Trotter decomposition at a given time step can be written as

$$e^{-iH\Delta t} = e^{-iH_{\text{odd}}\Delta t/2} e^{-iH_{\text{even}}\Delta t} e^{-iH_{\text{odd}}\Delta t/2} + \mathcal{O}((\Delta t)^3), \quad (\text{II.46})$$

where the error has been reduced by an order of magnitude in the step size. If the Hamiltonian does not change after every time step, the exponential involving half time steps can be combined into a full time step, leaving only two half time step operators at the ends. This reduces the error drastically with no extra computational cost. However, if measurements are to be made at every time step, we cannot play the same trick. If, on the other hand, the Hamiltonian is changed at every time step these exponentials cannot be combined trivially. In the ALPS MPS code, we used the second order Trotter decomposition to run the time evolution simulations.

## 2.6 Efficiency and errors in the DMRG algorithm

The method employed for finding the ground state is a variational method, thus not exact. Only when  $D \rightarrow \infty$ , the method becomes exact. This, however, is not achievable in practice. Although it is observed that the MPS method and DMRG optimisation works very well for 1D systems, it does come with its own set of challenges. One possible source of error could be that the initial guess for

the tensor  $M^\sigma$  is a bad one. This requires a large number of iterations for the eigensolvers making the method quite inefficient. Another challenge could be that the eigensolver is stuck in a local minimum, failing to give the right ground state eigenvalue and eigenvector for the matrix. We could try to come up with ways to tackle these issues. One possibility could be to vary the number of iterations for the eigensolver during the course of the algorithm. In the initial sweeps, assuming the guess would generally be bad, we could start with a smaller bond dimension but more number of iterations for the eigensolver. Further as the accuracy of the initial states for the eigensolvers gets more refined, we could increase the bond dimension and reduce the number of iterations needed for the eigensolver. We could also start with a reasonable guess for the initial state rather than a randomly generated matrix. This guess could either be based on the physics behind the problem or could be obtained from an infinite-system DMRG ground state. Care must be taken so as not to bias the solution towards the initial guess. An important check for the right convergence of DMRG simulations is to run the algorithm for different number of sweeps and varying the bond dimension to see any effects of these parameters on the results.

For time evolution there are two sources of errors. The first one is due to the Trotter decomposition, that scales as  $\mathcal{O}((\Delta t)^{n+1})$  for  $n^{\text{th}}$  order Trotter decomposition. Higher order Trotter decompositions being associated with smaller errors. The total time  $T$  is divided into  $T/\Delta t$  number of steps, the total error  $\mathcal{O}((\Delta t)^n T)$  is linear in time. Slower ramps are also associated with slightly larger errors for a given step size. The linear increase could be tacked by reducing the step size. Another important source of error is the truncation carried out after applying each set of operators. These errors could blow exponentially in time. The reason behind this growth goes back to a possible up to linear increase in the entanglement with time. It turns out that for out-of-equilibrium states the entanglement actually grows linearly with time, demanding a corresponding exponential growth of the bond dimension. A truncation process that retains only  $D$  largest singular values does not take that into account leading to large errors. However, in most cases, the bound of linearly increasing entanglement is not reached and we are safe to implement a truncation procedure.



# Chapter III

## Ladders of non-Abelian anyons

In this chapter we describe our study and analysis of interacting, itinerant Fibonacci anyons on ladders composed of two or three coupled chains. We begin with a basic introduction of Fibonacci anyons that are described by the  $SU(2)_3$  theories. Thereafter, we write down models of interacting and itinerant Fibonacci anyons, starting with one dimensional models and moving on to 2D. We review all the phases obtained in the two- and three-leg doped ladders and establish the occurrence of spin-charge separation. Furthermore, we discuss a novel heavy-light  $\tau$  model and the phases associated with it.

### 1 Introduction

$SU(2)_k$  Chern-Simons theories [61, 147] are so-called quantum deformations of the  $SU(2)$  algebra. Their degrees of freedom are encoded by ‘topological charges’  $j$ , which are generalised angular momenta. In contrast to  $SU(2)$ , in  $SU(2)_k$  theories the total ‘spin’  $j$  is limited to be  $j = 0, \frac{1}{2}, \dots, \frac{k}{2}$ .

Akin to the tensor product of spins, non-Abelian anyons can be ‘fused’ according to fusion rules given by

$$j_1 \times j_2 = \sum_{j_3=|j_1-j_2|}^{\min\{j_1+j_2, k-j_1-j_2\}} j_3. \quad (\text{III.1})$$

For example, for the fusion of two anyons with  $j_{1,2} = \frac{1}{2}$ , these rules would mean  $\frac{1}{2} \otimes \frac{1}{2} = 0 \oplus 1$  (for  $k \geq 2$ ). Similarly, for the case of Fibonacci anyons ( $k = 3$ ), when  $j_{1,2} = 1$  the fusion rule reads as  $1 \otimes 1 = 0 \oplus 1$ . Note that this is different from what one would obtain under a tensor product of  $SU(2)$  spin-1 particles. In the limit  $k \rightarrow \infty$ , however, we recover the  $SU(2)$  algebra and the rule simply describes the tensor product of two ordinary  $SU(2)$  spins.

In the rest of this thesis, we focus only to the Fibonacci theory of anyons with  $k = 3$ , unless otherwise stated. There the allowed values for the topological charges

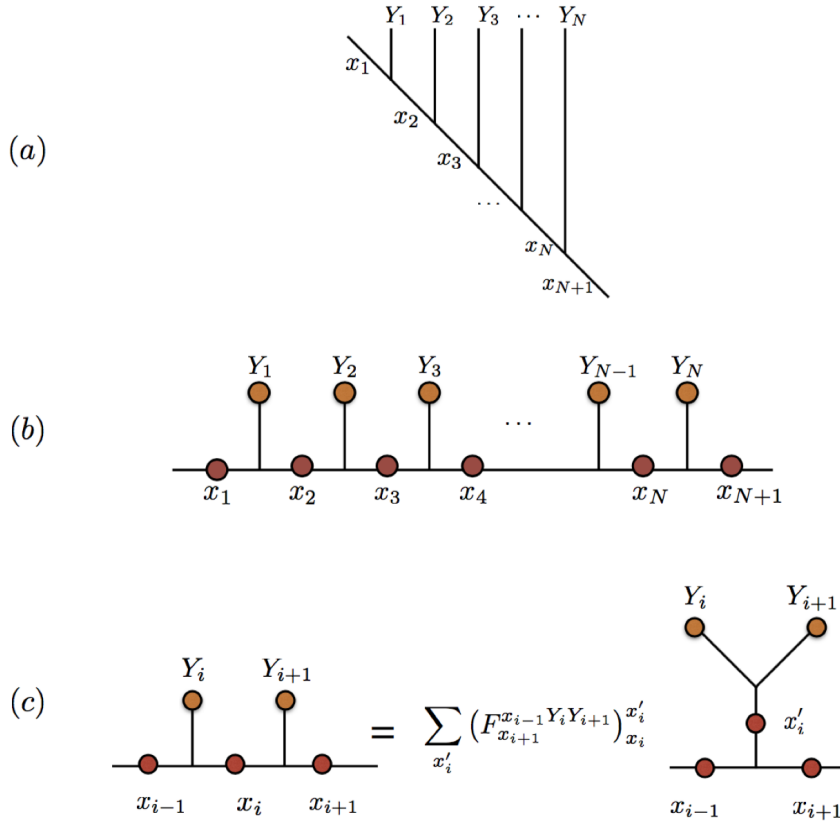


Figure III.1: (a) Illustration of the standard fusion tree with site labels  $Y_i$  (that can be either  $\tau$  or  $\mathbf{1}$ ) and bond labels  $x_i$ . (b) The flat version of the fusion tree. (c) A basis change to a different fusion tree using an  $F$ -move.

are  $j = 0, \frac{1}{2}, 1, \frac{3}{2}$ . But if we look closely at the fusion rules, we can make the identification  $0 \leftrightarrow \frac{3}{2}$  and  $1 \leftrightarrow \frac{1}{2}$ . Thus, the Fibonacci theory has two distinct types of *particles* which we denote as  $\mathbf{1}$  for the trivial particle with  $j = 0$  and  $\tau$  for the Fibonacci anyon with  $j = 1$  respectively. Using these, the fusion rules read

$$\begin{aligned}
 \mathbf{1} \otimes \mathbf{1} &= \mathbf{1} \\
 \tau \otimes \mathbf{1} &= \mathbf{1} \otimes \tau = \tau \\
 \tau \otimes \tau &= \mathbf{1} \oplus \tau.
 \end{aligned} \tag{III.2}$$

We represent a system of  $N$  anyons by means of a *fusion tree* as shown in Fig. III.1(a), where the anyonic charges of the individual anyons are labelled by  $Y_i$ . The fusion outcome of successive fusion of the anyons are encoded by the ‘bond’ labels (links) in the fusion tree, labelled by  $x_i$  in Fig. III.1(a). The constraints on the bond labels due to fusion rules which must be satisfied at each vertex significantly reduce the size of the internal Hilbert space. For  $N$  Fibonacci anyons ( $\tau$ ) the Hilbert space grows asymptotically as  $\phi^N$  where  $\phi = (\sqrt{5} + 1)/2$  is the golden ratio. From now on we draw a flat version of the fusion tree, as shown in Fig. III.1(b).

To perform an operation on nearest neighbour anyons, it is advantageous to change

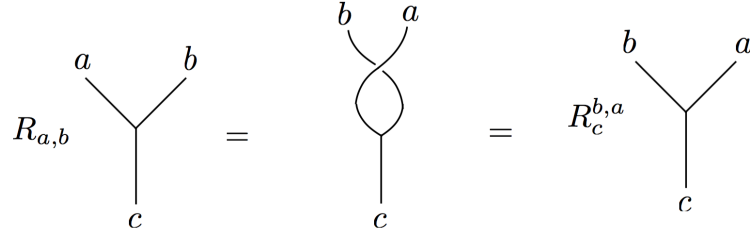


Figure III.2: Convention for the right handed braid to exchange two particles.

to a different basis in which the two-particle fusion outcome is explicit. This is done via the  $F$ -move shown schematically in Fig. III.1(c). The  $F$ -move depends on the two site labels  $Y_i$  and  $Y_{i+1}$  and the bond labels  $x_{i-1}$  and  $x_{i+1}$ . If at least one of these four labels is  $\mathbf{1}$ , then there is only one choice of bond labels that satisfies the fusion algebra and the  $F$ -move is trivial. A non-trivial matrix is obtained only when all the four labels are  $\tau$  anyons. Specialising to the case where  $Y_i = Y_{i+1} = \tau$ , the labels for the three bonds  $|x_{i-1}, x_i, x_{i+1}\rangle$  allowed by the fusion rules are

$$\{|\mathbf{1}, \tau, \mathbf{1}\rangle, |\mathbf{1}, \tau, \tau\rangle, |\tau, \tau, \mathbf{1}\rangle, |\tau, \mathbf{1}, \tau\rangle, |\tau, \tau, \tau\rangle\} \quad (\text{III.3})$$

which transforms to a new basis  $|x_{i-1}, x'_i, x_{i+1}\rangle$  after the  $F$ -move:

$$\{|\mathbf{1}, \mathbf{1}, \mathbf{1}\rangle, |\mathbf{1}, \tau, \tau\rangle, |\tau, \tau, \mathbf{1}\rangle, |\tau, \mathbf{1}, \tau\rangle, |\tau, \tau, \tau\rangle\}.$$

Using these bases the  $F$ -matrix is represented as,

$$F = \begin{bmatrix} 1 & & & & \\ & 1 & & & \\ & & 1 & & \\ & & & \phi^{-1} & \phi^{-1/2} \\ & & & \phi^{-1/2} & -\phi^{-1} \end{bmatrix}, \quad (\text{III.4})$$

where as mentioned above we have a non-trivial  $2 \times 2$  submatrix only when also  $x_{i-1} = x_{i+1} = \tau$ .

Another operation that we need to perform on nearest neighbour anyons is that of exchanging (or braiding) them. In Fig. III.2, we show our convention for a right-handed braid. The left-hand braiding is the inverse of the process shown here. Under a right-handed braid anyons  $a$  and  $b$  pick up a phase  $R_c^{b,a}$  depending on the anyon types,  $a$  and  $b$ , that are undergoing an exchange and their fusion outcome

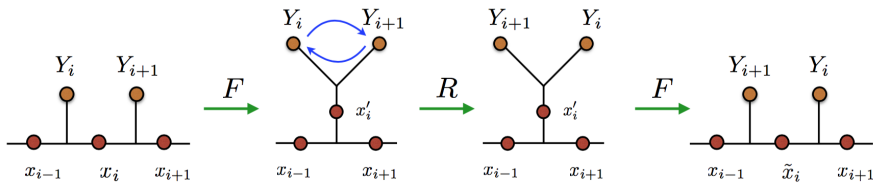


Figure III.3: Schematic representation of a braid on the fusion tree.



*c.* Note that whenever  $a$  or  $b$  are  $\mathbf{1}$ , the phase is trivial. Non-trivial phases are only obtained are for  $a = b = \tau$ :

$$R_{\mathbf{1}}^{\tau\tau} = e^{+4\pi i/5}, R_{\tau}^{\tau\tau} = e^{-3\pi i/5}. \quad (\text{III.5})$$

In order to implement a braid on the standard fusion tree, we first have to change basis using an  $F$ -move to make the fusion outcome of the two anyons explicit, and then braid. This process is shown schematically in Fig. III.3. This is represented by a Braid matrix  $B$  acting on the bond labels  $|x_{i-1}, x_i, x_{i+1}\rangle$ . The only non-trivial Braid matrix is obtained when both the sites are occupied by  $\tau$  anyons. In the basis of Eq. (III.3) we obtain:

$$B = F R F = \begin{bmatrix} e^{4i\pi/5} & 0 & 0 & 0 & 0 \\ 0 & e^{-3i\pi/5} & 0 & 0 & 0 \\ 0 & 0 & e^{-3i\pi/5} & 0 & 0 \\ 0 & 0 & 0 & \frac{1}{\phi^2}e^{4i\pi/5} + \frac{1}{\phi}e^{-3i\pi/5} & \frac{1}{\phi^{3/2}}(e^{4i\pi/5} - e^{-3i\pi/5}) \\ 0 & 0 & 0 & \frac{1}{\phi^{3/2}}(e^{4i\pi/5} - e^{-3i\pi/5}) & \frac{1}{\phi^2}e^{-3i\pi/5} + \frac{1}{\phi}e^{4i\pi/5} \end{bmatrix}. \quad (\text{III.6})$$

Note that when the two site labels are a  $\mathbf{1}$  and a  $\tau$ , the  $F$ -moves and the exchange phases are all trivial. The Braid matrix is effectively the hopping of the anyon to the adjacent site. When both the site labels are  $\mathbf{1}$ , the Braid matrix is simply given by the identity matrix.

## 2 Warmup: One dimensional models

### 2.1 Golden chain model

In this section we review the so-called ‘golden chains’, consisting of 1D arrays of localised Fibonacci anyons with pairwise interactions between nearest neighbours [62]. In this model the Hamiltonian for the magnetic interactions between anyons is defined in analogy to the Heisenberg exchange interaction. We assign an energy  $-J$  if the fusion outcome of two interacting anyons is trivial. For AFM couplings ( $J > 0$ ), this favours the fusion outcome of two neighbouring anyons to be trivial, while for FM couplings ( $J < 0$ ), the fusion of two anyons is preferred to be  $\tau$ . This interaction between nearest neighbour anyons is depicted schematically in Fig. III.4(a) and is implemented by projecting on the identity fusion channel

$$H_{\text{mag}} = J h_{\text{mag}} = -J(F P^{\mathbf{1}} F^{-1}). \quad (\text{III.7})$$

where  $F$  is the operator corresponding to the  $F$ -move (see Eq. (III.4)) and  $P^{\mathbf{1}}$  is an operator that projects onto the  $\mathbf{1}$  state. In the basis of Eq. (III.3), the

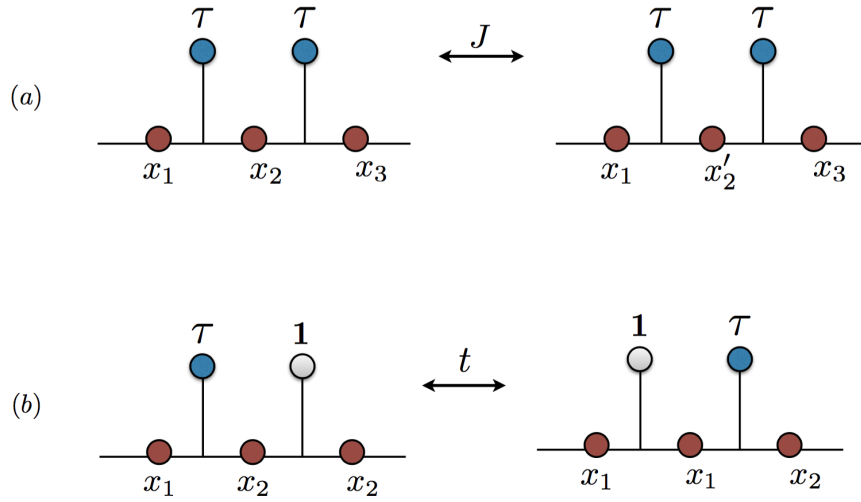


Figure III.4: (a) Nearest neighbour magnetic interaction of amplitude  $J$ . (b) The kinetic hopping (of amplitude  $t$ ) of an anyon to its nearest neighbour vacant site. The blue circles represent  $\tau$  anyons while the white circles denote vacant sites or holes.

matrix representation for the (dimensionless) magnetic interaction can be written explicitly as:

$$h_{\text{mag}} = - \begin{bmatrix} 1 & & & & \\ & 0 & & & \\ & & 0 & & \\ & & & \phi^{-2} & \phi^{-3/2} \\ & & & \phi^{-3/2} & \phi^{-1} \end{bmatrix}. \quad (\text{III.8})$$

Golden chains with AFM couplings are described by the  $k = 3$  restricted solid on solid (RSOS) model which is a CFT with central charge  $c = 7/10$ . For ferromagnetic couplings the corresponding CFT is that of the critical 3-state Potts model with  $c = 4/5$  [62, 148].

## 2.2 Itinerant Fibonacci anyons in 1D

To model itinerant anyons we introduce holes, *i.e.* sites with a trivial anyon  $\mathbf{1}$  on some of the sites. The holes and  $\tau$  anyons are labelled by different  $U(1)$  (electric) charges and anyonic (non-Abelian) charges. The  $\tau$  anyons (referred to simply as ‘anyons’ or ‘ $\tau$  particles’ hereafter) can move on the chain which results in an additional kinetic energy contribution. This kinetic process is schematically shown in Fig. III.4(b). It involves the hopping of a particle, along with its electric and anyonic charge to a neighbouring site.

Our specific model of itinerant anyons is a generalisation of the electronic  $t$ - $J$  model [72]. Assuming a large on-site charging energy, we eliminate the possibility

of doubly occupied sites and allow anyons to only hop to empty sites. As in the case of electrons, the low-energy effective  $t$ - $J$  model allows hopping of the anyons to nearest neighbour vacant sites and an exchange interaction between nearest neighbour anyons analogous to the Heisenberg interactions explained above in Sec. 2.1. The kinetic term can then be written as  $H_{\text{kin}} = -th_{\text{kin}}$ , where  $h_{\text{kin}}$  is the (dimensionless) operator corresponding to the nearest neighbour hopping process shown in Fig. III.4(b). A  $t$ - $J$  chain of itinerant anyons was studied for Ising and Fibonacci anyons [77, 78], revealing a separation of excitations into charge and anyonic excitations, similar to spin-charge separation in its electronic counterpart.

### 3 Ladders of Fibonacci anyons

#### 3.1 Undoped ladders

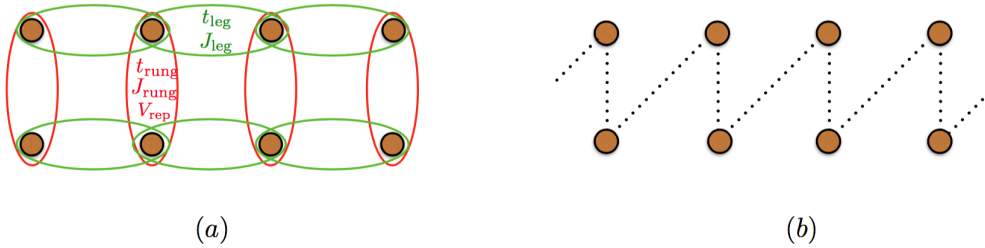


Figure III.5: Two-leg ladder: (a) Interactions along the leg and rung directions. (b) The zig-zag fusion path. The couplings have been indicated.

Ladders of Fibonacci anyons are formed by coupling chains of localised anyons [82]. Anyons interact with their nearest neighbours along the leg and rung directions via  $J_{\text{leg}}$  and  $J_{\text{rung}}$ . These interactions are shown schematically in Fig. III.5(a). As fusion path we choose the *zig-zag path* shown in Fig. III.5(b), since it minimises the effective range of interactions on the fusion path. We choose periodic boundary conditions along the leg direction and open boundary conditions along the rungs.

With this choice of fusion path, nearest neighbour interactions on the rungs are also nearest neighbour along the fusion path, while those between anyons on the same leg are longer range along the fusion path. Nearest neighbour rung interactions can be implemented in exactly the same way as for nearest neighbour on a chain (see Sec. 2.1). In order to evaluate the interactions between  $\tau$  particles on the same leg, we have to implement a change of basis, this time by braiding them in a clockwise manner until they are neighbours along the fusion path. This braiding is performed by the unitary braid matrix  $B$  (see Eq. (III.6)). Once the  $\tau$  particles are nearest neighbours along the path they can interact with the same term as discussed above in Sec. 2.1. After carrying out the interaction, the anyons have to be braided back to their original positions.

More specifically, for a two-leg ladder, adjacent anyons along the leg direction are

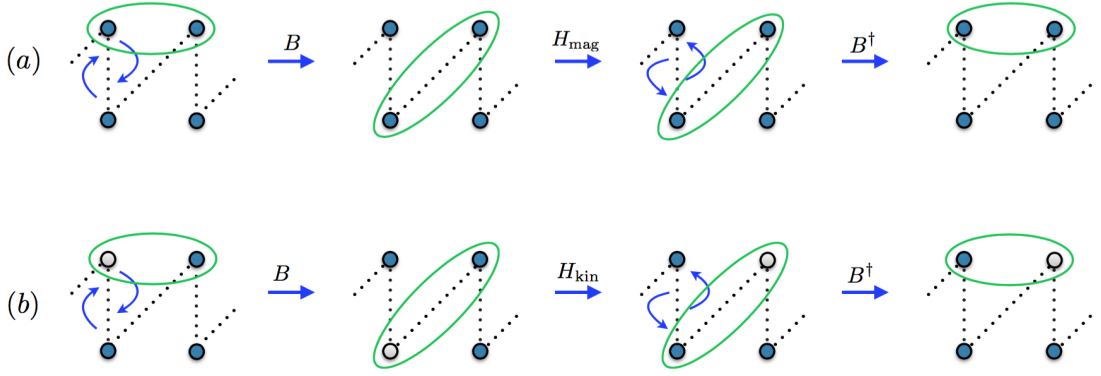


Figure III.6: Evaluation of Hamiltonian terms on a two-leg ladder along the leg direction that involve the braid operation. The blue circles represent  $\tau$  particles and the white circles are for vacant sites. The green ellipses denote the particles that are interacting along the leg direction. (a) the magnetic term (b) the kinetic term.

next nearest neighbours along the fusion path (see Fig. III.5(b)). Thus, one needs to implement one braid operation. The Hamiltonian for the magnetic interactions between nearest neighbour rungs  $r$  and  $r + 1$  on the upper leg is given by

$$(H_{\text{mag}}^1)_r = J_{\text{leg}} B_{2r-1}^\dagger (h_{\text{mag}})_{2r} B_{2r-1}, \quad (\text{III.9})$$

and on the lower leg as

$$(H_{\text{mag}}^2)_r = J_{\text{leg}} B_{2r+1}^\dagger (h_{\text{mag}})_{2r} B_{2r+1}, \quad (\text{III.10})$$

where  $h_{\text{mag}}$  has been defined in Eq. (III.8) and  $r$  labels the rungs (so that  $i = 2r$  labels the diagonal bonds along the path). In Fig. III.6(a), we summarise the magnetic interactions between nearest neighbour along the leg direction for a two-leg ladder.

For a three-leg ladder, the leg interactions are longer ranged interactions, since adjacent anyons on a leg are third neighbours along the fusion path. Thus, nearest neighbour leg interactions on a three-leg ladder require two braids before particles are nearest neighbours on the fusion path [82]. One gets for interaction between rungs  $r$  and  $r + 1$  on the upper leg,

$$(H_{\text{mag}}^1)_r = J_{\text{leg}} B_{3r-2}^\dagger B_{3r-1}^\dagger (h_{\text{mag}})_{3r} B_{3r-1} B_{3r-2}, \quad (\text{III.11})$$

on the middle leg,

$$(H_{\text{mag}}^2)_r = J_{\text{leg}} B_{3r+1}^\dagger B_{3r-1}^\dagger (h_{\text{mag}})_{3r} B_{3r-1} B_{3r+1}, \quad (\text{III.12})$$

and on the lower leg,

$$(H_{\text{mag}}^3)_r = J_{\text{leg}} B_{3r+2}^\dagger B_{3r+1}^\dagger (h_{\text{mag}})_{3r} B_{3r+1} B_{3r+2}, \quad (\text{III.13})$$

where  $i = 3r$  labels the diagonal bonds along the path.

The full magnetic Hamiltonian on the legs is obtained by adding all contributions,  $H_{\text{mag}}^{\text{leg}} = \sum_1^W H_{\text{mag}}^l$ , where  $W$  is the number of legs. As an implementation detail we want to mention that the action of the operator  $H_{\text{mag}}^l$  can generate up to  $2^{2W-1}$  states for each bond interaction. The operator mixes spin labels, thus generates multiple images for each two-body interaction. This exponential increase in the number of resulting states leads to denser Hamiltonian matrices as one increases the width  $W$  of the ladder and restricts us from exploring larger system sizes.

For ladders of localised Fibonacci anyons it was shown that similar odd-even effects as seen for  $SU(2)$  spins continue to exist in the limit of strong AFM rungs [82]. AFM coupled ladders of Fibonacci anyons with even number of legs are gapped while those with odd number of legs are critical and are described by the same CFT as the golden chain. On the other hand, Fibonacci ladders with FM rung couplings are quite different from their  $SU(2)$  counterparts [82]. Fibonacci ladders with a width that is a multiple of three are gapped since the rungs form singlets ( $j = 0$ ). Other widths are gapless since the isolated rungs effectively form  $\tau$ 's, thereby yielding a gapless chain as the effective low-energy model. This is different from  $SU(2)$  spins, for which an even number form a singlet ground state, and where thus all even width ladders are gapped.

### 3.2 Doped ladders

In this thesis we focus on itinerant ladders of Fibonacci anyons. As schematically represented in Fig. III.5(a) we denote the interaction strengths along the leg direction by  $J_{\text{leg}}$  and  $t_{\text{leg}}$  for the magnetic and kinetic terms respectively. Along the perpendicular direction, the couplings  $J_{\text{rung}}$  and  $t_{\text{rung}}$  denote respectively the magnetic and kinetic terms.

The magnetic interactions for the ladder have already been described in the section 3.1 and we thus only need to discuss the kinetic terms. Once again, the two sites on a rung are adjacent on the fusion path and the hopping is thus implemented as for the 1D  $t$ - $J$  chain (see section 2.2). For a  $\tau$  particle and hole lying on adjacent sites on the same leg of the ladder, we need to, once again, braid the sites to bring them to adjacent positions on the fusion tree. For a two-leg ladder, the kinetic term between rungs  $r$  and  $r + 1$  on the upper leg is given by

$$(H_{\text{kin}}^1)_r = t_{\text{leg}} B_{2r-1}^\dagger (h_{\text{kin}})_{2r} B_{2r-1}, \quad (\text{III.14})$$

and on the lower leg as

$$(H_{\text{kin}}^2)_r = t_{\text{leg}} B_{2r+1}^\dagger (h_{\text{kin}})_{2r} B_{2r+1}, \quad (\text{III.15})$$

where  $h_{\text{kin}}$  has been defined above and  $r$  labels the rungs. In Fig. III.6(b), we summarise the kinetic process between nearest neighbour sites along the leg direction for a two-leg ladder.

For a three-leg ladder, a  $\tau$  particle and hole lying on adjacent sites on a leg are third neighbours along the fusion path. Thus, nearest neighbour leg interaction

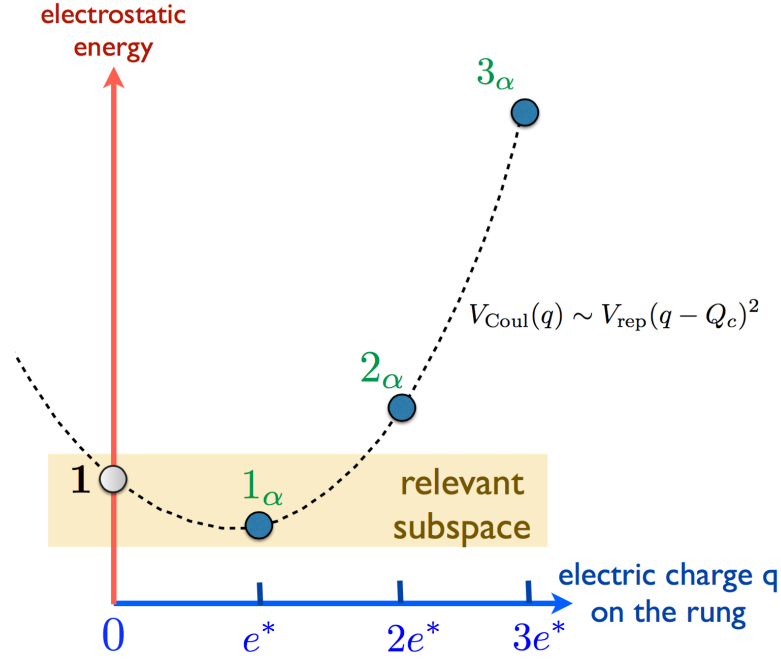


Figure III.7: Schematic energy spectra in the presence of a parabolic Coulombic charging energy. One can tune the chemical potential and the repulsion between the particles in order to gap out the higher energy sectors. This allows restricting the calculations to a low energy subspace.

on a three-leg ladder requires two braids before the  $\tau$  particle and the hole are nearest neighbours on the fusion path. One gets for kinetic terms between rungs  $r$  and  $r + 1$  on the upper leg,

$$(H_{\text{kin}}^1)_r = t_{\text{leg}} B_{3r-2}^\dagger B_{3r-1}^\dagger (h_{\text{kin}})_{3r} B_{3r-1} B_{3r-2}, \quad (\text{III.16})$$

on the middle leg,

$$(H_{\text{kin}}^2)_r = t_{\text{leg}} B_{3r+1}^\dagger B_{3r-1}^\dagger (h_{\text{kin}})_{3r} B_{3r-1} B_{3r+1}, \quad (\text{III.17})$$

and on the lower leg,

$$(H_{\text{kin}}^3)_r = t_{\text{leg}} B_{3r+2}^\dagger B_{3r+1}^\dagger (h_{\text{kin}})_{3r} B_{3r+1} B_{3r+2}, \quad (\text{III.18})$$

where  $i = 3r$  labels the diagonal bonds along the path.

Note that, in the above equations, some of the braids may be trivial, in contrast to the case of the magnetic interactions. The full kinetic Hamiltonian on the legs is obtained by adding all contributions,  $H_{\text{kin}}^{\text{leg}} = \sum_1^W H_{\text{kin}}^l$ . Here, the action of the operator  $H_{\text{kin}}^l$  can generate up to  $2^{2W-2}$  states for each bond interaction.

We also consider models with an additional rung charging term

$$V_{\text{Coul}}(q) \sim V_{\text{rep}}(q - Q_c)^2, \quad (\text{III.19})$$

where  $q$  is the number of anyons on a rung and  $Q_c$  is determined by the implicit chemical potential. Fig. III.7 shows the energy profile for a given rung composition

on the ladder. For the three-leg ladder under consideration, this term acts pairwise between all the three possible pairs of particles that can exist on the three-site rung. Assuming a charging energy which is much larger compared to the exchange energy, we can consider the limit  $V_{\text{rep}} \rightarrow \infty$ . In this limit we can restrict our calculations to just two values of the occupation on the rung,  $n$  and  $n + 1$ , with  $n$  ranging from 0 to  $W - 1$ . This reduces the Hilbert space and thus allows us to perform simulations of larger ladders.

## 4 Phase diagrams

### 4.1 Isolated rung limit

Analogous to standard electronic  $t$ - $J$  ladders the physics of anyonic  $t$ - $J$  ladders can be understood starting from the strong rung coupling limit [149, 150]. We thus begin by identifying the low-lying states of isolated rungs.

In Fig. III.8, we show the five rung configurations on isolated rungs for a two-leg ladder, and the total  $U(1)$  and anyonic charges that are possible for these rung configurations. When there are two holes on a rung, both of these charges are trivially zero. When the rung is occupied by two  $\tau$  particles, the net  $U(1)$  charge is 2, however the topological charge may be either  $\mathbf{1}$  or  $\tau$ , giving rise to two different quantum states  $|2, \tau\rangle$  (named “heavy  $\tau$ ”) and  $|2, \mathbf{1}\rangle$  (named “heavy hole” – an empty rung being a “light hole”). In the case when there is a single  $\tau$  on the rung, it can be either on the upper or on the lower leg with charges denoted as  $(1^U, \tau)$  and  $(1^L, \tau)$  respectively. The corresponding quantum states are respectively  $|1^U, \tau\rangle$  and  $|1^L, \tau\rangle$ . The bonding and anti-bonding states  $|1^\pm, \tau\rangle$  (named “light  $\tau$ ”) are formed by linear superpositions of the configurations with charges  $(1^U, \tau)$  and  $(1^L, \tau)$  given by

$$|1^\pm, \tau\rangle = \frac{1}{\sqrt{2}}(|1^U, \tau\rangle \pm |1^L, \tau\rangle). \quad (\text{III.20})$$

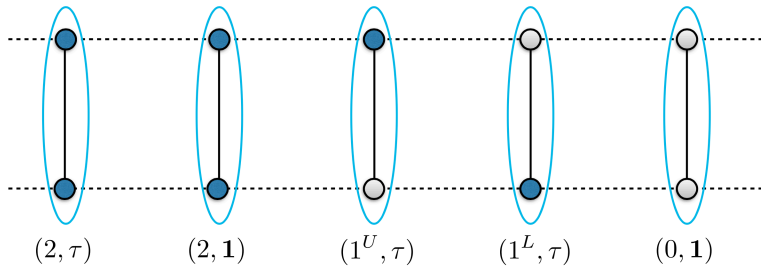


Figure III.8: All possible fusion outcomes for a rung of a two-leg ladder. The blue circles represent  $\tau$ 's while white circles represent vacant sites. The  $U(1)$  and topological charges for the different configurations are denoted in the parenthesis. The superscript  $U(L)$  refers to the  $\tau$  lying on the upper (lower) leg.

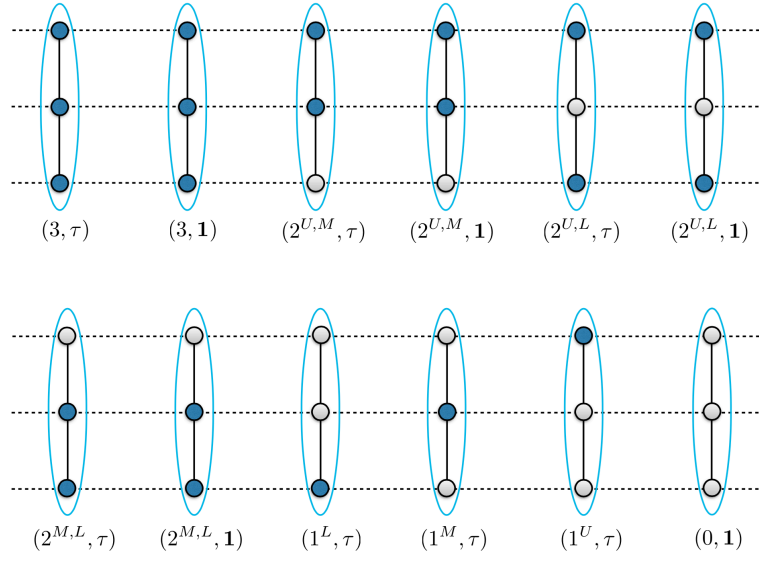


Figure III.9: The various fusion outcomes possible for a doped three-leg ladder. The blue circles represent  $\tau$ 's while white circles represent vacant sites. The first labels in the parenthesis signify the  $U(1)$  charge, corresponding to the number of  $\tau$ 's present on each rung and the second refers to their fusion outcome. The superscripts  $U, M, L$  refer to the positions of the  $\tau$  on the different legs (upper, middle, lower) of the ladder.

For a three-leg ladder, many more states are possible, as shown in Fig. III.9. When there is a single  $\tau$  on the rung ( $N_{\text{rung}} = 1$ ), the “light  $\tau$ ” quantum states formed by linear superpositions of the three different positions of the  $\tau$  particle are given by

$$|1^\pm, \tau\rangle = \frac{1}{2}(|1^U, \tau\rangle + |1^L, \tau\rangle \pm \sqrt{2}|1^M, \tau\rangle), \quad (\text{III.21})$$

$$|1^0, \tau\rangle = \frac{1}{\sqrt{2}}(|1^U, \tau\rangle - |1^L, \tau\rangle). \quad (\text{III.22})$$

Depending on the sign of the hopping, one of the states  $|1^\pm, \tau\rangle$  acquires the lowest energy. Likewise, when there are two  $\tau$  anyons on a rung ( $N_{\text{rung}} = 2$ ) we can form quantum states as linear superpositions of the states with the same  $U(1)$  and topological charges. For  $J_{\text{rung}} > 0$ , one of the “heavy hole” states

$$|2^\pm, \mathbf{1}\rangle = \frac{1}{\sqrt{2 + \alpha^2}}(|2^{U,M}, \mathbf{1}\rangle + |2^{M,L}, \mathbf{1}\rangle \pm \alpha|2^{U,L}, \mathbf{1}\rangle) \quad (\text{III.23})$$

is the ground state, with

$$\alpha = \frac{\sqrt{J_{\text{rung}}^2 + 8t_{\text{rung}}^2} - J_{\text{rung}}}{2t_{\text{rung}}}. \quad (\text{III.24})$$

If for simplicity, we consider  $J_{\text{rung}} = t_{\text{rung}}$ , then  $\alpha = 1$ . For  $J_{\text{rung}} < 0$  either of the “heavy  $\tau$ ” states

$$|2^\pm, \tau\rangle = \frac{1}{2}(|2^{U,M}, \tau\rangle + |2^{M,L}, \tau\rangle \pm \sqrt{2}|2^{U,L}, \tau\rangle) \quad (\text{III.25})$$



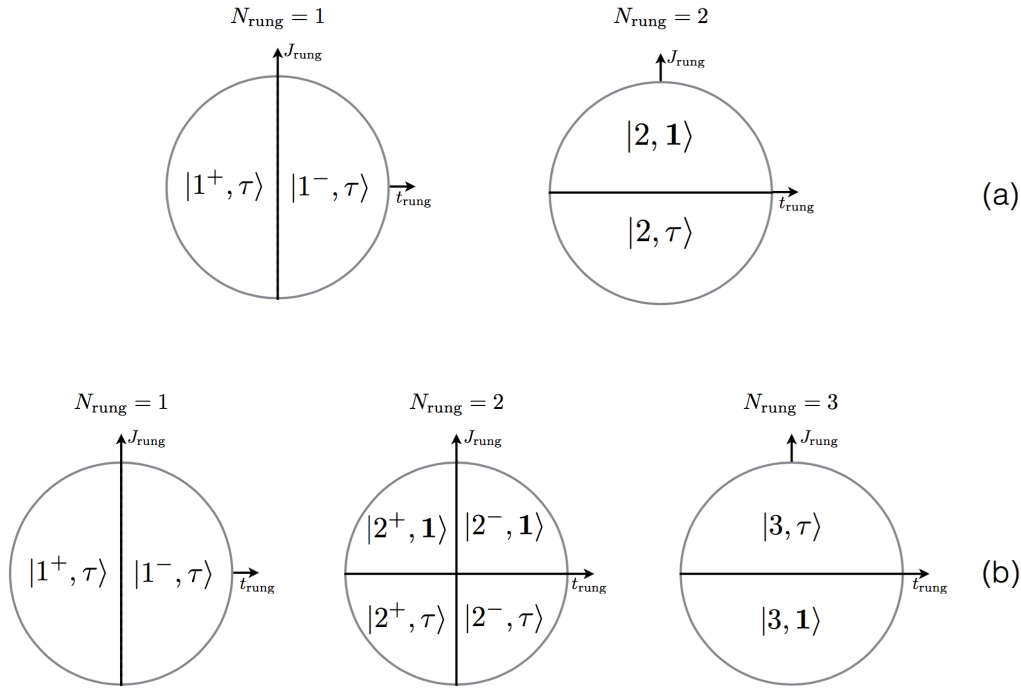


Figure III.10: Ground state phase diagram for (a) two-leg ladder and (b) three-leg ladder in the isolated rung limit (with or without charging energy). The lowest energy sectors for isolated rungs with different anyon numbers (labelled by  $N_{\text{rung}}$ ) on a ladders of itinerant Fibonacci anyons are indicated. The notations are the same as in Figs. III.8 and III.9.

has lowest energy depending on the sign of the hopping  $t_{\text{rung}}$ . When the rung is occupied by three  $\tau$  particles, the total  $U(1)$  charge on the rung is 3, and the possible quantum states are  $|3, \tau\rangle$  (named “super-heavy”  $\tau$ ) and  $|3, \mathbf{1}\rangle$  (named “super-heavy hole”) depending on the net fusion outcome.

In the limit of independent rungs and by parametrising the rung couplings as  $t_{\text{rung}} = \cos \theta$  and  $J_{\text{rung}} = \sin \theta$ , we have mapped out the parameter space on a unit circle. In Fig. III.10 we show the ground state phase diagram for an isolated rung on a two-leg or a three-leg ladder for different number  $N_{\text{rung}}$  of  $\tau$  anyons on the rung. Note that these phase diagrams do not depend on the charging energy which only gives a constant energy shift  $V_{\text{rep}}(N_{\text{rung}}e^* - Q_c)^2$  (depending on the  $N_{\text{rung}}$  sector).

## 4.2 Phase diagrams of weakly coupled rungs

Our goal is now to understand the phase diagram of anyonic ladders by starting from the isolated rung coupling limits. We do this by turning on small couplings  $t_{\text{leg}}$  and  $J_{\text{leg}}$  between the strongly coupled rungs such that  $|t_{\text{leg}}|, |J_{\text{leg}}| \ll |t_{\text{rung}}|, |J_{\text{rung}}|$ , in order to ensure that there is no transition to excited state of the isolated rungs. Figures III.11 and III.12 summarise the phase diagrams for two and three-leg

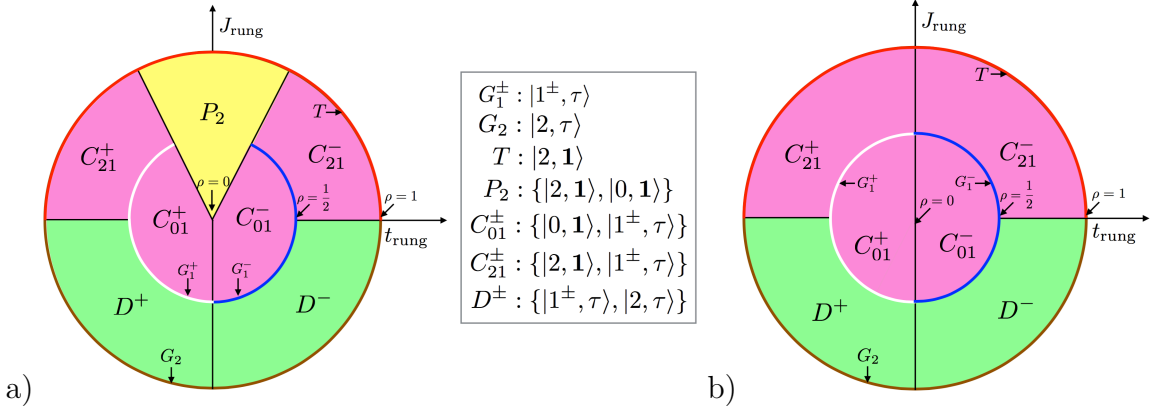


Figure III.11: Phase diagrams of the two-leg ladder in the strong rung coupling limit. a) is without a rung charging term and b) with a large rung charging term  $V_{\text{rep}}$ . Here the radius denotes the density of anyons. Depending on filling and couplings several phases can be distinguished: a totally gapped phase (T), effective golden chain models (G), effective  $t$ - $J$  chains (C), paired phases (P), and a phase with two different types of  $\tau$  anyons (D). The legend indicates which rung states are relevant in the various phases. See the text for details.

ladders.

Depending on the low-energy states on each rung we find six different types of phases:

- Totally gapped phases ( $T$ ) appear when there are exactly two (for  $J_{\text{rung}} > 0$ ) or three (for  $J_{\text{rung}} < 0$ ) anyons per rung that fuse into the trivial channel. These phases will not be discussed further.
- Effective golden chains ( $G^\pm$ ) when there are exactly  $n$   $\tau$  anyons on every rung that fuse into a total  $\tau$ . An optional  $\pm$  superscript indicates whether the particles are in a bonding (+) or antibonding(-) state on a rung. These phases will be discussed in Sec. 5.2.
- Paired phases ( $P$ ) where two anyons on a rung fuse in the trivial channel, forming hard-core bosons. These phases will be discussed in Sec. 5.1
- Effective  $t$ - $J$  chains ( $C_{nm}^\pm$ ) consisting of an effective hole that arises from  $n$  anyons on a rung fusing in the trivial channel and an effective  $\tau$  anyon arising from  $m$  anyons fusing in the  $\tau$  channel. The  $\pm$  superscript indicates whether the particles on a rung are in a bonding or antibonding state. These phases will be discussed in Sec. 5.3 and 5.4.
- Effective models consisting of two flavours of  $\tau$  anyons ( $D_{mn}^\pm$ ) that are formed by fusing  $m$  and  $n$  anyons on a rung respectively. Again the  $\pm$  superscript indicates whether the particles on a rung are in a bonding or antibonding state.
- A phase separated region  $PS_{03}$  originated from an effective  $t$ - $J$  chain with

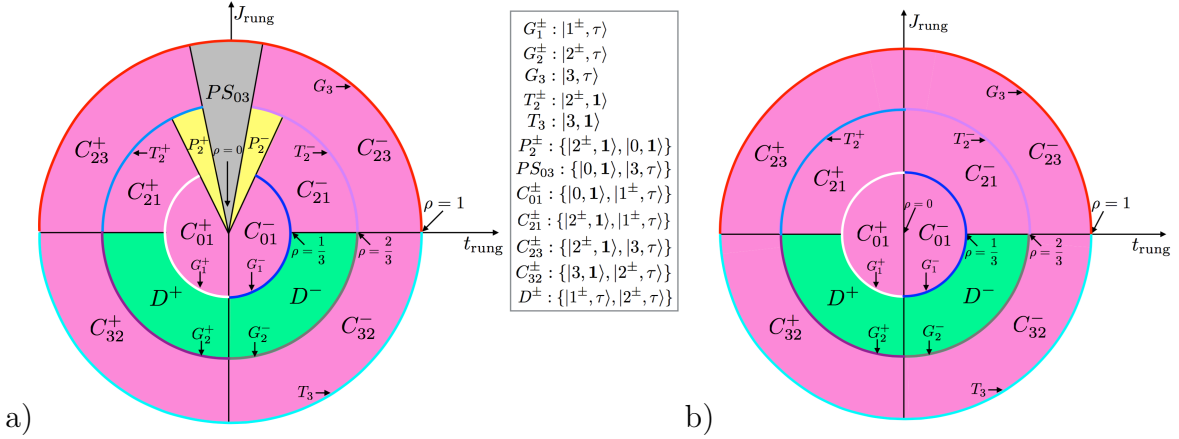


Figure III.12: Phase diagrams of the three-leg ladder in the strong rung coupling limit. a) is without a rung charging term and b) with a large rung charging term  $V_{\text{rep}}$ . Here the radius denotes the density of anyons. Depending on filling and coupling several phases can be distinguished: a totally gapped phase (T), effective golden chain models (G), effective  $t$ - $J$  chains (C), paired phases (P), phase separated phases (PS) and a phase with two different types of  $\tau$  anyons (D). The legend indicates which rung states are relevant in the various phases. See the text for details.

dominant attraction between the effective super-heavy  $\tau$  anyons.

The effect of a large rung charging energy  $V_{\text{rep}}$  is to suppress pairing and phase separation in two-leg and three-leg ladders. The other phases are unchanged when adding this term. We will thus use  $V_{\text{rep}} = \infty$  to reduce the Hilbert space dimension when numerically investigating the latter phases.

## 5 Discussion of phases and effective models

### 5.1 Pairing and effective hard-core boson models

We start our detailed discussion with paired phases that arise when two  $\tau$  anyons on a rung fuse into an effective trivial particle and are then described by mobile hard core bosons. In the case of the two-leg ladder this phase appears when  $J_{\text{rung}} > 2|t_{\text{rung}}|$ . Identifying  $|0, 1\rangle$  with an empty site and  $|2, 1\rangle$  with a hard-core boson we end up with an effective hard-core boson (HCB) model,

$$H_{\text{HCB}} = t \sum_i (b_i^\dagger b_{i+1} + h.c.) + V \sum_i n_i (1 - n_{i+1}), \quad (\text{III.26})$$

where  $b_i^\dagger$  creates a boson at site  $i$  and  $n_i = b_i^\dagger b_i$  is the boson density. The effective hopping matrix element of this hard-core boson model is obtained from second-

order perturbation theory in  $t_{\text{leg}}$  to be

$$t = -\frac{2t_{\text{leg}}^2}{J_{\text{rung}} - 2|t_{\text{rung}}|}. \quad (\text{III.27})$$

An effective nearest neighbour attraction between different types of holes comes also in second-order and is given by

$$V = -\frac{2t_{\text{leg}}^2}{J_{\text{rung}} - 2|t_{\text{rung}}|}. \quad (\text{III.28})$$

This is similar to fermionic  $t$ - $J$  ladders mapping to a Luther-Emery liquid of Cooper pairs.

In the three leg ladder, similar paired phases described by the same hard-core boson model are found when  $\rho < 2/3$  and the rung couplings satisfy

$$3\phi|t_{\text{rung}}| > J_{\text{rung}} > \frac{3}{\sqrt{2}}|t_{\text{rung}}|. \quad (\text{III.29})$$

The effective hopping matrix element of this hard-core boson model is

$$t = -\frac{2t_{\text{leg}}^2}{E_D}, \quad (\text{III.30})$$

where  $E_D = -2\sqrt{2}|t_{\text{rung}}| + \frac{J_{\text{rung}}}{2} + \frac{\sqrt{J_{\text{rung}}^2 + 8t_{\text{rung}}^2}}{2}$  and a proof is provided in Eq. (A.74). An additional effective attraction between different types of holes is given by

$$V = -\frac{2t_{\text{leg}}^2}{E_D}, \quad (\text{III.31})$$

as shown in Eq. (A.73).

## 5.2 Effective golden chains

If all rungs are at the same integer filling  $n$ , the effective model is either in a trivial gapped phase if the  $n$  anyons fuse into the trivial channel, or an effective golden chain model if they form a total  $\tau$ . We label the latter phases as  $G_n$  or  $G_n^\pm$ , where the optional  $\pm$  index indicates whether the anyons are in a bonding state (+) or antibonding state (-) on the rung.

The phase  $G_1^\pm$  appears in the two-leg ladder at unit filling (outside of the paired phase). With two  $\tau$  particles per rung and  $J_{\text{rung}} < 0$  we obtain the phase  $G_2$ .

Analogously, the three leg ladder has effective golden chain phases for specific densities  $\rho = 1/3, 2/3, 1$  on the ladder. In the case when all the rungs have exactly one  $\tau$  particle, the phase  $G_1^\pm$  is obtained. When there are two  $\tau$  anyons per rung and  $J_{\text{rung}} < 0$ , the phase  $G_2^\pm$  appears. Finally, for three  $\tau$  particles per rung and  $J_{\text{rung}} > 0$ , we obtain the  $G_3$  phase.

All coupling constants  $J$  of the effective Golden chains are listed in Table III.1.

Table III.1: Effective couplings for the various golden chain phases as a function of the ladder width  $W$  and density  $\rho$ .

$W$	$\rho$	Phase	$J/J_{\text{leg}}$	Derivation Eq.
2	$\frac{1}{2}$	$G_1^\pm$	$\frac{1}{2}$	(A.4)
2	1	$G_2$	$\frac{2}{\phi^2}$	(A.12)
3	$\frac{1}{3}$	$G_1^\pm$	$\frac{3}{8}$	(A.21)
3	$\frac{2}{3}$	$G_2^\pm$	$\frac{11}{8\phi^2}$	(A.25)
3	1	$G_3$	1	(A.30)

### 5.3 Effective $t$ - $J$ models: Two-leg ladder

Doping the  $\rho = 1/2$   $G_1^\pm$  golden chain with (light) holes one obtains an effective anyonic  $t$ - $J$  chain ( $C_{01}^\pm$ ). The magnetic coupling  $J$  is the same as for the  $G_1^\pm$  golden chain.

Increasing the  $U(1)$  charge density ( $\rho > 1/2$ ), by effectively doping the  $G_1^\pm$  golden chain with heavy holes, one obtains a similar  $C_{21}^\pm$   $t$ - $J$  chain for AFM rung couplings  $J_{\text{rung}} > 0$  with a sign change of the hopping term.

Coupling constants are summarised in Table III.2.

#### 5.3.1 Effective model for charge degrees of freedom

From the mapping of a doped ladder to an effective 1D  $t$ - $J$  chain we expect its spectrum to fractionalize into charge and anyon (called also “spin”) degrees of freedom. To investigate spin-charge separation in the ladder, we first examine the pure  $U(1)$  charge spectrum when  $J_{\text{leg}} = 0$ .

In the  $J = 0$  limit of an anyonic  $t$ - $J$  chain the itinerant anyons behave like HCBs which can be mapped onto a system of spinless fermions. Adding an external flux in the ring, the HCB spectrum is therefore given by charge excitation parabolas,

$$E_{\text{HCB}}(p, \phi_{\text{ext}}) = -2t \sum_{j(p)} \cos \left[ \frac{2\pi}{L} \left( j + \frac{1}{2} \right) + \frac{\phi_{\text{ext}}}{L} \right], \quad (\text{III.32})$$

Table III.2: Effective couplings for the various  $t$ - $J$  phases of the two-leg ladder as a function of the density  $\rho$ .

Filling	Phase	$J/J_{\text{leg}}$	$t/t_{\text{leg}}$	Derivation Eq.
$\rho < \frac{1}{2}$	$C_{01}^\pm$	$\frac{1}{2}$	$\frac{1}{2}$	(A.37)
$\rho > \frac{1}{2}$	$C_{21}^\pm$	$\frac{1}{2}$	$-\frac{1}{2}$	(A.42)

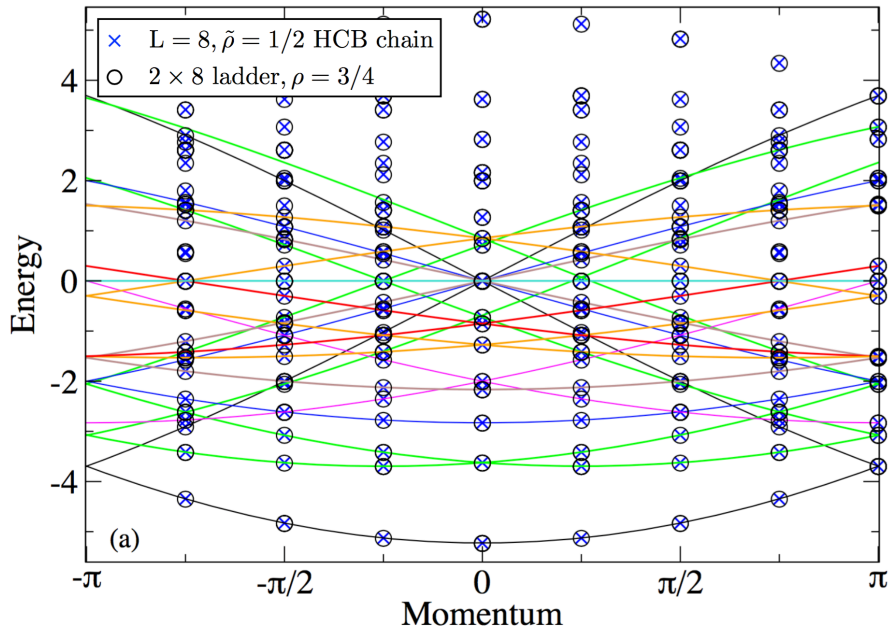


Figure III.13: Charge spectrum at  $J_{\text{rung}} = t_{\text{rung}} = 1000$ ,  $t_{\text{leg}} = 1$ ,  $J_{\text{leg}} = 0$ ,  $V_{\text{rep}} = \infty$ . The solid lines denote the HCB spectrum (with an external flux) given by Eq. (III.32), different colours corresponding to the different charge branches (labelled by  $p$  in Eq. (III.32)). The black circles denote the spectrum of a  $2 \times 8$  ladder with  $\rho = 3/4$ . The blue crosses correspond to the effective chain spectrum for  $L = 8$ ,  $\tilde{\rho} = 1/2$  (see Eq. (III.33)).

where  $\{j(p)\}$  is a set of integers (labelled by the branch index  $p$ ) which determine the continuous momenta, given by  $K = \frac{2\pi}{L} \sum_{j(p)} (j + \frac{1}{2}) + \tilde{\rho} \phi_{\text{ext}}$ ,  $\tilde{\rho}$  being the density of particles in the system. In the  $J = 0$  limit we must be careful since the fusion tree labels make the anyons distinguishable. Thus, in the absence of magnetic interactions the energy levels show a high degree of degeneracy that arises due to the built in non-Abelian nature of the Fibonacci anyons. Moving an anyon across the boundary cyclically translates the fusion tree labels. All  $N$  particles must be translated over the boundary to be able to have the original labelling. This brings about a phase shift of  $\phi_n = 2\pi n/N$ ,  $n$  being an integer. The charge spectrum of the anyonic chain can then be described as a union of all HCB spectra for all discrete values of  $\phi_n$ , with no external flux:

$$E_{\text{charge}}^{p,n} = E_{\text{HCB}}(p, \phi_n). \quad (\text{III.33})$$

The states are labelled by their total momentum  $K_{p,n} = K_p + 2\pi \frac{n}{N}$ .

Our numerical results show that, as expected, the charge spectrum of the ladder corresponds exactly to that of the effective chain. As an example, Fig. III.13 shows the  $J_{\text{leg}} = 0$  spectrum of a  $2 \times 8$  ladder with  $\rho = 3/4$ , which is in perfect agreement with the spectrum of an effective  $J = 0$  chain with  $L = 8$  and  $\tilde{\rho} = 1/2$  and with the HCB spectrum given by the cosine branches according to Eqs. (III.32) and

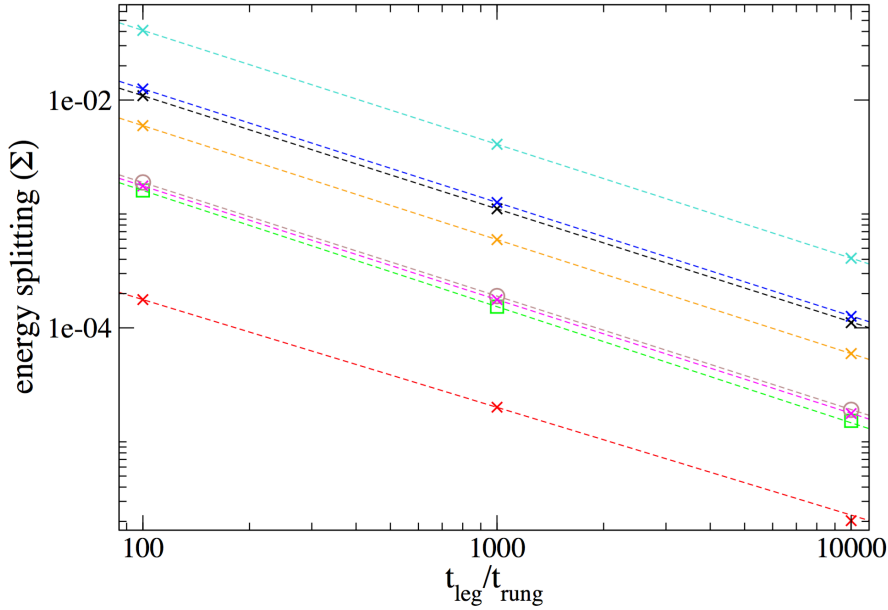


Figure III.14: Energy splittings of each of the eight  $E \leq 0$  energy levels at  $K = 0$  of the  $2 \times 8$  ladder with  $\rho = 3/4$  (symbol/line colours here match the colours of the parabolic branches of Fig. III.13) as a function of  $t_{\text{leg}}/t_{\text{rung}}$ . The values of the leg couplings are  $t_{\text{leg}} = 1$ ,  $J_{\text{leg}} = 0$ ,  $V_{\text{rep}} = \infty$  and  $t_{\text{rung}} (= J_{\text{rung}})$  takes different values from 100 to 10000. The fits correspond to the expected  $t_{\text{rung}}^{-1}$  behaviour.

(III.33). Note that there is a global shift in energy between the ladder and the chain spectra given by

$$E_{\text{shift}} = -t_{\text{rung}}N_s - J_{\text{rung}}N_d, \quad (\text{III.34})$$

where  $N_s$  ( $N_d$ ) are the number of rungs carrying a single (two)  $\tau$  (s).

Lastly, we would like to mention that the mapping is exact only in the limit when the rung couplings tend to infinity. For large, yet finite, rung couplings the energy levels of the ladder model in each parabola are split into an exponential number of energy levels over a finite energy range  $\Sigma$ . This is due to second order processes to higher energy states that give rise to a broadening of order  $\Sigma \sim t_{\text{leg}}^2/t_{\text{rung}}$  and  $t_{\text{leg}}^2/J_{\text{rung}}$  of the energy levels, as shown in Fig. III.14.

### 5.3.2 Numerical comparison between microscopic model and 1D t-J model

We next turn on a small  $J_{\text{leg}}$  and adiabatically follow the splitting of the charge parabolas. Fig. III.15(a) zooms into the low energy spectrum to show how the highly degenerate energy levels are split by a small  $J_{\text{leg}} = 0.1$ . Fig. III.15(b) shows results for a larger coupling  $J_{\text{leg}} = 1$ . We see that magnetic interactions lift the degeneracy of the states with an energy spread proportional to  $LJ_{\text{leg}}$ . This is consistent with the behaviour of the effective  $t$ - $J$  chain exhibiting “spin-charge

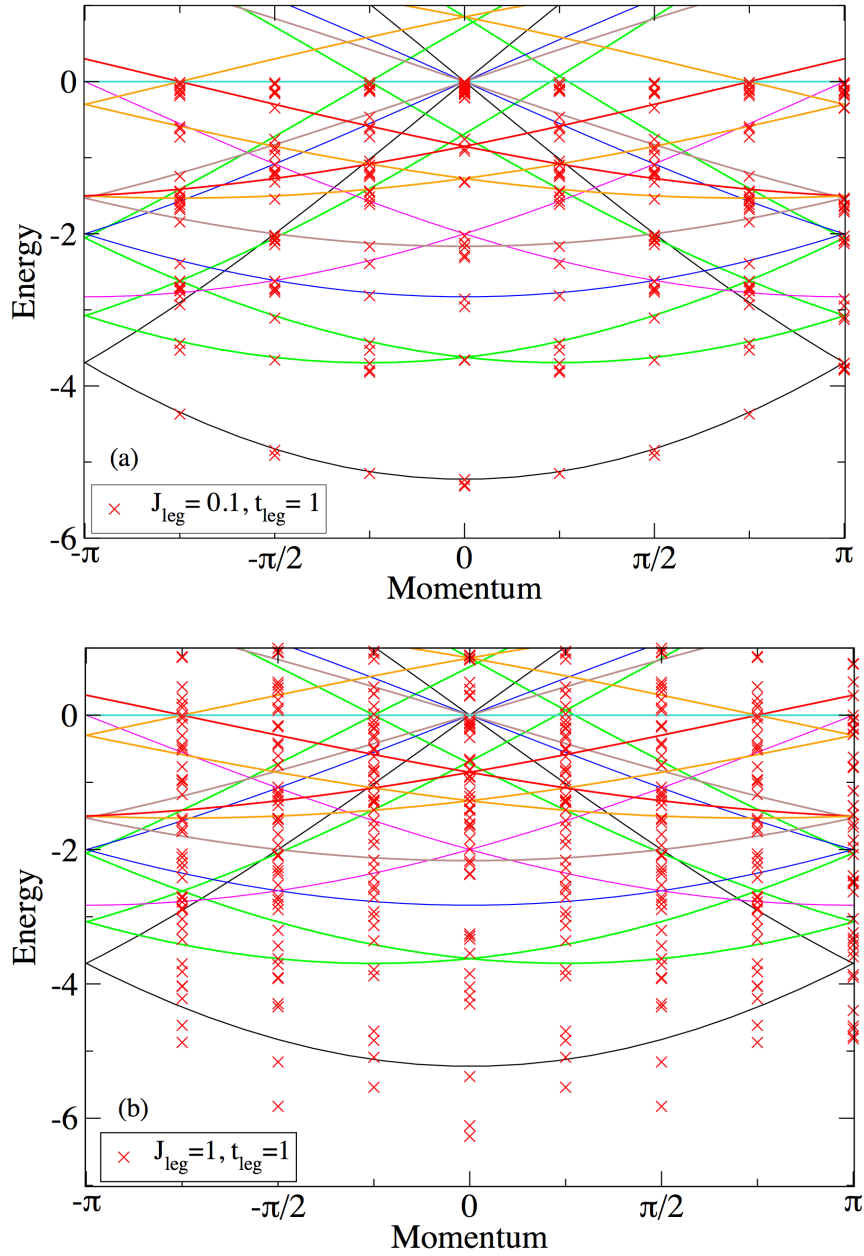


Figure III.15: Splitting of the degenerate levels on switching on different values of  $J_{\text{leg}}$  on a  $2 \times 8$  ladder with  $\rho = 3/4$  and  $J_{\text{rung}} = t_{\text{rung}} = 1000$ ,  $t_{\text{leg}} = 1$ ,  $V_{\text{rep}} = \infty$ . The parabolas show the continuous HCB spectrum relevant for  $J_{\text{leg}} = 0$  (see Fig. III.13) and the red crosses represent the ladder spectrum at (a)  $J_{\text{leg}} = 0.1$  (b)  $J_{\text{leg}} = 1$ .

separation”: in Refs. [77, 78] we showed that the full excitation spectrum of an itinerant anyon chain is made up of two independent contributions originating from the charge degrees of freedom (described in section 5.3.1) and the anyon degrees of freedom which are given by a *squeezed* (undoped) anyon chain of length  $L_a = \tilde{\rho}L$  where  $\tilde{\rho}$  is the anyon density on a  $L$  site  $t$ - $J$  chain of anyons.

We now perform a quantitative comparison of the spectra of the anyonic ladder and



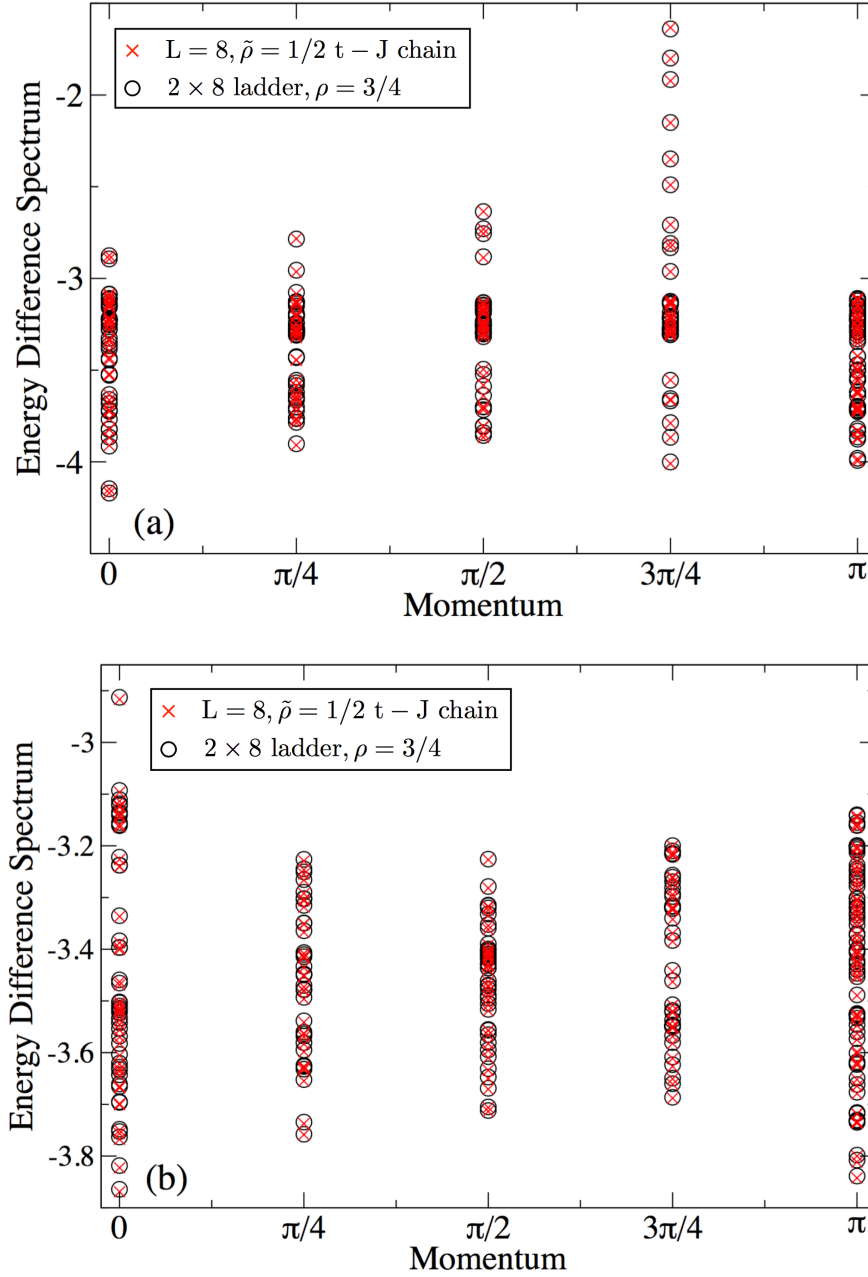


Figure III.16: Comparison of the energy difference spectra, after subtracting the charge contribution to the energy of each state, of a  $2 \times 8$  ladder,  $\rho = 3/4$  with that of the effective  $t$ - $J$  chain  $L = 8, \tilde{\rho} = 1/2$ . The couplings on the ladder are  $J_{\text{rung}} = t_{\text{rung}} = 1000, t_{\text{leg}} = 1, V_{\text{rep}} = \infty$  and (a)  $J_{\text{leg}} = 0.1$  and (b)  $J_{\text{leg}} = 1$ .

its corresponding effective anyonic chain. As the charge spectra match, we focus on the energy difference spectrum (EDS) obtained by subtracting the (supposed) charge excitation component to each state. By construction, the EDS then carries the information about the anyon degrees of freedom. Note that this procedure is only possible at low energy and for small enough  $J_{\text{leg}}$ , *i.e.* when a well defined parabolic charge branch can be assigned unambiguously to the levels we consider.

However, even when a large splitting of the energy levels is seen as in Fig. III.15(b), we have been able to identify exactly the charge excitations corresponding to the various levels in the low energy spectrum up to an excitation energy of order  $5t_{\text{leg}}$  and hence obtain the corresponding EDS. The numerical results for the EDS on a  $2 \times 8$  ladder with anyon density  $\rho = 3/4$  for small  $J_{\text{leg}} = 0.1t_{\text{leg}}$  and intermediate

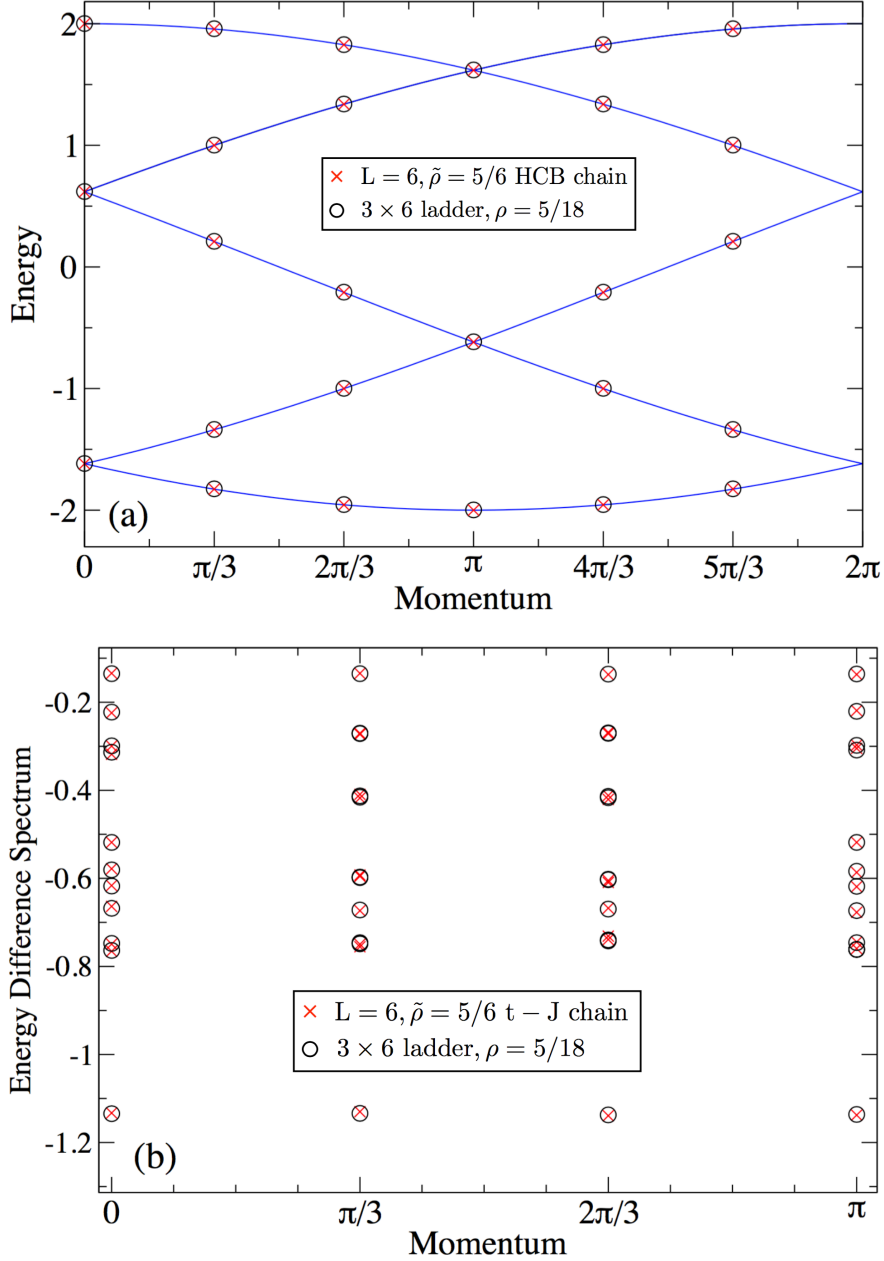


Figure III.17: Three-leg ladder: The black circles denote the spectrum of a  $3 \times 6$  ladder with  $\rho = 5/18$  while the red crosses are for the effective chain with  $L = 6$  and  $\tilde{\rho} = 5/6$ . The couplings on the ladder are  $J_{\text{rung}} = t_{\text{rung}} = 1000, t_{\text{leg}} = 1, V_{\text{rep}} = \infty$ . (a) Charge spectrum at  $J_{\text{leg}} = 0$ . The solid lines denote the HCB spectrum. (b) energy difference spectrum for  $J_{\text{leg}} = 0.1$ .

$J_{\text{leg}} = t_{\text{leg}}$  are shown in Figs. III.16(a) and (b) respectively. We find the EDS of the ladder and of the effective chain to be in perfect agreement. The perfect mapping of the two-leg ladder physics to the physics of the chain hence implies straightforwardly that the concept of spin-charge fractionalisation is not strictly 1D but also applies to the two-leg anyonic ladder, in contrast to the electronic ladder analog.

Note that the EDS subtracted spectrum must not be confused with the actual energy spectrum of the corresponding squeezed golden chain. In our prescription, subtracting the charge excitations from the full spectrum, we get the spectrum corresponding to the anyon degrees of freedom as a function of the total momentum of the ladder/ $t$ - $J$  chain, rather than that of the squeezed golden chain. Thus the spectra shown in Figs. III.16(a),(b) are qualitatively different from the golden chain spectra.

## 5.4 Effective $t$ - $J$ models: Three-leg ladder

All results about the  $t$ - $J$  phases are summarised in Table III.3 and we provide a short description below.

### 5.4.1 Density $\rho < 1/3$

For  $\rho < 1/3$ , the effective model upon doping the effective golden chain  $G_1^\pm$  is again a  $t$ - $J$  chain ( $C_{01}^\pm$ ) independent of the sign of the couplings. Our numerical spectra agree well with the effective model, as shown in Fig. III.17 for a  $3 \times 6$  ladder with  $\rho = 5/18$ .

Note that, analogously to the case of the two-leg ladder, the mapping to the effective model is exact only in the limit of infinite rung couplings. In Fig. III.18, we show the log-log plot for the broadenings  $\Sigma$  for each  $E \leq 0$  energy levels in the  $K = 0$  sector as a function of the inverse rung couplings for a three-leg ladder. The slope of  $-1$  shows again that, for large but finite rung couplings, there are second order effective processes involving higher energy states of the rungs.

### 5.4.2 Density $1/3 < \rho < 2/3$ and $J_{\text{rung}} > 0$

In the density regime  $1/3 < \rho < 2/3$ , we find an effective  $t$ - $J$  model ( $C_{21}^\pm$ ) upon doping the  $\rho = 1/3$   $G_1^\pm$  golden chain with heavy holes (increasing the U(1) charge density) or, equivalently, doping the totally gapped  $\rho = 2/3$   $T_2^\pm$  phase with effective light  $\tau$  particles (reducing the U(1) charge density). Numerical simulations of three-leg ladders in this density regime gives an effective hopping that agrees very well with the analytical estimate.

Filling	$J_{\text{rung}}$	Phase	$J/J_{\text{leg}}$	$t/t_{\text{leg}}$	Derivation Eq.	$V/J_{\text{leg}}$	Derivation Eq.
$\rho < \frac{1}{3}$	any	$C_{01}^{\pm}$	$\frac{3}{8}$	1	(A.49)	—	—
$\frac{1}{3} < \rho < \frac{2}{3}$	$> 0$	$C_{21}^{\pm}$	$\frac{3}{8}$	$\frac{1}{(2+\alpha^2)2\phi} \left[ (3 + \alpha^2 + 2\sqrt{2}\alpha) \left( \cos \frac{4\pi}{5} \right) + 1 \right]$	(A.55)	—	—
$\rho > \frac{2}{3}$	$> 0$	$C_{23}^{\pm}$	1	$\frac{1}{2+\alpha^2} \left[ \frac{1}{\phi^2} + \frac{\alpha^2}{2\phi} + \frac{\alpha^2}{\phi^3} + 1 \right]$	(A.60)	$-\frac{2}{\phi^2}$	(A.29)
$\rho > \frac{2}{3}$	$< 0$	$C_{32}^{\pm}$	$\frac{11}{8\phi^2}$	$\frac{1}{2\phi} - \frac{1}{4}$	(A.65)	$\frac{11}{8\phi^3}$	(A.26)
any	$> 3\phi t_{\text{rung}} $	$PS_{03}$	1	$\frac{t_{\text{leg}}^2}{E_D^2} (3\phi^{-2} + 2\phi^{-3} + \phi^{-2} e^{8\pi i/5})$	(A.84)	$-\frac{2}{\phi^2}$	(A.29)

Table III.3: Effective couplings for the  $t$ - $J$  phases of the three-leg ladder. Here  $E_D = (-\phi + \frac{1}{2})J_{\text{rung}} + \sqrt{2}t_{\text{rung}} + \sqrt{\frac{J_{\text{rung}}^2 + 8t_{\text{rung}}^2}{2}}$ .

### 5.4.3 Density $\rho > 2/3$ and $J_{\text{rung}} > 0$

In the strong antiferromagnetic  $J_{\text{rung}} > 0$  rung coupling limit, increasing the U(1) charge density starting from the  $T_2^\pm$  gapped chain of heavy holes, introduces super-heavy  $\tau$  anyons (*i.e.*  $|3, \tau\rangle$  states). The system is described by a  $C_{23}^\pm$  (modified)  $t$ - $J$  chain. Unlike in the previous simple  $t$ - $J$  chains, the super-heavy  $\tau$ 's experience an effective nearest neighbour *attractive* potential.

### 5.4.4 Density $\rho > 2/3$ and $J_{\text{rung}} < 0$

For ferromagnetic  $J_{\text{rung}} < 0$  at a density  $\rho > 2/3$ , we map to an effective (modified)  $t$ - $J$  chain  $C_{32}^\pm$  phase of heavy  $\tau$ 's and super-heavy holes. The heavy  $\tau$ 's experience a nearest neighbour *repulsive* potential. Our numerical simulations match very well the analytical estimates.

## 5.5 Phase separation at large $J_{\text{rung}} > 0$

In the absence of a rung charging energy  $V_{\text{rep}}$  an additional phase  $PS_{03}$ , that exhibits phase separation, appears for large  $J_{\text{rung}} > 3\phi|t_{\text{rung}}|$ . The physics of the interacting light holes and super-heavy  $\tau$  particles is described by an extended 1D  $t$ - $J$ - $V$  model that contains the usual couplings of the regular  $t$ - $J$  model and, in addition, the nearest neighbour attractive potential  $V$  between the super-heavy  $\tau$

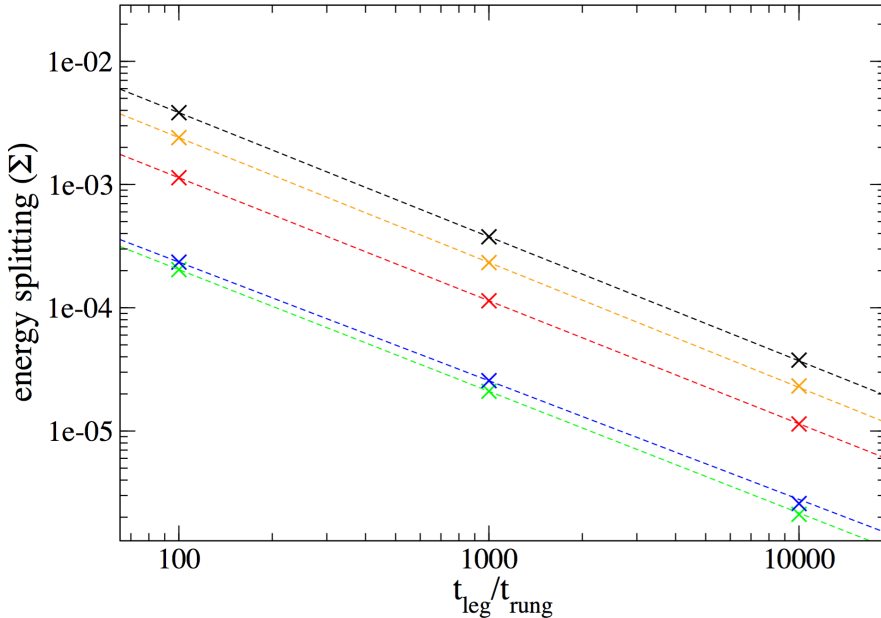


Figure III.18: Energy splittings of all  $E \leq 0$  energy levels at  $K = 0$  of the  $3 \times 6$  ladder with  $\rho = 5/6$  as a function of  $t_{\text{leg}}/t_{\text{rung}}$ . The values of the couplings are  $t_{\text{leg}} = 1$ ,  $J_{\text{leg}} = 0$ ,  $V_{\text{rep}} = \infty$  and  $t_{\text{rung}} (= J_{\text{rung}})$  takes different values from 100 to 10000.

particles. The dominant attraction  $V$  leads to phase separation between an empty and a completely filled ladder.

## 6 Effective model of heavy and light Fibonacci anyons

### 6.1 The model

We now discuss a new model which appears for strong FM rung couplings on a two-leg ladder with  $\rho > 1/2$  and a large  $V_{\text{rep}}$ . A similar effective model also describes the three-leg ladder with FM rung couplings and  $1/3 < \rho < 2/3$ . When the rung couplings are FM, the fusion of two  $\tau$ 's results in a  $\tau$  charge. The fusion of a  $\tau$  and a hole always results in a  $\tau$ . One thus obtains an effective model with two *different* Fibonacci particles, the *heavy* and *light*  $\tau$ 's distinguished by their  $U(1)$  charge. For two-leg and three leg ladders, the magnetic interactions (similar to the Golden chain) and the potentials between the different flavours of  $\tau$  particles are listed in Table III.4.

Width	$\tau_1$	$\tau_2$	$J/J_{\text{leg}}$	Eq.	$V/J_{\text{leg}}$	Eq.
2	heavy	heavy	$\frac{2}{\phi^2}$	(A.12)	$\frac{2}{\phi^3}$	(A.11)
2	heavy	light	$-\frac{1}{\phi}$	(A.16)	$\frac{1}{\phi}$	(A.17)
2	light	light	$\frac{1}{2}$	(A.4)	—	—
3	heavy	heavy	$\frac{11}{8\phi^2}$	(A.25)	$\frac{11}{8\phi^3}$	(A.26)
3	heavy	light	$-\frac{5}{8\phi}$	(A.33)	$\frac{5}{8\phi}$	(A.34)
3	light	light	$\frac{3}{8}$	(A.21)	—	—

Table III.4: Interactions between heavy and light  $\tau$ 's in two-leg and three-leg ladders. The labels  $\tau_1$  and  $\tau_2$  indicate the type (heavy or light) of the two interacting particles.

In addition to the magnetic and potential terms one also gets a kinetic process exchanging heavy and light  $\tau$ 's on nearest neighbour rungs. This process is shown schematically in Fig. III.19(a),(b) for the microscopic ladder model and the effective chain respectively. Note that, in the  $t$ - $J$  chain, with holes and  $\tau$ 's, the hopping process shown in Fig. III.1(c) moves the entire particle along with its charges and spin labels. Whereas now, the scenario is very different, the spin labels mix with each other as the heavy  $\tau$ 's hop over to exchange positions with the light  $\tau$ 's. The effective 1D model (in the basis of Eq. (III.3)) for the hopping of heavy  $\tau$ 's is described by the Hamiltonian  $H_{\text{HL}}$  given below

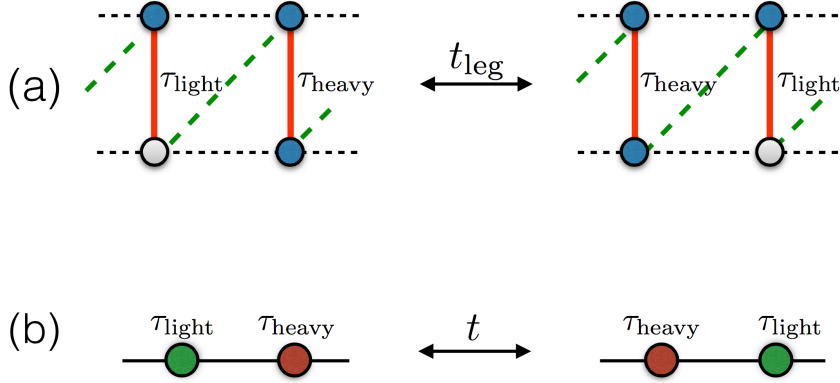


Figure III.19: Hopping of heavy (or equivalently light)  $\tau$ 's. (a) Microscopic ladder model: the blue circles denote  $\tau$  particles and the white circles are vacant sites on the ladder. (b) The effective chain.

$$H_{\text{HL}} = t \begin{bmatrix} 1 & & & & \\ & 0 & & & \\ & & 0 & & \\ & & & \phi^{-2} & \phi^{-3/2} \\ & & & \phi^{-3/2} & \phi^{-1} \end{bmatrix}, \quad (\text{III.35})$$

where  $t$  is the rescaled hopping amplitude. We have found that, for a two-leg ladder, the effective hopping amplitude is

$$t = \cos(3\pi/5)t_{\text{leg}}. \quad (\text{III.36})$$

A proof of this is provided in Eq. (A.47).

For a three-leg ladder, the same model applies in the density regime  $1/3 < \rho < 2/3$  (see Fig. III.12(b) showing the two new low energy states on the rungs) and the hopping amplitude is

$$t = \frac{1}{8} [1 + 9 \cos(3\pi/5)] t_{\text{leg}}, \quad (\text{III.37})$$

as shown in Eq. (A.71). Note that there exists a symmetry between the two kinds of  $\tau$ 's *i.e.* the number of heavy and light  $\tau$ 's in the system can be swapped, leaving the physics unchanged. We provide a detailed analytical derivation of this Hamiltonian in Appendix A.

These analytical considerations are found to be in very good agreement with our numerical results for  $J_{\text{leg}} = 0$ . Fig. III.20 shows the comparison between the low energy spectra of the effective single chain with heavy and light taus and the ladder model. Note that for  $J_{\text{leg}} = 0$  there is an exact  $E \rightarrow -E$  symmetry in the spectrum (not shown here) that emanates from a symmetry of exchanging heavy and light  $\tau$ 's. When there is an odd number of both particle types, the momenta are shifted by  $\pi$  under this exchange.

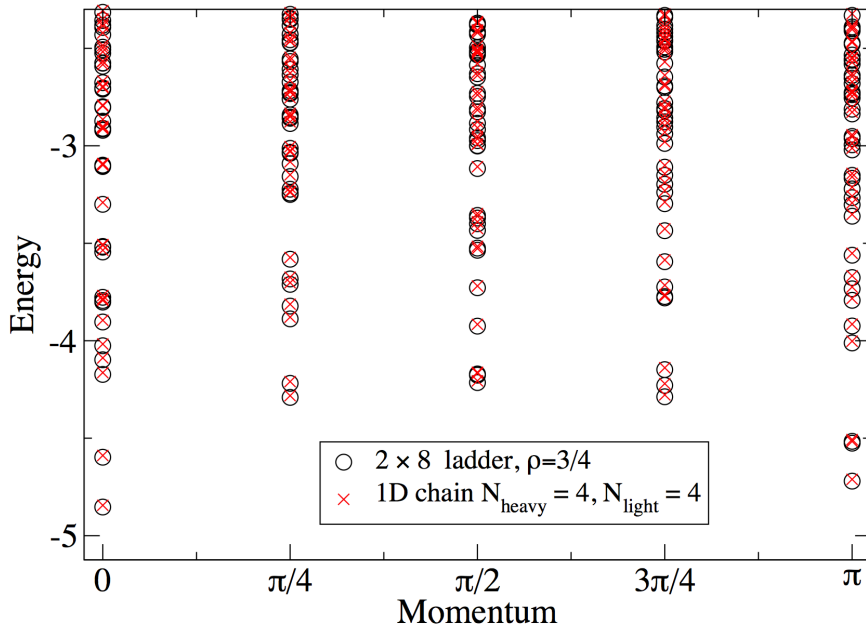


Figure III.20: Low energy spectrum of the two-leg ladder with strong FM rung couplings compared to the 1D heavy and light  $\tau$  model. The black circles are for a  $2 \times 8$  ladder and anyon density  $\rho = 3/4$ , while the red crosses are for the effective chain that it maps to ( $L = 8, \tilde{\rho} = 1/2$ ). The values of the couplings are  $t_{\text{leg}} = 1, J_{\text{leg}} = 0, V_{\text{rep}} = \infty$  and  $J_{\text{rung}} = -2t_{\text{rung}} = -2000$ .

The 1D model allows us to numerically solve larger systems with smaller finite size corrections. We, however, restrict ourselves to the case  $J_{\text{leg}} = 0$  when there are no magnetic interactions between  $\tau$  particles along the leg direction but only a small hopping  $t_{\text{leg}}$  operates between the rungs since already this simple model raises several open questions.

## 6.2 Single particle dispersion

We start with the simplest problem of a single light (heavy)  $\tau$  moving in a background of  $L - 1$   $\tau$ 's of heavy (light)  $\tau$ . We choose  $t = -1$  in order to avoid even-odd chain length effects (although for  $L$  even the sign of  $t$  is irrelevant). In the spectra shown in Fig. III.21 for several chain lengths we observe that the dispersion minimum is always at  $K = 0$  and a local minimum appears around an incommensurate momentum. The bandwidth is about  $0.015|t|$ , independent of whether we consider a single heavy or light  $\tau$ .

## 6.3 Critical phase at generic fillings

We next consider a finite density  $\tilde{\rho}$  of heavy  $\tau$ 's and a corresponding filling of  $1 - \tilde{\rho}$  light  $\tau$ 's. Note that due to the symmetry between the heavy and light



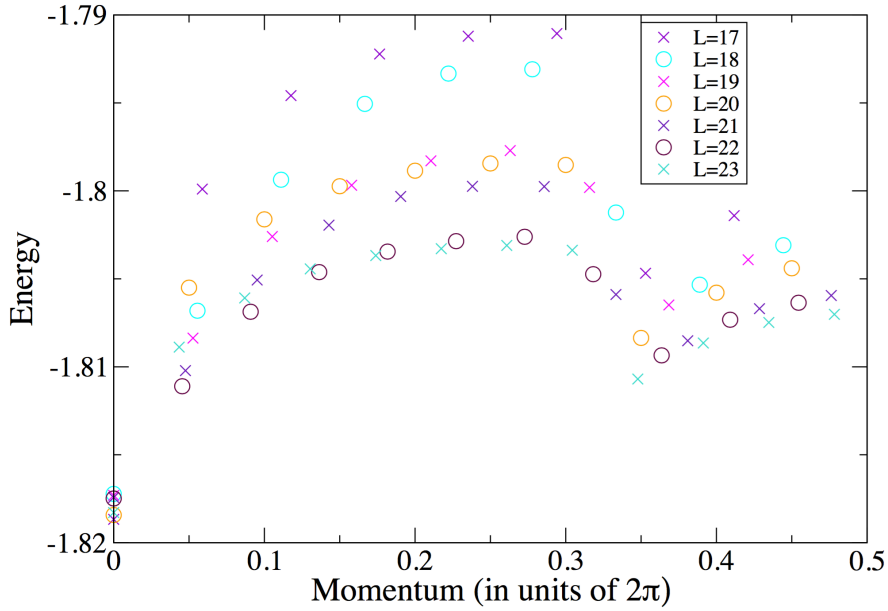


Figure III.21: Energy dispersions of a single heavy (or light)  $\tau$  amidst  $L - 1$  light (or heavy)  $\tau$ 's for even (circles) and odd (crosses) length chains, with couplings  $t = -1$  and  $J = 0$ .

$\tau$ 's, densities  $\tilde{\rho}$  and  $1 - \tilde{\rho}$  are equivalent. We expect the same behaviour for all densities except for the half-filled case  $\tilde{\rho} = 1/2$ , which we shall consider separately in the next section. For simplicity we thus choose  $\tilde{\rho} = 1/4$  since it allows us to perform a finite size analysis using three different chain lengths  $L = 12, 16, 20$ . The corresponding spectra are shown in Fig. III.22(a).

One-dimensional gapless systems are often described by a CFT and their lowest energy levels are then given by

$$E(L) = e_T L + \frac{2\pi v}{L} \left( -\frac{c}{12} + h_L + h_R \right). \quad (\text{III.38})$$

where  $c$  is the central charge and  $h_L, h_R$  are the scaling dimensions of the 'primary fields' of the CFT. The (thermodynamic) ground state energy per site  $e_T$  and the velocity  $v$  are non-universal constants. The finite size ground state energy  $E_0(L)$  corresponds to  $h_L = h_R = 0$ .

To test the CFT prediction, we performed a finite-size scaling analysis of the first few energy gaps vs  $1/L$ . As shown in Fig. III.22(b), we observe that the gaps around  $K = \pi$  show a linear scaling with  $1/L$ , suggesting gapless modes. This behaviour is, in principle, consistent with the CFT scaling of Eq. (III.38). However, at this point, we could not identify the CFT that describes our model, being limited in Lanczos exact diagonalisation to system sizes of less than twenty sites. Using the density matrix renormalisation group (DMRG) might help to obtain the central charge, but is left for future studies.

The energy spectrum around  $K = 0$  shows a different behaviour: as shown in Fig. III.22(b), the finite size gaps of the first excited states at momentum  $K = 0$

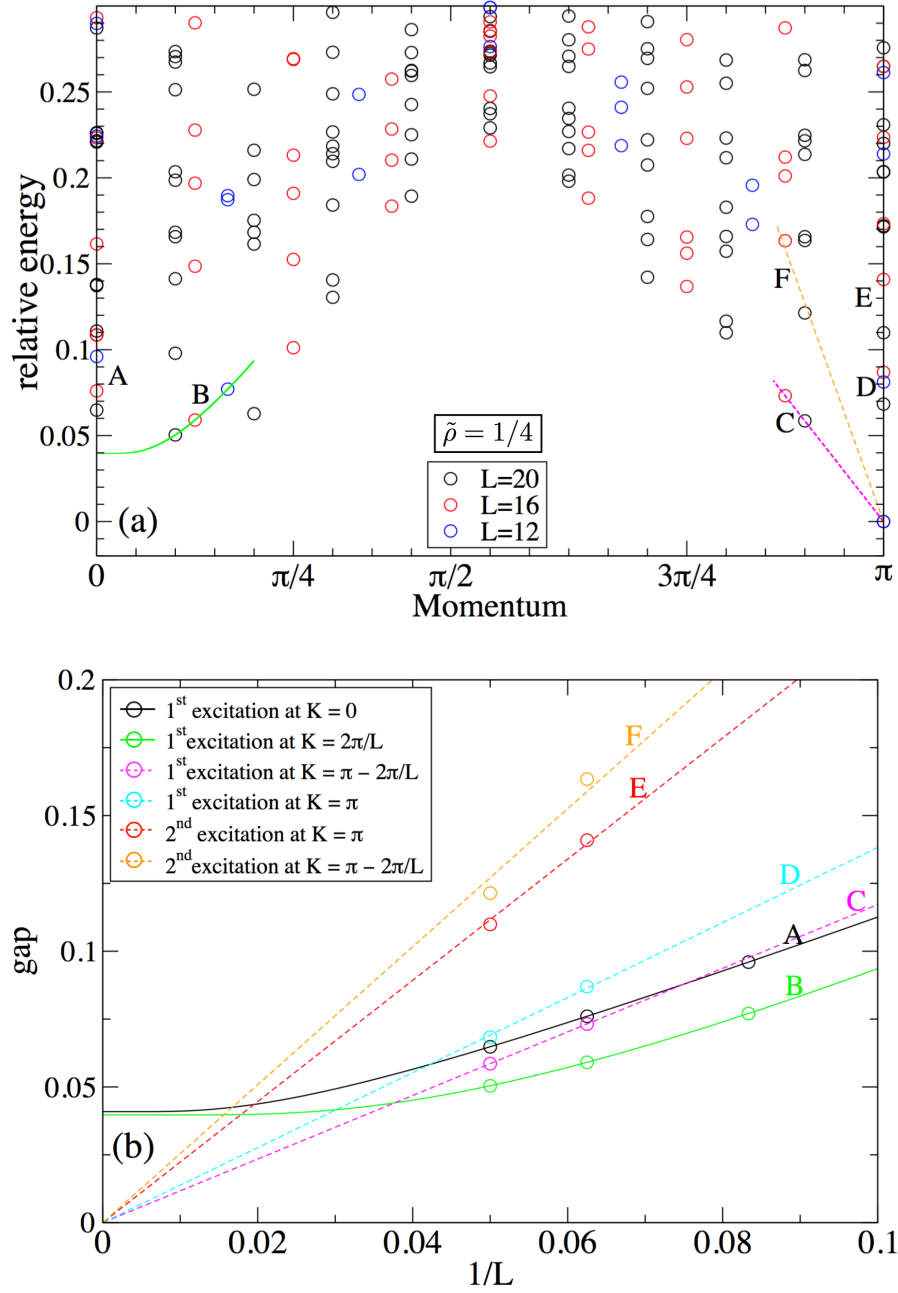


Figure III.22: (a) Spectra for the effective chains for heavy and light  $\tau$ 's at  $\tilde{\rho} = 1/4$  with  $t = 1$ ,  $J = 0$ . Note the momenta have been shifted by  $\pi$  for  $L$  odd to make all spectra similar and the ground state energy has been subtracted out. The lowest energy levels at momenta  $0$ ,  $2\pi/L$ ,  $\pi - 2\pi/L$  and  $\pi$  have been tagged as A, B, C and D, respectively. The second excitations at momenta  $\pi$  and  $\pi - 2\pi/L$  are labeled by E and F, respectively. (b) Finite-size scaling analysis of the A, B, C, D, E and F energy excitations. Linear (dashed lines) and exponential (full lines) fits are shown around  $K = \pi$  and  $K = 0$ , respectively (see text). The scalings of the B, C and F gaps are also reported in (a).

and  $K = 2\pi/L$  could be fitted as  $\Delta(L) = \Delta(\infty) + C/L \exp(-L/\xi)$ , where  $\Delta(\infty) \simeq 0.04$  is a finite energy gap and  $\xi > 10$  is a correlation length. This suggests that, at density  $\tilde{\rho} = 1/4$ , the energy spectrum shows both a gapless mode with linear dispersion, described by a CFT, and additional gapped modes.

#### 6.4 Possible topological gapped phase at $\tilde{\rho} = 1/2$

Next we consider the density  $\tilde{\rho} = 1/2$  where there is an equal number of heavy and light  $\tau$ 's. We simulated chains with lengths  $L = 14, 16, 18,$  and  $20$  and show these spectra in Fig. III.23(a), revealing low energy excitations at momenta  $K = 0$  and  $K = \pi$ . Performing a finite size scaling analysis on the low lying states using system sizes  $L$  ranging from 14 to 20 sites, as shown in Fig. III.23(b) we find that an exponential form like  $\Delta(L) = \Delta(\infty) + C/L \exp(-L/\xi)$  provides reasonably good fits of the data. These fits suggest that three of the gaps extrapolate to zero and the next higher energy excitations extrapolate to a finite value  $\Delta(\infty) \sim 0.05$ . Note however, that the correlation lengths extracted from the fits are of the order of the system size so that our extrapolations have to be taken with caution. However, if correct, our findings would indicate a topological gapped phase with a four-fold degenerate ground state, although dimerisation is not excluded (since ground state momenta are both 0 and  $\pi$ ). In any case, we believe half-filling is a special case and very different from the other density regimes we considered. This behaviour is also notably different from the golden chains which are known to be gapless for both FM and AFM leg couplings.

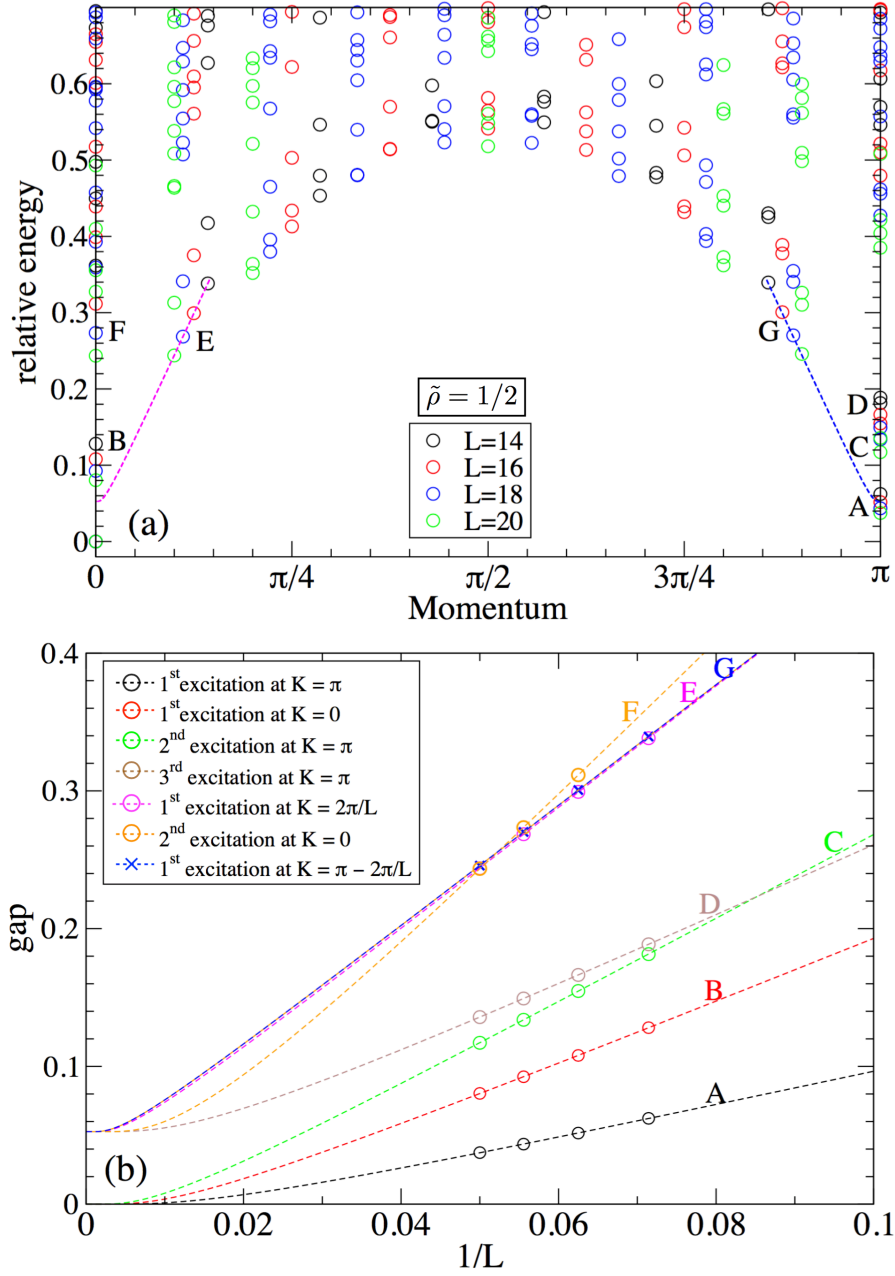


Figure III.23: (a) Spectra of the chains of heavy and light  $\tau$ 's of different sizes at  $\tilde{\rho} = 1/2$  and  $t = 1, J = 0$ . The ground state energy has been subtracted out and the momenta are shifted by  $\pi$  for odd number of particles of each type so as to get the same zero ground state momentum in all cases. The lowest energy levels at momenta 0,  $2\pi/L$ ,  $\pi - 2\pi/L$  and  $\pi$  have been tagged as B, E, G, A, respectively. The second excitations at momenta 0 and  $\pi$  are labeled by F and C, respectively. The third excitation at momentum  $\pi$  is labeled by D. (b) Finite-size scaling analysis of the energy gaps of (a) vs  $1/L$  (see text). The scalings of the E and G gaps are also reported in (a).



# Chapter IV

## Fermions in optical lattices

## 1 Introduction

An optical lattice is an effective periodic potential created by the induced dipole interaction between neutral atoms and electromagnetic waves. There are specific potential minima that are able to localise the particles, thereby corresponding to a lattice. Such a lattice, for instance, can be realised by the interference between two counter propagating laser beams. This potential, with periodicity  $d = \lambda/2$  (where  $\lambda$  is the wavelength of the laser beam), could then have minima at either the intensity maxima or minima of the laser beam depending on the frequency of the laser beam. It is these minima of the potential that form the lattice sites where, in the absence of other interaction terms, the particles eventually tend to reside. Furthermore, we can allow laser beams to interfere along various directions to create higher dimensional lattices or even those with different geometries such as dimers [151], triangular lattices [152], kagome lattices [153] etc. The optical lattice is created using Gaussian laser beams, thereby leading to a periodic potential with concomitant harmonic trap that confines the particles in the lattice.

For the case of fermions, s-wave scattering is not allowed due to the Pauli Exclusion Principle and for low energies the higher partial waves are suppressed. So the fermions are naturally non-interacting. To include the effect of interactions one has to use other methods. In the present day experiments, it is possible to tune the nature of the interaction (attractive or repulsive) and also its strength to almost any possible value. The study of strongly correlated systems is facilitated by the advances in modern cold atom experiments. This is done very efficiently by using the method of Feshbach resonances. The interaction strength is directly related to the scattering length which can be tuned by varying the applied magnetic field in the experiments. The scattering length is given by

$$a = a_{\text{BG}} \left( 1 - \frac{\Delta B}{B - B_0} \right), \quad (\text{IV.1})$$

where  $a_{\text{BG}}$  is the background scattering length set by the highest vibrationally excited state in the open channel,  $B_0$  is the position of the resonance and  $\Delta B$  is its width. At the resonance position the scattering length diverges and the only length scale in the problem is the inter-particle spacing  $\sim k_F^{-1}$ .

The presence of a harmonic trap is efficient for spatial confinement of the system. The single particle states are limited to a smaller finite region of the extent of the lattice, making the system tractable in experiments. The trapping potential appears in the Hamiltonian as a spatially dependent term. The Hamiltonian is no longer translational invariant. In such a case, the Bloch function description of the wavefunctions is not valid in a strict sense. However, if the length scale associated with the trapping potential is much larger than the lattice spacing then the system can be considered locally homogenous. This limit where the potential is only slowly varying is called the Local Density Approximation. When the energy difference between two neighbouring sites is smaller than any other energy scale in the problem then we can approximate it to a homogenous system. The chemical

potential is shifted to include the site dependent piece, treating the problem in a similar way as before. The locally varying chemical potential, depending on the interaction strength, can lead to the coexistence of conducting and insulating phases, for example a Mott insulator at the boundaries along with a metallic state in the bulk.

Although the optical lattice under study is strictly speaking not a homogenous lattice due to the presence of the confining potential, it is nevertheless instructive to study the underlying physical concept of particle in a periodic potential. Though the single-particle picture is a non-interacting system, it does help us understand our interacting system better. According to the Bloch theorem the wavefunction of a particle in a periodic potential can be written as a plane wave times a periodic function, that has the same periodicity as the potential. The wavefunction is characterised by quasimomentum  $q$ , a good quantum number corresponding to the translational symmetry of the potential. Periodicity tells us that the momentum values are repeated after a certain interval, denoted as the Brillouin zone. For a given value of  $q$ , we have multiple solutions of the Schrodinger equation which belong to different energy bands, denoted by the index  $n$ . The wavefunction can be written as

$$\phi_q^{(n)}(x) = e^{iqx/\hbar} u_q^{(n)}(x), \quad (\text{IV.2})$$

where  $u$  is a periodic function that obeys the same periodicity as the potential. The separation between these bands depends on the quasimomentum value and the lattice depth. In the absence of an optical lattice there are no energy gaps between the bands and the particles trace out energy-momentum parabolas as if they were free particles. As soon as the lattice depth becomes finite, an energy gap opens up and deviations from the quadratic energy-momentum dispersion are observed. Additionally, a decrease in band width is seen. For the case of very deep lattices, the energy gap between the lowest and the subsequent energy band is large enough to approximate the low-energy physics to a single-band Hubbard model. Such a limit also witnesses the lowest energy band to be more or less flat, i.e. a degeneracy in  $q$ . The Bloch wavefunctions are completely delocalised and extend over the entire length of the lattice. For the atoms localised on lattice site, it is more natural to consider an alternate basis, namely the Wannier basis that is described by localised wavefunctions for each lattice site. They can be obtained by constructive superpositions of Bloch wavefunctions and for a particle localised at site  $i$  in the  $n^{\text{th}}$  band are given by:

$$w_n(x - x_i) = \frac{1}{\sqrt{N}} \sum_q e^{-iqx} \phi_q^{(n)}(x), \quad (\text{IV.3})$$

where  $N$  is a normalisation constant.

The process of lattice loading begins in the extreme limit of shallow lattices, where the lattice potential is turned off. The lattice potential is then ramped up extremely slowly, ideally adiabatically, to minimise any deviations from the ground state of the instantaneous Hamiltonian. In experiments, however, deviations from the true adiabatic regime are bound to arise since the lattice loading can only be



done in a finite amount of time. The hope remains that the system ends up in the ground state of the desired final Hamiltonian by means of a time evolution from the initial state. The non-adiabaticities, quite often, lead to the population of some low-lying excitations, and eventually a rise in the temperature of the system. Deep lattices are legitimate to be approximated by a single-band Hubbard model and suppress the population of higher bands due to the large energy gap, thus the target Hamiltonian lies in that regime. However, the initial state has a vanishing lattice depth, thus does not have a band gap, rendering the Wannier basis inappropriate for our use. We thus use real space discretisation to obtain a continuum model which can be used to study the entire lattice loading schedule, from the early stages right until the end. This allows us to systematically study the time evolution of the loading process, without the need to change basis during the process.

## 2 Model

The Hubbard model is one of the simplest models that captures efficiently the many-body effects for fermions. The ground state is determined by the competition between several different energy scales, namely the kinetic energy that delocalises the particles and the on-site potential that may or may not favour double occupied lattice sites, depending on whether it is attractive or repulsive.

In this work we consider a continuum model of spin-1/2 fermions that can be written in continuous space as a function of the field operators  $\hat{\psi}_\sigma^\dagger(x)$  that creates a fermion of mass  $m$  and spin  $\sigma$  at the position  $x$ . The corresponding annihilation operator is  $\hat{\psi}_\sigma(x)$ . The Hamiltonian of a 1D system of size  $L$  can then be written as:

$$\begin{aligned} \mathcal{H} = & \sum_{\sigma} \int_0^L dx \hat{\psi}_\sigma^\dagger(x) \left[ -\frac{\hbar^2}{2m} \frac{d^2}{dx^2} + V(x) \right] \hat{\psi}_\sigma(x) \\ & + \frac{g}{2} \sum_{\sigma\sigma'} \int_0^L dx \hat{\psi}_\sigma^\dagger(x) \hat{\psi}_{\sigma'}^\dagger(x) \hat{\psi}_{\sigma'}(x) \hat{\psi}_\sigma(x), \end{aligned} \quad (\text{IV.4})$$

where the first term is the kinetic energy and the second one is a site dependent external potential energy. The four-operator term is the contact interaction characterised by the interaction strength  $g$ , which is obtained from the single particle scattering length [154]. The external potential carries the potential created by the interfering lattice beams along with the harmonic trap used for confining the system. It is given by

$$V(x) = V_0 \cos^2(kx) + \frac{1}{2} m \omega^2 x^2, \quad (\text{IV.5})$$

where  $V_0$  is the lattice depth,  $k = \frac{2\pi}{\lambda}$  is the wave vector of the laser beam and  $\omega$  is the frequency of the harmonic trap. The natural energy scale in the problem is the recoil energy defined as  $E_r = \frac{\hbar^2 k^2}{2m}$ . Our results will be presented in units of  $E_r$ .

In order to simulate numerically the continuum model described in Eq. (IV.4), we first map it to a discrete space basis by considering a unit cell of length  $a$ , which is discretised with  $N_{\text{discr}} = 16$  grid points. This leads to a grid spacing of length  $d = a/N_{\text{discr}}$ . For the optical lattice the natural choice for the unit cell is to be one minimum of the external optical lattice potential, i.e.  $a = \lambda/2 = \pi/k$ . The continuum Hamiltonian is then mapped to a lattice Hubbard model written in terms of creation and annihilation operators  $c_{i,\sigma}^\dagger$  and  $c_{i,\sigma}$  respectively,  $i$  being the grid site index and  $\sigma$  is the spin of the fermion. The Hamiltonian is written as

$$\begin{aligned} \mathcal{H} = & - J(d) \sum_{\sigma} \sum_{\langle ij \rangle} c_{i,\sigma}^\dagger c_{j,\sigma} + \text{h.c.} \\ & + \sum_{\sigma\sigma'} \sum_i \frac{U(d)}{2} c_{i,\sigma}^\dagger c_{i,\sigma'}^\dagger c_{i,\sigma'} c_{i,\sigma} + \sum_{\sigma} \sum_i \epsilon_i(d) n_{i\sigma}, \end{aligned} \quad (\text{IV.6})$$

where the kinetic term becomes the hopping amplitude  $J(d) = (\hbar^2/2m)/d^2$  between adjacent grid sites  $i$  and  $j$ , the contact interaction turns into an on-site interaction  $U(d) = g/d$  and the external potential is implemented as a site-dependent chemical potential  $\epsilon_i(d) = V(d/2 + id) + 2(\hbar^2/2m)/d^2$ .

The choice of the real-space discretisation allows to simulate the continuum model in the very shallow lattice as well deep lattice regimes without the need to change basis during the time evolution of the loading process.

By changing the number of particles in the system and tuning the model parameters, one obtains very different phases in the ground state that could be used for one or another experiment. Moreover, the presence of a harmonic trapping potential realises different phases in different spatial regions. This allows us to simulate several different target states which we present in sec. 5.

### 3 Method

Analogous to the previous study of bosonic systems [123] we simulate a fermionic optical lattice model numerically with the density matrix renormalisation group method (DMRG) [155, 156]. The DMRG method can be understood in terms of the matrix product state (MPS), which is a variational ansatz wave function that for one-dimensional quantum systems reduces the exponentially growing complexity to just a polynomial scaling by limiting the amount of entanglement which is captured by the ansatz. The accuracy of the algorithm is systematically improved with an increase of the MPS bond dimension  $M$ . This algorithm is known to work exceptionally well for obtaining the low-lying spectra of 1D systems in good agreement with experimental results [157, 158].

The standard DMRG approach has serious convergence problems for large dilute lattices that arise from the real-space discretisation needed to represent the continuum system during the lattice loading. To overcome these problems we use the multigrid DMRG algorithm [142] which leads to fast convergence.

Time evolution within the MPS framework is performed making use of the time-dependent variants of DMRG [134, 135, 159], which split non-commuting terms in the unitary time evolution operator via a second-order Suzuki-Trotter decomposition on a small time step  $dt = 0.01 \hbar/E_r$ . For a nearest-neighbours model this decomposition allows to sequentially apply two-site gates to the MPS wave function. In the worst case scenario of a local perturbation propagating through the system, the MPS bond dimension needs to grow exponentially with the number of time steps, however, since our goal is to evolve the system being as adiabatic as possible, the MPS truncation is still controllable even for relative long time scales. In our simulations this is achieved by reaching a bond dimension between  $M = 400$  and  $M = 600$ . The simulations were performed using the ALPS MPS code [139–141] on the Mönch cluster of ETH Zurich.

Note that our simulations do not suffer from any boundary effects that may arise due to the choice of open boundary conditions. The reason is that the presence of a trapping potential and our choice of particle filling ensures that the extent of the system with a non-zero local density is effectively reduced compared to  $L$ . Thus, the system remains confined well within the boundaries. This reduced extent of the actual length serves as an effective system size and is referred to as  $L_{\text{eff}}$  in the following section.

## 4 Lattice loading protocols and observables

To simulate the effects of the optical lattice loading process we use the ground state optimisation to prepare the initial wave function in the state  $|\psi_{\text{init}}\rangle$ , where the lattice potential is switched off *i.e.*  $V_0(t = 0) = V_i = 0$ . This state is then time-evolved with a time-dependent Hamiltonian such that at any time  $t$  during the evolution the state is given by  $|\psi(t)\rangle$  with a time dependent lattice potential  $V_0(t)$ . In our simulations we use a ramp that linearly interpolates between the initial depth  $V_i$  and final depth  $V_f$  of the optical lattice as:

$$V_0(t) = V_i + (V_f - V_i) \frac{t}{t_R}, \quad (\text{IV.7})$$

where  $t_R$  is total ramp time. At the end of the lattice loading the model is expected to have reached the target state with lattice potential  $V_0(t_R) = V_f (= 8 E_r)$ . The final state  $|\psi_{\text{final}}\rangle \equiv |\psi(t = t_R)\rangle$  is compared to the target state  $|\psi_{\text{target}}\rangle$  to quantify the defects. We repeat this process for several initial states, different loading protocols, as well as multiple ramp times.

To quantify and understand the origin of the defects we can address several observables both during the evolution of the wave function  $|\psi(t)\rangle$  and at the final state  $|\psi_{\text{final}}\rangle$ . In our study we examine observables only at the end of ramp time. Of particular interest are the excess energy per particle

$$q|_{(t=t_R)} = (E[|\psi_{\text{final}}\rangle] - E[|\psi_{\text{target}}\rangle])/N, \quad (\text{IV.8})$$

and the fidelity with respect to the ground state of the instantaneous Hamiltonian, which at the end of loading is given by

$$f|_{(t=t_R)} = |\langle \psi_{\text{target}} | \psi_{\text{final}} \rangle|. \quad (\text{IV.9})$$

We also study the time-evolution of the local density

$$n_\sigma(x, t) = \langle \psi(t) | \hat{n}_\sigma(x) | \psi(t) \rangle. \quad (\text{IV.10})$$

In the following results we will report only the total density per grid point  $n(x) = n_\uparrow(x) + n_\downarrow(x)$  since no local magnetisation effects have been observed. Additionally, we compute the local density integrated over one optical lattice unit cell

$$\bar{n}(i) = \sum_{k=1}^{N_{\text{discr}}} n(x) \Big|_{x=(i+k-1)a} \quad (\text{IV.11})$$

which simplifies the analysis in terms of the effective lattice model, e.g. one expects  $\bar{n}(i) = 1$  in the Mott regime and  $\bar{n}(i) = 2$  in the band insulating regime.

Note that the above lattice loading schedule linearly modulates the lattice potential at every time step, keeping all other parameters fixed during the time evolution. In our simulations, as we will explain in the upcoming sections, we encounter heating effects for certain target states. In order to reduce these effects with the eventual goal being to attain desired low temperatures in experiments, we propose an improved loading schedule that dynamically changes one or more parameters of the Hamiltonian, in addition to the lattice depth. This effect will be incorporated in the time dependent Hamiltonian and will be reflected in the state  $|\psi(t)\rangle$  during the evolution.

The first protocol follows the approach of [123] to dynamically reshape the trap potential, by linearly modulating the trap frequency  $\omega$ . Starting with an initial value  $\omega_{\text{in}}$ , we increase  $\omega$  linearly during the lattice loading to reach the desired target value  $\omega_f$  at the end of ramp time. At time  $t$  the trap frequency is given by

$$\omega(t) = \omega_{\text{in}} + (\omega_f - \omega_{\text{in}}) \frac{t}{t_R}. \quad (\text{IV.12})$$

We perform simulations with different values of  $w_{\text{in}}$  and different ramp times to study the scaling behaviour. Our results for the improvements observed with this protocol are shown in sections 5.3 and 5.4.

Alternatively, we could continuously tune the interaction strength during the time evolution, which is usually an easier parameter to address in experimental setups via Feshbach resonance [14, 160]. Since the spread of the local density of the initial state is found to be too narrow compared to the target state, we prepare a new set of initial states with a larger initial value of  $g_{\text{in}}$ , which would broaden the system. The value of the interaction strength during the lattice loading  $g(t)$  is then linearly reduced to its target value  $g_f$ , according to

$$g(t) = g_{\text{in}} - (g_{\text{in}} - g_f) \frac{t}{t_R}. \quad (\text{IV.13})$$

This scheme is studied for the target state of section 5.4. Note that if the initial state is observed to have a rather broad spread of the local density in comparison to the target state, one should aim to narrow it down by starting from a weaker interaction strength.

We propose a third scheme that is also seen to be useful in enhancing the fidelity and reducing the excess heat during lattice loading. In this approach, one combines both the above approaches in order to tune the trap frequency *and* the interaction strength during lattice loading. Although we find that the first protocol is able to achieve slightly higher fidelity than the other two protocols, it might not be the easiest one to implement in experiments. The other two schemes are not far behind in improving the fidelity and more practical from the experimental perspective.

## 5 Investigation of various target states

### 5.1 Metallic target state

We begin by studying the metallic states, where the fermions are delocalised over the lattice. Such a state is observed for a small number of particles  $N < L_{\text{eff}}$  and with a weak contact interaction. If the repulsive interaction is not too strong compared to the tunnelling between unit cells, the fermions are free to hop to the neighbouring one gaining kinetic energy. This results in a continuous density distribution throughout the length of the system.

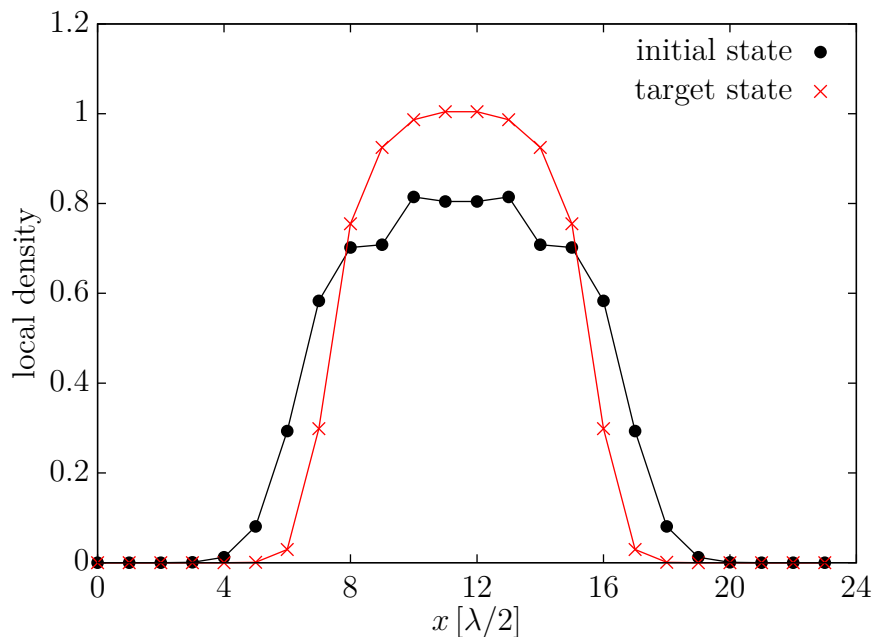


Figure IV.1: Local density distribution of the initial state ( $V_i = 0$ ) and the metallic target state ( $V_f = V_0 = 8E_r$ ) integrated over each unit cell.

We simulated a chain with  $N = 8$  particles *i.e.*  $N_{\uparrow} = N_{\downarrow} = 4$ . The interaction strength was chosen to be  $g = 0.2 E_r \lambda / 2$  along with a trap frequency of  $\omega = 0.1 (\hbar/E_r)^{-1}$ . The local density of this target state and the corresponding initial state without lattice potential are depicted in Fig. IV.1.

We allow the initial state to evolve in time by linearly increasing the lattice potential such that at the end of ramp time the system has the full strength of the lattice potential *i.e.*  $V_0(t = t_R) = V_f$ . We compute the excess heat and the fidelity for such a state using different ramp times approaching the limit of adiabatically loading of the lattice, and we do not observe any pronounced heating effects. Fig. IV.2 shows the heating and fidelity as a function of ramp time.

Our simulations reveal that it is possible to reach a final state fairly close to the target state just by being slower in loading the lattice. For  $t_R = 256 \hbar/E_r$ , we observe a fidelity of more than 94% and reduce the heating by a factor of 10 compared to shorter ramp times  $t_R = 16 \hbar/E_r$ .

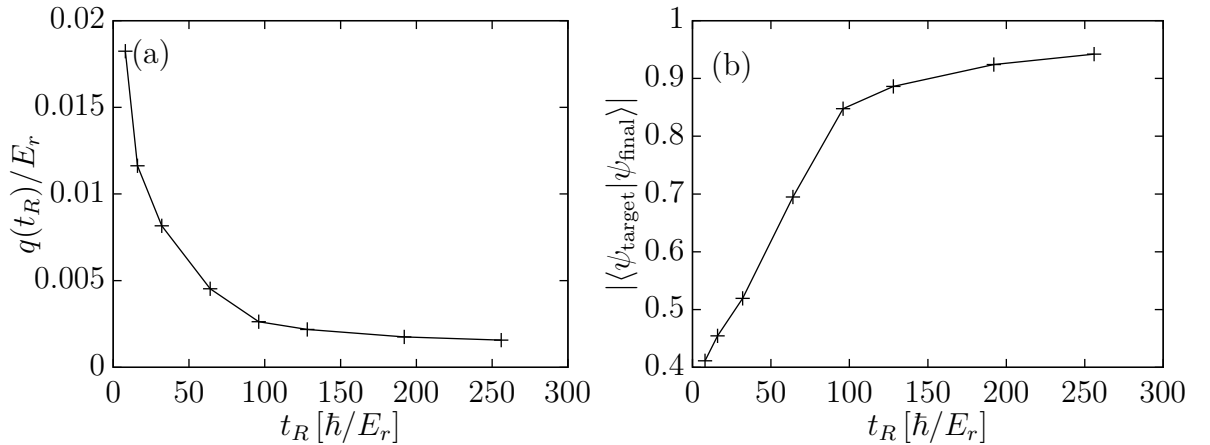


Figure IV.2: Dependence of the (a) excess heat and (b) fidelity on ramp time for the metallic target state.

Intuitively one might think of the metallic state as a gapless state, with continuous excitations in momentum space. Hence this lattice loading could be extremely capable of populating low-lying excited states and at the risk of generating a lot of heat. However, given the finite system size originating from the harmonic confinement, there is always a finite gap that drastically reduces the excitations.

Additionally, the qualitative correspondence of the density profiles between the initial and the target states allows the system to evolve without almost any defect. This is illustrated in the Fig. IV.3 showing snapshots of the density profile that have been collected at several time steps during the longest lattice loading up to  $t_R = 256 \hbar/E_r$ . The final state (orange curve) shows only very minimal deviations from the target state (red curve).

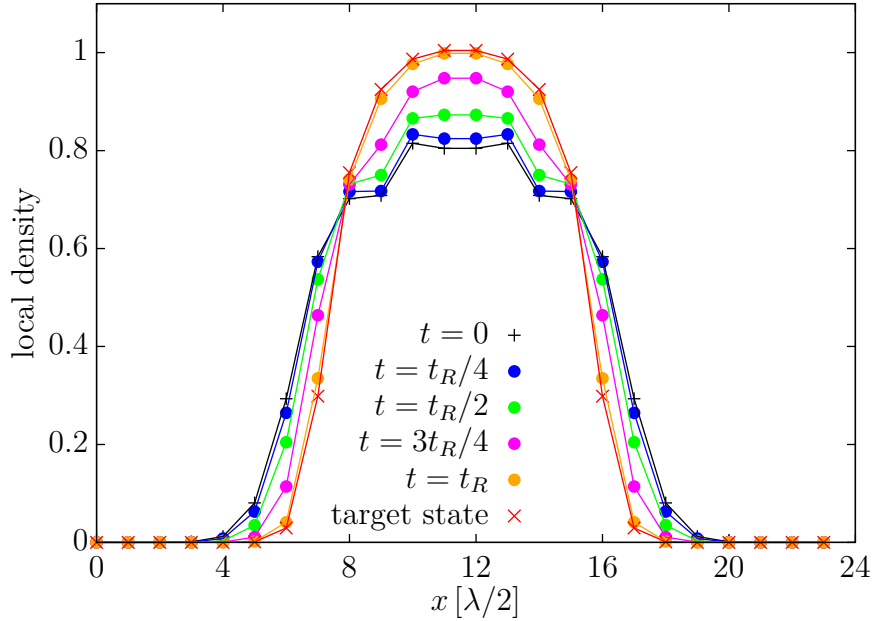


Figure IV.3: Evolution of the density profile during the ramp up for a metallic target state with ramp time  $t_R = 256 \hbar/E_r$ .

## 5.2 Central band insulator

Next we examine a target state that exhibits the co-existence of two phases: a bulk band insulator flanked by a Mott insulator on both sides. Both these phases are incompressible and characterised by special values of the average local density per unit cell. The Mott phase has one particle per lattice site, while the band insulator has an occupancy of two particles per site.

For simulating such a target state, we consider a chain with a particle number  $N$  close to (but less than) twice the effective system size  $L_{\text{eff}}$ . In the specific we consider  $N = 20$  particles ( $N_{\uparrow} = N_{\downarrow} = 10$ ) with interaction strength  $g = E_r \lambda/2$  and trap frequency  $\omega = 0.3 (\hbar/E_r)^{-1}$ .

The integrated local density distributions for the initial and target states are shown in Fig. IV.4. In the target state the bulk of the system shows a band insulator phase while the edges are in the Mott insulator phase.

Note that the density distributions of the initial state and the target state resemble each other in two important ways, namely the spatial spread of the system along with the peak value and its position in the density profile. This is the main reason why we notice that such a system does not incur too much heating if the lattice loading is done with ramp times that are long enough.

The heating and fidelity as a function of the ramp time are shown in Fig. IV.5(a) and (b) respectively. The fidelity grows rather rapidly initially upon increasing the loading time but then tends to saturate more or less around 90%. For the shortest ramp time, the final density distribution is far from that of the target

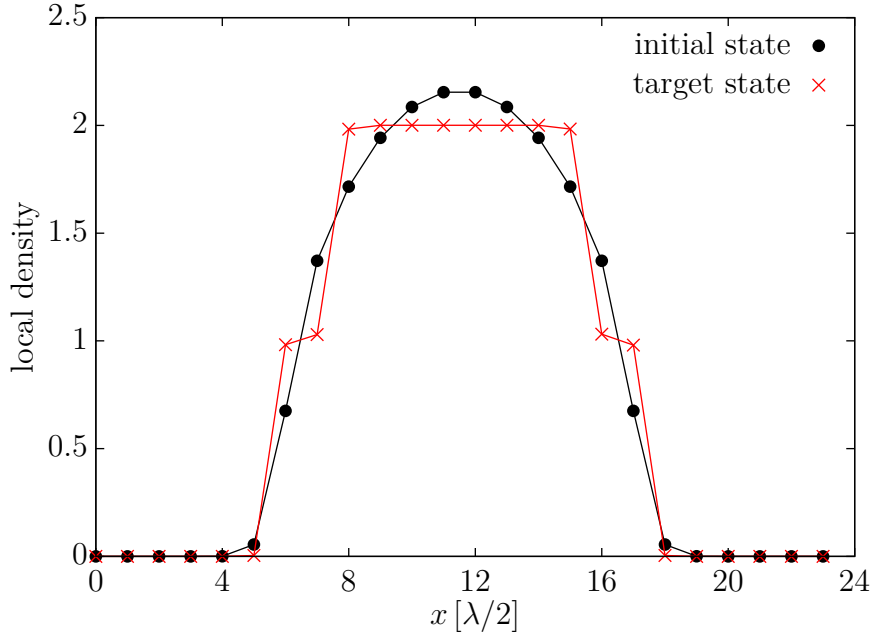


Figure IV.4: Local density distribution of the initial state ( $V_i = 0$ ) and the Mott insulator with bulk bad insulator target state ( $V_f = V_0 = 8E_r$ ) integrated over each unit cell.

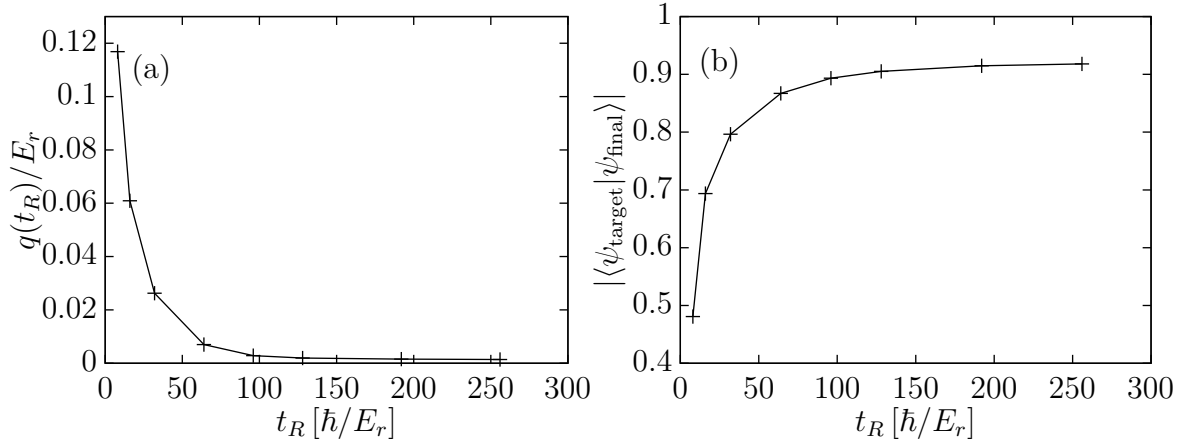


Figure IV.5: Dependence of the (a) excess heat and (b) fidelity on ramp time for a central band insulator.

state. The proximity to the target state increases rapidly for the first few ramp times that we considered due to rapid changes in the density profile during the loading. Thereafter, the final state matches the target state to a good degree and further slowing down loading only brings about slight modifications in the density profile. This is what leads to a saturation in the scaling of the fidelity.

Note that although this target state is inherently incompressible as opposed to the metallic state studied in Section 5.1, it still does not suffer from adverse heating effects. This is a manifestation of the fact that the density distribution of the initial state that is in close qualitative correspondence in terms of  $L_{\text{eff}}$  and peak



value, allowing an appropriate redistribution of particles during the ramp to reach the desired target state, as shown in fig. IV.6.

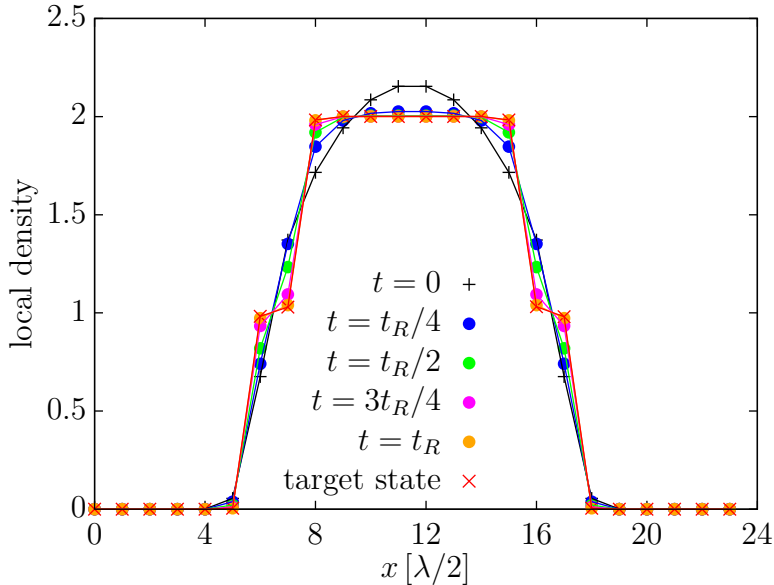


Figure IV.6: Evolution of the density profile during the ramp up of a central band insulator for ramp time  $t_R = 256 \hbar/E_r$ .

### 5.3 Mott insulator target state

Our next choice of the target state is a pure Mott insulator state with a unit average local density per unit cell throughout the effective length of the system. We simulate this target state by choosing  $N = 12$  particles ( $N_\uparrow = N_\downarrow = 6$ ) with interaction strength  $g = 2 E_r \lambda/2$  and trap frequency  $\omega = 0.25 (\hbar/E_r)^{-1}$ . The local density profile of the initial state and the target state are shown in Fig. IV.7.

We repeat the protocol followed in the previous sections, where the optical lattice potential was linearly ramped up. However, for this target state we observe that this approach does not scale with the ramp time. We note that even for the longest ramp time that we considered ( $t_R = 256 \hbar/E_r$ ), the maximum fidelity we are able to achieve is only about 15%, and the decrease in the excess heat is not significant either. Though by further increasing the ramp time, we should be able to get a better fidelity but possibly not an impressive increase. The slow increase of fidelity with ramp time is a clear indication that simulating the lattice loading with a finite ramp time is not the main cause of heating in the system.

We begin to investigate the lattice loading for this target state by first switching off the trap to understand the homogenous system. A fermionic Mott insulator state in a homogenous system without a trapping potential does not suffer from strong defects and both the excess heat and the fidelity scale well up to, for instance, a fidelity of 80% for ramp time  $t_R = 256 \hbar/E_r$ , which is far from the value observed

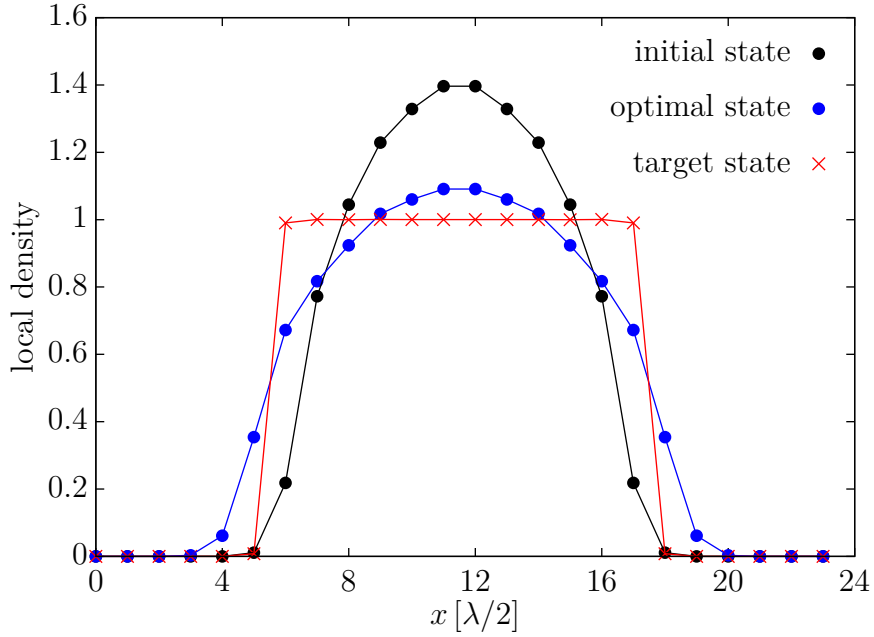


Figure IV.7: Local density distribution of the initial state ( $V_i = 0$ ) and the Mott insulator target state ( $V_f = V_0 = 8E_r$ ) integrated over each unit cell. The blue curve shows the density distribution of the optimal state when linearly modulating the trap frequency  $\omega$ .

for the trapped Mott insulator. Moreover, we try three different ramp shapes, namely linear, exponential and sigmoid defined respectively by the equations:

$$V_0^{\text{linear}}(t) = V_f \frac{t}{t_R} \quad (\text{IV.14})$$

$$V_0^{\text{exp}}(t) = V_f \frac{e^{t/\tau} - 1}{e^{t_R/\tau} - 1} \quad (\text{IV.15})$$

$$V_0^{\text{sigmoid}}(t) = V_f \left( \frac{t}{t_R} \right)^2 [-2(t/t_R) + 3], \quad (\text{IV.16})$$

with  $\tau = t_R/4$ .

Fig. IV.9 shows the fidelity as a function of ramp time for the three ramp shapes considered. We observe from the fidelity curves that for short ramp times the exponential ramp achieves significantly higher fidelity than the others. This can be attributed to the shape of the exponential ramp, that grows rather slowly during the initial time steps of the ramp. This part of the loading is in the shallow lattice regime, with a small gap to the excitations. The exponential ramp is able to minimise the excitations to higher bands, thus yielding a good fidelity to the target state. We also learn from the study of the homogenous system that for long enough ramp times, the ramp shape is not important. Eventually the fidelity tends to saturate around the same value for all the three ramp shapes considered. The rather good fidelity achieved for the homogenous system is far from the value obtained for the trapped Mott insulator, leading us to believe that the harmonic trap is one of the major sources that leads to heating during lattice loading.

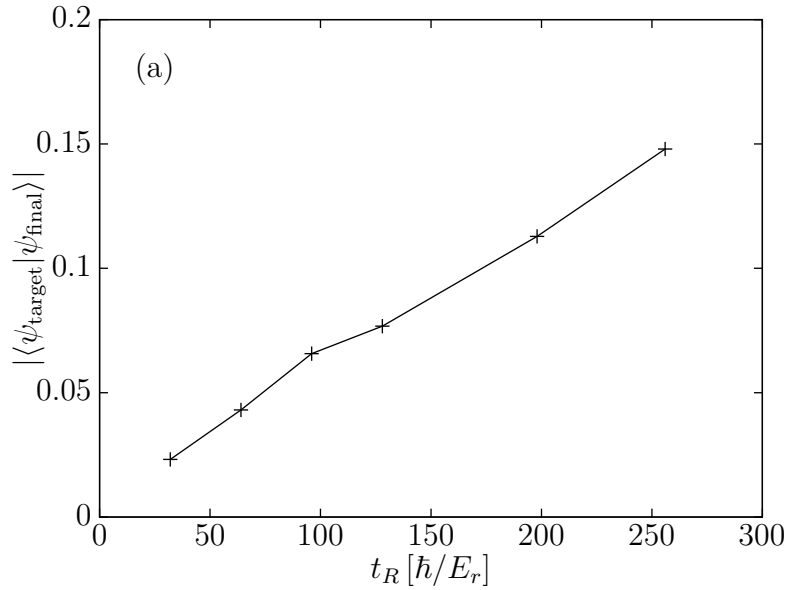


Figure IV.8: Dependence of the fidelity on ramp time for a Mott insulator target state in the trapped case.

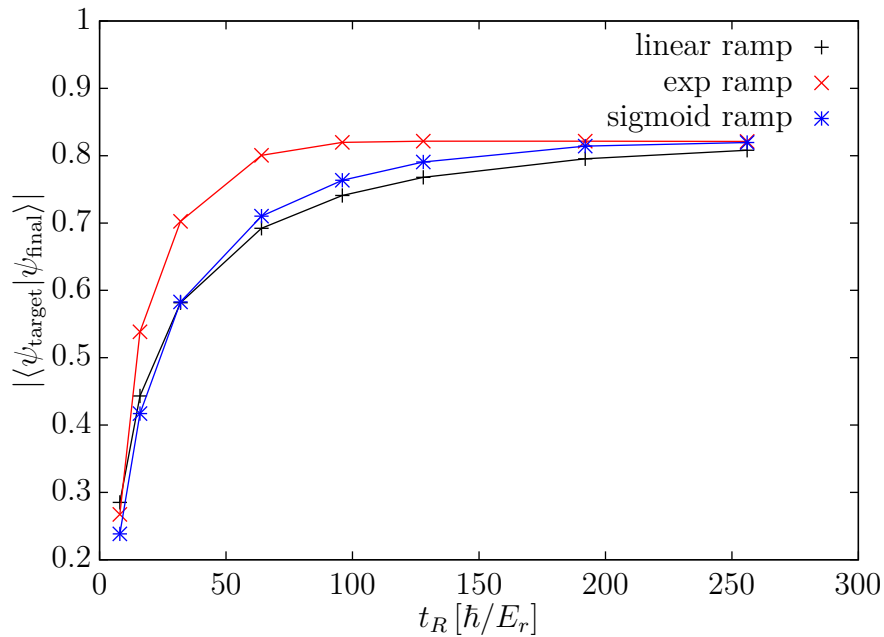


Figure IV.9: Dependence of the fidelity on ramp time for a Mott insulator target state in the homogenous case for different ramp shapes: linear, exponential and sigmoid.

We analyse the schedule of lattice loading by tracing the density profile during the ramp up. In Fig. IV.10(a) we show the density profile during the time evolution of the state at certain fractions of the total ramp time  $t_R = 256 \hbar/E_r$ . This plot unveils that starting from the initial state the loading process is not able to distribute particles in the desired way, thus deviating significantly from the target state. As it is evident from the figure, the evolution tends to keep the particles

close to the trap centre and this peak remains until the end of the ramp time. This increased local density in the trap centre is a huge deviation from the target Mott state that is expected to show a unit filling throughout the system.

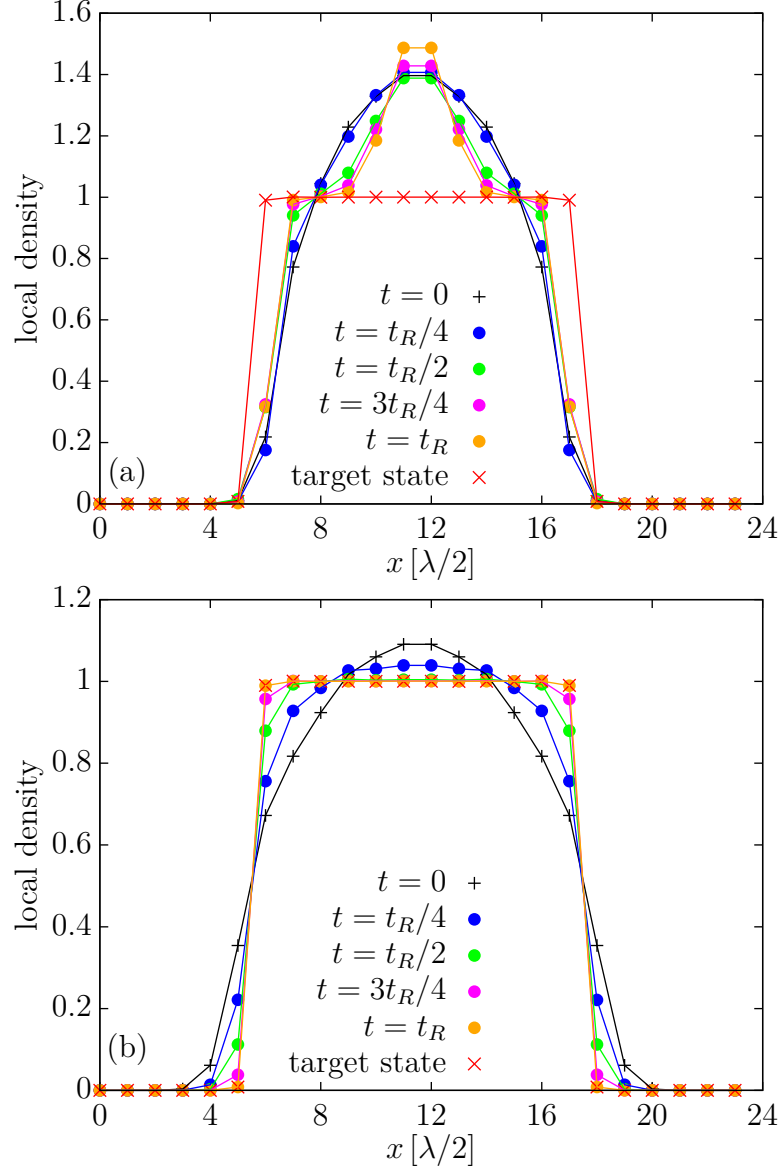


Figure IV.10: Evolution of the density profile during the ramp up of a Mott insulator for ramp time  $t_R = 256 \hbar/E_r$  (a) without tuning the trap frequency (b) with linear modulation of the frequency, for the optimal value of initial frequency ( $w_i = 0.16$ ). The black line corresponds to the target state.

Learning from our previous analyses in sections 5.1 and 5.2, we understand that a qualitative match between the density of the initial and target states is imperative to avoid strong density defects during lattice loading. Our approach is to dynamically change one or more experimentally accessible parameters in order to achieve such a match.

We implement the first modified lattice loading protocol explained in section 4, linearly modulating the trap frequency. Fig. IV.11 reports the excess heat and fidelity scanning different initial trap frequencies  $\omega_{\text{in}}$ . The different colours correspond to different ramp times. We witness a huge improvement in the fidelity and a sizeable decrease in the excess heat, compared to the case when the trap frequency is fixed during the lattice loading, which corresponds to the right-most point in the plots.

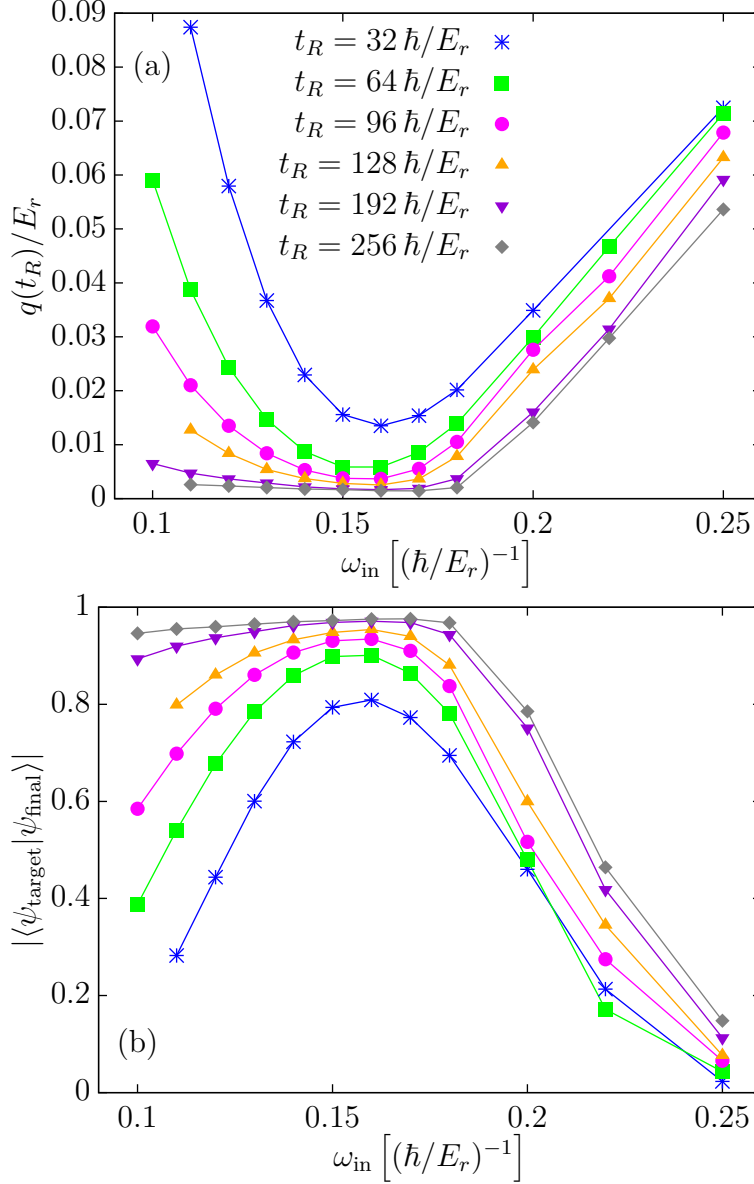


Figure IV.11: Variation of (a) excess heat and (b) fidelity as a function of the initial frequency for the Mott insulator target state. The different colours correspond to different ramp times.

From the shape of the curves we can identify three different scaling behaviours. For frequency values close to the target  $\omega_f$  the observables do not show any appreciable scaling and the results are always significantly different than the target state, while

wide initial traps (low  $\omega_{\text{in}}$ ) reach the target state, but this process scales slowly. An *optimal* and fast scaling is observed for intermediate values of the initial frequency. We can identify an optimal initial state marked by a maximum in the fidelity curve, which happens to be at  $w_i = 0.16(\hbar/E_r)^{-1}$  for our particular simulation.

The local density distribution of the optimal initial state is shown by the blue curve in Fig. IV.7. The maximum fidelity achieved for  $t_R = 256 \hbar/E_r$  is almost 98% and the heating is reduced by a factor 50.

In Fig. IV.10(b) we show the evolution of the density profile for this optimal state during the lattice loading for  $t_R = 256 \hbar/E_r$ . This is in stark contrast with the evolution plot of Fig. IV.10(a) where the trap frequency remained constant during the entire process of loading. From  $t = 0$  to already at time  $t_1 = t_R/4$ , the density profile is changed drastically when the trap frequency is modulated which was not the case earlier. Also the time evolved state at time  $t_1$  is nearly a Mott state in the trap centre whereas it had a more metallic nature in the previous case. At the end of ramp time, the density profile of the final state is almost exactly that of the target state, corresponding to an overlap of almost 98% (as can be seen in fig. IV.11(b)).

We can thus conclude that density redistribution is the main cause of heating. By tuning the trap frequency during the lattice loading we are able to distribute the particles more efficiently, thus we observe a remarkable jump in the fidelity. An optimal initial state is the one with a considerable matching to the target density profiles.

#### 5.4 Mott insulator with a metallic core

The last target state we investigate is the Mott insulator state with a (continuous) metallic density distribution in the bulk, as represented in Fig. IV.12. The harmonic trap allows for the co-existence of two phases in this target state, the metallic phase and the Mott phase. A strong interaction strength and filling of at least one particle per site characterises this state. Our simulations are done with  $N = 20$  particles ( $N_{\uparrow} = N_{\downarrow} = 10$ ) with interaction strength  $g = 3 E_r \lambda/2$  and trap frequency  $\omega = 0.25 (\hbar/E_r)^{-1}$ .

The ramp up of the lattice potential alone shows severe heating effects and the overlap with the target state remains less than 2% even for the longest ramp times simulated ( $t_R = 256 \hbar/E_r$ ). To see why even at significantly large ramp times the overlap remains exceptionally low, we track the evolution of the local density during the ramp up, as we show in Fig. IV.13(a). It reveals that the final state has a core with a substantial number of sites having a local density of two particles per unit cell. The figure suggests that the state, during the course of evolution in time, tends towards one with a band insulator core rather than metallic. In addition, the Mott insulator section of the final state is also severely reduced. Thus, the initial state is not able to redistribute the particles to follow the density distribution of the target state.

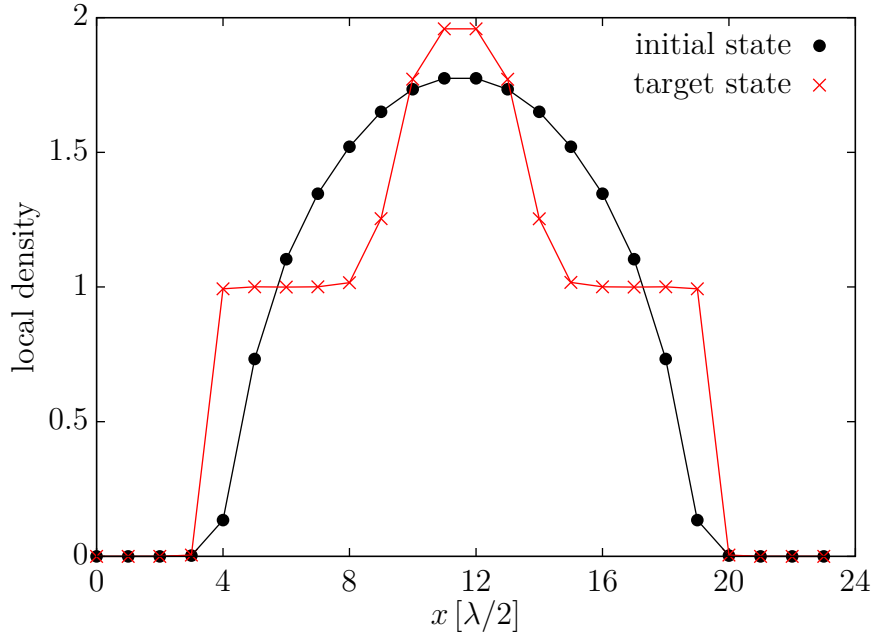


Figure IV.12: Local density distribution of the initial state ( $V_i = 0$ ) and the Mott insulator with a metallic core target state ( $V_f = V_0 = 8E_r$ ) integrated over each unit cell.

In order to reduce these defects we tune one or more model parameters. One approach is to vary the trap frequency as described in Section 5.3 for the Mott insulating target state. This manages to improve the fidelity compared to the target state to about 96% at ramp time  $t_R = 256 \hbar/E_r$  for the optimal state that is observed at  $\omega_{\text{in}} = 0.19(\hbar/E_r)^{-1}$ . The excess heat is also reduced significantly. We present the results for the heating and fidelity under trap modulation for different ramp times in Fig. IV.14.

This approach reduces the density defects as shown in Fig. IV.13(b). This optimal state has two characteristic features, first that it mimics the target state in the extent of the density distribution and secondly it lowers down the peak value of the density in the initial state. The first characteristic is intuitively clear while the second one is justified as the metallic core has only a few sites with highest possible local density for fermions, i.e. very few sites in the core are close to double occupation. The increased extent of the density distribution in the initial state aids in improving the evolution towards the desired Mott insulator regime while lowering the peak around the trap centre drives the initial state towards the targeted metallic core and not a band insulator one.

Additionally, we simulate a loading schedule where the interaction strength is modulated during the ramp according to Eq. (IV.13). This approach also provides a quantitatively similar rise in fidelity. Although the actual value of maximum fidelity is slightly lower in this case compared to the trap shaping procedure, its ease in experimental implementation should make this approach extremely useful. Fig. IV.15 shows the fidelity as a function of interaction strength for different ramp times. It is evident that this protocol leads to a more extended optimal

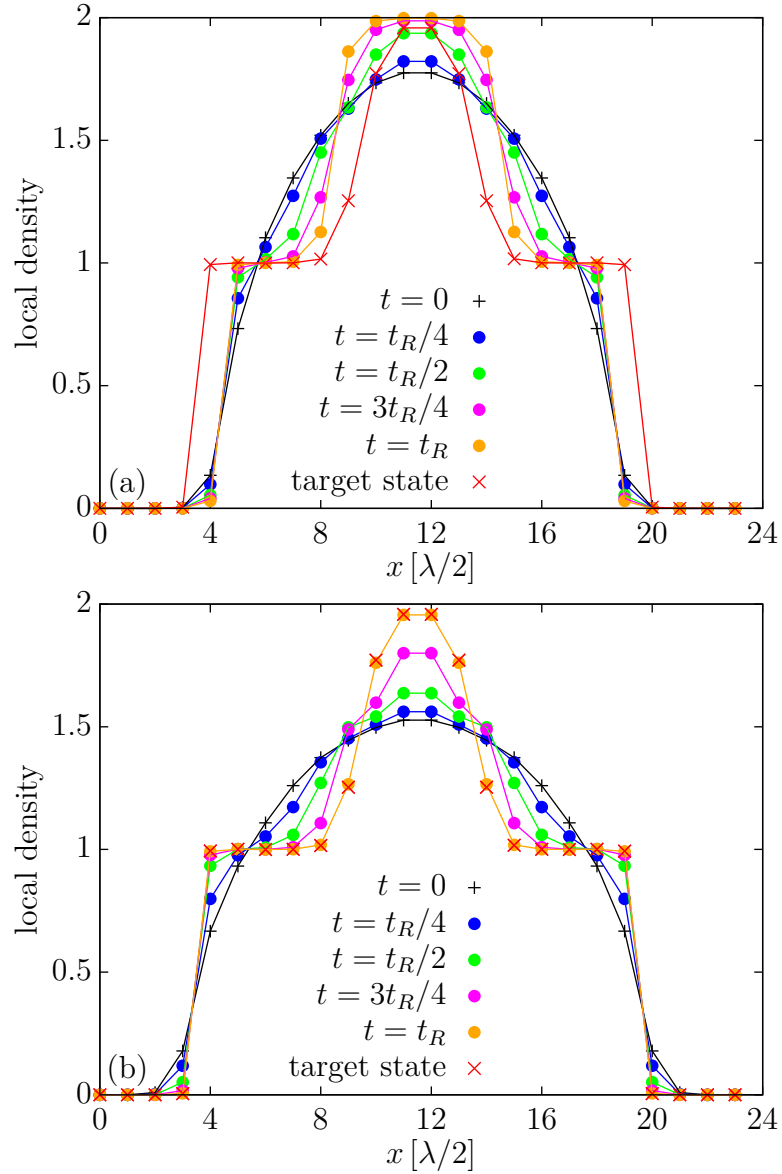


Figure IV.13: Evolution of the density profile during the ramp up for a Mott insulator with a metallic core with ramp time  $t_R = 256 \hbar/E_r$  (a) without tuning the trap frequency (b) with linear modulation of the frequency, for the optimal value of initial frequency ( $w_i = 0.19$ ). The red line corresponds to the target state.

regime where the fidelity is maximised. A similar pattern for the evolution of local density with longest ramp time is observed as in Fig. IV.13(b) starting from initial states with interaction strength lying at the optimal plateau.

Yet another approach could be to combine the above two approaches. In such a scenario, we tune both the interaction strength and the trap frequency during the lattice loading. This could be beneficial from some experiments where tuning one parameter is accompanied by an automatic modulation in another one. In our simulations, we see that linearly modulating both trap frequency and interaction strength, starting from a good candidate state, efficiently distributes the particles



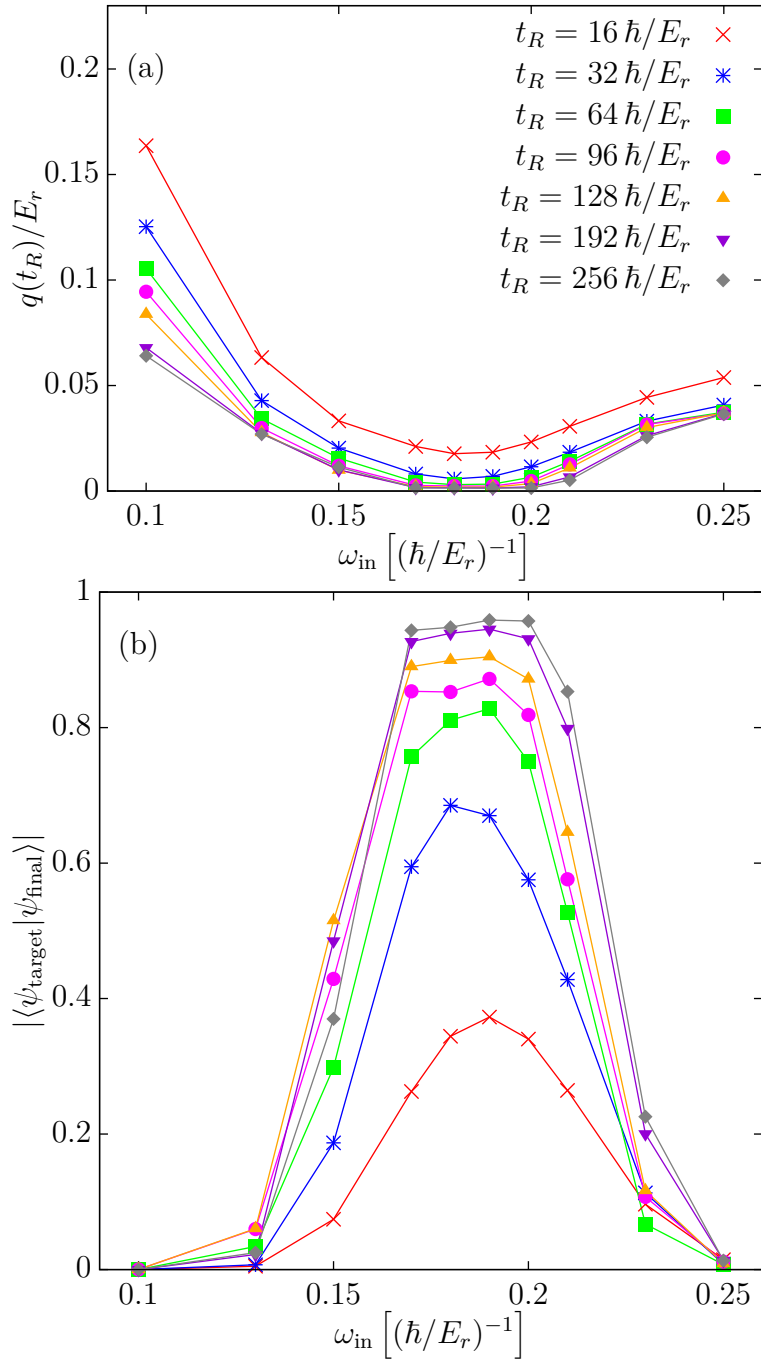


Figure IV.14: Variation of (a) excess heat and (b) fidelity as a function of the initial frequency for a Mott insulator with a metallic core. The different colours correspond to different ramp times.

during the lattice loading.

In order to test this scheme, we choose a value of the trap frequency lying in the optimal scaling region of Fig. IV.14, and then vary the interaction strength to find a good candidate state as the initial state. If we keep both  $\omega_{\text{in}}$  and  $g_{\text{in}}$  at their optimal values obtained from the two protocols, we will end up in a highly spread

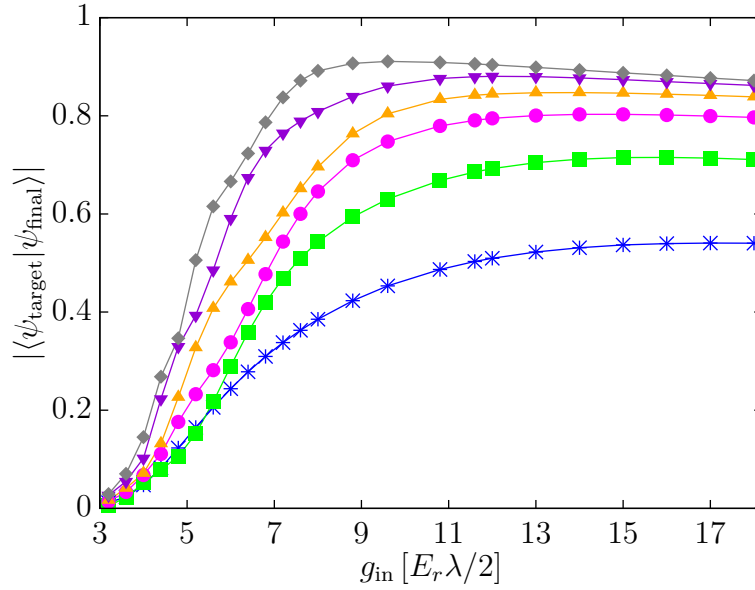


Figure IV.15: Variation of the fidelity as a function of the interaction strength for a Mott insulator with a metallic core. The different colours correspond to different ramp times. Colour scheme remains same as in Fig. IV.14.

out density distribution, once again deviating from that of the target state. It is evident that one needs to start with a lower (than target) value of the interaction strength and increase it dynamically during the lattice loading to reach the target value since we are already in the optimal  $\omega$  regime which helps to broaden the initial density distribution. We try several values of  $(g_{\text{in}}, \omega_{\text{in}})$  in order to obtain a state that fits our two essential qualitative properties and thus turns out to be a good initial state. In Fig. IV.16(a) we show the density profile of the optimal state obtained for this protocol which is observed at  $\omega_{\text{in}} = 0.16 (\hbar/E_r)^{-1}$ ,  $g_{\text{in}} = 1.4 E_r \lambda / 2$ . This search for the optimal state is by no means complete, one could definitely survey a larger set of parameters to arrive at a state that outperforms the other schemes by a good margin. In order to make a comparison, we plot the density profiles of the optimal states of all the three protocols in Fig. IV.16(a) which are fairly similar.

In Fig. IV.16(b) we show the fidelity as a function of ramp for the optimal states obtained in each protocol in order to compare them. For this target state, all the three approaches mentioned scale well with ramp time and approach the same value of fidelity as ramp times are increased. The modified protocols achieve a significant improvement in the fidelity, and there exists an optimal state where the maximum value is attained. The simplest lattice loading procedure where none of the parameters except the lattice depth are modulated during the ramp (pink curve) shows exceptionally low fidelity, with the value remaining close to zero and poor scaling with ramp time. Even with a much slower ramp, one would not expect a remarkable rise in the fidelity. All the other approaches where one or more parameters are tuned during the lattice loading perform well, which is demonstrated by a significant increase in fidelity. Although tuning the interaction

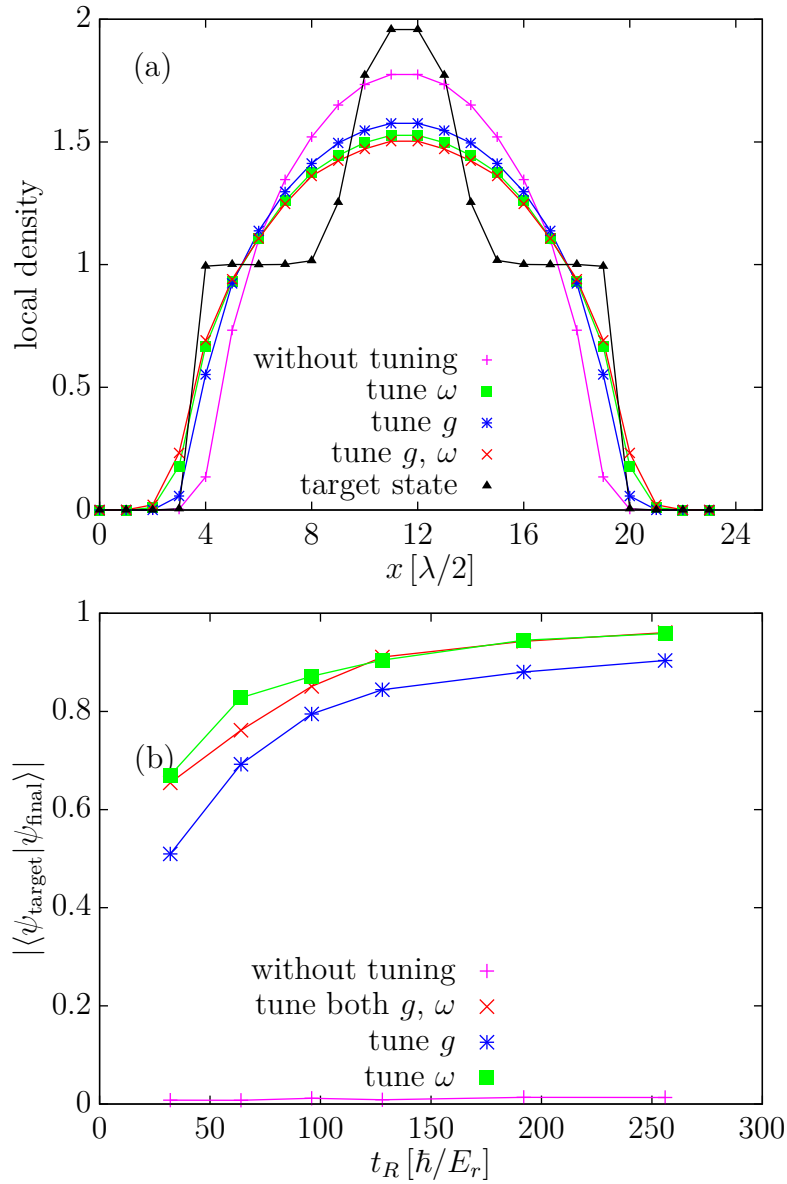


Figure IV.16: Mott insulator with a metallic core: (a) Local density distribution profiles for the optimal initial states obtained from all lattice loading protocols. The target state is shown for reference. (b) Comparison of the dependence of the fidelity on ramp time (starting from the optimal state) for all lattice loading methods. Pink curve shows the simplest loading procedure where lattice depth is ramped up without any change in other parameters of the model. The blue, red and green curves show respectively the scaling of the fidelity for the modified protocols where respectively the interaction strength, trap frequency or both are simultaneously modulated during the ramp.

---

strength (blue curve) fares slightly below the other two protocols we devised, it does turn out to be the most easily accessible parameter in experiments, making this protocol an interesting one. The other two methods scale equally well for the optimal states shown in this figure. Our comparison is based on the optimal state that we achieved by trying a few values for initial  $\omega$  and  $g$ .

We conclude that all approaches where the parameters of the model are tuned in order to redistribute density efficiently provide a significant improvement in fidelity and restore its scaling behaviour. This highlights once more that density defects are a relevant cause of heating that can be solved by adjusting the model parameters to achieve efficient particle redistribution.



# Chapter V

## Conclusion and perspectives

The possible realisation of Fibonacci anyons in experiments and their potential application to topological quantum computing continues to fascinate many physicists to work with such systems. In this thesis, we have addressed some questions on the physics of itinerant interacting Fibonacci anyons in two dimensions. We have studied two and three-leg ladders of doped Fibonacci anyons and mapped out their phase diagrams. Motivated by the construction of this model that forms an anyonic generalisation of the fermionic  $t - J$  model, we employed a similar scheme of analysis by working in the strong rung coupling limit. We start off with the limit of isolated rungs and then couple them weakly by switching on small interactions along the leg direction.

In this limit we find several different phases: totally gapped phases, paired phases described by hard core bosons, golden chain phases,  $t - J$  phases that carry  $\tau$  anyons and trivial particles and lastly the heavy and light  $\tau$  phase that carries two flavours of Fibonacci anyons. The bosonic phases as well as the anyonic phases of the golden chain/ladder and the  $t - J$  phases have been studied before. However, in addition to the existing known phases, our study of doped Fibonacci ladders has revealed a new heavy-light  $\tau$  model that can possibly realise a topological gapped state for some special filling, whereas a critical phase otherwise. For each of the above-mentioned phases we have analytically constructed effective low energy models and shown that they indeed corroborate our numerical simulations.

The golden chain phases ( $G$ ) appear for special commensurate fillings, where each rung of the ladder carries a topological charge in the same quantum state. The ladder can hence be mapped onto a golden chain with rescaled couplings. Depending on the sign of the rung couplings, we also obtain totally gapped phases ( $T$ ), where all the rungs carry a trivial topological charge. We obtain additional paired phases ( $P$ ) described by an effective hard-core boson model, similar to fermionic  $t - J$  ladders mapping to a Luther-Emery liquid of Cooper pairs. This phase is obtained in a two-leg ladder whenever anyons on a rung always combine to a totally trivial charge.

The most common phase is described by effective  $t - J$  models ( $C_{nm}$ ). In the case

of a three-leg ladder with  $J_{\text{rung}} > 3\phi|t_{\text{rung}}|$  a dominant attraction leads to phase separation. All other phases show itinerant behaviour. The mapping onto a  $t - J$  chain shows that spin-charge fractionalisation, which was initially found for 1D chains of non-Abelian anyons, also occurs in ladders.

For FM rung couplings, a new phase occurs in which the low-energy model contains Fibonacci anyons carrying different electric charges but the same topological charge. The corresponding effective model is hence very different. This phase ( $D_{mn}$ ) is seen when  $J_{\text{rung}} < 0$  and  $\rho > 1/2$  for a two-leg ladder while  $1/3 < \rho < 2/3$  for a three-leg ladder. This model allows magnetic interactions between the different flavours of anyons in addition to an exchange of the two particle species, where a heavy and light swap positions. We have analysed this model in the limit when there are no magnetic interactions between the different flavours of particles, since it is very rich in itself leading to several open questions, including a potential topological gapped phase at half-filling. For other densities, we find evidence for gapless modes described by a CFT. At this stage, it is unclear what is the central charge and the CFT that describes our model. These issues deserve further studies.

An important point established in this study of anyons is that we can map 2D doped Fibonacci ladders to effective 1D models of Fibonacci anyons, some of which have been well studied in the past. By introducing the idea of an energy difference spectrum and building on our mapping to effective 1D models, we have shown that the phenomenon of spin-charge separation continues to hold even in two-dimensions on ladders of non-Abelian anyons.

The mapping to effective 1D models would allow these ladder models of interacting anyons to be easily simulated numerically by efficient 1D algorithms such as DMRG which pave the way for other potential studies that could be carried out on these systems. There are still some questions for the heavy-light  $\tau$  model that remain unanswered, which would certainly give us more insight into the physics of the model. In particular, we have identified gapless modes for (certain fillings of) the heavy-light  $\tau$  model, but are restricted by means of computational power to ascertain the CFT that governs this model. Our exact diagonalisation simulations do not allow us to probe very large system sizes, hence extrapolate the behaviour of the system to the thermodynamic limit. This open question could perhaps be tackled by means of efficient 1D computational methods.

For our work on fermions in optical lattices, we have explored different target states namely metallic states, Mott insulating states and states that admit co-existence of phases such as a Mott state with the metallic or band insulating core. Although lattice loading over a finite interval of time is a deviation from the adiabatic limit, it was observed that for some target states the scaling of the fidelity with ramp time is extremely slow, hinting at other possible reasons behind excess heat generation.

Our key result is that density redistribution is the most important cause for excess heat produced in the system, inhibiting the experiments to reach a low temperature in the lattice as they can already obtain in the initial atomic cloud. This finding

---

prompts us to find ways to adapt the density distribution during the lattice loading in order to maintain it qualitatively and quantitatively similar to that of the desired target state. The physical problem provides many parameters that could be tuned in order to minimise the effects of non-adiabaticities.

The frequency of the underlying harmonic trap allows to modulate the density profile during lattice loading. Additionally, the interaction strength allows us to even reshape the density profile more easily, since its strength can be tuned in current experiments by means of Feshbach resonances. Another approach could be to address more than one parameter simultaneously. This can also be quite relevant to the experiments as tuning one parameter sometimes implies a concomitant change in other quantities. Our numerical simulations show that all the three approaches are equally efficient, thus leaving room to select the one that is best suited to experimental setup. The fidelity of the final state is significantly improved up to by a factor  $\times 50$ .

Though we have performed dynamical simulations in one dimensional fermionic optical lattices, we believe this result can be generalised to higher dimensions as well. However extending similar dynamical DMRG simulations to two dimensions is a hard task from the computational perspective. DMRG time evolution simulations are currently constrained to one dimension because of the growing need of computational resources in higher dimensions. Two- and three-dimensional systems could be tackled by other numerical techniques, with which one could devise an optimal ramp up by studying easier static simulations at different stages of the lattice loading. The lattice loading can then be optimised

This work gives us the confidence that examining the local density distribution during lattice loading paves the way for exploring many fresh ideas that could indeed ameliorate the present day cold atom experimental methods to realise lower temperatures both in bosonic and fermionic systems. A large number of possible paths could be explored so as to understand the loading process. For instance, one could try to optimise the loading schedule to evaluate which ramp shape could be best suited for the system, or whether the ramp up should be monotonic or not. Another aspect that could be probed is to study different trapping potentials, for instance an anharmonic trap. Such anharmonic traps could be investigated for bosons, fermions or mixtures in one-dimensional optical lattices.





# Appendices



# Appendix A

## Effective models

In this Appendix we explain the derivation of the effective models. We perturbatively derive the nearest neighbour couplings of the effective 1D models assuming large rung couplings and small leg couplings:  $|J_{\text{rung}}|, |t_{\text{rung}}| \gg |J_{\text{leg}}|, |t_{\text{leg}}|$ .

### 1 Magnetic and Potential Interactions

Magnetic interactions will only be present in effective models if two neighbouring sites each have a total anyonic  $\tau$  charge. A rung state with a total anyonic  $\tau$  charge can have one (light  $\tau$ ), two (heavy  $\tau$ ) or three (super heavy  $\tau$ )  $\tau$  particles on the rung, as shown in Table A.1. The possible magnetic interactions are marked by pink arrows. Below we investigate all possible combinations for two neighbouring rungs in two-leg and three-leg ladders, respectively and compute the effective interactions from first-order perturbation in  $J_{\text{leg}}$ .

#### 1.1 Two-leg ladder

For the two-leg ladder the rungs have to be in the light  $\tau$  state

$$|1^\pm, \tau\rangle = \frac{1}{\sqrt{2}}(|1^U, \tau\rangle \pm |1^L, \tau\rangle) \equiv \frac{|U\rangle \pm |L\rangle}{\sqrt{2}}, \quad (\text{A.1})$$

or in the heavy  $\tau$  state  $|2, \tau\rangle$ , where we introduced short hand notations  $|U\rangle$  and  $|L\rangle$  for an anyon on the upper or lower site of a rung, respectively. We review three possible cases below.

**Light  $\tau$  – light  $\tau$  :** We enumerate the steps for the calculation diagrammatically in Fig. reffig:light.

$j \backslash U(1)$	0	1	2	3
0	light	×	heavy	super heavy
1	×	light	heavy	super heavy

Table A.1: The various rung states classified according to their  $U(1)$  charge (columns) and topological charge (lines).  $j = 0$  ( $j = 1$ ) corresponds to holes ( $\tau$  particles). The possible magnetic interactions (in the present models) are indicated by pink arrows and the green arrows represent the possible kinetic terms arising in first-order perturbation in  $t_{\text{leg}}$ . The leading kinetic and potential interactions can also arise only in second or third-order in  $t_{\text{leg}}$ , marked by blue and orange arrows respectively.

We first evaluate the matrix element  $\langle \psi | H_{\text{magn}}^{\text{leg}} | \psi \rangle$  of the state

$$\begin{aligned}
 |\psi\rangle &= |1^\pm, \tau\rangle \otimes |1^\pm, \tau\rangle \\
 &= \frac{1}{2}(|UU\rangle \pm |LU\rangle \pm |UL\rangle + |LL\rangle),
 \end{aligned} \tag{A.2}$$

where  $H_{\text{magn}}^{\text{leg}}$  is the (part of the) Hamiltonian that describes the magnetic interaction between two anyons once they are nearest neighbours along a leg of the ladder (see main text).

The only non-vanishing matrix elements for the magnetic interaction in the effective model arise when the two anyons are on the same leg of the ladder. Thus, we have

$$\begin{aligned}
 \langle \psi | H_{\text{magn}}^{\text{leg}} | \psi \rangle &= \frac{1}{4}(\langle UU | H_{\text{magn}}^{\text{leg}} | UU \rangle + \langle LL | H_{\text{magn}}^{\text{leg}} | LL \rangle) \\
 &= \frac{1}{2} \langle UU | H_{\text{magn}}^{\text{leg}} | UU \rangle.
 \end{aligned} \tag{A.3}$$

The second step follows since the contributions from magnetic interactions on the upper and lower legs of the ladder are equal in magnitude. It follows immediately that the effective magnetic interaction is half the bare interaction:

$$J = \frac{1}{2} J_{\text{leg}}. \tag{A.4}$$

**Heavy  $\tau$  – heavy  $\tau$  :** Let us now consider the case where both rungs are in the heavy  $\tau$  state. The state  $|\psi\rangle$  is now defined by

$$|\psi\rangle = |2, \tau\rangle \otimes |2, \tau\rangle. \tag{A.5}$$

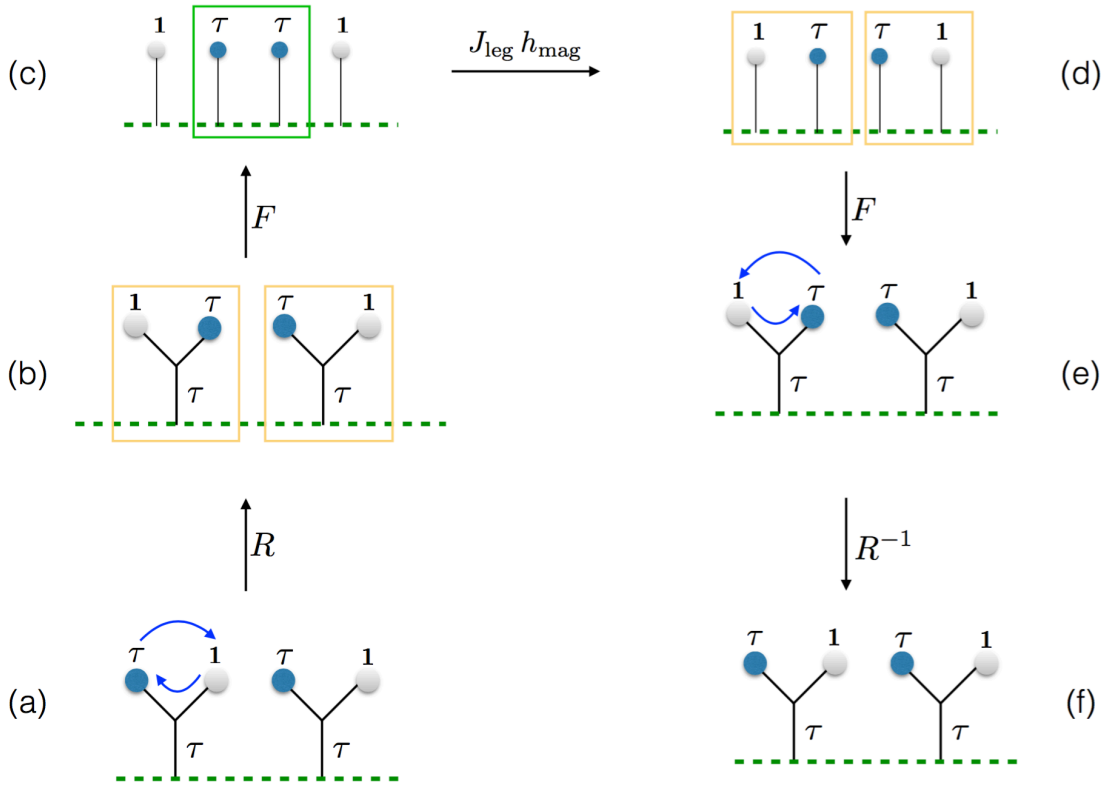


Figure A.1: Sequence of steps for calculation of effective models for a two-leg ladder with light  $\tau$ 's on adjacent rungs. (a) The initial state (b) State obtained after one braid on the left rung (c) State after  $F$  moves on each rung to reduce the ladder model to an effective chain (d) State after implementing the interaction (e) (Inverse)  $F$  moves applied to go back to the ladder picture (f) Inverse braid to bring back the particles to their original positions.

We calculate the matrix element  $\langle \psi | H_{\text{magn}}^{\text{leg}} | \psi \rangle$  for this state to obtain

$$\begin{aligned} \langle \psi | H_{\text{magn}}^{\text{leg}} | \psi \rangle &= (\langle UU | H_{\text{magn}}^{\text{leg}} | UU \rangle + \langle LL | H_{\text{magn}}^{\text{leg}} | LL \rangle) \\ &= 2 \langle UU | H_{\text{magn}}^{\text{leg}} | UU \rangle, \end{aligned} \quad (\text{A.6})$$

where the second step follows since both terms have the same contribution.

To evaluate the contribution of such a term, we need to calculate explicitly the matrix elements for all bond labels. The bond labels belong to the set  $\mathcal{S}$  defined in Eq. (III.3), which we rewrite here for convenience

$$\mathcal{S} = \{ |1\tau 1\rangle, |1\tau\tau\rangle, |\tau\tau 1\rangle, |\tau 1\tau\rangle, |\tau\tau\tau\rangle \}. \quad (\text{A.7})$$

We denote the initial quantum state (including site and bond labels) as:

$$|\Psi_\alpha\rangle = |\psi; \xi_\alpha\rangle, \quad (\text{A.8})$$

where  $|\xi_\alpha\rangle \in \mathcal{S}$ . The final states after the magnetic process are given by :

$$|\Psi_\beta\rangle = |\psi; \xi_\beta\rangle, \quad (\text{A.9})$$

where  $|\xi_\beta\rangle \in \mathcal{S}$ .

Then, the matrix elements for this process in the basis  $\mathcal{S}$  are given by:

$$H_{\text{magn}}^{\text{leg}} = -J_{\text{leg}} \begin{bmatrix} \phi^{-1} & & & & & \\ & \phi^{-3} & & & & \\ & & \phi^{-3} & & & \\ & & & \phi^{-2} & \phi^{-7/2} & \\ & & & \phi^{-7/2} & \phi^{-2} + \phi^{-5} & \end{bmatrix}. \quad (\text{A.10})$$

This effective Hamiltonian is proportional to the golden chain Hamiltonian (up to an overall shift) and the contribution to the effective coupling on each leg is  $\phi^{-2}J_{\text{leg}}$ . Thus, the effective potential between the two heavy  $\tau$ 's is given by

$$V = 2\phi^{-3}J_{\text{leg}}, \quad (\text{A.11})$$

and the effective magnetic interaction for the entire process obtained by combining contributions from both the legs (see Eq. (A.6)), is thus given by

$$J = 2\phi^{-2}J_{\text{leg}}. \quad (\text{A.12})$$

**Light  $\tau$  – heavy  $\tau$  :** Finally, we consider the case where we have a heavy  $\tau$  and light  $\tau$  on neighbouring rungs. The state  $|\psi\rangle$  is now defined as

$$|\psi\rangle = |1^\pm, \tau\rangle \otimes |2, \tau\rangle. \quad (\text{A.13})$$

We calculate the matrix element  $\langle\psi|H_{\text{magn}}^{\text{leg}}|\psi\rangle$  for this state to obtain

$$\begin{aligned} \langle\psi|H_{\text{magn}}^{\text{leg}}|\psi\rangle &= \frac{1}{2}(\langle UU|H_{\text{magn}}^{\text{leg}}|UU\rangle + \langle LL|H_{\text{magn}}^{\text{leg}}|LL\rangle) \\ &= \langle UU|H_{\text{magn}}^{\text{leg}}|UU\rangle, \end{aligned} \quad (\text{A.14})$$

where the second steps follows since both the terms have the same contribution. As before we denote the initial and final states as defined in Eq. (A.8) and Eq. (A.9) respectively. Then, the matrix elements for this process in the basis  $\mathcal{S}$  are given by:

$$H_{\text{magn}}^{\text{leg}} = -J_{\text{leg}} \begin{bmatrix} 0 & & & & & \\ & \phi^{-1} & & & & \\ & & \phi^{-1} & & & \\ & & & \phi^{-2} & -\phi^{-5/2} & \\ & & & -\phi^{-5/2} & \phi^{-3} & \end{bmatrix}. \quad (\text{A.15})$$

This Hamiltonian matrix is equivalent to the golden chain Hamiltonian with the effective coupling

$$J = -\phi^{-1}J_{\text{leg}} \quad (\text{A.16})$$

and an effective potential

$$V = \phi^{-1}J_{\text{leg}} \quad (\text{A.17})$$

## 1.2 Three-leg ladder

For three legs, a rung has a total anyonic  $\tau$  charge if it is in one of the  $|1^\pm, \tau\rangle$  (light),  $|2^\pm, \tau\rangle$  (heavy) or  $|3, \tau\rangle$  (super heavy) state. Below we consider all possible cases for neighbouring rungs both with a total anyonic  $\tau$  charge.

**Light  $\tau$  – light  $\tau$  :** We first assume that the two rungs are both in the state

$$\begin{aligned} |1^\pm, \tau\rangle &= \frac{1}{2}(|1^U, \tau\rangle + |1^L, \tau\rangle \pm \sqrt{2}|1^M, \tau\rangle) \\ &= \frac{1}{2}|L\rangle \pm \frac{1}{\sqrt{2}}|M\rangle + \frac{1}{2}|U\rangle, \end{aligned} \quad (\text{A.18})$$

where the states  $|L\rangle, |M\rangle, |U\rangle$  denote the position of the anyon on the lower, middle or upper leg respectively, and  $\pm$  depends on the sign of  $t_{\text{rung}}$ . As above we calculate the matrix element for the state

$$|\psi\rangle = |1^\pm, \tau\rangle \otimes |1^\pm, \tau\rangle \quad (\text{A.19})$$

and obtain

$$\begin{aligned} \langle\psi|H_{\text{magn}}^{\text{leg}}|\psi\rangle &= \frac{1}{16}(\langle UU|H_{\text{magn}}^{\text{leg}}|UU\rangle + \langle LL|H_{\text{magn}}^{\text{leg}}|LL\rangle) \\ &\quad + \frac{1}{4}\langle MM|H_{\text{magn}}^{\text{leg}}|MM\rangle) \\ &= \frac{3}{8}\langle UU|H_{\text{magn}}^{\text{leg}}|UU\rangle, \end{aligned} \quad (\text{A.20})$$

resulting in an effective coupling

$$J = \frac{3}{8}J_{\text{leg}}. \quad (\text{A.21})$$

**Heavy  $\tau$  – heavy  $\tau$  :** Let us now assume the effective  $\tau$ 's on the rungs are in the heavy  $\tau$  state

$$\begin{aligned} |2^\pm, \tau\rangle &= \frac{1}{2}(|1^{U,M}, \tau\rangle + |1^{M,L}, \tau\rangle \pm \sqrt{2}|1^{U,L}, \tau\rangle) \\ &\equiv \frac{1}{2}(|UM\rangle + |ML\rangle \pm \sqrt{2}|UL\rangle), \end{aligned} \quad (\text{A.22})$$

where we have used the short hand notation  $|AB\rangle$  denoting that the  $\tau$  lies on the leg  $A$  and  $B$  and the net fusion channel outcome being a  $\tau$  is implicit.

As above we calculate the matrix element for the state

$$\begin{aligned} |\psi\rangle &= |2^\pm, \tau\rangle \otimes |2^\pm, \tau\rangle \\ &= \frac{1}{4}(|UM, UM\rangle + |UM, ML\rangle + \sqrt{2}|UM, UL\rangle) \\ &\quad + |ML, UM\rangle + |ML, ML\rangle + \sqrt{2}|ML, UL\rangle \\ &\quad + \sqrt{2}|UL, UM\rangle + \sqrt{2}|UL, ML\rangle + 2|UL, UL\rangle) \end{aligned} \quad (\text{A.23})$$



and obtain

$$\begin{aligned}
\langle \psi | H_{\text{magn}}^{\text{leg}} | \psi \rangle &= \frac{1}{16} \left( \langle UM, UM | H_{\text{magn}}^{\text{leg}} | UM, UM \rangle + \langle ML, ML | H_{\text{magn}}^{\text{leg}} | ML, ML \rangle \right. \\
&+ 2 \langle UL, UL | H_{\text{magn}}^{\text{leg}} | UL, UL \rangle + \langle UM, ML | H_{\text{magn}}^{\text{leg}} | UM, ML \rangle \\
&+ \sqrt{2} \langle UM, UL | H_{\text{magn}}^{\text{leg}} | UM, UL \rangle + \langle ML, UM | H_{\text{magn}}^{\text{leg}} | ML, UM \rangle \\
&+ \sqrt{2} \langle ML, UL | H_{\text{magn}}^{\text{leg}} | ML, UL \rangle + \sqrt{2} \langle UL, UM | H_{\text{magn}}^{\text{leg}} | UL, UM \rangle \\
&\left. + \sqrt{2} \langle UL, ML | H_{\text{magn}}^{\text{leg}} | UL, ML \rangle \right). \tag{A.24}
\end{aligned}$$

The first three terms have two magnetic interactions each along the leg direction while all the others have only one. Moreover all these magnetic interactions are equal in magnitude, the contribution of a single term giving the effective coupling  $J = \phi^{-2} J_{\text{leg}}$  (see Eq. (A.12)). Taking into account the contributions from all the terms, it follows immediately that the effectively magnetic coupling is

$$J = \frac{11}{8} \phi^{-2} J_{\text{leg}} \tag{A.25}$$

and the effective potential is given by

$$V = \frac{11}{8} \phi^{-3} J_{\text{leg}}. \tag{A.26}$$

**Super-heavy  $\tau$  – super-heavy  $\tau$  :** Let us now assume the states on the rungs with total anyonic charge  $\tau$  are both given by  $|3, \tau\rangle$  (super-heavy  $\tau$ 's). Then, we calculate the matrix element for the state

$$|\psi\rangle = |3, \tau\rangle \otimes |3, \tau\rangle \tag{A.27}$$

and obtain

$$\langle \psi | H_{\text{magn}}^{\text{leg}} | \psi \rangle = \left( \langle UU | H_{\text{magn}}^{\text{leg}} | UU \rangle + \langle LL | H_{\text{magn}}^{\text{leg}} | LL \rangle + \langle MM | H_{\text{magn}}^{\text{leg}} | MM \rangle \right). \tag{A.28}$$

Magnetic interactions on the upper and middle leg contribute to a potential in the effective Hamiltonian given by

$$V = -2\phi^{-2} J_{\text{leg}}, \tag{A.29}$$

while the magnetic process on the lower leg results in an effective magnetic coupling given by

$$J = J_{\text{leg}}. \tag{A.30}$$

**Light  $\tau$  – heavy  $\tau$  :** Finally, we consider the case when the two  $\tau$ 's on the neighbouring rungs are in the  $|1^\pm, \tau\rangle$  and the  $|2^\pm, \tau\rangle$  states. The state  $|\psi\rangle$  is now

given by

$$\begin{aligned}
|\psi\rangle &= |2^\pm, \tau\rangle \otimes |1^\pm, \tau\rangle \tag{A.31} \\
&= \frac{1}{2}(|UM\rangle + |ML\rangle + \sqrt{2}|UL\rangle) \otimes \frac{1}{2}(|U\rangle + |L\rangle + \sqrt{2}|M\rangle) \\
&= |UM, U\rangle + |UM, L\rangle + \sqrt{2}|UM, M\rangle + |ML, U\rangle + |ML, M\rangle \\
&\quad + \sqrt{2}|ML, M\rangle + \sqrt{2}|UL, U\rangle + \sqrt{2}|UL, L\rangle + 2|UL, M\rangle.
\end{aligned}$$

As before we calculate the matrix element

$$\begin{aligned}
\langle\psi|H_{\text{magn}}^{\text{leg}}|\psi\rangle &= \frac{1}{16}(\langle UM, U|H_{\text{magn}}^{\text{leg}}|UM, U\rangle + 2\langle UM, M|H_{\text{magn}}^{\text{leg}}|UM, M\rangle \\
&\quad + \langle ML, L|H_{\text{magn}}^{\text{leg}}|ML, L\rangle + 2\langle ML, M|H_{\text{magn}}^{\text{leg}}|ML, M\rangle \\
&\quad + 2\langle UL, U|H_{\text{magn}}^{\text{leg}}|UL, U\rangle + 2\langle UL, L|H_{\text{magn}}^{\text{leg}}|UL, L\rangle). \tag{A.32}
\end{aligned}$$

The contributions of each of these terms to the effective coupling is  $(-\phi^{-1})J_{\text{leg}}$  (see Eq. (A.16)), thus the net effective coupling for this magnetic process is given by

$$J = -\frac{5}{8\phi}J_{\text{leg}} \tag{A.33}$$

and the effective potential is

$$V = \frac{5}{8\phi}J_{\text{leg}} \tag{A.34}$$

## 2 Kinetic terms

Whenever the total  $U(1)$  charges of the two neighbouring rung states differ by  $\pm 1$ , a hopping process occurs in first order in  $t_{\text{leg}}$ . It is the case for a charge-1 (light)  $\tau$  and a charge-0 (light) or charge-2 (heavy) hole, a charge-1 (light)  $\tau$  and a charge-2 (heavy)  $\tau$ , a charge-2 (heavy) hole and a charge-3 (super heavy)  $\tau$ , a charge-2 (heavy)  $\tau$  and a charge-3 (super heavy) hole. All these are marked schematically by green arrows in Table. A.1. Below we investigate all these possibilities in two leg and three leg ladders, respectively.

### 2.1 Two-leg ladder

Let us first evaluate the effective hopping in a two-leg ladder arising when there is a  $\tau$  particle in the state  $|1^\pm, \tau\rangle$  and an effective hole in either the empty  $|e\rangle = |0, \mathbf{1}\rangle$  (case 1) or the fully occupied  $|f\rangle = |2, \mathbf{1}\rangle$  (case 2) rung state on adjacent rungs.

**Light hole – light  $\tau$  :** First, we need to evaluate the matrix element  $\langle \Psi_1 | H_{\text{kin}}^{\text{leg}} | \Psi_2 \rangle$  between the two states

$$|\Psi_1\rangle = |1^\pm, \tau\rangle \otimes |e\rangle \equiv \frac{|Ue\rangle \pm |Le\rangle}{\sqrt{2}} \quad (\text{A.35})$$

and

$$|\Psi_2\rangle = |e\rangle \otimes |1^\pm, \tau\rangle \equiv \frac{|eU\rangle \pm |eL\rangle}{\sqrt{2}}, \quad (\text{A.36})$$

where  $H_{\text{kin}}^{\text{leg}}$  is the kinetic part of the ladder Hamiltonian living on the legs (see main text). Similar to the case of magnetic interactions one gets a factor  $1/2$  and obtains for the effective hopping

$$t = \frac{1}{2} t_{\text{leg}}. \quad (\text{A.37})$$

**Heavy hole – light  $\tau$  :** We elaborate the steps for the calculation in Fig. A.2.

One evaluates the matrix element between the states

$$|\Psi_1\rangle = |1^\pm, \tau\rangle \otimes |f\rangle \equiv \frac{|Uf\rangle \pm |Lf\rangle}{\sqrt{2}} \quad (\text{A.38})$$

and

$$|\Psi_2\rangle = |f\rangle \otimes |1^\pm, \tau\rangle \equiv \frac{|fU\rangle \pm |fL\rangle}{\sqrt{2}}. \quad (\text{A.39})$$

The matrix elements are written explicitly as

$$\langle \Psi_2 | H_{\text{kin}}^{\text{leg}} | \Psi_1 \rangle = \frac{1}{2} \langle fU | H_{\text{kin}}^{\text{leg}} | Uf \rangle + \frac{1}{2} \langle fL | H_{\text{kin}}^{\text{leg}} | Lf \rangle. \quad (\text{A.40})$$

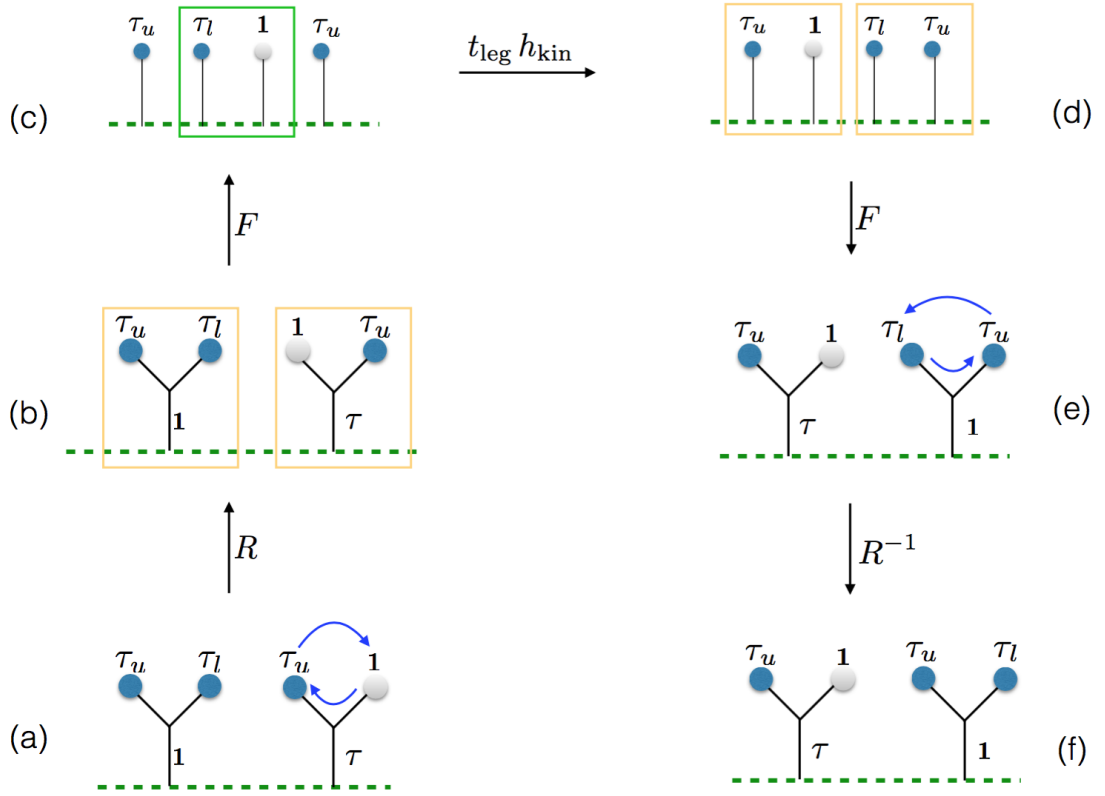


Figure A.2: Sequence of steps for calculation of effective models for kinetic term on a two-leg ladder with a heavy hole and a light  $\tau$  on adjacent rungs. (a) The initial state (b) State obtained after one (trivial) braid on the right rung (c) State after  $F$  moves on each rung to reduce the ladder model to an effective chain (d) State after implementing the kinetic hopping (f) (Inverse)  $F$  moves applied to go back to the ladder picture (g) Inverse braid to obtain the same labelling of the fusion path.

The derivation is identical but involves two non-trivial braids. The contributions from the hopping on the two legs are thus given by

$$\begin{aligned}
 \langle fU|H_{\text{kin}}^{\text{leg}}|Uf\rangle &= e^{4\pi i/5}\phi^{-1}t_{\text{leg}}\langle \mathbf{1}\tau|h_{\text{kin}}|\tau\mathbf{1}\rangle, \\
 \langle fL|H_{\text{kin}}^{\text{leg}}|Lf\rangle &= e^{-4\pi i/5}\phi^{-1}t_{\text{leg}}\langle \mathbf{1}\tau|h_{\text{kin}}|\tau\mathbf{1}\rangle.
 \end{aligned}
 \tag{A.41}$$

Adding both the terms we get an overall  $-1$  factor, compared to the previous case:

$$t = -\frac{1}{2}t_{\text{leg}}. \tag{A.42}$$

**Light  $\tau$  – heavy  $\tau$  :** Finally, let us consider two nearest neighbour rungs, one carrying a heavy  $\tau$  and the other with a light  $\tau$ . Here, the bond labels belong to the set  $\mathcal{S}$  defined in Eq. (A.7). We denote the ‘initial’ quantum state (including

site and bond labels) with a light (heavy)  $\tau$  on the first (second) rung as:

$$|\Psi_{i,\alpha}\rangle = |1_l 2_h; \xi_\alpha\rangle, \quad (\text{A.43})$$

where  $i$  stands for initial and  $|\xi_\alpha\rangle \in \mathcal{S}$ . The ‘final’ states after the hopping process are given by :

$$|\Psi_{f,\beta}\rangle = |1_h 2_l; \xi_\beta\rangle, \quad (\text{A.44})$$

where  $f$  is for final and  $|\xi_\beta\rangle \in \mathcal{S}$ . One needs to compute all matrix elements  $\langle \Psi_\beta | H_{\text{kin}}^{\text{leg}} | \Psi_\alpha \rangle$ . In Fig. A.3 we explain the sequence of steps for bond labels  $|1\tau\tau\rangle$ . The matrix elements for the hopping of a heavy and a light  $\tau$  on the lower leg of the ladder are found to be:

$$\begin{aligned} \langle 1_h 2_l; \mathbf{1}\tau\mathbf{1} | H_{\text{kin}}^{\text{leg}} | 1_l 2_h; \mathbf{1}\tau\mathbf{1} \rangle &= t_{\text{leg}} e^{-3\pi i/5} \langle \mathbf{1}\tau | h_{\text{kin}} | \tau\mathbf{1} \rangle, \\ \langle 1_h 2_l; \mathbf{1}\tau\tau | H_{\text{kin}}^{\text{leg}} | 1_l 2_h; \mathbf{1}\tau\tau \rangle &= -t_{\text{leg}} e^{-3\pi i/5} \phi^{-1} \langle \mathbf{1}\tau | h_{\text{kin}} | \tau\mathbf{1} \rangle, \\ \langle 1_h 2_l; \tau\tau\mathbf{1} | H_{\text{kin}}^{\text{leg}} | 1_l 2_h; \tau\tau\mathbf{1} \rangle &= -t_{\text{leg}} e^{-3\pi i/5} \phi^{-1} \langle \mathbf{1}\tau | h_{\text{kin}} | \tau\mathbf{1} \rangle, \\ \langle 1_h 2_l; \tau\mathbf{1}\tau | H_{\text{kin}}^{\text{leg}} | 1_l 2_h; \tau\tau\tau \rangle &= \langle 1_h 2_l; \tau\tau\tau | H_{\text{kin}}^{\text{leg}} | 1_l 2_h; \tau\mathbf{1}\tau \rangle \\ &= t_{\text{leg}} e^{-3\pi i/5} \phi^{-1/2} \langle \mathbf{1}\tau | h_{\text{kin}} | \tau\mathbf{1} \rangle, \\ \langle 1_h 2_l; \tau\tau\tau | H_{\text{kin}}^{\text{leg}} | 1_l 2_h; \tau\tau\tau \rangle &= t_{\text{leg}} e^{-3\pi i/5} \phi^{-2} \langle \mathbf{1}\tau | h_{\text{kin}} | \tau\mathbf{1} \rangle. \end{aligned} \quad (\text{A.45})$$

The matrix elements for hopping on the other leg remain the same except for the direction of the braid being reversed, *i.e.* all phase factors  $e^{-3\pi i/5} \rightarrow e^{3\pi i/5}$ . As we sum up contributions from both the legs, the phase factors add up and the entire matrix (in the basis (A.7)) is written as :

$$H_{\text{eff}} = t \begin{bmatrix} 1 & & & & \\ & -\phi^{-1} & & & \\ & & -\phi^{-1} & & \\ & & & 0 & \phi^{-1/2} \\ & & & \phi^{-1/2} & \phi^{-2} \end{bmatrix}, \quad (\text{A.46})$$

where the effective hopping amplitude is

$$t = (\cos(3\pi/5)) t_{\text{leg}}. \quad (\text{A.47})$$

A characteristic feature of this effective hopping Hamiltonian is that it mixes the spin labels. This is remarkably different from the simple hopping process between a hole and a  $\tau$ . In the text, we have quoted the effective Hamiltonian matrix for this process as  $H_{\text{HL}}$  described in Eq. (III.35), which is related to  $H_{\text{eff}}$  by rescaling it such that the  $2 \times 2$  block has eigenvalues 0 and 1. More precisely,  $H_{\text{HL}} = aH_{\text{eff}} + b\mathbb{I}$  with  $a = \phi^{-1}$  and  $b = \phi^{-2}$  (where  $\mathbb{I}$  is the identity matrix).

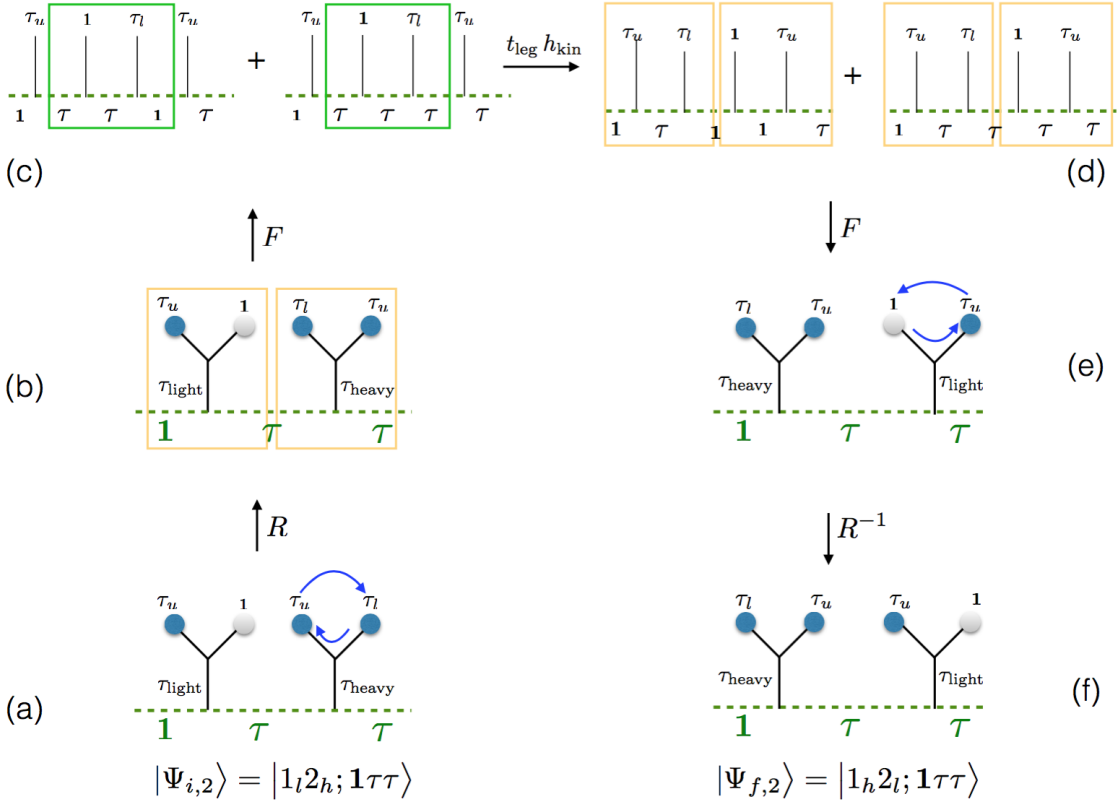


Figure A.3: Sequence of steps for calculation of effective heavy light  $\tau$  models for a two-leg ladder. (a) The initial state (b) State obtained after one braid on the right rung (c) State after  $F$  moves on each rung to reduce the ladder model to an effective chain. Note that two states are obtained due to non-trivial  $F$  move. (d) State after implementing the kinetic hopping (e) (Inverse)  $F$  moves applied to go back to the ladder picture (f) Inverse braid to obtain the same fusion path labelling.

## 2.2 Three-leg ladder

For a three-leg ladder, we can derive the relevant matrix elements in a similar way.

**Light hole – light  $\tau$**  : Let us start with the simplest case and compute the matrix element  $\langle \Psi_1 | H_{\text{kin}}^{\text{leg}} | \Psi_2 \rangle$  where  $|\Psi_1\rangle = |s\rangle \otimes |e\rangle$ ,  $|\Psi_2\rangle = |e\rangle \otimes |s\rangle$ ,  $|s\rangle \equiv |1^\pm, \tau\rangle$  is defined in (A.18) and  $|e\rangle$  is the empty rung. Using obvious notations,

$$\begin{aligned} \langle \Psi_1 | H_{\text{kin}}^{\text{leg}} | \Psi_2 \rangle &= \frac{1}{4} \left( \langle eU | H_{\text{kin}}^{\text{leg}} | Ue \rangle + 2 \langle eM | H_{\text{kin}}^{\text{leg}} | Me \rangle + \langle eL | H_{\text{kin}}^{\text{leg}} | Le \rangle \right) \\ &= \langle eU | H_{\text{kin}}^{\text{leg}} | Ue \rangle, \end{aligned} \quad (\text{A.48})$$

Since all the  $F$ -moves are trivial because of the holes on the rungs and there would be no phase factors due to the braidings either, we get the effective hopping:

$$t = t_{\text{leg}}. \quad (\text{A.49})$$

**Heavy hole – light  $\tau$**  : The calculation is slightly more involved when the effective hole state  $|d\rangle$  involves two  $\tau$  anyons on the rung,

$$|d\rangle = \frac{1}{\sqrt{2 + \alpha^2}} (|\bar{L}\rangle + |\bar{U}\rangle + \alpha|\bar{M}\rangle), \quad (\text{A.50})$$

where  $\bar{X}$  means a vacant site on the rung at position  $X$ . The matrix element  $\langle \Psi_1 | H_{\text{kin}}^{\text{leg}} | \Psi_2 \rangle$  now involves the initial and final states,

$$\begin{aligned} |\Psi_1\rangle &= |s\rangle \otimes |d\rangle \\ &= \frac{1}{2\sqrt{2 + \alpha^2}} \left( |U\bar{U}\rangle + \sqrt{2}|M\bar{U}\rangle + |L\bar{U}\rangle + \alpha|U\bar{M}\rangle + \sqrt{2}\alpha|M\bar{M}\rangle \right. \\ &\quad \left. + \alpha|L\bar{M}\rangle + |U\bar{L}\rangle + \sqrt{2}|M\bar{L}\rangle + |L\bar{L}\rangle \right) \end{aligned} \quad (\text{A.51})$$

$$\begin{aligned} |\Psi_2\rangle &= |d\rangle \otimes |s\rangle \\ &= \frac{1}{2\sqrt{2 + \alpha^2}} \left( |\bar{U}U\rangle + \sqrt{2}|\bar{U}M\rangle + |\bar{U}L\rangle + \alpha|\bar{M}U\rangle + \sqrt{2}\alpha|\bar{M}M\rangle \right. \\ &\quad \left. + \alpha|\bar{M}L\rangle + |\bar{L}U\rangle + \sqrt{2}|\bar{L}M\rangle + |\bar{L}L\rangle \right). \end{aligned} \quad (\text{A.52})$$

After expanding both sides one gets,

$$\begin{aligned} \langle \Psi_1 | H_{\text{kin}}^{\text{leg}} | \Psi_2 \rangle &= \frac{1}{4(2 + \alpha^2)} \left( \langle \bar{L}L | H_{\text{kin}}^{\text{leg}} | U\bar{U} \rangle + \sqrt{2}\alpha \langle \bar{M}M | H_{\text{kin}}^{\text{leg}} | U\bar{U} \rangle \right. \\ &\quad + \langle \bar{U}L | H_{\text{kin}}^{\text{leg}} | L\bar{U} \rangle + \alpha^2 \langle \bar{M}U | H_{\text{kin}}^{\text{leg}} | U\bar{M} \rangle + \sqrt{2}\alpha \langle \bar{L}L | H_{\text{kin}}^{\text{leg}} | M\bar{M} \rangle \\ &\quad + \sqrt{2}\alpha \langle \bar{U}U | H_{\text{kin}}^{\text{leg}} | M\bar{M} \rangle + \alpha^2 \langle \bar{M}L | H_{\text{kin}}^{\text{leg}} | L\bar{M} \rangle + \langle \bar{L}U | H_{\text{kin}}^{\text{leg}} | U\bar{L} \rangle \\ &\quad + 2 \langle \bar{L}M | H_{\text{kin}}^{\text{leg}} | M\bar{L} \rangle + \sqrt{2}\alpha \langle \bar{M}M | H_{\text{kin}}^{\text{leg}} | L\bar{L} \rangle + \langle \bar{U}U | H_{\text{kin}}^{\text{leg}} | L\bar{L} \rangle \\ &\quad \left. + 2 \langle \bar{U}M | H_{\text{kin}}^{\text{leg}} | M\bar{U} \rangle \right). \end{aligned} \quad (\text{A.53})$$

The contributions of the individual terms are as follows:

$$\begin{aligned}
\langle \bar{L}L | H_{\text{kin}}^{\text{leg}} | U\bar{U} \rangle &= \langle \bar{U}U | H_{\text{kin}}^{\text{leg}} | L\bar{L} \rangle = \phi^{-1} t_{\text{leg}} \langle \mathbf{1}\tau | h_{\text{kin}} | \tau\mathbf{1} \rangle, \\
\langle \bar{M}M | H_{\text{kin}}^{\text{leg}} | U\bar{U} \rangle &= \langle \bar{U}M | H_{\text{kin}}^{\text{leg}} | M\bar{U} \rangle = \langle \bar{L}U | H_{\text{kin}}^{\text{leg}} | U\bar{L} \rangle = e^{4\pi i/5} \phi^{-1} t_{\text{leg}} \langle \mathbf{1}\tau | h_{\text{kin}} | \tau\mathbf{1} \rangle, \\
\langle \bar{L}L | H_{\text{kin}}^{\text{leg}} | M\bar{M} \rangle &= \langle \bar{U}L | H_{\text{kin}}^{\text{leg}} | L\bar{U} \rangle = \langle \bar{M}M | H_{\text{kin}}^{\text{leg}} | L\bar{L} \rangle = e^{-4\pi i/5} \phi^{-1} t_{\text{leg}} \langle \mathbf{1}\tau | h_{\text{kin}} | \tau\mathbf{1} \rangle, \\
\langle \bar{M}U | H_{\text{kin}}^{\text{leg}} | U\bar{M} \rangle &= \langle \bar{U}U | H_{\text{kin}}^{\text{leg}} | M\bar{M} \rangle = e^{4\pi i/5} \phi^{-1} t_{\text{leg}} \langle \mathbf{1}\tau | h_{\text{kin}} | \tau\mathbf{1} \rangle, \\
\langle \bar{M}L | H_{\text{kin}}^{\text{leg}} | L\bar{M} \rangle &= \langle \bar{L}M | H_{\text{kin}}^{\text{leg}} | M\bar{L} \rangle = e^{-4\pi i/5} \phi^{-1} t_{\text{leg}} \langle \mathbf{1}\tau | h_{\text{kin}} | \tau\mathbf{1} \rangle.
\end{aligned} \tag{A.54}$$

Replacing (A.54) into (A.53) one gets the effective hopping,

$$\begin{aligned}
t &= \frac{\langle \Psi_1 | H_{\text{kin}}^{\text{leg}} | \Psi_2 \rangle}{\langle \mathbf{1}\tau | h_{\text{kin}} | \tau\mathbf{1} \rangle} \\
&= \frac{1}{(2 + \alpha^2)2\phi} \left[ (3 + \alpha^2 + 2\sqrt{2}\alpha) \left( \cos \frac{4\pi}{5} \right) + 1 \right] t_{\text{leg}}
\end{aligned} \tag{A.55}$$

**Heavy hole – super-heavy  $\tau$  :** The third case corresponds to the effective hole state  $|d\rangle$  defined in (A.50) and the effective  $\tau$  particle state defined by the fully occupied rung  $|f\rangle = |\mathbf{3}, \tau\rangle$ . The initial and final states  $|\Psi_1\rangle$  and  $|\Psi_2\rangle$  are now given by :

$$\begin{aligned}
|\Psi_1\rangle &= |d\rangle \otimes |f\rangle \\
&= \frac{1}{\sqrt{2 + \alpha^2}} \left( |\bar{U}f\rangle + \alpha |\bar{M}f\rangle + |\bar{L}f\rangle \right),
\end{aligned} \tag{A.56}$$

$$\begin{aligned}
|\Psi_2\rangle &= |f\rangle \otimes |d\rangle \\
&= \frac{1}{\sqrt{2 + \alpha^2}} \left( |f\bar{U}\rangle + \alpha |f\bar{M}\rangle + |f\bar{L}\rangle \right).
\end{aligned} \tag{A.57}$$

The matrix element for the kinetic Hamiltonian on the legs is now expressed as :

$$\langle \Psi_2 | H_{\text{kin}}^{\text{leg}} | \Psi_1 \rangle = \frac{1}{2 + \alpha^2} \left( \langle f\bar{U} | H_{\text{kin}}^{\text{leg}} | \bar{U}f \rangle + \alpha^2 \langle f\bar{M} | H_{\text{kin}}^{\text{leg}} | \bar{M}f \rangle + \langle f\bar{L} | H_{\text{kin}}^{\text{leg}} | \bar{L}f \rangle \right). \tag{A.58}$$

The individual contributions of these terms are:

$$\begin{aligned}
\langle f\bar{U} | H_{\text{kin}}^{\text{leg}} | U\bar{f} \rangle &= \phi^{-2} t_{\text{leg}} \langle \mathbf{1}\tau | h_{\text{kin}} | \tau\mathbf{1} \rangle, \\
\langle f\bar{M} | H_{\text{kin}}^{\text{leg}} | M\bar{f} \rangle &= \left( \frac{1}{2\phi} + \phi^{-3} \right) t_{\text{leg}} \langle \mathbf{1}\tau | h_{\text{kin}} | \tau\mathbf{1} \rangle, \\
\langle f\bar{L} | H_{\text{kin}}^{\text{leg}} | L\bar{f} \rangle &= t_{\text{leg}} \langle \mathbf{1}\tau | h_{\text{kin}} | \tau\mathbf{1} \rangle.
\end{aligned} \tag{A.59}$$



Adding the contributions of the three terms we get:

$$\begin{aligned} t &= \frac{\langle \Psi_2 | H_{\text{kin}}^{\text{leg}} | \Psi_1 \rangle}{\langle \mathbf{1}\tau | h_{\text{kin}} | \tau \mathbf{1} \rangle} \\ &= \frac{1}{2 + \alpha^2} \left[ \frac{1}{\phi^2} + \frac{\alpha^2}{2\phi} + \frac{\alpha^2}{\phi^3} + 1 \right] t_{\text{leg}}. \end{aligned} \quad (\text{A.60})$$

**Super-heavy hole – heavy  $\tau$  :** The fourth case corresponds to a  $\tau$  in the state  $|2^\pm, \tau\rangle$  defined in Eq. (A.22). The effective hole on the ladder is defined by the fully occupied state  $|f\rangle \equiv |3, \mathbf{1}\rangle$ . We calculate the matrix element of the states

$$\begin{aligned} |\Psi_1\rangle &= |2^\pm, \tau\rangle \otimes |f\rangle \\ &\equiv \frac{1}{2} (|UM, f\rangle + |ML, f\rangle \pm \sqrt{2}|UL, f\rangle) \end{aligned} \quad (\text{A.61})$$

and

$$\begin{aligned} |\Psi_2\rangle &= |f\rangle \otimes |2^\pm, \tau\rangle \\ &\equiv \frac{1}{2} (|f, UM\rangle + |f, ML\rangle \pm \sqrt{2}|f, UL\rangle). \end{aligned} \quad (\text{A.62})$$

The matrix elements are given by

$$\begin{aligned} \langle \Psi_2 | H_{\text{kin}}^{\text{leg}} | \Psi_1 \rangle &= \frac{1}{4} (\langle f, UM | H_{\text{kin}}^{\text{leg}} | UM, f \rangle + \langle f, ML | H_{\text{kin}}^{\text{leg}} | ML, f \rangle \\ &\quad + 2 \langle f, UL | H_{\text{kin}}^{\text{leg}} | UL, f \rangle). \end{aligned} \quad (\text{A.63})$$

The contributions of the individual hopping terms are

$$\begin{aligned} \langle f, UM | H_{\text{kin}}^{\text{leg}} | UM, f \rangle &= \phi^{-1} e^{6\pi i/5} \langle \mathbf{1}\tau | h_{\text{kin}} | \tau \mathbf{1} \rangle, \\ \langle f, UL | H_{\text{kin}}^{\text{leg}} | UL, f \rangle &= \phi^{-1} e^{-6\pi i/5} \langle \mathbf{1}\tau | h_{\text{kin}} | \tau \mathbf{1} \rangle, \\ \langle f, ML | H_{\text{kin}}^{\text{leg}} | ML, f \rangle &= \phi^{-1} \langle \mathbf{1}\tau | h_{\text{kin}} | \tau \mathbf{1} \rangle. \end{aligned} \quad (\text{A.64})$$

Using Eqs. A.64 in Eq. (A.63), we get

$$\begin{aligned} t &= \frac{\langle \Psi_2 | H_{\text{kin}}^{\text{leg}} | \Psi_1 \rangle}{\langle \mathbf{1}\tau | h_{\text{kin}} | \tau \mathbf{1} \rangle} \\ &= \left( \frac{1}{2\phi} - \frac{1}{4} \right) t_{\text{leg}}. \end{aligned} \quad (\text{A.65})$$

**Light  $\tau$  – Heavy  $\tau$  :** Finally, we consider two rungs with a light  $\tau$  defined by the state  $|s\rangle$  in (A.18) and a heavy  $\tau$  defined by the state  $|h\rangle$  given as :

$$|h\rangle = \frac{1}{2} (|\bar{L}\rangle + \sqrt{2}|\bar{M}\rangle + |\bar{U}\rangle). \quad (\text{A.66})$$

The initial and final states, formed by the tensor product of  $|s\rangle$  and  $|h\rangle$  are defined as:

$$\begin{aligned}
|\Psi_1\rangle &= |s\rangle \otimes |h\rangle \\
&= \frac{1}{4} \left( |UU\rangle + \sqrt{2}|MU\rangle + |LU\rangle + \sqrt{2}|UM\rangle + 2|M\bar{M}\rangle \right. \\
&\quad \left. + \sqrt{2}|L\bar{M}\rangle + |UL\rangle + \sqrt{2}|ML\rangle + |L\bar{L}\rangle \right)
\end{aligned} \tag{A.67}$$

and,

$$\begin{aligned}
|\Psi_2\rangle &= |h\rangle \otimes |s\rangle \\
&= \frac{1}{4} \left( |\bar{U}U\rangle + \sqrt{2}|\bar{U}M\rangle + |\bar{U}L\rangle + \sqrt{2}|\bar{M}U\rangle + \sqrt{2}|\bar{M}M\rangle \right. \\
&\quad \left. + \sqrt{2}|\bar{M}L\rangle + |\bar{L}U\rangle + \sqrt{2}|\bar{L}M\rangle + |\bar{L}L\rangle \right).
\end{aligned} \tag{A.68}$$

The matrix elements corresponding to the hopping along the leg on the ladder can be expanded using the expression of the states to give :

$$\begin{aligned}
\langle \Psi_1 | H_{\text{kin}}^{\text{leg}} | \Psi_2 \rangle &= \frac{1}{16} \left( \langle \bar{L}L | H_{\text{kin}}^{\text{leg}} | UU \rangle + 2\langle \bar{M}M | H_{\text{kin}}^{\text{leg}} | UU \rangle + 2\langle \bar{U}M | H_{\text{kin}}^{\text{leg}} | MU \rangle \right. \\
&\quad + \langle \bar{U}L | H_{\text{kin}}^{\text{leg}} | LU \rangle + 2\langle \bar{M}U | H_{\text{kin}}^{\text{leg}} | UM \rangle + 2\langle \bar{L}L | H_{\text{kin}}^{\text{leg}} | M\bar{M} \rangle \\
&\quad + 2\langle \bar{U}U | H_{\text{kin}}^{\text{leg}} | M\bar{M} \rangle + 2\langle \bar{M}L | H_{\text{kin}}^{\text{leg}} | LM \rangle + \langle \bar{L}U | H_{\text{kin}}^{\text{leg}} | UL \rangle \\
&\quad \left. + 2\langle \bar{L}M | H_{\text{kin}}^{\text{leg}} | ML \rangle + 2\langle \bar{M}M | H_{\text{kin}}^{\text{leg}} | LL \rangle + \langle \bar{U}U | H_{\text{kin}}^{\text{leg}} | LL \rangle \right).
\end{aligned} \tag{A.69}$$

The contributions of the individual terms are as follows:

$$\begin{aligned}
\langle \bar{L}L | H_{\text{kin}}^{\text{leg}} | UU \rangle &= \langle \bar{U}U | H_{\text{kin}}^{\text{leg}} | LL \rangle = t_{\text{leg}} \langle \mathbf{1}\tau | h_{\text{kin}} | \tau \mathbf{1} \rangle, \\
\langle \bar{M}M | H_{\text{kin}}^{\text{leg}} | UU \rangle &= \langle \bar{U}M | H_{\text{kin}}^{\text{leg}} | MU \rangle = \langle \bar{L}U | H_{\text{kin}}^{\text{leg}} | UL \rangle = t_{\text{leg}} e^{-3\pi i/5} \langle \mathbf{1}\tau | h_{\text{kin}} | \tau \mathbf{1} \rangle, \\
\langle \bar{U}L | H_{\text{kin}}^{\text{leg}} | LU \rangle &= \langle \bar{L}L | H_{\text{kin}}^{\text{leg}} | M\bar{M} \rangle = \langle \bar{M}L | H_{\text{kin}}^{\text{leg}} | LM \rangle = t_{\text{leg}} e^{3\pi i/5} \langle \mathbf{1}\tau | h_{\text{kin}} | \tau \mathbf{1} \rangle, \\
\langle \bar{M}U | H_{\text{kin}}^{\text{leg}} | UM \rangle &= \langle \bar{U}U | H_{\text{kin}}^{\text{leg}} | M\bar{M} \rangle = t_{\text{leg}} e^{-3\pi i/5} \langle \mathbf{1}\tau | h_{\text{kin}} | \tau \mathbf{1} \rangle, \\
\langle \bar{M}M | H_{\text{kin}}^{\text{leg}} | LL \rangle &= \langle \bar{L}M | H_{\text{kin}}^{\text{leg}} | ML \rangle = t_{\text{leg}} e^{3\pi i/5} \langle \mathbf{1}\tau | h_{\text{kin}} | \tau \mathbf{1} \rangle.
\end{aligned} \tag{A.70}$$

Replacing (A.70) into (A.69) one gets the effective hopping,

$$\begin{aligned}
t &= \frac{\langle \Psi_1 | H_{\text{kin}}^{\text{leg}} | \Psi_2 \rangle}{\langle \mathbf{1}\tau | h_{\text{kin}} | \tau \mathbf{1} \rangle} \\
&= \frac{1}{8} [1 + 9 \cos(3\pi/5)] t_{\text{leg}}.
\end{aligned} \tag{A.71}$$

### 3 Higher order terms

In addition to the above cases, we can also have a kinetic and potential terms when the difference in the  $U(1)$  charges on neighbouring rungs is larger than 1. Such process occurs e.g. (i) between a charge-0 (light) hole and a charge-2 (heavy) hole (marked by blue arrows in Table. A.1) in the  $P_2$  paired phase or (ii) between a charge-0 (light) hole and a charge-3 (super heavy)  $\tau$  (marked by orange arrows in Table. A.1) in the  $PS_{03}$  phase.

In case (i), one needs to hop twice to be able to come back to a configuration  $|\Psi_J\rangle$  that has the same  $U(1)$  charges as the initial configuration  $|\Psi_I\rangle$ , so the effective Hamiltonian (leaving in the relevant subspace) is obtained in second-order perturbation, in  $t_{\text{leg}}$  [161, 162]

$$\langle\Psi_I|H_{\text{eff}}|\Psi_J\rangle = -\sum_r \frac{\langle\Psi_I|H_{\text{kin}}^{\text{leg}}|\Psi_r\rangle\langle\Psi_r|H_{\text{kin}}^{\text{leg}}|\Psi_J\rangle}{E_r - E_J}, \quad (\text{A.72})$$

where the sum is on the intermediate states corresponding to two (light)  $\tau$ 's on neighbouring sites. The energy denominator is given by  $E_D = (-2t_{\text{rung}} + J_{\text{rung}})$  and matrix elements for all the intermediate states are  $(-t_{\text{leg}})$  so that one gets for  $I = J$  a potential energy

$$V = -\frac{2t_{\text{leg}}^2}{E_D} \quad (\text{A.73})$$

and for  $I \neq J$  a hopping term

$$t = -\frac{2t_{\text{leg}}^2}{E_D}. \quad (\text{A.74})$$

In case (ii), one needs to hop three times to be able to come back to a configuration that has the same  $U(1)$  charges as the initial configuration, so the effective Hamiltonian is now obtained in third-order perturbation in  $t_{\text{leg}}$ : [161, 162]

$$\langle\Psi_I|H_{\text{eff}}|\Psi_J\rangle = \sum_{r,s} \frac{\langle\Psi_I|H_{\text{kin}}^{\text{leg}}|\Psi_r\rangle\langle\Psi_r|H_{\text{kin}}^{\text{leg}}|\Psi_s\rangle\langle\Psi_s|H_{\text{kin}}^{\text{leg}}|\Psi_J\rangle}{(E_s - E_J)(E_r - E_J)}, \quad (\text{A.75})$$

where the intermediate states  $|\Psi_r\rangle$  and  $|\Psi_s\rangle$  carry a heavy hole and a light  $\tau$  on neighbouring rungs. The energy denominators given by the difference in energy between the initial (degenerate with the final) state and the intermediate states thus take the value

$$E_D = \left(\phi - \frac{1}{2}\right)J_{\text{rung}} - \sqrt{2}t_{\text{rung}} - \frac{\sqrt{J_{\text{rung}}^2 + 8t_{\text{rung}}^2}}{2}. \quad (\text{A.76})$$

Starting from an initial state  $|3, \tau\rangle \otimes |e\rangle$  a simple hopping yields the intermediate state  $|2, \mathbf{1}\rangle \otimes |1, \tau\rangle$  with the matrix elements given by for hopping on the upper leg

$$t_U^1 = \phi^{-1}t_{\text{leg}}, \quad (\text{A.77})$$

on the middle leg,

$$t_M^1 = \phi^{-1}e^{-4i\pi/5}t_{\text{leg}}, \quad (\text{A.78})$$

and on the lower leg,

$$t_L^1 = t_{\text{leg}}. \quad (\text{A.79})$$

Subsequently, a second hopping yields the intermediate state  $|1, \tau\rangle \otimes |2, \mathbf{1}\rangle$  with hopping matrix elements on the upper leg

$$t_U^2 = \phi^{-1} e^{-4i\pi/5} t_{\text{leg}}, \quad (\text{A.80})$$

on the middle leg,

$$t_M^2 = \phi^{-1} t_{\text{leg}}, \quad (\text{A.81})$$

and on the lower leg,

$$t_L^2 = \phi^{-1} e^{4i\pi/5} t_{\text{leg}}. \quad (\text{A.82})$$

Finally to come back to a state carrying the same  $U(1)$  charges on the rungs, the hopping amplitudes for the three legs are just the complex conjugate of those described in Eqs. (A.77)-(A.79), thus giving for  $I = J$  a potential energy

$$V = \frac{(2\phi^{-2} + 1)t_{\text{leg}}^2}{E_D} \quad (\text{A.83})$$

and for  $I \neq J$  a hopping term

$$t = \frac{t_{\text{leg}}^3}{E_D^2} (3\phi^{-2} + 2\phi^{-3} + \phi^{-2} e^{8\pi i/5}). \quad (\text{A.84})$$



# Bibliography

- [1] D. C. Tsui, H. L. Stormer, and A. C. Gossard, “Two-Dimensional Magnetotransport in the Extreme Quantum Limit”, *Phys. Rev. Lett.* **48**, 1559 (1982).
- [2] R. B. Laughlin, “Anomalous Quantum Hall Effect: An Incompressible Quantum Fluid with Fractionally Charged Excitations”, *Phys. Rev. Lett.* **50**, 1395 (1983).
- [3] H. L. Stormer, “Nobel Lecture: The fractional quantum Hall effect”, *Rev. Mod. Phys.* **71**, 875 (1999).
- [4] S. Chu, “Nobel Lecture: The manipulation of neutral particles”, *Rev. Mod. Phys.* **70**, 685 (1998).
- [5] C. N. Cohen-Tannoudji, “Nobel Lecture: Manipulating atoms with photons”, *Rev. Mod. Phys.* **70**, 707 (1998).
- [6] W. D. Phillips, “Nobel Lecture: Laser cooling and trapping of neutral atoms”, *Rev. Mod. Phys.* **70**, 721 (1998).
- [7] A. J. Leggett, “Bose-Einstein condensation in the alkali gases: Some fundamental concepts”, *Rev. Mod. Phys.* **73**, 307 (2001).
- [8] I. Bloch, “Ultracold quantum gases in optical lattices”, *Nature Physics* **1**, 23 (2005).
- [9] D. Jaksch and P. Zoller, “The cold atom Hubbard toolbox”, *Annals of Physics* **315**, 52 (2005) cond-mat/0410614.
- [10] O. Morsch and M. Oberthaler, “Dynamics of Bose-Einstein condensates in optical lattices”, *Rev. Mod. Phys.* **78**, 179 (2006).
- [11] M. Lewenstein, A. Sanpera, V. Ahufinger, B. Damski, A. Sen(De), and U. Sen, “Ultracold atomic gases in optical lattices: mimicking condensed matter physics and beyond”, *Advances in Physics* **56**, 243 (2007) <http://dx.doi.org/10.1080/00018730701223200>.
- [12] I. Bloch, J. Dalibard, and W. Zwerger, “Many-body physics with ultracold gases”, *Rev. Mod. Phys.* **80**, 885 (2008).
- [13] S. Giorgini, L. P. Pitaevskii, and S. Stringari, “Theory of ultracold atomic Fermi gases”, *Rev. Mod. Phys.* **80**, 1215 (2008).

- [14] T. Esslinger, “Fermi-Hubbard Physics with Atoms in an Optical Lattice”, *Annual Review of Condensed Matter Physics* **1**, 129 (2010).
- [15] T. Keilmann, S. Lanzmich, I. McCulloch, and M. Roncaglia, “Statistically induced phase transitions and anyons in 1D optical lattices”, *Nat Commun* **2**, 361 (2011).
- [16] S. Greschner and L. Santos, “Anyon Hubbard Model in One-Dimensional Optical Lattices”, *Phys. Rev. Lett.* **115**, 053002 (2015).
- [17] G. Tang, S. Eggert, and A. Pelster, “Ground-state properties of anyons in a one-dimensional lattice”, *New Journal of Physics* **17**, 123016 (2015).
- [18] F. D. M. Haldane, ““Fractional statistics” in arbitrary dimensions: A generalization of the Pauli principle”, *Phys. Rev. Lett.* **67**, 937 (1991).
- [19] A. Kundu, “Exact Solution of Double  $\delta$  Function Bose Gas through an Interacting Anyon Gas”, *Phys. Rev. Lett.* **83**, 1275 (1999).
- [20] M. T. Batchelor and X.-W. Guan, “Generalized exclusion statistics and degenerate signature of strongly interacting anyons”, *Phys. Rev. B* **74**, 195121 (2006).
- [21] K. Fredenhagen, K. H. Rehren, and B. Schroer, “Superselection sectors with braid group statistics and exchange algebras”, *Communications in Mathematical Physics* **125**, 201.
- [22] J. Fröhlich and F. Gabbiani, “Braid statistics in local quantum theory”, *Rev. Math. Phys.* **02**, 251 (1990) <http://www.worldscientific.com/doi/pdf/10.1142/S0129055X90000107>.
- [23] J. M. Leinaas and J. Myrheim, “On the theory of identical particles”, *Il Nuovo Cimento B (1971-1996)* **37**, 1 (2007).
- [24] F. Wilczek, “Quantum Mechanics of Fractional-Spin Particles”, *Phys. Rev. Lett.* **49**, 957 (1982).
- [25] G. S. Canright and S. M. Girvin, “Fractional statistics: quantum possibilities in two dimensions”, *Science* **247** (1990).
- [26] J. Preskill, *Introduction to Quantum Computation* (World Scientific, Singapore, 1998), chap. Fault Tolerant Quantum Computation.
- [27] A. Stern and N. H. Lindner, “Topological Quantum Computation—From Basic Concepts to First Experiments”, *Science* **339**, 1179 (2013).
- [28] C. Nayak, S. H. Simon, A. Stern, M. Freedman, and S. Das Sarma, “Non-Abelian anyons and topological quantum computation”, *Rev. Mod. Phys.* **80**, 1083 (2008).
- [29] M. Freedman, A. Kitaev, M. Larsen, and Z. Wang, “Topological quantum computation”, *Bull. Amer. Math. Soc.* **40**, 31 (2003).

- [30] A. Kitaev, “Fault-tolerant quantum computation by anyons”, *Annals of Physics* **303**, 2 (2003).
- [31] A. Kitaev, “Anyons in an exactly solved model and beyond”, *Annals of Physics* **321**, 2 (2006), January Special Issue.
- [32] R. P. Feynman, “Simulating physics with computers”, *International Journal of Theor. Physics* **21** (1982).
- [33] P. Shor, in *Proceedings of the 35th Annual Symposium on Foundations of Computer Science* pp. 124–134 IEEE Computer Society Press 1994.
- [34] M. A. Nielsen and I. L. Chuang, *Quantum Computation and Quantum Information* (Cambridge University Press, Cambridge, 2000).
- [35] J. Preskill, “Fault-tolerant quantum computation”, 1997.
- [36] C. Mochon, “Anyons from nonsolvable finite groups are sufficient for universal quantum computation”, *Phys. Rev. A* **67**, 022315 (2003).
- [37] C. Mochon, “Anyon computers with smaller groups”, *Phys. Rev. A* **69**, 032306 (2004).
- [38] J. K. Pachos, *Introduction to Topological Quantum Computation* (Cambridge University Press, Cambridge, 2012).
- [39] D. J. Clarke, J. Alicea, and K. Shtengel, “Exotic non-Abelian anyons from conventional fractional quantum Hall states”, *Nat Commun* **4**, 1348 (2013).
- [40] G. Moore and N. Read, “Nonabelions in the fractional quantum hall effect”, *Nuclear Physics B* **360**, 362 (1991).
- [41] N. Read and E. Rezayi, “Beyond paired quantum Hall states: Parafermions and incompressible states in the first excited Landau level”, *Phys. Rev. B* **59**, 8084 (1999).
- [42] D. J. Clarke, J. Alicea, and K. Shtengel, “Exotic circuit elements from zero-modes in hybrid superconductor-quantum-Hall systems”, *Nat Phys* **10**, 877 (2014).
- [43] J. Alicea, Y. Oreg, G. Refael, F. von Oppen, and M. P. A. Fisher, “Non-Abelian statistics and topological quantum information processing in 1D wire networks”, *Nat Phys* **7**, 412 (2011).
- [44] M. A. Levin and X.-G. Wen, “String-net condensation: A physical mechanism for topological phases”, *Phys. Rev. B* **71**, 045110 (2005).
- [45] N. E. Bonesteel and D. P. DiVincenzo, “Quantum circuits for measuring Levin-Wen operators”, *Phys. Rev. B* **86**, 165113 (2012).
- [46] E. Kapit and S. H. Simon, “Three- and four-body interactions from two-body interactions in spin models: A route to Abelian and non-Abelian fractional Chern insulators”, *Phys. Rev. B* **88**, 184409 (2013).



- [47] G. Palumbo and J. K. Pachos, “Non-Abelian Chern-Simons theory from a Hubbard-like model”, *Phys. Rev. D* **90**, 027703 (2014).
- [48] N. Read and D. Green, “Paired states of fermions in two dimensions with breaking of parity and time-reversal symmetries and the fractional quantum Hall effect”, *Phys. Rev. B* **61**, 10267 (2000).
- [49] A. Y. Kitaev, “Unpaired Majorana fermions in quantum wires”, *Physics-Uspokhi* **44**, 131 (2001).
- [50] L. Fu and C. L. Kane, “Superconducting Proximity Effect and Majorana Fermions at the Surface of a Topological Insulator”, *Phys. Rev. Lett.* **100**, 096407 (2008).
- [51] J. D. Sau, R. M. Lutchyn, S. Tewari, and S. Das Sarma, “Generic New Platform for Topological Quantum Computation Using Semiconductor Heterostructures”, *Phys. Rev. Lett.* **104**, 040502 (2010).
- [52] R. M. Lutchyn, J. D. Sau, and S. Das Sarma, “Majorana Fermions and a Topological Phase Transition in Semiconductor-Superconductor Heterostructures”, *Phys. Rev. Lett.* **105**, 077001 (2010).
- [53] R. S. K. Mong, D. J. Clarke, J. Alicea, N. H. Lindner, P. Fendley, C. Nayak, Y. Oreg, A. Stern, E. Berg, K. Shtengel, and M. P. A. Fisher, “Universal Topological Quantum Computation from a Superconductor-Abelian Quantum Hall Heterostructure”, *Phys. Rev. X* **4**, 011036 (2014).
- [54] N. R. Cooper, N. K. Wilkin, and J. M. F. Gunn, “Quantum Phases of Vortices in Rotating Bose-Einstein Condensates”, *Phys. Rev. Lett.* **87**, 120405 (2001).
- [55] J. Slingerland and F. Bais, “Quantum groups and non-Abelian braiding in quantum Hall systems”, *Nuclear Physics B* **612**, 229 (2001).
- [56] V. Mourik, K. Zuo, S. M. Frolov, S. R. Plissard, E. P. A. M. Bakkers, and L. P. Kouwenhoven, “Signatures of Majorana Fermions in Hybrid Superconductor-Semiconductor Nanowire Devices”, *Science* **336**, 1003 (2012).
- [57] A. Das, Y. Ronen, Y. Most, Y. Oreg, M. Heiblum, and H. Shtrikman, “Zero-bias peaks and splitting in an Al-InAs nanowire topological superconductor as a signature of Majorana fermions”, *Nat Phys* **8**, 887 (2012).
- [58] L. P. Rokhinson, X. Liu, and J. K. Furdyna, “The fractional a.c. Josephson effect in a semiconductor-superconductor nanowire as a signature of Majorana particles”, *Nat Phys* **8**, 795 (2012).
- [59] A. D. K. Finck, D. J. Van Harlingen, P. K. Mohseni, K. Jung, and X. Li, “Anomalous Modulation of a Zero-Bias Peak in a Hybrid Nanowire-Superconductor Device”, *Phys. Rev. Lett.* **110**, 126406 (2013).
- [60] H. O. H. Churchill, V. Fatemi, K. Grove-Rasmussen, M. T. Deng, P. Caroff,

- H. Q. Xu, and C. M. Marcus, “Superconductor-nanowire devices from tunneling to the multichannel regime: Zero-bias oscillations and magnetoconductance crossover”, *Phys. Rev. B* **87**, 241401 (2013).
- [61] S. Trebst, M. Troyer, Z. Wang, and A. W. W. Ludwig, “A Short Introduction to Fibonacci Anyon Models”, *Progress of Theoretical Physics Supplement* **176**, 384 (2008).
- [62] A. Feiguin, S. Trebst, A. W. W. Ludwig, M. Troyer, A. Kitaev, Z. Wang, and M. H. Freedman, “Interacting Anyons in Topological Quantum Liquids: The Golden Chain”, *Phys. Rev. Lett.* **98**, 160409 (2007).
- [63] S. Trebst, E. Ardonne, A. Feiguin, D. A. Huse, A. W. W. Ludwig, and M. Troyer, “Collective States of Interacting Fibonacci Anyons”, *Phys. Rev. Lett.* **101**, 050401 (2008).
- [64] C. Gils, E. Ardonne, S. Trebst, A. W. W. Ludwig, M. Troyer, and Z. Wang, “Collective States of Interacting Anyons, Edge States, and the Nucleation of Topological Liquids”, *Phys. Rev. Lett.* **103**, 070401 (2009).
- [65] C. Gils, E. Ardonne, S. Trebst, D. A. Huse, A. W. W. Ludwig, M. Troyer, and Z. Wang, “Anyonic quantum spin chains: Spin-1 generalizations and topological stability”, *Phys. Rev. B* **87**, 235120 (2013).
- [66] P. E. Finch and H. Frahm, “The  $D(D_3)$ -anyon chain: integrable boundary conditions and excitation spectra”, *New Journal of Physics* **15**, 053035 (2013).
- [67] P. E. Finch, M. Flohr, and H. Frahm, “Integrable anyon chains: From fusion rules to face models to effective field theories”, *Nuclear Physics B* **889**, 299 (2014).
- [68] P. E. Finch, H. Frahm, M. Lewerenz, A. Milsted, and T. J. Osborne, “Quantum phases of a chain of strongly interacting anyons”, *Phys. Rev. B* **90**, 081111 (2014).
- [69] R. N. C. Pfeifer, O. Buerschaper, S. Trebst, A. W. W. Ludwig, M. Troyer, and G. Vidal, “Translation invariance, topology, and protection of criticality in chains of interacting anyons”, *Phys. Rev. B* **86**, 155111 (2012).
- [70] N. E. Bonesteel and K. Yang, “Infinite-Randomness Fixed Points for Chains of Non-Abelian Quasiparticles”, *Phys. Rev. Lett.* **99**, 140405 (2007).
- [71] L. Fidkowski, G. Refael, N. E. Bonesteel, and J. E. Moore, “ $c$ -theorem violation for effective central charge of infinite-randomness fixed points”, *Phys. Rev. B* **78**, 224204 (2008).
- [72] F. C. Zhang and T. M. Rice, “Effective Hamiltonian for the superconducting Cu oxides”, *Phys. Rev. B* **37**, 3759 (1988).
- [73] J. Hubbard, “Electron Correlations in Narrow Energy Bands”, *Proceedings*

- of the Royal Society of London A: *Mathematical, Physical and Engineering Sciences* **276**, 238 (1963).
- [74] M. C. Gutzwiller, “Effect of Correlation on the Ferromagnetism of Transition Metals”, *Phys. Rev. Lett.* **10**, 159 (1963).
- [75] J. Kanamori, “Electron Correlation and Ferromagnetism of Transition Metals”, *Progress of Theoretical Physics* **30**, 275 (1963).
- [76] P. W. Anderson, “Ground State of a Magnetic Impurity in a Metal”, *Phys. Rev.* **164**, 352 (1967).
- [77] D. Poilblanc, M. Troyer, E. Ardonne, and P. Bonderson, “Fractionalization of Itinerant Anyons in One-Dimensional Chains”, *Phys. Rev. Lett.* **108**, 207201 (2012).
- [78] D. Poilblanc, A. Feiguin, M. Troyer, E. Ardonne, and P. Bonderson, “One-dimensional itinerant interacting non-Abelian anyons”, *Phys. Rev. B* **87**, 085106 (2013).
- [79] S. Tomonaga, “Remarks on Bloch’s Method of Sound Waves applied to Many-Fermion Problems”, *Progress of Theoretical Physics* **5**, 544 (1950).
- [80] J. M. Luttinger, “An Exactly Soluble Model of a Many-Fermion System”, *Journal of Mathematical Physics* **4**, 1154 (1963).
- [81] F. D. M. Haldane, “‘Luttinger liquid theory’ of one-dimensional quantum fluids. I. Properties of the Luttinger model and their extension to the general 1D interacting spinless Fermi gas”, *Journal of Physics C: Solid State Physics* **14**, 2585 (1981).
- [82] D. Poilblanc, A. W. W. Ludwig, S. Trebst, and M. Troyer, “Quantum spin ladders of non-Abelian anyons”, *Phys. Rev. B* **83**, 134439 (2011).
- [83] A. W. W. Ludwig, D. Poilblanc, S. Trebst, and M. Troyer, “Two-dimensional quantum liquids from interacting non-Abelian anyons”, *New Journal of Physics* **13**, 045014 (2011).
- [84] M. H. Anderson, J. R. Ensher, M. R. Matthews, C. E. Wieman, and E. A. Cornell, “Observation of Bose-Einstein Condensation in a Dilute Atomic Vapor”, *Science* **269**, 198 (1995).
- [85] C. C. Bradley, C. A. Sackett, J. J. Tollett, and R. G. Hulet, “Evidence of Bose-Einstein Condensation in an Atomic Gas with Attractive Interactions”, *Phys. Rev. Lett.* **75**, 1687 (1995).
- [86] K. B. Davis, M. O. Mewes, M. R. Andrews, N. J. van Druten, D. S. Durfee, D. M. Kurn, and W. Ketterle, “Bose-Einstein Condensation in a Gas of Sodium Atoms”, *Phys. Rev. Lett.* **75**, 3969 (1995).
- [87] B. DeMarco and D. S. Jin, “Onset of Fermi Degeneracy in a Trapped Atomic Gas”, *Science* **285**, 1703 (1999).

- [88] F. Dalfovo, S. Giorgini, L. P. Pitaevskii, and S. Stringari, “Theory of Bose-Einstein condensation in trapped gases”, *Rev. Mod. Phys.* **71**, 463 (1999).
- [89] F. Schreck, L. Khaykovich, K. L. Corwin, G. Ferrari, T. Bourdel, J. Cubizolles, and C. Salomon, “Quasipure Bose-Einstein Condensate Immersed in a Fermi Sea”, *Phys. Rev. Lett.* **87**, 080403 (2001).
- [90] A. G. Truscott, K. E. Strecker, W. I. McAlexander, G. B. Partridge, and R. G. Hulet, “Observation of Fermi Pressure in a Gas of Trapped Atoms”, *Science* **291**, 2570 (2001).
- [91] G. Roati, F. Riboli, G. Modugno, and M. Inguscio, “Fermi-Bose Quantum Degenerate  $^{40}\text{K}$ - $^{87}\text{Rb}$  Mixture with Attractive Interaction”, *Phys. Rev. Lett.* **89**, 150403 (2002).
- [92] Z. Hadzibabic, S. Gupta, C. A. Stan, C. H. Schunck, M. W. Zwierlein, K. Dieckmann, and W. Ketterle, “Fiftyfold Improvement in the Number of Quantum Degenerate Fermionic Atoms”, *Phys. Rev. Lett.* **91**, 160401 (2003).
- [93] M. Greiner, C. A. Regal, and D. S. Jin, “Emergence of a molecular Bose-Einstein condensate from a Fermi gas”, *Nature* **426**, 537 (2003).
- [94] S. Jochim, M. Bartenstein, A. Altmeyer, G. Hendl, S. Riedl, C. Chin, J. Hecker Denschlag, and R. Grimm, “Bose-Einstein Condensation of Molecules”, *Science* **302**, 2101 (2003).
- [95] C. A. Regal, M. Greiner, and D. S. Jin, “Observation of Resonance Condensation of Fermionic Atom Pairs”, *Phys. Rev. Lett.* **92**, 040403 (2004).
- [96] M. W. Zwierlein, C. A. Stan, C. H. Schunck, S. M. F. Raupach, A. J. Kerman, and W. Ketterle, “Condensation of Pairs of Fermionic Atoms near a Feshbach Resonance”, *Phys. Rev. Lett.* **92**, 120403 (2004).
- [97] J. Kinast, S. L. Hemmer, M. E. Gehm, A. Turlapov, and J. E. Thomas, “Evidence for Superfluidity in a Resonantly Interacting Fermi Gas”, *Phys. Rev. Lett.* **92**, 150402 (2004).
- [98] T. Bourdel, L. Khaykovich, J. Cubizolles, J. Zhang, F. Chevy, M. Teichmann, L. Tarruell, S. J. J. M. F. Kokkelmans, and C. Salomon, “Experimental Study of the BEC-BCS Crossover Region in Lithium 6”, *Phys. Rev. Lett.* **93**, 050401 (2004).
- [99] G. B. Partridge, K. E. Strecker, R. I. Kamar, M. W. Jack, and R. G. Hulet, “Molecular Probe of Pairing in the BEC-BCS Crossover”, *Phys. Rev. Lett.* **95**, 020404 (2005).
- [100] M. P. A. Fisher, P. B. Weichman, G. Grinstein, and D. S. Fisher, “Boson localization and the superfluid-insulator transition”, *Phys. Rev. B* **40**, 546 (1989).
- [101] D. Jaksch, C. Bruder, J. I. Cirac, C. W. Gardiner, and P. Zoller, “Cold Bosonic Atoms in Optical Lattices”, *Phys. Rev. Lett.* **81**, 3108 (1998).

- [102] M. Greiner, O. Mandel, T. Esslinger, T. W. Hansch, and I. Bloch, “Quantum phase transition from a superfluid to a Mott insulator in a gas of ultracold atoms”, *Nature* **415**, 39 (2002).
- [103] M. Köhl, H. Moritz, T. Stöferle, K. Günter, and T. Esslinger, “Fermionic Atoms in a Three Dimensional Optical Lattice: Observing Fermi Surfaces, Dynamics, and Interactions”, *Phys. Rev. Lett.* **94**, 080403 (2005).
- [104] K. Günter, T. Stöferle, H. Moritz, M. Köhl, and T. Esslinger, “Bose-Fermi Mixtures in a Three-Dimensional Optical Lattice”, *Phys. Rev. Lett.* **96**, 180402 (2006).
- [105] S. Ospelkaus, C. Ospelkaus, O. Wille, M. Succo, P. Ernst, K. Sengstock, and K. Bongs, “Localization of Bosonic Atoms by Fermionic Impurities in a Three-Dimensional Optical Lattice”, *Phys. Rev. Lett.* **96**, 180403 (2006).
- [106] C. Kollath, A. Iucci, I. P. McCulloch, and T. Giamarchi, “Modulation spectroscopy with ultracold fermions in an optical lattice”, *Phys. Rev. A* **74**, 041604 (2006).
- [107] N. Strohmaier, Y. Takasu, K. Günter, R. Jördens, M. Köhl, H. Moritz, and T. Esslinger, “Interaction-Controlled Transport of an Ultracold Fermi Gas”, *Phys. Rev. Lett.* **99**, 220601 (2007).
- [108] R. Jördens, N. Strohmaier, K. Günter, H. Moritz, and T. Esslinger, “A Mott insulator of fermionic atoms in an optical lattice”, *Nature* **455**, 204 (2008).
- [109] U. Schneider, L. Hackermüller, S. Will, T. Best, I. Bloch, T. A. Costi, R. W. Helmes, D. Rasch, and A. Rosch, “Metallic and Insulating Phases of Repulsively Interacting Fermions in a 3D Optical Lattice”, *Science* **322**, 1520 (2008).
- [110] D. Greif, L. Tarruell, T. Uehlinger, R. Jördens, and T. Esslinger, “Probing Nearest-Neighbor Correlations of Ultracold Fermions in an Optical Lattice”, *Phys. Rev. Lett.* **106**, 145302 (2011).
- [111] D. Greif, T. Uehlinger, G. Jotzu, L. Tarruell, and T. Esslinger, “Short-Range Quantum Magnetism of Ultracold Fermions in an Optical Lattice”, *Science* (2013).
- [112] M. Messer, R. Desbuquois, T. Uehlinger, G. Jotzu, S. Huber, D. Greif, and T. Esslinger, “Exploring Competing Density Order in the Ionic Hubbard Model with Ultracold Fermions”, *Phys. Rev. Lett.* **115**, 115303 (2015).
- [113] A. S. Maciej Lewenstein and V. Ahufinger, *Ultracold Atoms in Optical Lattices Simulating quantum many-body systems* (Oxford University Press, 2012).
- [114] P. Törmä and K. Sengstock, editors, *Quantum Gas Experiments Exploring Many-Body States* volume 3 (Imperial College Press, 2015).
- [115] R. Jördens, L. Tarruell, D. Greif, T. Uehlinger, N. Strohmaier, H. Moritz,

- T. Esslinger, L. De Leo, C. Kollath, A. Georges, V. Scarola, L. Pollet, E. Burovski, E. Kozik, and M. Troyer, “Quantitative Determination of Temperature in the Approach to Magnetic Order of Ultracold Fermions in an Optical Lattice”, *Phys. Rev. Lett.* **104**, 180401 (2010).
- [116] D. C. McKay and B. DeMarco, “Cooling in strongly correlated optical lattices: prospects and challenges”, *Reports on Progress in Physics* **74**, 054401 (2011).
- [117] B. Wolf, A. Honecker, W. Hofstetter, U. Tutsch, and M. Lang, “Cooling through quantum criticality and many-body effects in condensed matter and cold gases”, *International Journal of Modern Physics B* **28**, 1430017 (2014).
- [118] J. Zakrzewski and D. Delande, “Breakdown of adiabaticity when loading ultracold atoms in optical lattices”, *Phys. Rev. A* **80**, 013602 (2009).
- [119] S. Masuda, K. Nakamura, and A. del Campo, “High-Fidelity Rapid Ground-State Loading of an Ultracold Gas into an Optical Lattice”, *Phys. Rev. Lett.* **113**, 063003 (2014).
- [120] P. N. Ma, K. Y. Yang, L. Pollet, J. V. Porto, M. Troyer, and F. C. Zhang, “Influence of the trap shape on the detection of the superfluid–Mott-insulator transition”, *Phys. Rev. A* **78**, 023605 (2008).
- [121] J.-S. Bernier, C. Kollath, A. Georges, L. De Leo, F. Gerbier, C. Salomon, and M. Köhl, “Cooling fermionic atoms in optical lattices by shaping the confinement”, *Phys. Rev. A* **79**, 061601 (2009).
- [122] T. Paiva, Y. L. Loh, M. Randeria, R. T. Scalettar, and N. Trivedi, “Fermions in 3D Optical Lattices: Cooling Protocol to Obtain Antiferromagnetism”, *Phys. Rev. Lett.* **107**, 086401 (2011).
- [123] M. Dolfi, A. Kantian, B. Bauer, and M. Troyer, “Minimizing nonadiabaticities in optical-lattice loading”, *Phys. Rev. A* **91**, 033407 (2015).
- [124] Y. Prasad, A. Medhi, and V. B. Shenoy, “Fermionic superfluid from a bilayer band insulator in an optical lattice”, *Phys. Rev. A* **89**, 043605 (2014).
- [125] C. J. M. Mathy, D. A. Huse, and R. G. Hulet, “Enlarging and cooling the Néel state in an optical lattice”, *Phys. Rev. A* **86**, 023606 (2012).
- [126] T. Paiva, E. Khatami, S. Yang, V. Rousseau, M. Jarrell, J. Moreno, R. G. Hulet, and R. T. Scalettar, “Cooling Atomic Gases With Disorder”, *Phys. Rev. Lett.* **115**, 240402 (2015).
- [127] C. Grenier, A. Georges, and C. Kollath, “Peltier Cooling of Fermionic Quantum Gases”, *Phys. Rev. Lett.* **113**, 200601 (2014).
- [128] A. Sheikhan and C. Kollath, “Loading and detecting a three-dimensional Fermi gas in a one-dimensional optical superlattice”, *Phys. Rev. A* **91**, 043611 (2015).

- [129] T.-L. Ho and Q. Zhou, “Squeezing out the entropy of fermions in optical lattices”, *PNAS* **106**, 6916 (2009).
- [130] A. W. Sandvik, “Computational Studies of Quantum Spin Systems”, in *Lectures on the Physics of strongly correlated systems XIV: Fourteenth Training Course in the Physics of Strongly Correlated Systems*, edited by A. Avella and F. Mancini volume 1297 2009.
- [131] N. Laflorencie and D. Poilblanc, *Simulations of pure and doped low-dimensional spin-1/2 gapped systems* (Springer Berlin Heidelberg, Berlin, Heidelberg, 2004), pp. 227–252.
- [132] R. M. Noack and S. R. Manmana, “Diagonalization- and Numerical Renormalization-Group-Based Methods for Interacting Quantum Systems”, in *Lectures on the Physics of Highly Correlated Electron Systems IX* volume 789 pp. 93–163 2005.
- [133] G. Vidal, “Efficient Simulation of One-Dimensional Quantum Many-Body Systems”, *Phys. Rev. Lett.* **93**, 040502 (2004).
- [134] S. R. White and A. E. Feiguin, “Real-Time Evolution Using the Density Matrix Renormalization Group”, *Phys. Rev. Lett.* **93**, 076401 (2004).
- [135] A. J. Daley, C. Kollath, U. Schollwöck, and G. Vidal, “Time-dependent density-matrix renormalization-group using adaptive effective Hilbert spaces”, *J. Stat. Mech. Theor. Exp.* **2004**, P04005 (2004).
- [136] F. Verstraete, J. J. García-Ripoll, and J. I. Cirac, “Matrix Product Density Operators: Simulation of Finite-Temperature and Dissipative Systems”, *Phys. Rev. Lett.* **93**, 207204 (2004).
- [137] M. Zwolak and G. Vidal, “Mixed-State Dynamics in One-Dimensional Quantum Lattice Systems: A Time-Dependent Superoperator Renormalization Algorithm”, *Phys. Rev. Lett.* **93**, 207205 (2004).
- [138] A. E. Feiguin and S. R. White, “Finite-temperature density matrix renormalization using an enlarged Hilbert space”, *Phys. Rev. B* **72**, 220401 (2005).
- [139] A. Albuquerque *et al.*, “The {ALPS} project release 1.3: Open-source software for strongly correlated systems”, *J. Magn. Magn. Mater.* **310**, 1187 (2007).
- [140] B. Bauer *et al.*, “The ALPS project release 2.0: open source software for strongly correlated systems”, *J. Stat. Mech.* **2011**, P05001 (2011).
- [141] M. Dolfi, B. Bauer, S. Keller, A. Kosenkov, T. Ewart, A. Kantian, T. Giamarchi, and M. Troyer, “Matrix product state applications for the {ALPS} project”, *Comput. Phys. Commun.* **185**, 3430 (2014).
- [142] M. Dolfi, B. Bauer, M. Troyer, and Z. Ristivojevic, “Multigrid Algorithms for Tensor Network States”, *Phys. Rev. Lett.* **109**, 020604 (2012).

- [143] U. Schollwöck, “The Density-Matrix Renormalization Group in the Age of Matrix Product States”, *Annals of Physics* **326**, 96 (2011).
- [144] R. Orús, “A practical introduction to tensor networks: Matrix product states and projected entangled pair states”, *Annals of Physics* **349**, 117 (2014).
- [145] J. Goodman and A. D. Sokal, “Multigrid Monte Carlo Method for Lattice Field Theories”, *Phys. Rev. Lett.* **56**, 1015 (1986).
- [146] M. Heiskanen, T. Torsti, M. J. Puska, and R. M. Nieminen, “Multigrid method for electronic structure calculations”, *Phys. Rev. B* **63**, 245106 (2001).
- [147] E. Witten, “Quantum field theory and the Jones polynomial”, *Communications in Mathematical Physics* **121**, 351.
- [148] P. D. Francesco, P. Mathieu, and D. Sénéchal, *Conformal Field Theory* (Springer, New York, 1997).
- [149] E. Dagotto and T. M. Rice, “Surprises on the Way from One- to Two-Dimensional Quantum Magnets: The Ladder Materials”, *Science* **271**, 618 (1996).
- [150] M. Greven, R. J. Birgeneau, and U. J. Wiese, “Monte Carlo Study of Correlations in Quantum Spin Ladders”, *Phys. Rev. Lett.* **77**, 1865 (1996).
- [151] D. Greif, G. Jotzu, M. Messer, R. Desbuquois, and T. Esslinger, “Formation and Dynamics of Antiferromagnetic Correlations in Tunable Optical Lattices”, *Phys. Rev. Lett.* **115**, 260401 (2015).
- [152] J. Struck, C. Ölschläger, R. Le Targat, P. Soltan-Panahi, A. Eckardt, M. Lewenstein, P. Windpassinger, and K. Sengstock, “Quantum Simulation of Frustrated Classical Magnetism in Triangular Optical Lattices”, *Science* **333**, 996 (2011).
- [153] G. Liu, S.-L. Zhu, S. Jiang, F. Sun, and W. M. Liu, “Simulating and detecting the quantum spin Hall effect in the kagome optical lattice”, *Phys. Rev. A* **82**, 053605 (2010).
- [154] M. Olshanii, “Atomic Scattering in the Presence of an External Confinement and a Gas of Impenetrable Bosons”, *Phys. Rev. Lett.* **81**, 938 (1998).
- [155] S. R. White, “Density matrix formulation for quantum renormalization groups”, *Phys. Rev. Lett.* **69**, 2863 (1992).
- [156] U. Schollwöck, “The density-matrix renormalization group in the age of matrix product states”, *Ann. Phys. (N.Y.)* **326**, 96 (2011).
- [157] T. Fukuhara, A. Kantian, M. Endres, M. Cheneau, P. Schausz, S. Hild, D. Bellem, U. Schollwöck, T. Giamarchi, C. Gross, I. Bloch, and S. Kuhr, “Quantum dynamics of a mobile spin impurity”, *Nat Phys* **9**, 235 (2013).



- [158] M. Cheneau, P. Barmettler, D. Poletti, M. Endres, P. Schausz, T. Fukuhara, C. Gross, I. Bloch, C. Kollath, and S. Kuhr, “Light-cone-like spreading of correlations in a quantum many-body system”, *Nature* **481**, 484 (2012).
- [159] G. Vidal, “Efficient Classical Simulation of Slightly Entangled Quantum Computations”, *Phys. Rev. Lett.* **91**, 147902 (2003).
- [160] C. Chin, R. Grimm, P. Julienne, and E. Tiesinga, “Feshbach resonances in ultracold gases”, *Rev. Mod. Phys.* **82**, 1225 (2010).
- [161] I. d. P. R. Moreira, N. Suaud, N. Guihéry, J. P. Malrieu, R. Caballol, J. M. Bofill, and F. Illas, “Derivation of spin Hamiltonians from the exact Hamiltonian: Application to systems with two unpaired electrons per magnetic site”, *Phys. Rev. B* **66**, 134430 (2002).
- [162] J. P. Malrieu, R. Caballol, C. J. Calzado, C. de Graaf, and N. Guihéry, “Magnetic Interactions in Molecules and Highly Correlated Materials: Physical Content, Analytical Derivation, and Rigorous Extraction of Magnetic Hamiltonians”, *Chemical Reviews* **114**, 429 (2014) <http://dx.doi.org/10.1021/cr300500z>, PMID: 24102410.

# List of Publications

- [1] M. Soni, M. Troyer, and D. Poilblanc, “Effective models of doped quantum ladders of non-Abelian anyons”, *Physical Review B* **93**, 035124 (2016).
- [2] M. Soni, M. Dolfi, and M. Troyer, “Density redistribution effects in fermionic optical lattices”, arXiv:1607.06352.



# Résumé

## 1 Introduction

En physique de la matière condensée, nous avons une large variété de modèles intéressants dont certains sont bien compris tandis que d'autres restent ambigus à ce jour. Les systèmes fortement corrélés forment un domaine intéressant de la recherche et offrent beaucoup de systèmes qui présentent des propriétés fascinantes. Des exemples de tels effets fortement corrélés peuvent être trouvés dans une large variété de systèmes physiques, tels que les superconducteurs, les systèmes magnétiques, les systèmes quantiques de Hall, les systèmes électroniques unidimensionnels, des atomes ultra froids dans des réseaux optiques, etc. Cette thèse comprend l'étude des deux projets. La première traitant de anyons non-abéliens et la seconde s'intéresse à l'étude de fermions dans un réseau optique dimensionnelles. Plusieurs travaux ont exploré la combinaison d'anyons et de réseaux optiques [15–17] selon la généralisation de principe de Pauli [18–20].

Constituant une première étape vers un système à deux dimensions, les modèles d'anyons ont été étudiés sur des chaînes couplées pour former ce qu'on appelle échelles quantique de anyons non-abéliennes, qui fournissent des généralisations anyonic des quantiques 2D aimants [82, 83]. Dans le premier projet de cette thèse, nous avons analysé la physique des anyons non-abéliens mobiles au-delà d'une dimension, qui est une question fondamentale. Notre objectif a été de construire le modèle le plus simple possible d'anyons en 2D itinérants et interagissants en étroite analogie avec systèmes fermionique et inspiré par les études précédentes sur les anyons. Comme discuté plus tard, ce modèle prend la forme d'une modèle anyonique  $t - J$  2D très similaire à son analogue 2D électronique et à sa version anyonique en 1D mentionnée ci-dessus. Il existe une géométrie naturelle à considérer, interpolation entre 1D et 2D, qui est la géométrie de l'échelle - par exemple un système d'un nombre fini de chaînes couplées - est utilisé à la fois pour les spins électroniques et anyons localisés. En particulier, nous posons la question si la séparation spin-charge survit dans le modèle d'échelle pour anyons non abéliens. De plus, dans l'étude de ce modèle, nous avons découvert une nouvelle phase incompressible pouvant présenter un caractère topologique.

Le deuxième projet dans cette thèse étudie les effets de redistribution de la densité dans le système 1D de réseaux optiques fermioniques. Nous cherchons à comprendre si les défauts causés par une mauvaise répartition des particules pendant

le chargement de réseau sont importantes pour le cas fermionique, interdisant aux atomes de se refroidir au niveau souhaité. Ici, nous examinons quatre états différents, qui seront appelés *états cibles* dans les sections suivantes. Les états cibles sont caractérisés par des profils de densité différents et dépendant des paramètres choisis du modèle. Nous montrons d'abord que, pour certains états cibles, la rampe adiabatique simple montre déjà des défauts négligeables, alors que les autres états souffrent d'effets de chauffage pendant le chargement du réseau. Une analyse de l'évolution temporelle du profil de densité locale nous amène à conclure qu'en effet les défauts de densité sont le principal problème, donc nous nous concentrons notre attention sur la conception de protocoles qui permettent une meilleure redistribution des particules lors de la montée en puissance. Comme dans le cas de bosons, notre dispositif améliore les méthodes de rampe des systèmes où nous changeons dynamiquement un ou plusieurs paramètres du système afin de réduire les défauts de densité. La première approche consiste à tester le protocole mis en avant pour les bosons, à savoir pour remodeler dynamiquement le potentiel de piégeage. De plus, dans ce travail, nous montrons que le réglage de la force d'interaction, qui apparaît comme un des paramètres les plus faciles à maîtriser dans les expériences, est une autre façon d'obtenir des températures plus basses. Nous mentionnons également une autre approche dans laquelle la force d'interaction et le potentiel de piégeage peuvent être réglés en même temps pendant le chargement de réseau qui réduit en effet la chaleur en excès dans le système de manière significative.

## 2 Échelles d'anyons Fibonacci

Les théories  $SU(2)_k$  de Chern-Simons [61, 147] sont dites de déformations quantiques de l'algèbre  $SU(2)$ . Leurs degrés de liberté sont codés par de charges topologiques  $j$ , qui sont des moments angulaires généralisés. Contrairement à  $SU(2)$ , dans les théories  $SU(2)_k$  le spin total  $j$  est limité à  $j = 0, \frac{1}{2}, \dots, \frac{k}{2}$ .

Comme pour le produit de tenseur de spins, anyons non-abéliens peuvent être fusionnés selon les règles de fusion données par

$$j_1 \times j_2 = \sum_{j_3=|j_1-j_2|}^{\min\{j_1+j_2, k-j_1-j_2\}} j_3. \quad (1)$$

La théorie de Fibonacci a deux types de *particules* distinctes que l'on note que  $\mathbf{1}$  pour la particule triviale avec  $j = 0$  et  $\tau$  pour l'anyon de Fibonacci avec  $j = 1$ , respectivement, et les règles de fusion non triviales sont  $\tau \otimes \tau = \mathbf{1} \oplus \tau$ .

Nous représentons un système de  $N$  anyons au moyen d'un *arbre de fusion* comme montré dans la figure 1(a), où les charges anyoniques des anyons individuels sont repérés par  $Y_i$ . Le résultat de la fusion successive des anyons sont codées par les labels de liens dans l'arbre de fusion, marqués par  $x_i$  dans la figure 1(a). Les contraintes sur les labels des liens en raison de règles de fusion qui doivent être

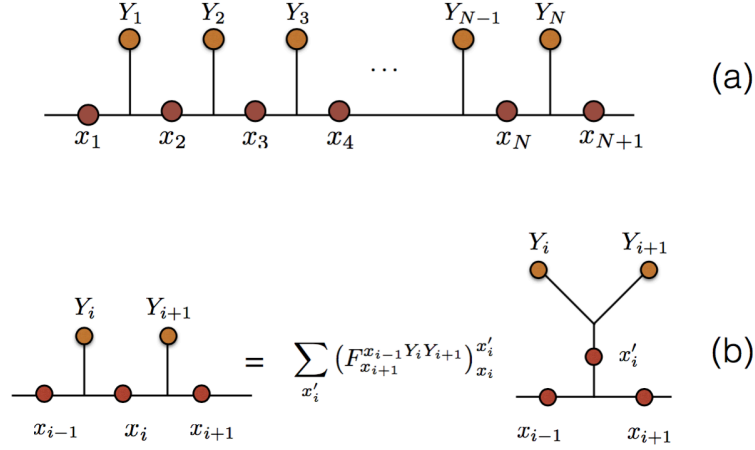


Figure 1: (a) Illustration de l'arbre de fusion standard avec des sites de label  $Y_i$  (qui peut être soit  $\tau$  ou  $\mathbf{1}$ ) et des liens de label  $X_i$ . (b) Un changement de base aboutissant à un arbre de fusion différent en utilisant un  $F$  matrice.

remplies à chaque sommet réduisent de manière significative la taille de l'espace interne de Hilbert.

Pour effectuer une opération sur la proximité anyons voisin, il est avantageux de passer à une autre base, dans lequel la fusion issue de deux particules est explicite. Cela se fait via le  $F$  matrice montré schématiquement la figure 1 (b). Une matrice non-trivial est obtenu uniquement lorsque tous les quatre labels externes sont  $\tau$  anyons. Spécialisations au cas où  $Y_i = Y_{i+1} = \tau$ , les labels pour les trois liaisons  $|x_{i-1}, x_i, x_{i+1}\rangle$  autorisé par les règles de fusion sont

$$\{|\mathbf{1}, \tau, \mathbf{1}\rangle, |\mathbf{1}, \tau, \tau\rangle, |\tau, \tau, \mathbf{1}\rangle, |\tau, \mathbf{1}, \tau\rangle, |\tau, \tau, \tau\rangle\} \quad (2)$$

qui transforme une nouvelle base  $|x_{i-1}, x_i, x_{i+1}\rangle$  après le  $F$  matrice. L'utilisation de ces bases le matrice  $F$  est représentée comme,

$$F = \begin{bmatrix} 1 & & & & & \\ & 1 & & & & \\ & & 1 & & & \\ & & & \phi^{-1} & \phi^{-1/2} & \\ & & & \phi^{-1/2} & -\phi^{-1} & \end{bmatrix}, \quad (3)$$

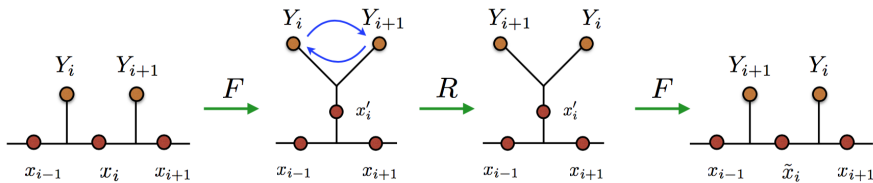


Figure 2: Représentation schématique d'une tresse sur l'arbre de fusion.

où, comme mentionné ci-dessus, nous avons un non-trivial  $2 \times 2$  seulement sous-matrice quand aussi  $x_{i-1} = x_{i+1} = \tau$ .

Une autre opération que nous avons besoin d'effectuer le plus proche anyons voisin est celui de l'échange (ou tressage) eux. En vertu d'un droitier anyons tresse  $a$  et  $b$  ramasser une phase  $R_c^{b,a}$  selon les types de anyon,  $a$  et  $b$ , qui sont en cours d'échange et de leur fusion résultats  $c$ . Notez que chaque fois que  $a$  ou  $b$  sont  $\mathbf{1}$ , la phase est trivial. Phases non triviaux ne sont obtenus pour  $a = b = \tau$  donnée par  $R_{\mathbf{1}}^{\tau\tau} = e^{+4\pi i/5}$ ,  $R_{\tau}^{\tau\tau} = e^{-3\pi i/5}$ .

Afin de réaliser une tresse sur l'arbre de fusion standard, nous devons d'abord changer base en utilisant un  $F$  matrice pour que les résultats de la fusion des deux anyons explicite, puis tresse. Ce processus est représenté schématiquement sur la figure 2. Ceci est représenté par une matrice Braid  $B$  agissant sur la labels de lien  $|x_{i-1}, x_i, x_{i+1}\rangle$ . La seule matrice Braid non-trivial est obtenu lorsque les deux sites sont occupés par  $\tau$  anyons. Dans la base de l'équation 2, on obtient:

$$B = FRF = \begin{bmatrix} e^{4i\pi/5} & 0 & 0 & 0 & 0 \\ 0 & e^{-3i\pi/5} & 0 & 0 & 0 \\ 0 & 0 & e^{-3i\pi/5} & 0 & 0 \\ 0 & 0 & 0 & \frac{1}{\phi^2}e^{4i\pi/5} + \frac{1}{\phi}e^{-3i\pi/5} & \frac{1}{\phi^{3/2}}(e^{4i\pi/5} - e^{-3i\pi/5}) \\ 0 & 0 & 0 & \frac{1}{\phi^{3/2}}(e^{4i\pi/5} - e^{-3i\pi/5}) & \frac{1}{\phi^2}e^{-3i\pi/5} + \frac{1}{\phi}e^{4i\pi/5} \end{bmatrix}. \quad (4)$$

Notez que lorsque les deux labels de site sont un  $\mathbf{1}$  et  $\tau$ , les matrices  $F$  et les phases de tresse sont trivial. La matrice Braid est effectivement le saut de l'anyon sur le site adjacent. Lorsque les deux marqueurs de site sont  $\mathbf{1}$ , la matrice de tresse est simplement donnée par la matrice d'identité.

## 2.1 Modèles dans une dimension

Les soi-disant des chaînes d'or sont des tableaux 1D de anyons Fibonacci localisés avec des interactions par paire entre les plus proches voisins [62]. L'hamiltonien d'interactions magnétiques entre anyons est défini par analogie avec l'interaction d'échange de Heisenberg. Nous attribuons une énergie  $-J$  si le résultat de la fusion de deux anyons interagissant est trivial. Pour les accouplements AFM ( $J > 0$ ), ce qui favorise le résultat de la fusion de deux anyons voisins d'être trivial, alors que pour les accouplements FM ( $J < 0$ ), la fusion de deux anyons est préféré à  $\tau$ . Cette interaction entre les plus proches anyons voisins est exécuter par projection sur le secteur de fusion d'identité:  $H_{\text{mag}} = Jh_{\text{mag}} = -J(FP^{\mathbf{1}}F^{-1})$ , où  $F$  est l'opérateur correspondant au  $F$  matrice (voir l'équation (3)) et  $P^{\mathbf{1}}$  est un opérateur que les projets sur le  $\mathbf{1}$  état.

Pour modéliser anyons itinérants nous introduisons des trous, à savoir sites avec un trivial anyon  $\mathbf{1}$  sur certains des sites. Les trous et anyons  $\tau$  sont marqués par différents  $U(1)$  charges (abéliennes électriques) et charges anyonic (non-abéliennes). Les anyons  $\tau$  (appelée plus simplement 'anyons' ou ' $\tau$  particules' ci-après) peuvent

se déplacer sur la chaîne (avec sa charge électrique et anyonic) à un site voisin qui se traduit par une contribution supplémentaire d'énergie cinétique. Elle implique le saut d'une particule, ainsi que sa charge électrique et anyonic à un site voisin.

## 2.2 Échelles dopées

Dans cette thèse, nous nous concentrons sur des échelles itinérants de anyons Fibonacci. On indique les couplages forts le long de la direction de la jambe par  $J_{\text{leg}}$  et  $t_{\text{leg}}$  pour les termes magnétiques et cinétiques respectivement comme indiqué sur la Fig. 3(a). Le long de la direction perpendiculaire que nous appelons "la direction rung", les couplages  $J_{\text{rung}}$  et  $t_{\text{rung}}$  désignent respectivement les termes magnétiques et cinétiques. Comme chemin de la fusion, nous choisissons le chemin en zig-zag représenté sur la figure 3(b), car il minimise la portée effective des interactions sur le chemin de la fusion. Nous choisissons des conditions aux limites périodiques le long de la direction de la jambe et les conditions aux limites ouvertes le long des rungs.

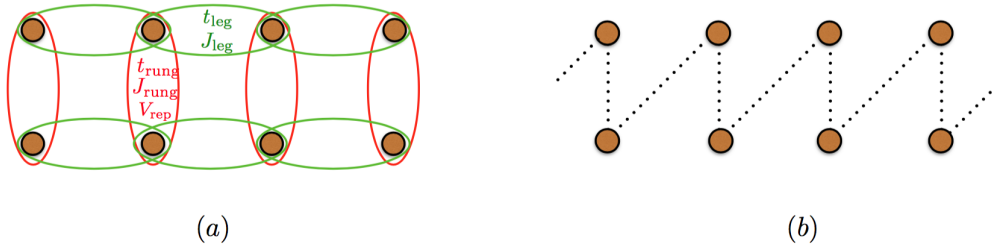


Figure 3: Échelle à deux jambes: (a) Interactions le long de la jambe et directions sonné, (b) Le chemin de la fusion en zigzag. Les accouplements ont été indiqués.

Avec ce choix du chemin de fusion, les interactions entre premières voisins sur les rungs sont également premier voisin le long du chemin de fusion, tandis que celles qui existent entre anyons sur la même jambe sont une portée plus longue le long du chemin de fusion.

Interactions premières voisins échelon peuvent être réaliser exactement de la même manière que pour premières voisins sur une chaîne (voir Sec. 2.1). Afin d'évaluer les interactions entre  $\tau$  particules sur la même jambe, nous devons effectuer un changement de base, cette fois par les tresser dans le sens horaire manière jusqu'à ce qu'ils soient premières voisins le long du chemin de fusion. Cette tresse est réalisée par la matrice unitaire de tresse  $B$  (voir l'équation (4.)). Une fois que les particules sont premières voisins le long du chemin, ils peuvent interagir avec le même terme tel que discuté ci-dessus dans Sec. 2.1. Après avoir procédé à l'interaction, les anyons doivent être tressés à leurs positions d'origine.

Plus précisément, pour une échelle à deux jambes, anyons adjacentes de la direction jambe sont deuxième voisins du chemin de fusion (voir la figure 3(b)). Ainsi, il



faut faire une opération de tresse. Pour une échelle à trois jambes, les interactions de jambe sont plus les interactions ont varié, puisque anyons adjacentes sur une jambe sont troisièmes voisins le long du chemin de fusion. Ainsi, les plus proches des interactions de jambe voisin sur une échelle à trois branches ont besoin de deux tresses avant particules sont plus proches voisins sur la voie de fusion [82].

Nous considérons également des modèles avec un terme supplémentaire sonné la charge

$$V_{\text{Coul}}(q) \sim V_{\text{rep}}(q - Q_c)^2, \quad (5)$$

où  $q$  est le nombre de anyons sur un échelon et  $Q_c$  est déterminé par le potentiel chimique implicite. Pour l'échelle de trois jambes à l'étude, ce terme agit par paires entre tous les trois paires possibles de particules qui peuvent exister sur les trois site échelon. En supposant une énergie de charge qui est beaucoup plus grande par rapport à l'énergie d'échange, nous pouvons considérer la limite  $V_{\text{rep}} \rightarrow \infty$ . Dans cette limite, nous pouvons limiter nos calculs à seulement deux valeurs de l'occupation sur le barreau,  $n$  et  $n + 1$ , avec  $n$  allant de 0 à  $W - 1$ . Cela réduit l'espace de Hilbert et nous permet d'effectuer des simulations de plus grandes échelles ainsi.

### 2.3 Les diagrammes de phase d'échelles dopées

Quand il y a deux trous sur un échelon, à la fois le  $U(1)$  et charges topologiques sont trivialement zéro. Lorsque la ligne est occupée par deux particules  $\tau$ , le net  $U(1)$  charge est 2, mais la charge topologique peut être soit  $\mathbf{1}$  ou  $\tau$ , donnant lieu à deux états quantiques différents  $|2, \tau\rangle$  (nommé "lourds  $\tau$ ") et  $|2, \mathbf{1}\rangle$  (nommé "trou lourd" - un échelon vide étant un "léger trou"). Dans le cas où il y a un seul  $\tau$  sur l'échelon, il peut être soit sur le haut ou sur le bas de la jambe avec des charges désignées comme  $(1^U, \tau)$  et  $(1^L, \tau)$  respectivement. Les états quantiques correspondants sont respectivement  $|1^U, \tau\rangle$  et  $|1^L, \tau\rangle$ . Les liants et anti-collage états  $|1^\pm, \tau\rangle$  (nommé "léger  $\tau$ ") sont formés par des superpositions linéaires des configurations avec des charges  $(1^U, \tau)$  et  $(1^L, \tau)$ .

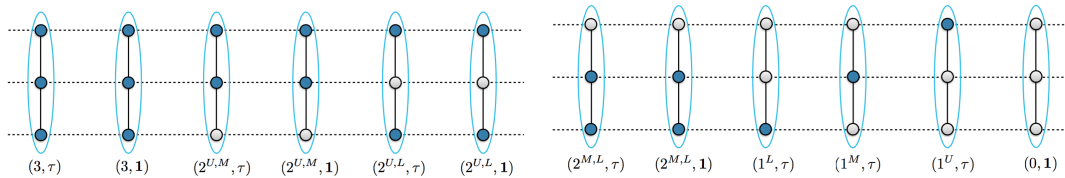


Figure 4: Les différents résultats possibles fusion pour une échelle à trois jambes dopé. Les cercles bleus représentent  $\tau$ 's tandis que les cercles blancs représentent des sites vacants. Les premières labels dans la parenthèse signifient le charge  $U(1)$ , correspondant au nombre de  $\tau$  présent sur chaque échelon et le second se réfère à leur résultat de la fusion. Les exposants  $U, M, L$  référer aux positions de la  $\tau$  sur les différentes branches (supérieur, moyen, bas) de l'échelle.

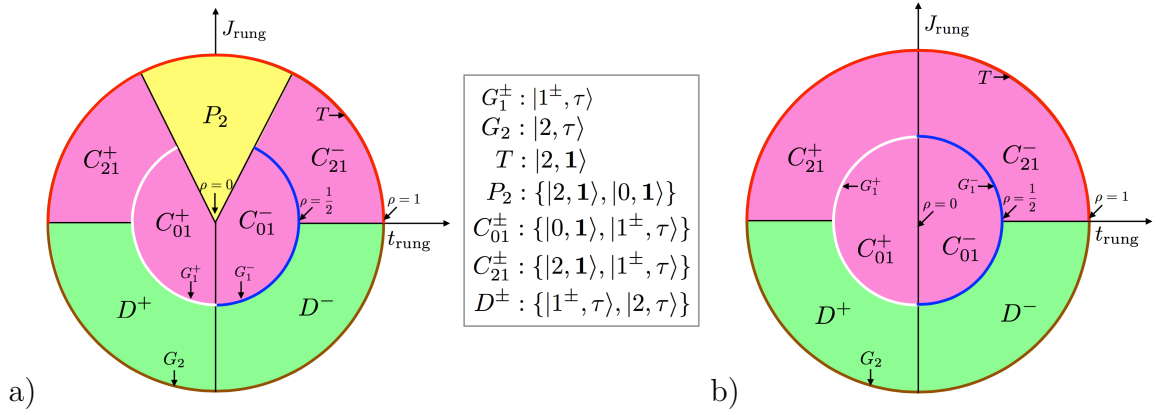


Figure 5: Diagrammes de phase pour l'échelle à deux pieds dans la limite forte de couplage échelon. a) est sans terme échelon de charge et b) avec un grand degré de charge terme  $V_{rmp}$ . Ici, le rayon désigne la densité de anyons. Selon le remplissage et les accouplements plusieurs phases peuvent être distinguées: une phase totalement entaillé (T), des modèles de chaîne d'or efficaces (G), à compter  $t - J$  chaînes (C), les phases appariées (P), et une phase avec deux types différents de  $t$  anyons (D). La légende indique que les Etats échelons sont pertinents dans les différentes phases. Voir le texte pour plus de détails.

Pour une échelle à trois jambes, beaucoup plus d'états sont possibles, comme le montre la figure 4. Plusieurs états quantiques sont obtenus comme des superpositions linéaires des Etats avec le même  $U(1)$  et les frais anyonic et sont étiquetés comme  $|1^\pm, \tau\rangle, |1^0, \tau\rangle, |2^\pm, \tau\rangle, |2^\pm, \mathbf{1}\rangle, |3, \tau\rangle$  (nommé "super-lourd"  $\tau$ ) et  $|3, \mathbf{1}\rangle$  (nommé "super-lourd" trou).

Nous passons sur les petits raccords  $t_{leg}$  et  $J_{leg}$  entre les barreaux fortement couplés de telle sorte que  $|t_{leg}|, |J_{leg}| \ll |t_{rung}|, |J_{rung}|$ , afin d'assurer qu'il n'y a pas de transition à l'état excité des barreaux isolés. Figures 5 et 6 résument les diagrammes de phase pour les échelles deux et trois jambes.

Selon les états de faible énergie sur chaque échelon, nous trouvons six différents types de phases (de dérivation des couplages efficaces pour toutes les phases peuvent être trouvées dans l'annexe):

- phases Totally éclateurs (T) apparaissent quand il y a exactement deux (pour  $J_{rung} > 0$ ) ou trois (pour  $J_{rung} < 0$ ) anyons par échelon qui fusionnent dans le canal trivial.
- des chaînes d'or efficaces ( $G^\pm$ ) quand il y a exactement  $n \tau$  anyons sur chaque échelon qui fusionnent en un total  $\tau$ . Une option  $\pm$  superscript indique si les particules sont dans une liaison (+) ou antiliante (-) Etat sur un échelon.
- phases paires (P) où deux anyons sur un fusible échelon dans le canal trivial, formant des bosons hard-core.
- Effective  $t - J$  chaînes ( $C_{nm}^\pm$ ) consistant en un trou efficace qui découle de  $n$  anyons sur une fusion échelon dans le canal trivial et un  $\tau$  anyon efficace

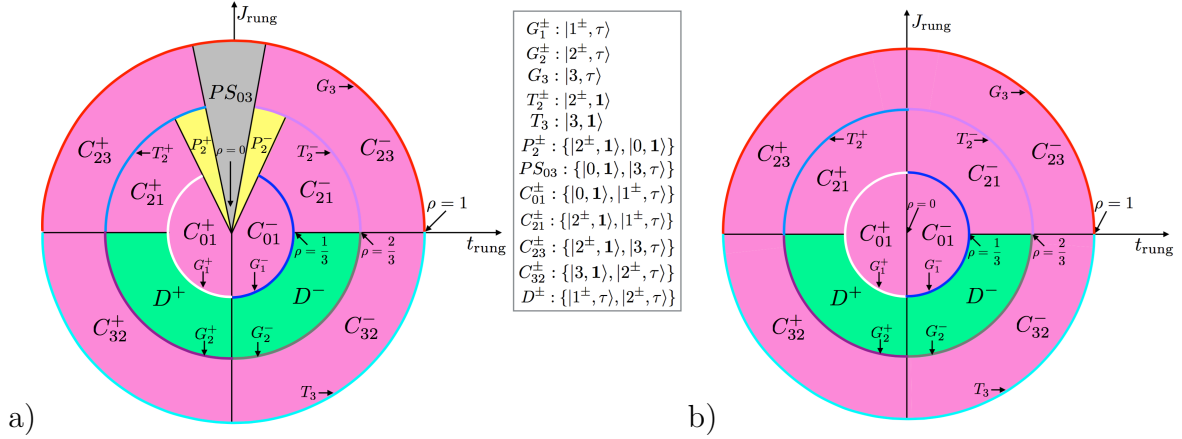


Figure 6: Diagrammes de phase pour l'échelle de trois jambe dans la limite forte de couplage échelon. a) est sans terme échelon de charge et b) avec un grand degré de charge terme  $V_{rmlrep}$ . Ici, le rayon désigne la densité de anyons. Selon le remplissage et le couplage de plusieurs phases peuvent être distinguées: une phase totalement entaillé (T), des modèles de chaîne d'or efficaces (G), à compter  $t - J$  chaînes (C), les phases paires (P), la phase phases séparées (PS) et une phase avec deux types différents de  $\tau$  anyons (D). La légende indique que les Etats échelons sont pertinents dans les différentes phases. Voir le texte pour plus de détails.

découlant à partir de  $m$  anyons fusion dans le canal  $\tau$ . Le  $\pm$  superscript indique si les particules sur un échelon sont dans un état de liaison ou antiliante.

- modèles efficaces consistant en deux saveurs de  $\tau$  anyons ( $D_{mn}^\pm$ ) qui sont formées par la fusion de  $m$  et  $n$  anyons sur un échelon respectivement. Encore une fois le  $\pm$  superscript indique si les particules sur un échelon sont dans un état de liaison ou antiliante.
- Une phase séparée région  $PS_{03}$  provient d'un  $t$  effective -  $J$  chaîne avec l'attraction dominante entre les super-lourds  $\tau$  anyons efficaces.

L'effet d'un grand échelon de charge d'énergie  $V_{rep}$  est de supprimer l'appariement et la séparation de phase dans deux jambes et trois jambes échelles. Les autres phases sont inchangées lors de l'ajout ce terme. Nous allons donc utiliser  $V_{rep} = \infty$  pour réduire l'espace de Hilbert dimension lors des enquêtes numériquement les dernières phases.

## 2.4 Séparation spin-charge dans $t$ - $J$ modèles

De la cartographie d'une échelle dopée à un 1D  $t$  effective -  $J$  chaîne nous nous attendons à son spectre à fractionalize en charge et anyon (également appelé "tour") degrés de liberté. Dans la limite  $J = 0$  d'un  $t$  anyonic -  $J$  chaîne les anyons itinérants se comportent comme HCB qui peuvent être mappés sur un système de fermions sans spin. Ajout d'un flux externe dans l'anneau, le spectre de HCB est

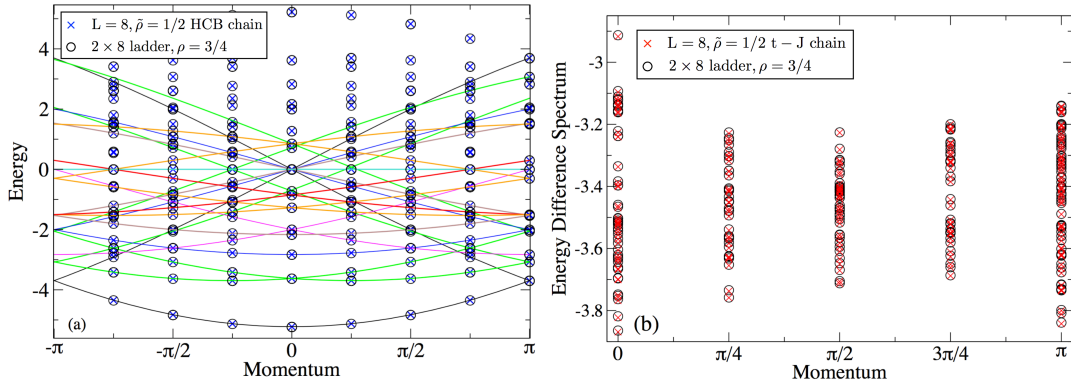


Figure 7: (a) Spectre de charge à  $J_{\text{rung}} = t_{\text{rung}} = 1000, t_{\text{leg}} = 1, J_{\text{leg}} = 0, V_{\text{rep}} = \infty$ . Les lignes pleines représentent le spectre de HCB (avec un flux externe) donnée par l'équation (6). Différentes couleurs correspondant aux différentes branches de charge (Marqué par  $p$  dans l'équation (6)) Les cercles noirs représentent le spectre d'un échelle  $2 \times 8$  avec  $\rho = 3/4$ . Les croix bleues correspondent au spectre de la chaîne efficace pour  $L = 8, \tilde{\rho} = 1/2$  (voir l'équation (7)) (b) La comparaison des spectres de différence d'énergie, après soustraction de la contribution de charge à l'énergie de chaque Etat, d'un échelle  $2 \times 8, \rho = 3/4$  avec celle de l'efficacité  $t - J$  chaîne  $L = 8, \tilde{\rho} = 1/2$ . Les accouplements sur l'échelle sont  $J_{\text{rung}} = t_{\text{rung}} = 1000, t_{\text{leg}} = 1, V_{\text{rep}} = \infty, J_{\text{leg}} = 1$ .

donc donné par paraboles chargé d'excitation,

$$E_{\text{HCB}}(p, \phi_{\text{ext}}) = -2t \sum_{j(p)} \cos \left[ \frac{2\pi}{L} \left( j + \frac{1}{2} \right) + \frac{\phi_{\text{ext}}}{L} \right], \quad (6)$$

où  $\{j(p)\}$  est un ensemble de nombres entiers (marqué par l'indice de branche  $p$ ) qui déterminent les moments continu, donnée par  $K = \frac{2\pi}{L} \sum_{j(p)} (j + \frac{1}{2}) + \tilde{\rho} \phi_{\text{ext}}$ ,  $\tilde{\rho}$  étant la densité des particules dans le système. Dans le  $\phi = 0$  *limit* J nous devons être prudents car les étiquettes d'arbres de fusion font les anyons distinguables. Ainsi, en l'absence d'interactions magnétiques, les niveaux d'énergie présentent un degré élevé de dégénérescence qui se pose en raison de la construction dans les non abélien nature des anyons de Fibonacci. Déplacement d'un anyon à travers la frontière se traduit de manière cyclique les étiquettes des arbres de fusion. Toutes les particules  $N$  doivent être traduits sur la limite pour être en mesure d'avoir l'étiquetage d'origine. Cela entraîne un décalage de phase de  $\phi_n = 2\pi n/N$ ,  $n$  étant un nombre entier. Le spectre de la chaîne anyonic de charge peut alors être décrit comme une union de tous les spectres de HCB pour toutes les valeurs discrètes de  $\phi_n$ , sans flux externe:

$$E_{\text{charge}}^{p,n} = E_{\text{HCB}}(p, \phi_n). \quad (7)$$

Les états sont marqués par leur mouvement totale  $K_{p,n} = KP + 2\pi \frac{n}{N}$ . Nos résultats numériques montrent que, comme prévu, le spectre de l'échelle de charge correspond exactement à celle de la chaîne efficace.

Nous passons ensuite sur un petit  $J_{\text{jambe}}$  et suivre adiabatique la séparation des paraboles de charge. Nous voyons que les interactions magnétiques soulèvent la

dégénérescence des états avec une énergie proportionnelle à répandre  $LJ_{\text{jambe}}$ . Ceci est cohérent avec le comportement de l'efficacité  $t - J$  chaîne présentant “ séparation spin-charge ”<sup>a</sup>: dans les références. [77, 78] nous avons montré que le spectre d'excitation complète d'une chaîne anyon itinérante est composée de deux contributions indépendantes provenant des degrés de charge de la liberté et les degrés de Anyon de liberté qui sont donnés par un *pressé* (non dopé) chaîne anyon de longueur  $L_a = \tilde{\rho}L$  où  $\tilde{\rho}$  est la densité de anyon sur  $l$  Site  $t - J$  chaîne de anyons.

Nous effectuons actuellement une comparaison quantitative des spectres de l'échelle et de son correspondant anyonic chaîne anyonic efficace. Comme le match de spectres de charge, nous nous concentrons sur le spectre de différence d'énergie (EDS) obtenue en soustrayant la (supposée) composant la charge d'excitation à chaque état. Par construction, l'EDS effectue ensuite les informations sur les degrés de liberté de Anyon. Les résultats numériques pour l'EDS sur un échelle  $2 \times 8$  avec la densité de anyon  $\rho = 3/4$  pour intermédiaire  $J_{\text{leg}} = t_{\text{leg}}$  sont présentés dans la figure 7(b). Nous trouvons l'EDS de l'échelle et de la chaîne efficace pour être en parfait accord. La cartographie parfaite des deux-jambe échelle physique à la physique de la chaîne implique donc carrément que le concept de spin-accusation fractionnalisation est pas strictement 1D mais applique également aux deux-jambe échelle anyonic, contrairement à l'analogie de l'échelle électronique.

## 2.5 Modèle de anyons de Fibonacci lourdes et légères

Nous discutons maintenant d'un nouveau modèle qui apparaît pour couplages rung ferromagnétique (FM) forts sur une échelle de deux chaînes avec  $\rho > 1/2$  et un grand  $V_{\text{rep}}$ . Un modèle efficace similaire décrit également l'échelle de trois chaînes avec accouplements FM et  $1/3 < \rho < 2/3$ . Avec les couplages rung qui sont FM, la fusion de deux  $\tau$ 's résultats dans un  $\tau$ . La fusion d'un  $\tau$  et un trou se traduit toujours par un  $\tau$ . On obtient ainsi un modèle efficace avec deux *différents* particules Fibonacci, le  $\tau$  *lourde* et  $\tau$  *légère* de distingués par leur  $U(1)$  charge .

Outre les termes magnétiques et potentiels on obtient aussi un processus cinétique échange entre les première voisins  $\tau$  lourde et  $\tau$  légère. Notez que, dans le  $t - J$  chaîne, avec des trous et de l' $\tau$ , le processus de saut déplace la particule entière avec ses charges et des marqueurs de spin. Alors que maintenant, le scénario est très différent, les marqueurs de spin se mélangent les uns aux autres que le lourd  $\tau$  's hop sur des positions de change avec la légère  $\tau$  's .

Le modèle 1D nous permet de résoudre numériquement plus grands systèmes avec de petites corrections de taille finie. Cependant, nous nous limitons au cas  $J_{\text{jambe}} = 0$  quand il n'y a pas d'interactions magnétiques entre  $\tau$  particules le long de la direction de la jambe, mais seulement un petit saut  $t_{\text{leg}}$  opère entre les barreaux depuis déjà cette simple modèle soulève plusieurs questions ouvertes.

**Phase critique à remplissages génériques** Nous examinons ensuite un fini densité  $\tilde{\rho}$  de lourds  $\tau$  de et un remplissage correspondant de  $1 - \tilde{\rho}$  de la légère  $\tau$ . Notez qu'en raison de la symétrie entre l' lourde et légère  $\tau$ , densités  $\tilde{\rho}$  et  $1 - \tilde{\rho}$  sont

équivalents. Nous prévoyons que le même comportement pour toutes les densités, sauf pour la demi-remplie cas  $\tilde{\rho} = 1/2$ , que nous allons examiner séparément dans la section suivante. Pour simplifier, nous choisissons donc  $\tilde{\rho} = 1/4$ , car il nous permet d'effectuer une analyse de taille finie en utilisant trois longueurs différentes de la chaîne  $L = 12, 16, 20$ . Les spectres correspondants sont présentés sur la Fig. 8 (a).

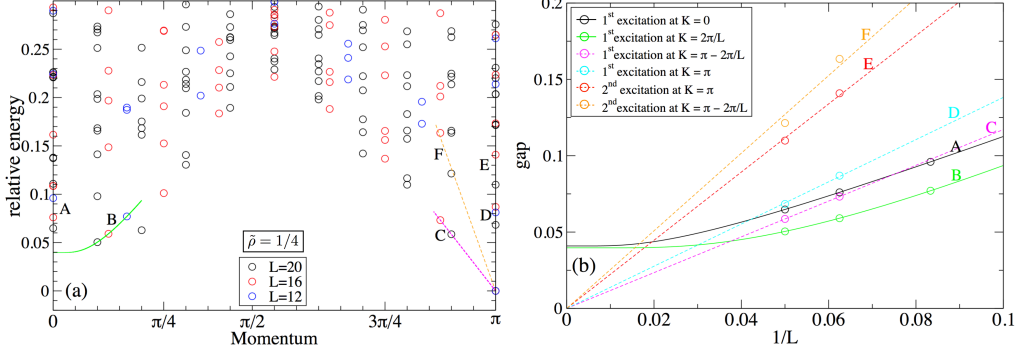


Figure 8: (a) Spectra pour les chaînes efficaces pour lourdes et légères  $\tau$  à  $\tilde{\rho} = 1/4$  avec  $t = 1, J = 0$ . (b) l'analyse Finite-size mise à l'échelle des excitations d'énergie A, B, C, D, E et F. Linéaire (lignes en pointillés) et exponentielles (traits pleins) ajustements sont présentés autour de  $K = \pi$  et  $K = 0$ , respectivement (voir le texte). Les normalisations de la B, C et F lacunes sont également signalées dans (a).

systèmes gapless unidimensionnels sont souvent décrites par un CFT et leurs niveaux d'énergie les plus bas sont alors données par  $E(L) = e_T L + \frac{2\pi v}{L}(-\frac{c}{12} + h_L + h_R)$ , où  $c$  est la charge centrale et  $h_L, h_R$  sont les dimensions de la mise à l'échelle des champs 'primaires' de la CFT. Le (thermodynamique) sol énergie de l'état par site  $E_T$  et la vitesse  $v$  sont des constantes non universelles. Le fini état fondamental de la taille de l'énergie  $E_0(L)$  correspond à  $h_L = h_R = 0$ .

Pour tester la prédiction de CFT, nous avons effectué une analyse de la mise à l'échelle de taille finie des premières lacunes de l'énergie contre  $1/L$ . Comme le montre la figure 8(b), nous observons que les lacunes autour de  $K = \pi$  montrent une échelle linéaire avec  $1/L$ , ce qui suggère des modes de gapless. Ce comportement est, en principe, compatible avec la mise à l'échelle de CFT. Le spectre d'énergie d'environ  $K = 0$  montre un comportement différent. Comme le montre la figure 8(b), les lacunes de taille finie des premiers états excités à l'élan  $K = 0$  et  $K = 2\pi/L$  pourrait être monté en  $\Delta(L) = \Delta(\infty) + C/L \exp(-L/\xi)$ , où  $\Delta(\infty) \simeq 0,04$  est un écart d'énergie finie et  $\xi > 10$  est une longueur de corrélation. Cela suggère que, à la densité  $\tilde{\rho} = 1/4$ , le spectre d'énergie indique à la fois un mode sans intervalle avec une dispersion linéaire, décrit par une FT, et les modes de gaps supplémentaires.

### Possible phase gappé topologique à $\tilde{\rho} = 1/2$

Ensuite, nous considérons la densité  $\tilde{\rho} = 1/2$  où il y a un nombre égal de lourd et léger  $\tau$ . Nous avons simulé des chaînes avec des longueurs  $L = 14, 16, 18, \text{ et } 20$  et

de montrer ces spectres dans la figure 9(a), révélant excitations de basse énergie à impulsions  $K = 0$  et  $K = \pi$ . Exécution d'une analyse finie taille de mise à l'échelle sur les états de faible altitude en utilisant système tailles  $L$  allant de 14 à 20 des sites, comme le montre la figure 9(b) nous constatons qu'une forme exponentielle comme  $\Delta(L) = \Delta(\infty) + C/L \exp(-L/\xi)$  fournit raisonnablement bons ajustements des données. Ces ajustements suggèrent que trois des gaps extrapoler à zéro et la prochaine excitations de l'énergie à extrapolent une valeur finie  $\Delta(\infty) \sim 0.05$ . Notez toutefois que les longueurs de corrélation extraites des ajustements sont de l'ordre de la taille du système de sorte que les extrapolations sont à prendre avec précaution. Cependant, si elle est correcte, nos résultats semblent indiquer une phase gappé topologique avec un état fondamental dégénéré quatre fois, bien que dimérisation ne soit pas exclue (puisque l'état fondamental sont les deux moments  $0$  et  $\pi$ ). Dans tous les cas, nous pensons que la moitié de remplissage est un cas particulier et très différent des autres régimes de densité que nous avons estimées. Ce comportement est aussi sensiblement différent des chaînes d'or qui sont connus pour être sans gap pour FM et AFM couplages de la jambe.

### 3 Fermions dans des réseaux optiques

#### 3.1 Modèle et méthode

Le modèle Hubbard est l'un des modèles les plus simples qui capture efficacement les effets à plusieurs corps pour fermions. L'état fondamental est déterminée par la concurrence entre plusieurs échelles d'énergie différentes, à savoir l'énergie cinétique qui délocalise les particules et le potentiel sur site qui peuvent ou pas favoriser doubles sites du réseau occupés, selon qu'elle est attractive ou répulsive.

Dans ce travail, nous considérons un modèle de continuum qui peut être écrit dans l'espace continu en fonction des opérateurs de champ  $\hat{\psi}_\sigma^\dagger(x)$  qui crée un fermion de

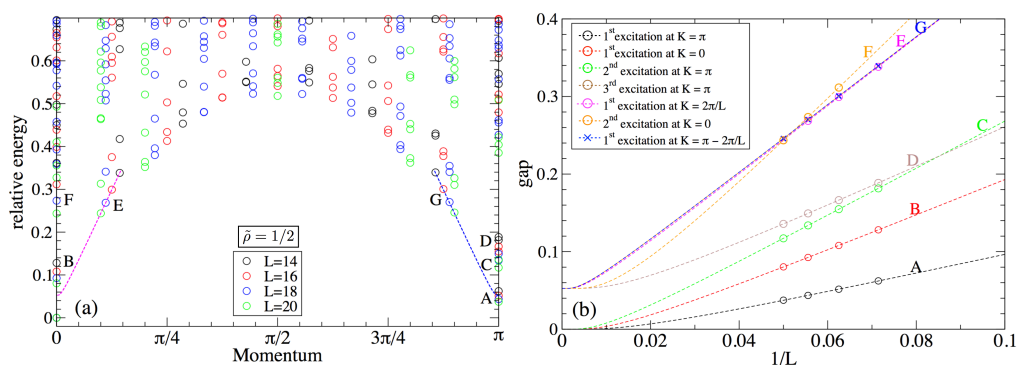


Figure 9: (a) Spectra des chaînes lourdes et légères de  $\tau$  de tailles différentes à  $\tilde{\rho} = 1/2$  et  $t = 1$ ,  $J = 0$ . (b) l'analyse Finite-size échelle des lacunes de l'énergie (a) vs  $1/L$  (voir le texte). Les battitures des écarts E et G sont également présentés en (a).

masse  $m$  et de spin  $\sigma$  à la position  $x$ . L'opérateur d'annihilation correspondant est  $\hat{\psi}_\sigma(x)$ . Le hamiltonien d'un système 1D de taille  $L$  peut alors être écrite comme:

$$\begin{aligned} \mathcal{H} = & \sum_{\sigma} \int_0^L dx \hat{\psi}_{\sigma}^{\dagger}(x) \left[ -\frac{\hbar^2}{2m} \frac{d^2}{dx^2} + V(x) \right] \hat{\psi}_{\sigma}(x) \\ & + \frac{g}{2} \sum_{\sigma\sigma'} \int_0^L dx \hat{\psi}_{\sigma}^{\dagger}(x) \hat{\psi}_{\sigma'}^{\dagger}(x) \hat{\psi}_{\sigma'}(x) \hat{\psi}_{\sigma}(x), \end{aligned} \quad (8)$$

où le premier terme est l'énergie cinétique et la seconde est l'énergie potentielle externe du site. Le terme de quatre opérateurs est l'interaction de contact caractérisé par la force d'interaction  $g$ , qui est obtenu à partir de la longueur de diffusion de une seule particule [154]. Le potentiel externe est la somme du potentiel créé par les poutres en treillis qui interfèrent et le piège harmonique utilisée pour confiner le système. Elle est donnée par  $V(x) = V_0 \cos^2(kx) + \frac{1}{2}m\omega^2 x^2$ , où  $V_0$  est la profondeur du réseau,  $k = \frac{2\pi}{\lambda}$  est le vecteur d'onde du faisceau laser et  $\omega$  est la fréquence du piège harmonique. L'échelle de l'énergie naturelle dans le problème est l'énergie de recul défini comme  $E_r = \frac{\hbar^2 k^2}{2m}$ . Nos résultats seront présentés en unités de  $E_r$ .

Afin de simuler numériquement le modèle continu est décrit dans l'équation (8) est représenté par une application de l'espace discret en considérant une cellule unité de longueur  $a$ , qui est discrétisée avec  $N_{\text{discr}} = 16$  points de la grille. Cela conduit à un espacement de grille de longueur  $d = a/N_{\text{discr}}$ . Pour le réseau optique le choix naturel pour la cellule de l'unité est d'être un minimum de potentiel externe de réseau optique, à savoir  $a = \lambda/2 = \pi/k$ . Le hamiltonien de continuum est ensuite mappé à un modèle de réseau Hubbard écrit en termes d'opérateurs de création et d'annihilation  $c_{i,\sigma}^{\dagger}$  et  $c_{i,\sigma}$ , respectivement,  $i$  étant l'index du site de la grille et  $\sigma$  est le spin de l'fermion. Le hamiltonien est écrit comme

$$\begin{aligned} \mathcal{H} = & -J(d) \sum_{\sigma} \sum_{\langle ij \rangle} c_{i,\sigma}^{\dagger} c_{j,\sigma} + \text{h.c.} \\ & + \sum_{\sigma\sigma'} \sum_i \frac{U(d)}{2} c_{i,\sigma}^{\dagger} c_{i,\sigma'}^{\dagger} c_{i,\sigma'} c_{i,\sigma} + \sum_{\sigma} \sum_i \epsilon_i(d) n_{i\sigma}, \end{aligned} \quad (9)$$

où le terme cinétique devient le saut d'amplitude  $J(d) = (\hbar^2/2m)/d^2$  entre les sites adjacents de la grille  $i$  et  $j$ , l'interaction de contact se transforme en un sur place interaction  $U(j) = g/j$  et le potentiel externe est réalisé en tant que potentiel chimique site dépendant  $\epsilon_i(d) = V(d/2 + i) + 2(\hbar^2/2m)/d^2$ .

Le choix de la discrétisation en espace réel permet de simuler le modèle de continuum dans le réseau très peu profonde et les régimes de treillis profonds sans la nécessité de changer base au cours de l'évolution temporelle du processus de chargement.

Analogue à l'étude précédente de systèmes bosoniques [123] nous simulons un modèle de réseau optique fermionique numériquement avec la méthode de la matrice de densité de groupe de renormalisation (DMRG) [155, 156]. L'approche DMRG standard a des problèmes de convergence graves pour les grands réseaux dilués qui découlent de la discrétisation en espace réel nécessaire pour représenter



le système de continuum pendant le chargement du réseau. Pour surmonter ces problèmes, nous utilisons l’algorithme de DMRG multigrille [142] qui conduit à une convergence rapide.

Evolution temporelle dans le cadre MPS est effectuée en utilisant les variantes dépendant du temps de DMRG [134, 135, 159], qui a divisé non-avancement termes de l’opérateur d’évolution temporelle unitaire via une décomposition deuxième ordre Suzuki-Trotter sur un temps petite étape  $dt = 0,01 \hbar/E_r$ . Dans nos simulations ceci est réalisé en atteignant une dimension de la liaison entre  $M = 400$  et  $M = 600$ . Les simulations ont été réalisées en utilisant le code ALPS MPS [139–141] sur le Mönch Cluster de l’ETH Zurich.

Notez que nos simulations ne souffrent pas des effets de bord qui peuvent survenir en raison du choix des conditions aux limites ouvertes. La raison en est que la présence d’un potentiel de piégeage et notre choix de remplissage des particules garantit que l’étendue du système avec une valeur non nulle densité locale est effectivement réduite par rapport à  $L$ . Ainsi, le système reste confiné bien en deçà des limites. Cette mesure réduit de la longueur réelle sert une taille de système efficace et est appelé  $L_{\text{eff}}$  dans la section suivante.

### 3.2 Protocoles et observables de chargement réseau optique

Pour simuler les effets du processus de réseau de chargement optique, nous utilisons l’optimisation de l’état fondamental pour préparer la fonction d’onde initiale dans l’état  $|\psi_{\text{init}}\rangle$ , où le potentiel de réseau est éteint ie  $V_0(t = 0) = v_i = 0$ . Cet état est alors temps évolué avec un hamiltonien dépendant du temps de telle sorte que, à tout moment  $t$  au cours de l’évolution de l’état est donné par  $|\psi(t)\rangle$  avec un temps de réseau dépendant de potentiel  $V_0(t)$ . Dans nos simulations, nous utilisons une rampe qui interpole linéairement entre la profondeur initiale  $v_i$  et profondeur finale  $v_F$  du réseau optique:  $V_0(t) = v_i + (v_F - v_i) \frac{t}{t_R}$ , où  $t_R$  est temps total de rampe. A la fin du chargement du réseau du modèle devrait avoir atteint l’état cible avec treillis potentiel  $V_0(t_R) = v_F (= 8 E_r)$ . L’état final  $|\psi_{\text{final}}\rangle \equiv |\psi(t = t_R)\rangle$  est comparé à la cible état  $|\psi_{\text{cible}}\rangle$  pour quantifier les défauts. Nous répétons ce processus pour plusieurs états initiaux, des protocoles de chargement différents, ainsi que de multiples temps de rampe.

Pour quantifier et comprendre l’origine des défauts, nous pouvons répondre à plusieurs observables tant au cours de l’évolution de la fonction d’onde  $|\psi(t)\rangle$  et à l’état final  $|\psi_{\text{final}}\rangle$ . Dans notre étude, nous examinons seulement observables à la fin du temps de rampe. D’intérêt particulier sont l’excès d’énergie par particule  $q|_{(t=t_R)} = (E[|\psi_{\text{final}}\rangle] - E[|\psi_{\text{target}}\rangle])/N$ , et la fidélité à l’égard de l’état fondamental de le hamiltonien instantanée, qui à la fin du chargement est donnée par  $f|_{(t=t_R)} = |\langle \psi_{\text{target}} | \psi_{\text{final}} \rangle|$ . Nous étudions également l’évolution temporelle de la densité locale  $n_\sigma(x, t) = \langle \psi(t) | \hat{n}_\sigma(x) | \psi(t) \rangle$ . Dans les résultats qui suivent, nous allons rendre

compte que la densité totale par grille de la  $n(x) = p_{\uparrow}(x) + p_{\downarrow}(x)$  depuis pas d'effets de magnétisation locales ont été observées. En outre, on calcule la densité locale intégrée sur une cellule unité de réseau optique  $\bar{n}(i) = \sum_{k=1}^{N_{\text{discr}}} n(x) \Big|_{x=(i+k-1)a}$  ce qui simplifie l'analyse en termes de modèle de réseau efficace, par exemple on attend  $\bar{n}(i) = 1$  dans le régime Mott et  $\bar{n}(i) = 2$  dans le régime de la bande isolante.

Notez que le calendrier de chargement de réseau ci-dessus modulant linéairement le potentiel du réseau à chaque pas de temps, en gardant tous les autres paramètres fixes au cours de l'évolution dans le temps. Dans nos simulations, comme nous allons l'expliquer dans les sections à venir, nous rencontrons des effets de chauffage pour certains états cibles. Afin de réduire ces effets dans le but ultime étant d'atteindre les basses températures souhaitées dans des expériences, nous proposons un calendrier de chargement amélioré qui modifie dynamiquement un ou plusieurs paramètres de le hamiltonien, en plus de la profondeur du réseau. Cet effet sera incorporé dans le hamiltonien dépendant du temps et sera reflété dans le d'état  $|\psi(t)\rangle$  au cours de l'évolution.

Le premier protocole suit l'approche de [123] pour remodeler dynamiquement le potentiel de piégeage, en modulant linéairement la fréquence de piège  $\omega$ . A partir d'une valeur initial  $\omega_{\text{in}}$ , nous augmentons  $\omega$  linéairement pendant le chargement du réseau pour atteindre la valeur cible souhaitée  $\omega_f$  à la fin du temps de rampe. Au moment de  $t$  la fréquence de piège est donnée par

$$\omega(t) = \omega_{\text{in}} + (\omega_f - \omega_{\text{in}}) \frac{t}{t_R}. \quad (10)$$

Nous effectuons des simulations avec des valeurs différentes de  $\omega_{\text{in}}$  et différents temps de rampe pour étudier le comportement de mise à l'échelle. Nos résultats pour les améliorations observées avec ce protocole sont présentés dans les sections 3.3.3 et 3.3.4.

Sinon, nous pourrions en permanence ajuster la force d'interaction au cours de l'évolution dans le temps, ce qui est généralement un paramètre plus facile à traiter dans des configurations expérimentales par résonance de Feshbach [14, 160]. Depuis la distribution de densité de l'état initial est jugée trop étroite par rapport à l'état cible, donc nous préparons un nouvel ensemble d'états initiaux avec une valeur initiale plus importante de  $g_{\text{in}}$ , qui élargirait le système. La valeur de la force d'interaction au cours du réseau de chargement  $g(t)$  est alors linéairement réduite à sa valeur cible  $g_f$ , selon

$$g(t) = g_{\text{in}} - (g_{\text{in}} - g_f) \frac{t}{t_R}. \quad (11)$$

Ce système est étudié pour l'état cible de la section 3.3.4. Notez que si l'état initial est observé pour avoir une assez large diffusion de la densité locale par rapport à l'état de la cible, on devrait viser à réduire en partant d'une force d'interaction plus faible.

Nous proposons un troisième régime qui est également considéré comme utile pour améliorer la fidélité et la réduction de l'excès de chaleur pendant le chargement

de réseau. Dans cette approche, on combine les deux approches ci-dessus afin d'accorder le piège fréquence *et* la force d'interaction lors réseau loading. Although nous constatons que le premier protocole est en mesure d'atteindre le maximum de fidélité, il pourrait ne pas être le plus facile un à mettre en œuvre dans des expériences. Les deux autres régimes ne sont pas loin derrière dans l'amélioration de la fidélité et plus pratique du point de vue expérimental.

### 3.3 Etude des différents états cibles

#### 3.3.1 État cible métallique

Nous commençons par étudier les états métalliques, où les fermions sont délocalisés sur le réseau. Un tel état est observé pour un petit nombre de particules  $N < L_{\text{eff}}$  et avec une faible interaction de contact. Si l'interaction répulsive est pas trop fort par rapport à l'effet tunnel entre les cellules unitaires, les fermions sont libres de monter à celui voisin gagner de l'énergie cinétique. Il en résulte une distribution de densité continue sur toute la longueur du système tel que représenté sur la Fig. 10 pour l'état initial et la cible.

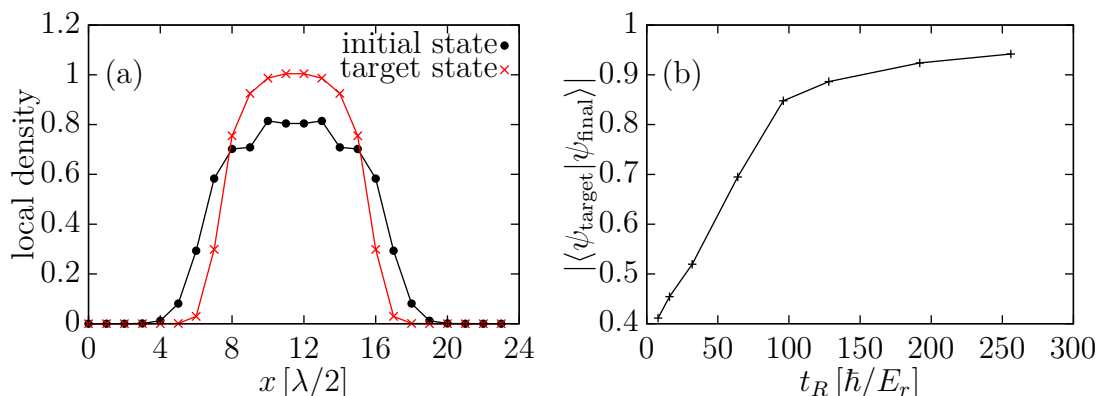


Figure 10: (a) Répartition de la densité locale de l'état initial ( $v_i = 0$ ) et de l'état cible métallique ( $V_f = V_0 = 8E_r$ ) intégrées sur chaque cellule de l'unité (b) de mise à l'échelle de la fidélité avec le temps de la rampe.  $L = 24, N = 8$  particules *i.e.*  $N_{\uparrow} = N_{\downarrow} = 4, g = 0.2 E_r \lambda/2, \omega = 0.1 (\hbar/E_r)^{-1}$ .

Nous permettons à l'état initial d'évoluer dans le temps en augmentant linéairement le potentiel du réseau de telle sorte que, à la fin du temps de rampe du système a la pleine puissance du potentiel du réseau *i.e.*  $V_0(t = t_R) = V_f$ . Nous calculons l'excès de chaleur et la fidélité pour un tel état en utilisant différents temps de rampe approchant la limite de chargement adiabatique du réseau, et nous ne voyons pas d'effets de chauffage graves. Figure. 10 (b) montre la fidélité en fonction du temps de rampe. Nos simulations montrent qu'il est possible d'atteindre un état final assez proche de l'état cible juste en étant plus lente dans le chargement du réseau. Pour  $t_R = 256 \hbar/E_r$ , nous observons une fidélité de plus de 94% et

réduire le chauffage par un facteur de 10 par rapport à la réduction des temps de rampe  $t_R = 16 \hbar/E_r$ .

### 3.3.2 Mott isolant avec un isolant de bande de coeur

Nous examinons ensuite un état cible qui présente la co-existence de deux phases: un isolateur Mott avec une masse qui est la bande isolante. Ces deux phases sont incompressibles et caractérisés par des valeurs particulières de la densité locale moyenne par cellule unitaire. La phase Mott a une particule par site du réseau, tandis que l'isolant de bande a une occupation de deux particules par site, donc nous considérons une chaîne avec un nombre de particules  $N$  près (mais moins) deux fois le taille de système efficace  $L_{\text{eff}}$ .

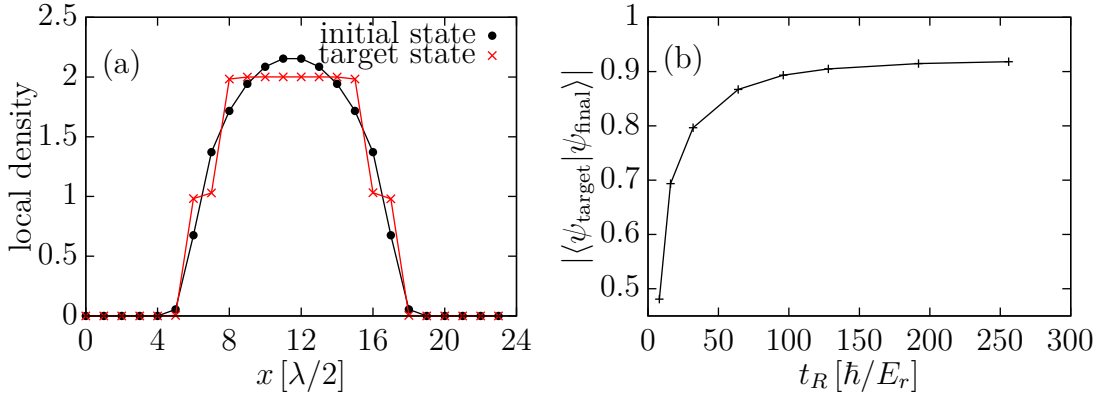


Figure 11: Répartition de la densité locale de l'état initial ( $V_i = 0$ ) et l'isolateur Mott avec en vrac mauvaises cibles d'isolant de l'état ( $V_f = V_0 = 8E_r$ ) intégré sur chaque cellule de l'unité.  $L = 24$ ,  $N = 20$  particules ( $N_{\uparrow} = N_{\downarrow} = 10$ ),  $g = E_r \lambda/2$ ,  $\omega = 0.3 (\hbar/E_r)^{-1}$ .

Les distributions de densité locale intégrée pour les états initiaux et de la cible sont représentées sur la Fig. 11 (a). Dans le but d'indiquer la majeure partie du système présente une phase bande isolante, tandis que les bords sont dans la phase d'isolateur Mott.

Notez que les distributions de densité de l'état initial et l'état cible se ressemblent de deux façons importantes, à savoir la propagation spatiale du système ainsi que la valeur de crête et sa position dans le profil de densité. Ceci est la principale raison pour laquelle nous constatons qu'un tel système ne comporte pas trop de chauffage si le chargement du réseau se fait avec des temps de rampe qui sont assez longues.

La fidélité en fonction de la durée de la rampe sont présentés sur la Fig. 11 (b). La fidélité croît assez rapidement au départ lors de l'augmentation du temps de chargement mais a tendance à saturer plus ou moins environ 90%. Pour la plus courte durée de la rampe, la distribution finale de densité est loin de celle de l'état cible. La proximité de l'augmentation de l'état cible rapidement pour les premiers

temps de rampe que nous avons estimé en raison de l'évolution rapide du profil de densité pendant le chargement. Par la suite, l'état final correspond à l'état cible à un bon degré et ralentir encore le chargement apporte seulement de légères modifications dans le profil de densité. Ceci est ce qui conduit à une saturation dans l'échelle de la fidélité.

Notez que bien que cet état de cible est intrinsèquement incompressible, par opposition à l'état métallique étudié dans la section 3.3.1, il ne souffre pas encore des effets de chauffage indésirables. Ceci est une manifestation du fait que la répartition de la densité de l'état initial qui est en correspondance qualitative proche en termes de  $L_{\text{eff}}$  et la valeur de crête, ce qui permet une redistribution appropriée des particules au cours de la rampe pour atteindre la cible souhaitée état.

### 3.3.3 Mott isolant état cible

Notre prochain choix de l'état cible est un état isolant de Mott pur avec une unité densité locale moyenne par cellule unitaire sur toute la longueur effective du système. Le profil de densité locale de l'état initial et l'état cible sont présentés sur la Fig. 12 (a).

Nous répétons le protocole suivi dans les sections précédentes, où le potentiel de réseau optique a été linéairement intensifié et trouvent que cette approche n'échelle avec le temps de rampe. Nous notons que, même pour la plus longue durée de la rampe que nous avons considéré ( $t_R = 256 \hbar/E_r$ ), le maximum de fidélité que nous sommes en mesure d'atteindre est seulement d'environ 15% et la diminution de l'excès de chaleur ne sont pas significative soit. Bien en augmentant encore le temps de rampe, nous devrions être en mesure d'obtenir une meilleure fidélité, mais peut-être pas une augmentation impressionnante. La lente augmentation de la fidélité avec le temps de la rampe est une indication claire que la simulation de la charge du réseau avec un temps de rampe finie est pas la cause principale de chauffage dans le système.

Montée en puissance de la profondeur de réseau pour un réseau homogène (sans le piège harmonique) donne une haute fidélité qui monte bien avec le temps de rampe comme indiqué sur la Fig. 12 (b). Nous analysons le calendrier des treillis de chargement en traçant le profil de densité lors de la montée en puissance. Fig. 13 (a), nous montrons le profil de densité au cours de l'évolution temporelle de l'état à certaines fractions du temps total de rampe  $t_R = 256 \hbar/E_r$ . Cette parcelle dévoile qu'à partir de l'état initial du processus de chargement ne sont pas en mesure de distribuer des particules de la manière souhaitée, écartant ainsi de manière significative de l'état cible. Comme il ressort de la figure, l'évolution tend à maintenir les particules à proximité du centre du piège et ce pic reste jusqu'à la fin de la durée de rampe. Cette densité locale accrue dans le centre-piège est un énorme écart par rapport à l'état Mott cible qui devrait montrer un remplissage de l'unité dans tout le système.

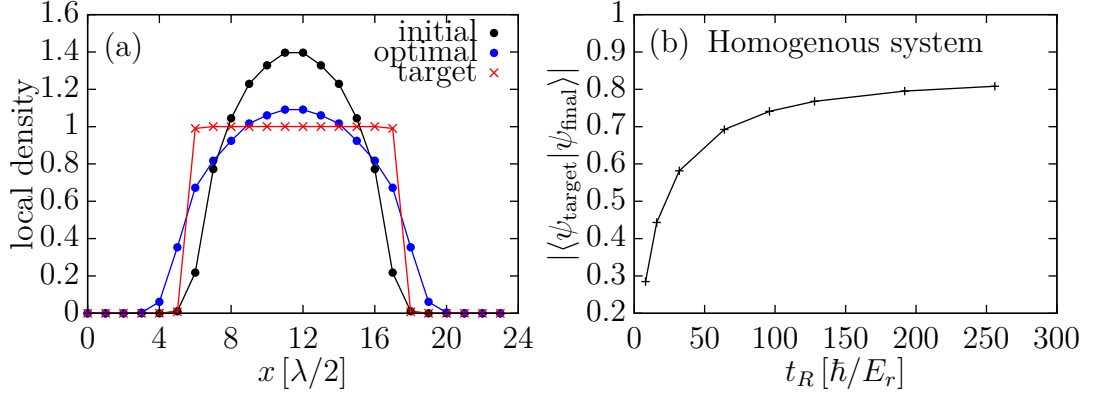


Figure 12: (a) Répartition de la densité locale de l'état initial ( $V_i = 0$ ) et les cibles d'isolant état Mott ( $V_f = V_0 = 8E_r$ ) intégrées sur chaque cellule de l'unité. La courbe bleue montre la répartition de la densité de l'état optimal lors d'odulation linéaire de la fréquence de piège  $\omega$ .  $N = 12$  particules ( $N_\uparrow = N_\downarrow = 6$ ),  $g = 2 E_r \lambda/2$ ,  $\omega_f = 0.25 (\hbar/E_r)^{-1}$ . (b) Mise à l'échelle de la fidélité pour le système homogène avec les mêmes paramètres, à l'exception  $\omega = 0$ .

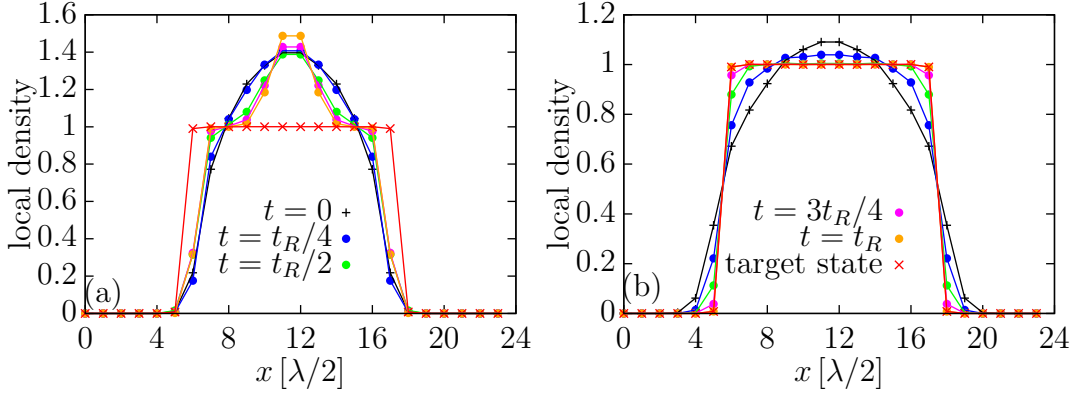


Figure 13: Evolution du profil de densité lors de la montée en puissance pour le temps de rampe  $t_R = 256 \hbar/E_r$ . (a) sans accorder la fréquence de piège (b) avec une modulation linéaire de la fréquence, pour la valeur optimale de fréquence initiale ( $w_i = 0, 16$ ). Les croix rouges correspondent à l'état de la cible et la légende commune est divisée entre les deux parcelles.

Nous mettons en œuvre le premier protocole de réseau de chargement modifié expliqué dans la section 3.2, modulant linéairement la fréquence de piège. Figure 14 rapporte le balayage de la chaleur et de la fidélité des fréquences différentes de pièges initiaux excédentaires  $\omega_{\text{in}}$ . Les différentes couleurs correspondent à des moments différents de la rampe. Nous assistons à une énorme amélioration de la fidélité et une diminution sensible de l'excès de chaleur, par rapport au cas où la fréquence de piège est fixé lors du chargement du réseau, ce qui correspond à l'extrême droite le point dans les parcelles.

De la forme des courbes, nous pouvons identifier trois comportements d'échelle différents. Pour des valeurs proches de la cible  $\omega_f$  les observables ne montrent pas

de mise à l'échelle appréciable et les résultats sont toujours sensiblement différente de celle de l'état cible fréquence, tandis que de larges pièges initiaux (bas  $\omega_{\text{in}}$ ) atteignent la cible état, mais ce processus échelles lentement. Une *optimale* mise à l'échelle rapide est observée pour la valeur intermédiaire de la fréquence initiale. Nous pouvons identifier un état initial optimal marqué par un maximum dans la courbe de fidélité, qui se trouve être à  $\omega_i = 0,16(\hbar/E_r)^{-1}$  pour notre simulation particulière.

La distribution de la densité locale de l'état initial optimal est représenté par la courbe de courbe bleue dans la figure. 12 (a). La fidélité maximale obtenue pour  $t_R = 256 \hbar/E_r$  est presque 98% et le chauffage est réduit d'un facteur 50.

Fig. 13 (b) nous montrent l'évolution du profil de densité pour cet état optimal pendant le chargement du réseau pour  $t_R = 256 \hbar/E_r$ . Ceci est en contraste frappant avec le tracé de l'évolution de la Fig. 13 (a) où la fréquence de piège est resté constant pendant tout le processus de chargement. De  $t = 0$  à déjà au temps  $t_1 = t_R/4$ , le profil de densité est radicalement changé lorsque la fréquence de piège est modulée qui n'a pas été le cas auparavant. De plus, le temps a évolué à préciser à  $t_1$  est presque un état Mott dans le centre du piège alors qu'il avait une nature plus métallique dans le cas précédent. A la fin du temps de rampe, le profil de densité de l'état final est presque exactement celle de l'état de la cible, ce qui correspond à un chevauchement de près de 98% (comme on peut le voir sur la figure 14. (b)).

### 3.3.4 Mott isolateur avec un noyau métallique

Le dernier état de la cible que nous étudions est l'état isolant de Mott avec une distribution de densité métallique (en continu) dans la masse, comme représenté sur la Fig. 15. A force d'interaction forte et le remplissage d'au moins une particule par taille caractérise cet état.

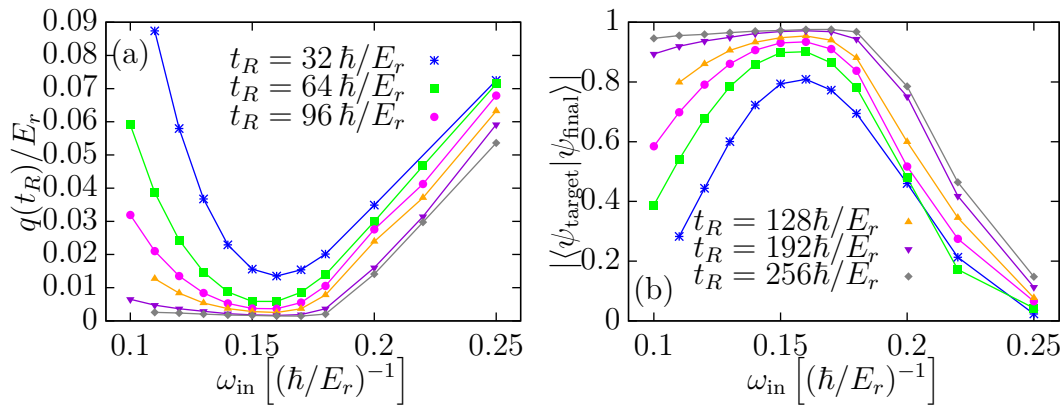


Figure 14: La variation de (a) un excès de chaleur et (b) la fidélité en fonction de la fréquence initiale. Les différentes couleurs correspondent à des moments différents de la rampe et la légende commune est divisée entre les deux chiffres.

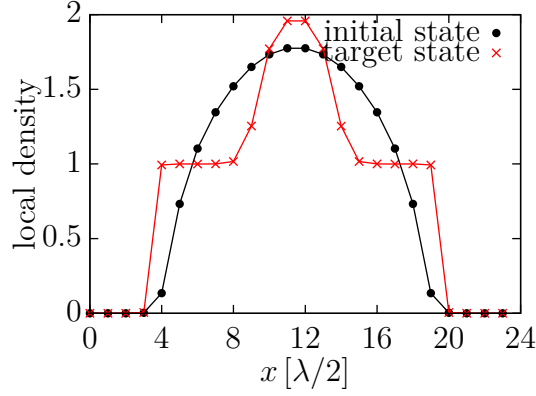


Figure 15: Répartition de la densité locale de l'état initial ( $V_i = 0$ ) et l'isolateur Mott avec un noyau métallique d'état cible ( $V_f = V_0 = 8E_r$ ) intégré sur chaque cellule de l'unité. ( $L = 24$ ,  $N = 20$  particles ( $N_\uparrow = N_\downarrow = 10$ ) with interaction strength  $g = 3 E_r \lambda/2$  and trap frequency  $\omega = 0.25 (\hbar/E_r)^{-1}$ )

La montée en puissance du potentiel du réseau seul montre les effets de chauffage graves et le chevauchement avec l'état cible reste inférieure à 2% même pour les plus longues durées de rampe simulées ( $t_R = 256 \hbar/E_r$ ) de . Pour voir pourquoi même à beaucoup de grands temps de rampe le chevauchement reste exceptionnellement faible, nous suivons l'évolution de la densité locale au cours de la montée en puissance, comme nous le montrons dans la figure. 16 (a). Elle révèle que l'état final présente un noyau avec un nombre important de sites ayant une densité locale de deux particules par cellule unitaire. Le chiffre suggère que l'état, au cours de l'évolution dans le temps, tend vers une avec un noyau bande isolante plutôt que métallique. En outre, la section de l'isolateur Mott de l'état final est également fortement réduite. Ainsi, l'état initial est pas en mesure de redistribuer les particules à suivre la répartition de la densité de l'état cible.

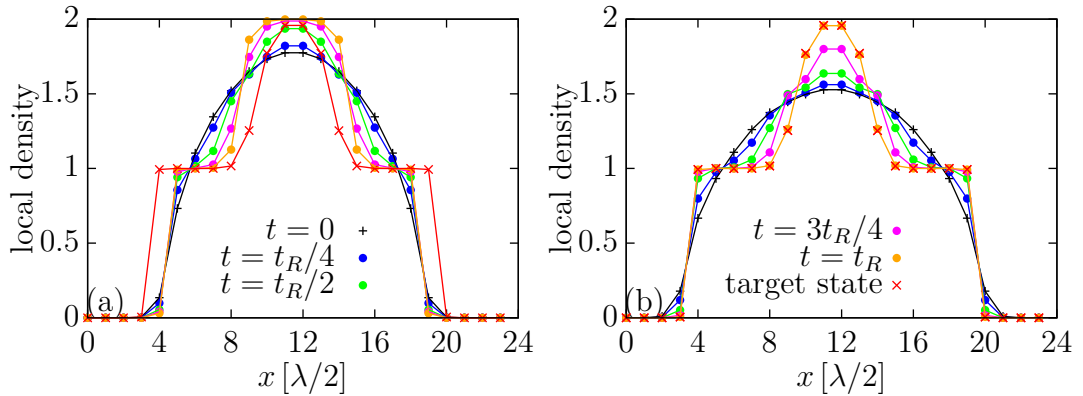


Figure 16: Evolution du profil de densité lors de la montée en puissance pour le temps de rampe  $t_R = 256 \hbar/E_r$  (a) sans accorder la fréquence de piège (b) avec une modulation linéaire de la fréquence, pour la valeur optimale de fréquence initiale ( $w_i = 0,19 (\hbar/E_r)^{-1}$ ). Les croix rouges correspondent à l'état de la cible et la légende commune est partagée entre les deux parcelles.



Afin de réduire ces défauts on syntonise un ou plusieurs paramètres du modèle. Une approche consiste à faire varier la fréquence de piège comme décrit dans la section 3.3.3 pour l'état cible Mott isolant, ce qui donne des parcelles qualitativement similaires comme avant. Cette parvient à améliorer la fidélité par rapport à l'état cible à environ 96% au moment de la rampe  $t_R = 256 \hbar/E_r$  pour l'état optimal qui est observé à  $\omega_{\text{in}} = 0,19 (\hbar/E_r)^{-1}$ . L'excès de chaleur est également réduite de manière significative. L'évolution temporelle de l'état avec ce protocole de chargement modifié est représenté sur la figure. 16 (b).

Cet état optimal présente deux caractéristiques, tout d'abord qu'il imite l'état cible dans l'étendue de la distribution de densité et d'autre part, il abaisse la valeur de crête de la densité à l'état initial. La première caractéristique est intuitivement évident alors que le second est justifié que le noyau métallique ne dispose que de quelques sites avec le plus élevé possible densité locale pour les fermions, à savoir très peu de sites dans le noyau sont proches en occupation double. Le degré accru de la distribution de densité dans les aides initiales de l'état dans l'amélioration de l'évolution vers le régime souhaité isolant de Mott tout en réduisant le pic autour du centre du piège entraîne l'état initial vers le noyau métallique ciblé et non pas une bande isolante.

De plus, nous simulons un calendrier de chargement où la force d'interaction est modulée au cours de la rampe selon l'équation. (11). Cette approche fournit également une hausse qualitativement semblable dans la fidélité. Bien que la valeur réelle de la fidélité maximale est légèrement plus faible dans ce cas par rapport à la procédure de mise en forme de piège, il est facilité dans la mise en œuvre expérimentale devrait rendre cette approche extrêmement utile. Figure. 17 (a) montre la fidélité en fonction de la force d'interaction pour différents temps de rampe. Il est évident que ce protocole conduit à un régime optimal plus étendue lorsque la fidélité est maximisée. Une tendance similaire pour l'évolution de la densité locale avec la plus longue durée de rampe est observée comme dans la figure. 16 (b) à partir de l'état initial avec la force d'interaction se trouvant sur le plateau optimal.

Une autre approche pourrait être de combiner les deux approches ci-dessus. Dans un tel scénario, nous avons mise au point à la fois la force d'interaction et de la fréquence d'interruption pendant le chargement du treillis. Cela pourrait être bénéfique de certaines expériences où le réglage d'un paramètre est accompagné d'une modulation automatique dans un autre. Dans nos simulations, nous voyons que la modulation linéaire à la fois la fréquence de piège et de la force d'interaction, à partir d'un bon état de candidat, distribue efficacement les particules pendant le chargement du réseau.

Afin de tester ce système, nous choisissons une valeur de la fréquence de piège se trouvant dans la région optimale de mise à l'échelle, puis varier la force d'interaction pour trouver un bon état de candidat comme l'état initial. Nous essayons plusieurs valeurs de  $(g_{\text{in}}, \omega_{\text{in}})$  afin d'obtenir un état qui correspond à nos deux propriétés qualitatives essentielles et se révèle être un bon état initial ainsi. Un tel état est obtenu pour  $\omega_{\text{in}} = 0,16 (\hbar/E_r)^{-1}$ ,  $g_{\text{in}} = 1.4 E_r \lambda/2$ . Cette recherche de l'état

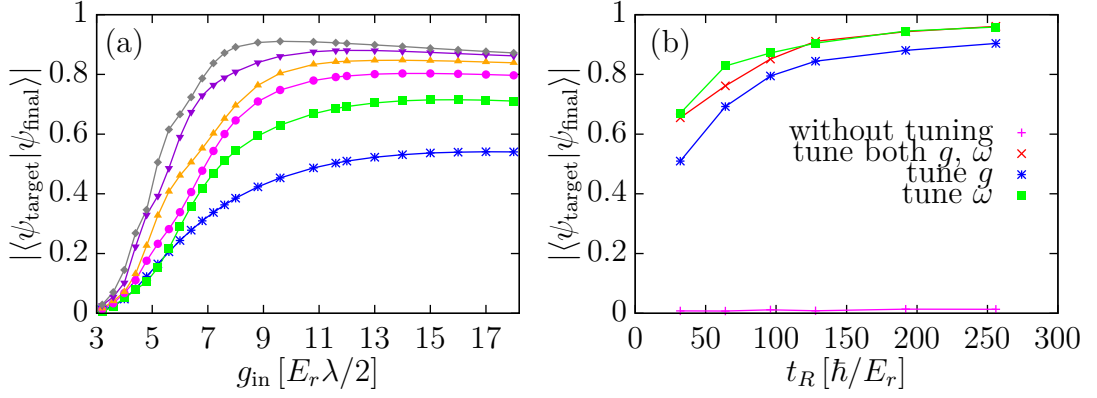


Figure 17: (a) Variation de la fidélité en fonction de la force d'interaction. Les différentes couleurs correspondent à des moments différents de la rampe. schéma de couleur reste identique à la figure. 14, (b) Comparaison du comportement de mise à l'échelle de la fidélité pour différents protocoles réseau de chargement. Courbe rose montre la procédure la plus simple de chargement où la profondeur de réseau est rampe sans aucun changement dans les autres paramètres du modèle. Les courbes bleues, rouges et vertes représentent respectivement la mise à l'échelle de la fidélité des protocoles modifiés, respectivement, où la force d'interaction, la fréquence de piégeage, ou les deux sont simultanément modulées au cours de la rampe.

optimal est nullement complète, on pourrait certainement étudier un plus grand nombre de paramètres pour arriver à un état qui surpasse les autres systèmes par une bonne marge.

Fig. 17 (b), nous montrons la fidélité en fonction de rampe pour les états optimaux obtenus dans chaque protocole afin de les comparer. Pour cet état cible, tous les trois approches mentionnées ci-dessus fonctionnent bien. Une amélioration significative de la fidélité est observée, et il existe un état optimal lorsque la valeur maximale est atteinte. Le plus simple, où aucun des paramètres à l'exception de la profondeur du réseau sont modulés au cours de la rampe (courbe rose) montre exceptionnellement basse fidélité, la valeur restant proche de zéro et une mauvaise mise à l'échelle avec le temps de la rampe. Même avec une rampe beaucoup plus lente, on ne serait pas attendre à une augmentation remarquable de la fidélité. Toutes les autres approches où un ou plusieurs paramètres sont des airs lors du chargement du réseau effectuent bien mis en évidence par une augmentation significative de la fidélité. Bien que le réglage de la force d'interaction (courbe bleue) des tarifs légèrement inférieurs aux deux autres protocoles que nous avons conçu, il ne se révèle être le paramètre le plus facilement accessible dans des expériences, ce qui rend ce protocole intéressant. Les deux autres méthodes échelle aussi bien pour les états optimaux représentés sur cette figure. Notre comparaison est basée sur l'état optimal que nous avons atteint en essayant quelques valeurs initiales  $\omega$  et  $g$ .

Nous concluons que toutes les approches où les paramètres du modèle sont accordés afin de redistribuer la densité efficacement, fournissent une amélioration

significative dans la fidélité. Cela met en évidence une fois de plus que les défauts de densité sont une cause importante de chauffage qui peut être résolu en ajustant les paramètres du modèle de redistributions de particules inférieures.

## 4 Conclusions et perspectives

Dans cette thèse, nous avons étudié échelles d'anyons de Fibonacci à deux et trois chaînes dopés et cartographié leurs diagrammes de phase. Dans la limite forte de couplage des échelons, nous trouvons plusieurs phases différentes: des phases totalement gappées, des phases appariés décrites par des bosons à noyau dur, les phases "golden chain", des phases  $t$ - $J$  qui portent des anyons  $\tau$  et des particules triviales et enfin la  $\tau$  phase lourde et légère de que porte deux saveurs d'anyons de Fibonacci. Cependant, en plus des phases connues existantes (bosoniques, "golden chain",  $t$ - $J$ ), notre étude des échelles de Fibonacci dopées a révélé un nouveau  $\tau$  modèle lourd-léger de qui peut éventuellement produire un entrefer topologique gappé pour certains remplissages spéciaux, ou une phase critique dans les autres cas. Pour chacune des étapes mentionnées ci-dessus, nous avons construit des modèles analytiquement efficaces à basse énergie, et ils en effet montré que corroborent les simulations numériques.

Un point important mis en place dans cette étude des anyons est que nous pouvons relier les échelles de Fibonacci en 2D dopées à des modèles 1D effectifs d'anyons Fibonacci, dont certains ont été bien étudiés dans le passé. En introduisant l'idée d'un spectre de différence d'énergie et en construisant notre relation avec des modèles 1D effectifs, nous avons montré que le phénomène responsable de la séparation spin-charge existe encore, même en deux dimensions sur des échelles de anyons non abéliens.

La projection sur des modèles 1D effectifs permettrait à ces modèles d'échelle d'interaction d'anyons d'être facilement simulé numériquement par des algorithmes 1D efficaces tels que DMRG qui pourrait éventuellement répondre aux questions ouvertes pour le  $\tau$  modèle lourd-léger et nous donner plus de d'indices sur la physique de ce modèle.

Pour notre travail sur fermions dans les réseaux optiques, nous avons exploré différents états cibles à savoir les états métalliques, les états de Mott et les états qui admettent la coexistence des phases isolantes telles qu'un état de Mott avec le métal ou d'une bande isolante de cœur. Bien que le chargement d'un réseau sur un intervalle de temps fini est une déviation par rapport à la limite adiabatique, il a été observé que pour certains états cibles, l'accroissement de la fidélité avec le temps de rampe est extrêmement lent, suggérant d'autres causes possibles de la génération de chaleur excessive.

Notre principal résultat est que la redistribution de la densité est la cause la plus importante pour l'excès de chaleur produite dans le système, rendant impossible aux expériences de parvenir à une aussi basse température dans le réseau que

celle obtenue dans le nuage atomique initial. Cette constatation nous incite à trouver des moyens d'adapter la distribution de densité pendant le chargement du réseau afin de la maintenir qualitativement et quantitativement similaire à celle de l'état cible souhaité. Le problème physique fournit de nombreux paramètres qui pourraient être accordés afin de minimiser les effets de la non-adiabaticité.

La fréquence du piège harmonique sous-jacent permet de moduler le profil de densité lors du chargement du réseau. En outre, la force d'interaction nous permet même de remodeler le profil de densité plus facilement, car sa force peut être réglée dans les expériences en cours au moyen de résonances de Feshbach. Une autre approche pourrait être de traiter plus d'un paramètre simultanément. Nos simulations numériques montrent que les trois approches sont toutes aussi efficaces, laissant ainsi de la place pour sélectionner celle qui convient le mieux à la configuration expérimentale.

Ce travail semble nous indiquer que l'examen de la répartition de la densité locale pendant le chargement du réseau ouvre la voie à de nombreuses nouvelles idées qui pourraient bien améliorer méthodes expérimentales actuelles dans le domaine des atomes froids, pour réaliser des températures plus basses à la fois dans les systèmes de bosons et de fermions. Un grand nombre de chemins possibles pourraient être explorés afin de comprendre le processus de chargement du réseau. Par exemple, on pourrait essayer d'optimiser la procédure de chargement pour évaluer quelle forme de rampe pourrait être la mieux adaptée pour le système, ou si la montée en puissance devrait être monotone ou non. Un autre aspect qui pourrait être sondé est d'étudier différents potentiels de piégeage, par exemple un piège anharmonique. Ces pièges anharmoniques pourraient être étudiés pour des bosons, fermions ou des mélanges dans les réseaux optiques à une dimension.



## Investigation of exotic correlated states of matter in low dimension

Quantum statistics is an important aspect of quantum mechanics and it lays down the rules for identifying different classes of particles. In this thesis, we study two projects, one that surveys models of Fibonacci anyons and another that delves into fermions in optical lattices. We analyse the physics of mobile non-Abelian anyons beyond one-dimension by constructing the simplest possible model of 2D itinerant interacting anyons in close analogy to fermionic systems and inspired by the previous anyonic studies. In particular, we ask the question if spin-charge separation survives in the ladder model for non-Abelian anyons. Furthermore, in the study of this model, we have found a novel physical effective model that possibly hosts a topological gapped state. For fermions in one dimensional optical lattices, we survey the effects of non-adiabatic lattice loading on four different target states, and propose protocols to minimise heating of quantum gases. The evaporative cooling of a trapped atomic cloud, i.e. without the optical lattice potential, has been proven to be a very effective process. Current protocols are able to achieve temperatures as low as  $T/T_F \approx 0.08$ , which are lost in the presence of the optical lattice. We aim to understand if defects caused by poor distribution of particles during lattice loading are important for the fermionic case, forbidding the atoms to cool down to the desired level. We devise improved ramp up schemes where we dynamically change one or more parameters of the system in order to reduce density defects.

*Keywords: Topological, correlated, low dimension, anyons, fermions, optical lattices*

## Étude d'états exotiques corrélés de la matière en basse dimension

La physique statistique quantique formule les règles permettant de classifier les différentes particules. Dans cette thèse nous avons étudié deux projets, l'un portant sur les anyons dits de "Fibonacci" et l'autre sur les fermions sur réseau optique. Ici, nous avons naturellement étendu cette étude aux cas pertinent d'anyons itinérants en interaction sur des échelles. Notre but a été de construire le modèle 2D le simple possible d'anyons itinérants en interaction, analogue direct des systèmes fermioniques et inspiré par les études précédentes. En particulier, nous nous sommes demandé si la séparation spin-charge, bien connu à 1D, pouvait subsister dans le cas d'anyons sur une échelle. De plus, dans l'étude de ce modèle, nous avons découvert une nouvelle phase incompressible pouvant présenter un caractère topologique. Dans le cas des fermions confinés sur un réseau optique unidimensionnel, nous avons étudié les effets d'un chargement non-adiabatique et proposé des protocoles visant à minimiser le réchauffement du gaz quantique. Les atomes ultra-froids sur réseau optique constituent une réalisation idéale pour étudier les systèmes fortement corrélés soumis à un potentiel périodique. Le refroidissement évaporatif d'un nuage d'atomes confiné, c.a.d. sans le potentiel du réseau, s'est avéré être un processus très efficace. Les protocoles courants permettent d'obtenir (pour des fermions) des températures aussi basses que  $T/T_F \approx 0.08$ , impossible à réaliser en présence du réseau optique. Notre étude concerne les effets de redistribution de densité pour un système 1D de fermions. Notre but était de voir si des défauts causés par la mauvaise répartition des particules lors du chargement du réseau optique pouvaient empêcher les atomes de se refroidir jusqu'à la température voulue. Nous avons conçu des scénarii améliorés où certains paramètres sont modifiés de façon dynamique afin de réduire la densité de défauts créés.

*Mots-Clés : Topologiques, corrélées, faible dimension, anyons, fermions, réseaux optiques*